Robust GNSS Point Positioning in the Presence of Cycle Slips and Observation Gaps

John Akhagbeme Momoh

Space Geodesy and Navigation Laboratory
Department of Civil, Environmental and Geomatic Engineering
University College London (UCL)
United Kingdom

May 2013

Supervisors:

Professor Marek Ziebart

Doctor Paul Groves

Thesis submitted for the degree of Doctor of Philosophy

I, John Akhagbeme Momoh, confirm that the work presented in this thesis is my own. Where information has been derived from other sources, I confirm that this has been indicated in the thesis.

Signature: .....

Date: .....

Abstract

Among the various factors limiting accurate positioning with a Global Navigation Satellite System (GNSS) is the inherent code error level on a code observation, cycle slip occurrence on a phase observation, inadequate accuracy in the broadcast ionospheric model for single-frequency receivers; and the occurrence of observation gaps, which are short duration satellite outages (temporal loss of an observed satellite).

The existing Cycle Slip Detection and Correction (CSDC) techniques are usually multi-satellite based; quite computationally intensive; and are often marred by the inherent code errors from the included code observations. Also, existing code-carrier smoothing techniques employed to mitigate code errors are limited by cycle slip occurrences on phase observations.

In this research, algorithms are proposed in order to facilitate simple, efficient and real-time cycle slip detection, determination and correction, on a standalone single- or dual-frequency receiver; to enable cycle-slip-resilient code errors mitigation; and to improve the broadcast ionospheric model for single-frequency receivers. The proposed single-satellite and phase-only-derived CSDC algorithms are based on adaptive time differencing of short time series phase observables. To further provide robustness to the impact of an observation gap occurrence for an observed satellite, post-gap ionospheric delay is predicted assuming a linearly varying ionospheric delay over a short interval, which consequently enables the dual-frequency post-gap cycle slip determination and code error mitigation.

The proposed CSDC algorithms showed good performance, with or without simulated cycle slips on actual data obtained with static and kinematic GNSS receivers. Over different simulated cycle slip conditions, a minimum of 97.3% correct detection and 79.8% correctly fixed cycle slips were achieved with single-frequency data; while a minimum of 99.9% correct detection and 95.1% correctly fixed cycle slips were achieved with dual-frequency data. The point positioning results obtained with the proposed methods that integrates the new code error mitigation and cycle slip detection and correction algorithms, showed significant improvement over the conventional code-carrier smoothing technique (i.e. a standalone Hatch filter, without inclusion of any cycle slip fixing method). Under different simulated cycle slip

scenarios, the new methods achieved 25-42% single-frequency positioning accuracy improvement over the standalone Hatch filter, and achieved 18-55% dual-frequency positioning accuracy improvement over the standalone Hatch filter.

Acknowledgments

First, I remain grateful and thankful to God Almighty for granting me wisdom and the enablement to sustain this academic pursuit. I also acknowledge and appreciate the support of my sponsor, the National Space Research and Development Agency (NASRDA) of Nigeria.

For achieving this milestone thus far, I must also acknowledge my ever supporting and encouraging principal supervisor, Prof. Marek Ziebart, and Dr. Paul Groves; Alex Parkins for making available the used kinematic SHIP data, and Christopher Atkins for processing the kinematic SHIP data to generate the reference truth trajectory; Ziyi Jiang, Santosh Bhattarai, Toby Webb, and other research members of the Space Geodesy and Navigation Laboratory at UCL, for their immense contributions and support in many ways.

Dedication

This PhD thesis is wholeheartedly dedicated to my lovely family: my adorable wife, Anita, whose support throughout my academic pursuit away from home is immeasurable; my precious sons, Sean and Evans; and my lovely daughter, Juanita; all of who have remained inspiration and joy to me.

The thesis is also dedicated to my late father, Augustine Momoh, who passed on after I began this long race. Daddy, how I wish you are alive to share in my joy and this God given success of my life.

Contents

List of Figures

List of Tables

Nomenclature

ADS Adaptively Differenced Sequence

ATD Adaptive Time Differencing

CRE Correction Residual Error

DFT Discrete Fourier Transform

DIS Decreasing-to-Increased Sigma

DOP Dilution of Precision

EGNOS European Geostationary Navigation Overlay Service

FD Frequency Domain

FFT Fast Fourier Transform

FIR Finite Impuls Response

GIM Global Ionospheric Maps

GLONASS GLObal NAvigation Satellite System

GNSS Global Navigation Satellite System

GNSS Global Navigation Satellite Systems

GPS Global Positioning System

GPST GPS System Time

GST Galileo System Time

HFT Hatch Filter Technique

IGS International GNSS Service

IPP Ionospheric Pierce Point

KF Kalman Filter

LAAS Local Area Augmentation System

LAMBDA Least-squares AMbiguity Decorrelation Adjustment

LC Linear Combination

LoS Line of Sight

LPF Low Pass Filter

PPP Precise Point Positioning

PSD Power Spectral Density

RF Radio Frequency

RNSS Radio Navigation Satellite Service

RTK Real-Time Kinematic

SBAS Satellite Based Augmentation Systems

TD Time Domain

TECU TEC unit

vTEC Vertical TEC

WAAS American Wide Area Augmentation System

Chapter 1.

Introduction

This chapter gives a background on Global Navigation Satellite System (GNSS), the GNSS receiver observations (measurements) and errors in the observations. It consequently unveils the motivation for this research, the research objectives and a brief outline of the entire thesis.

1.1. Background

The Global Positioning System (GPS) of the United States, and the Russian GLObalnaya NAvigatsionnaya Sputnikovaya Sistema (GLONASS), are examples of radio-based satellite navigation system generally called GNSS. Both GPS and GLONASS were intended originally for their military use with limited civilian access to the satellites' signals and services. Today, the emergence of high precision commercial and civilian applications of GNSS has revolutionized technological development in positioning, navigation and timing, whilst also enabling estimation and modeling of some geophysical and environmental phenomena. Unlike GPS and GLONASS, the imminent evolution of civilian-controlled GNSS such as the incoming European Galileo and the Chinese Beidou (Compass), would further increase users' exploitation and dependence on GNSS technology (Gleason & Gebre-Egziabher, 2009). However, depending on the application, the uptake of GNSS could be impeded by its limited accuracy and degraded integrity due to inherent errors in the measurements. Though a global system with global coverage, stand-alone GNSS performance also

deteriorates in indoor use and in urban environments (Bensky, 2008) due to limited availability and deterioration of tracked signals, as a result of blockages, reflection and attenuation of the GNSS signals.

The space segments of the aforementioned GNSSs are different in composition, as could be observed from the depictions in Figure 1.1, which depicts the GPS and Galileo constellations.

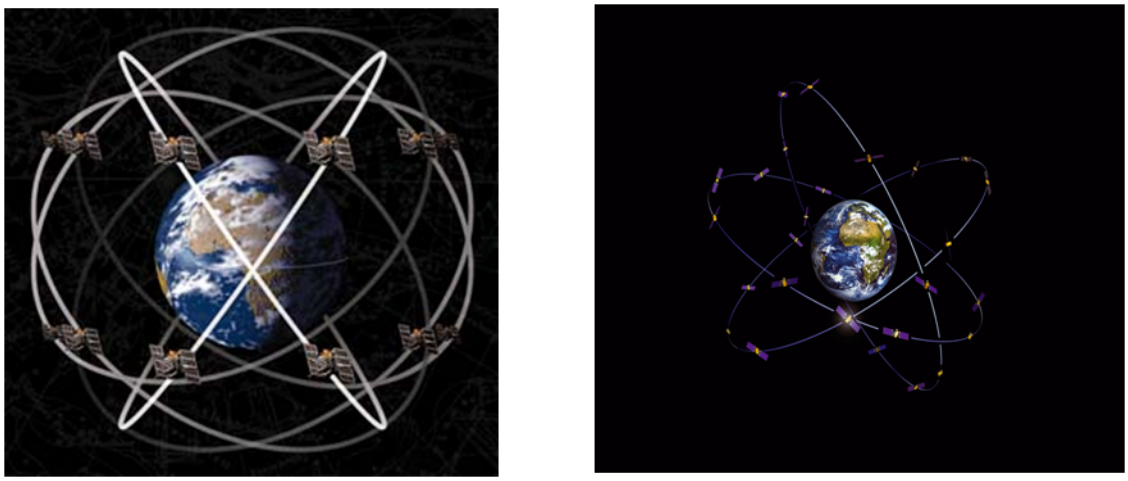

Figure 1.1.: Depictions of GPS (left) and Galileo (right) constellations. The depiction of the GPS constellation is obtained from http://nislab.bu.edu/sc546/546projects/langdon/const.jpg, accessed 26 November, 2010; and the depiction of the Galileo constellation obtained from http://www.ukspaceagency.bis.gov.uk/assets/channels/ our_planet/2-Galileo_System.jpg, accessed 26 November, 2011

The GPS constellation now consists of more than the nominal 24 satellites in 6 equally spaced orbital planes with uneven distribution of at least 4 satellites in each orbital plane so as to minimize outage (Hegarty, 2006). The satellites orbital period is half a sidereal day which is approximately 12 hours, with altitude of about 20,000km and an inclination angle of 55 degrees. The restored GLONASS, with additional satellites launched in November 2011 (RSA, 2012) completed the envisaged full orbital constellation of 24 satellites, enabling its full global coverage. The GLONASS constellation has 3 orbital planes, orbital altitude of about 19000km and period of 11hr 15mins, and with 64.8 degrees inclination. The European Union Galileo has been initiated by the GIOVE-A and GIOVE-B test satellites launched in 2005 and 2008 respectively (Waller *et al.*, 2008). As depicted in Figure 1.1, it is planned as a constellation of 27 satellites in 3 orbital planes, with

period of 14hr 4min, altitude of about 23000km and inclination of 56 degrees. The developing Compass with a few satellites already launched has also been reported to target a complete constellation of 35 satellites including satellites in geostationary/geosynchronous orbits. It became operational with coverage over China in December 2011 with 10 satellites in use and it is planned to offer services to customers in Asia-Pacific region, while the global system should be finished around 2020 (Beidou, 2012)

1.1.1. GNSS Operation

GNSS radio frequency (RF) bands are included in the allocated Radio Navigation Satellite Service (RNSS) spectrum that also includes part of the Aeronautical Radio Navigation Services (ARNS) spectrum. Within this spectrum, GPS operates as a Code Division Multiple Access (CDMA) system where each satellite in orbit has a unique pseudorandom noise (PRN) code (a unique 1023-long PRN code is also used to identify a particular GPS satellite). The broadcast navigation message from a satellite is represented by a sequence of binary digits called bits. A pseudorandom noise sequence is represented by a sequence of binary digits called chips, which are used to spread a satellite's navigation message. They are called chips to avoid confusing them with the message bits of a navigation message. The codes essentially do not contain information because both satellites and GPS receivers already know them and their generation patterns. The GPS codes include the 1023 chips long code with a chip rate of 1.023Mcps, which is broadcast as the civilian standard positioning service (SPS) referred to as coarse acquisition (C/A) code; and the $\sim 10^{14}$ chips long code with a chip rate of 10.23Mcps, which is broadcast as the precise positioning service (PPS) called P(Y) code. The codes are used for spreading the 50bps navigation message from a satellite (GPS-800A, 2010), knowing that each navigation message bit has a bit duration that comprises the duration of multiple chips. Compared to the autocorrelation of a satellite code, the low cross correlations between any two satellites' codes (PRNs) significantly mitigates their interference even though the satellites broadcast at the same frequencies. The spread binary navigation message, by binary phase shift keying (BPSK) modulation, modulates

the radio frequency (RF) carrier frequencies of 1575.42MHz (used for C/A and P(Y)) and 1227.6MHz (used for P(Y)) of the GPS satellites, respectively on the L1 and L2 bands. A satellite broadcasts the resulting modulated signal downwards to users' receivers. There is however the ongoing GPS modernisation for both civil and military use. The modernisation unveiled in McDonald (2002) includes the addition of two new civil signals to be broadcast on the L2 band called L2C, and the new L5 band with a broadcast carrier frequency of 1176.45MHz. The new block IIF satellites currently broadcast the L5 signal, and the block III satellites that would include another civil signal on the L1 band (L1C) and military code (M code) are envisaged to be launched after 2013 (SpaceComm, 2012).

The original GLONASS basically operates as a Frequency Division Multiple Access (FDMA) system where each satellite uses same pseudorandom code to spread its navigation message and broadcasts on its specific carrier frequencies. The earlier L1 and L2 bands allocations were G1 (1598.0625 - 1607.0625 MHz) and G2 (1242.9375 - 1249.9345 MHz). The carrier frequencies in both bands are in different channels (bandwidth) and are multiples of the channel spacing; the channel spacing being 0.5625MHz for G1 and 0.4375MHz for G2. Like GPS, the different GLONASS pseudorandom codes: the 511 chips long code at a chipping rate of 0.511Mcps is its C/A-like code while the 511000 chips long code at 0.511Mcps is its P(Y)-like code. Both codes on both bands are used for spreading the same 50bps navigation message before using the spread message to modulate the different satellite bands' carrier frequencies. Same channels are assigned to satellites on the opposite sides of the earth to accommodate the planned 24 satellites (Misra & Enge, 2006) thereby mitigating co-channel interference in the orthogonal FDMA system of GLONASS. GLONASS is also currently evolving; the inclusion of other signals, and transition to a CDMA GNSS system is underway (Revnivykh, 2011). As from 2014, the GLONASS-K2 satellites will have an FDMA signal in the L1 and L2 bands and CDMA signals in L1, L2, and L3 bands, and the constellation update is planned to be completed in 2021 (RSS, 2012a)

Galileo is planned to provide different services in different bands within the RNSS spectrum. These services are: the Open Service (OS) patterned after the GPS

SPS; the signal-encryption-controlled access services, namely, Safety of Life Service (SoL), the Public Regulated Service (PRS), and the Commercial Service (CS) service. Based on CDMA, each Galileo satellite is planned to transmit ten navigation signals but the Open Service will be transmitted in three of the frequency bands, which are E5a, E5b and E1/L1. The carrier frequencies for the Open Service signals in the E5a, E5b and E1 bands are respectively 1176.45, 1207.14 and 1575.42MHz. The navigation message data rates of 25bps and 125bps, and chip rates of 1.023Mcps and 10.23Mcps would be used for the different services.

The ground control segment of a GNSS includes a network of monitoring/tracking stations at precisely known positions in the defined reference frame of the GNSS, which are usually distributed across the globe or within a region of the globe. Part of the ground segment also includes a number of atomic frequency standards (clocks) that may be combined with the satellites' space-qualified on-board atomic clocks to define the system time of the GNSS. The GPS satellites on-board clocks across the different blocks (II/IIA, IIR/IIR-M, IIF) are either of the cesium or rubidium type, which have good enough frequency stability (Oaks *et al.*, 2005, 2007), thus minimizing a satellite's clock drift/offset from the GNSS system time over a span of several hours. The heart of the control segment of the currently fully functional GPS, called the master control segment (MCS) located in Colorado Springs in the United States of America, employs the measurements of the GPS monitoring stations based on its defined system time called GPS time (GPST), to generate some of the parameters in a navigation message. These parameters include satellite clock correction parameters, satellite ephemeris, etc. The MCS estimates, among others, satellites' positions, velocities satellites' clock offset and drift (frequency offset) and clock drift rate. These estimated parameters are then used to propagate satellites' positions and clock corrections into the future (called prediction). The predicted values are then fit to a set of equations and the fit coefficients uploaded as the broadcast ephemerides in the navigation message (Warren & Raquet, 2003). Though there could be slight differences in the ground control segments of the different GNSSs and their clocks composition and system time derivation, the fundamental constituents of a navigation message are usually similar.

GNSSs users see the presence of all GNSSs as added advantage as such could provide a receiver the opportunity to combine different GNSSs signals to improve positioning accuracy and availability. However, to actualize this possible advantage, the fundamental challenges of the time differences between the different systems' times and the difference in the coordinate reference frames need to be resolved, knowing that a same receiver can be positioned to different position coordinates by different GNSSs. These problems are being addressed as observed in Bykhanov (1999); Piriz *et al.* (2006). Moreover, with more GNSSs satellites in space, the positioning accuracy of a receiver would be affected by the number of satellites in view, and the satellites' distribution in space with respect to the receiver - the receiver-satellite geometry. The receiver-satellite geometry manifests as a dilution of precision (DOP) value that amplifies the positioning error. This DOP value is higher when the visible satellites distribution in space is 'poor' - appearing to be 'clustered' in a given direction; and low when all visible satellites are widely distributed in space with respect to the receiver (Groves, 2008).

1.1.2. User Segment and Observations

GNSS receivers of various types and capabilities exist today in the market, ranging from the cheap single-frequency low accuracy ones found in many mobile devices, to the more accurate and expensive multi-frequency ones such as used in geodetic and surveying applications. A user of GNSS essentially receives the GNSS broadcast signal received in one or more bands by the receiver antenna, and processed by the receiver to estimate the user (antenna) position, velocity and timing information.

The pseudorange between the satellite and the receiver antenna is obtained as the product of an estimated transit time and the speed of light, $c = 299792458$m/sec. This code pseudorange measurement is often called the code pseudorange observation.

Another measurement is the accumulated carrier phase from a given GNSS band, which can be referred to as phase observation. It is measured in number of cycles of the band nominal RF carrier frequency that is internally generated at the receiver carrier tracking loop. The receiver accumulates the phase differences between the

incoming satellite RF carrier signal phase and the receiver generated carrier phase since the starting point of an interval while the satellite remain tracked (Leick, 2004). It is the instantaneous phase difference plus the change in integer number of the carrier cycles in the interval. This accumulated carrier phase observation more effectively reflects the changes in distance between the receiver and the satellite compared to the code observation. The receiver could also measure the frequency shift (w.r.t the nominal frequency) in the incoming RF carrier frequency, called the Doppler shift, which is caused by the relative motion of the satellite and the receiver. The rate of change of the carrier phase observation gives the pseudorange rate while the accumulated Doppler or accumulated delta range (ADR) is the integral of the pseudorange rate over an interval, i.e. the change in the carrier phase observation over a certain time interval (Groves, 2008).

Most dual-frequency receivers, especially the geodetic types, measure and output the observed code and phase observations; while some receivers, in addition, also output the Doppler observations, observed from all the GNSS bands accessible by the user receiver. Most single-frequency receivers would output, at most, the code and phase observations if not only the code observation.

1.1.3. GNSS Performance Limitation Due to Errors

The phase and code observations from a GNSS satellite are contaminated by GNSS inherent system errors, in addition to the errors due to the impact of the environment in which the receiver and its antenna operate. The scope of errors limiting GNSS performance include atmosphere-induced errors, the GNSS satellite position and clock errors, multipath error, GNSS receiver clock error and random noise, errors caused by natural phenomena, etc. These errors originate from different sources. The broadcast GNSS satellites ephemerides and clock models are imperfect and contribute as system inherent error sources; the atmosphere-induced errors, composed of the ionosphere and troposphere induced errors (delays), are introduced as the transmitted signals from the GNSS satellites propagate through the ionosphere and troposphere to a downward receiver; while errors due to ocean and earth tides are consequences of natural phenomena. A transmitted signal often gets reflected by

objects within a GNSS receiver antenna environment, thus regenerating the signal replicas with various magnitudes and phase angles, which later recombine at the receiver antenna. This phenomenon called multipath could contribute tens of metres of multipath error on the L1 code pseudorange observation and up to 4.8cm on the L1 carrier phase observation (Kalyanaraman *et al.*, 2006). The absolute error limit on the C/A code observation due to multipath is around 150m. The instability in a receiver clock oscillator is a source of receiver clock error; and the receiver random noise is influenced by the receiver design components and/or the receiver type.

Both the code and carrier phase observations are affected by errors. The combined effect of these errors on the code pseudorange observation, called the User Range Error (URE), is usually up to tens of metres. The level of the error on the phase observation is much less than that on the code observation.

The observations from GNSS satellites allows for a variety of applications. Primarily for positioning, navigation and timing related applications, GNSS also enable estimation and modelling of some parameters such as the ionospheric total electron content. However, the performance of a GNSS in any one application is limited by the errors in the observation(s) from the GNSS satellites. For instance, the errors result in degraded positioning accuracy and precision - a negative impact in a critical application like surveying. The magnitude of the positioning error across C/A-code only receivers could be up to tens of a meter.

A GNSS performance is also limited in difficult environments such as urban canyons, where observation gaps or discontinuities are prevalent due to blockages. Observation gaps can cause frequent changes in the unknown integer ambiguity value (often referred to as cycle slip error (Kim & Langley, 2001)) in a phase observation, and consequently, phase ambiguity resolution could become frequent. The resolution of integer ambiguities is often a non-trivial process as the inherent errors often make the ambiguity fixing/resolution/determination process require long convergence time before a reliable post-gap fix can be obtained. This implies that before a post-cycle-slip ambiguity fix, the obtained precision and positioning accuracy would be degraded.

1.1.4. The Observation Error

Error corrective models do exist for 'correcting' (actually minimizing) some of the errors in GNSS observations. For instance, tropospheric, ionospheric, and earth and ocean tides errors can be minimised by using generalized corrective models such as applied in Le & Tiberius (2007). Moreover, GNSS satellites clocks and orbital position errors, errors due to antennae phase centre variations, are also corrected to a reasonable level through the use of corrective models generated with the correction parameters in the GNSS broadcast ephemerides or by accessing externally generated corrections. The application of an external error corrective model is often dependent on the accuracy required for a GNSS application, and also whether the external corrections can be obtained or are needed in real-time or not. However, due to limited accuracy in these error corrective models, residual error dubbed in this thesis as correction residual error (CRE), often results after the applications of such corrective models (Le & Tiberius, 2007).

Moreover, the multipath error, the receiver random noise and clock error, and all other unmodelled errors, which contribute largely to the error levels in GNSS observations, are not eliminated by any known generic corrective models. This is mainly because multipath error is quasi-random in nature and the receiver noise and clock errors are non-deterministic. Being localised, multipath error and noise are dependent on a receiver antenna environment and the user receiver itself.

In this research work, the combination of CRE, multipath error, receiver noise and clock error, and all other unmodelled errors in the used functional model of a GNSS phase or code observation, defines what is here referred to as the observation error in that phase or code observation. The level of the observation error in a code observation is significantly higher than the level of the observation error in a phase observation because of the higher multipath error and receiver noise on a code observation. The ultimate goal would be to eliminate the observation error in a given code or phase observation.

1.2. Motivation

The inherent observation error levels, especially on code observation from observed GNSS satellites, limit both the GNSS positioning performance and its application. Even after applying available or accessible error corrective models to a GNSS code observation to minimize those errors that have corrective models, the level of the left-over code observation error, which is often dominated by combined noise and multipath error in the GNSS code observation, is usually significant and capable of degrading positioning accuracy and precision. Also worrisome is the fact that the magnitude of uncorrelated errors would increase when any two raw code or phase observations are differenced or linearly combined, in a bid to eliminate other errors or parameters, or to estimate a combination parameter. Known cycle slip detection and correction algorithms such as given in Bisnath (2000); Banville & Langley (2009), apply such linear combination (LC) observables[1], and such detection and correction could be marred by the level of combined code observation error in the such LC. Developed techniques concentrating on mitigating the combined receiver noise and multipath error, as found in Hatch (1982); Gunther & Henkel (2010); Satirapod *et al.* (2003); Lau & Cross (2007), do exist, and will be reviewed in Chapter 3. However, none of these existing techniques has capability to mitigate the unwanted code observation error(s) when cycle slip(s) occur on the more precise phase observation(s) from a given satellite.

Positioning performance of a GNSS can also be degraded due to cycle slip occurrences in the phase observations. Cycle slips are big error sources, especially when they are not detected and corrected. Many known cycle slip detection algorithms exist for dual-frequency receivers only, e.g. (Banville & Langley, 2009), and depend on dual-frequency code observations that are usually affected by relatively large code observation errors. As such, a reliable and accurate cycle slip detection with these techniques could be impeded, since they involve code observations. Some

[1] In this thesis, the term *observation* is used to refer to a receiver's measurement, such as the raw code or phase observation, while the term *observable* is used to refer to the output obtained after any processing of the raw observation(s) that may include differencing, linear combination, filtering, applied corrections, etc.

of the techniques used for fixing cycle slip float values to integer values are similar to conventional ambiguity resolution techniques that involve large search spaces, which in turn leads to high computational workload on the receiver. A more desired goal is to improve the process of cycle slip detection and fixing via a much simpler, faster and less computationally intensive single-satellite phase-only algorithm. Such an algorithm would be attractive for use in a difficult environment where cycle slip occurrence may be rampant.

There is currently no well-defined single-frequency phase-only cycle slip detection and correction algorithm known to the author. Such an algorithm is considered necessary for the many single-frequency receivers that are available and are still being produced till date. The limited accuracy of the broadcast ionospheric model contributes to degrading single-frequency receiver positioning performance, especially in the polar and equatorial regions. Available external ionospheric corrections are not readily accessible in real-time, and many single-frequency receivers are not made-ready or enabled to use external ionospheric corrections. Thus, with a receiver-generated improved ionospheric model, single-frequency users worldwide will be able to achieve improved point positioning (positioning with a single receiver).

Another phenomenon affecting improve GNSS positioning today is the occurrence of observation gaps, which are short duration outages (temporal loss) of a satellite being observed by a receiver. When observation gaps occur, existing ambiguity resolution or cycle slip detection techniques, as well as existing code smoothing techniques, break down as they tend to re-initialise when the receiver re-locks to the temporarily lost (gapped) satellite. This re-initialisation often results in the long convergence time to resolve such post-gap ambiguities and the inability to mitigate code observation errors at a post-gap epoch. This consequently degrades the positioning accuracy and precision at a post-gap epoch and a few other subsequent epochs to a post-gap epoch. Developing a non-reinitialised cycle slip and code error mitigation technique will be a worthwhile solution to this challenge that is common in difficult environments.

In the sequel, this research is motivated by the need to significantly improve GNSS positioning performance by proposing new algorithms/techniques as solution

to the challenges mentioned above. To this end, one is motivated to develop simple algorithms that would achieve significant mitigation of the code observation error levels in the presence or absence of cycle slips; an accurate single-satellite phase-only and non-computationally intensive cycle slip detection and correction algorithm; and a receiver-generated improved single-frequency ionospheric model applicable in real-time, all with a view to enhancing point and relative positioning in all environments, irrespective of the receiver clock type and the receiver mode of operation - static or kinematic.

1.3. Research Objectives

In line with the motivation for this research, three broad objectives were initially set at the start of the research. These were: (i) to develop relevant real-time techniques to improve single-frequency positioning in all environments, with emphasis on an improved ionospheric correction model suitable for use even in the equatorial region; (ii) to adapt these proposed techniques for improved real-time dual-frequency positioning; and (iii) to quantify the comparative performance levels achievable by the proposed techniques via different single- and dual-frequency real-time positioning tests and analyses. The integration and computational load of the proposed techniques were required to be simple enough, to minimise drainage of a receiver's battery power, and ensure suitability for time-critical applications.

Consequently, the research started with the intension to first develop a single-frequency ionospheric correction model primarily suitable for the equatorial region. It became not feasible to acquire single- and dual-frequency data sets from receivers' with known trajectories and within the equatorial region. Moreover, single- and dual-frequency data obtained in difficult environments and with accurately known receiver positions/trajectories could not be acquired within the stipulated time for this research. Subsequently, for the continuation of the research, these initial objectives were later modified and evolved to give the final objectives.

The resulting and final objectives for this research are as follow:

(a) How would a real-time single-satellite phase-only-derived cycle slip detection

and determination algorithm usable by a static or moving single-frequency GNSS receiver be developed? What percentage of correct detection and correct fix of cycle slips do we expect from such an algorithm? This objective is intended to enable a single-frequency receiver detect and correct cycle slips on a single-frequency phase observation in a reliable, simple and non-computationally intensive manner.

(b) How would a single-satellite phase-only-derived cycle slip detection, fixing and validation algorithm, suitable for a dual-frequency receiver operating in either static or kinematic mode be developed? What percentage of correct detection and correct fix of cycle slips do we expect from such an algorithm? This achieved, it is intended to outperform many currently existing techniques that include dual-frequency code observations, which are often bedevilled by the code observation errors. Moreover, being a single-satellite and phase-only-derived algorithm, it is expected to be relatively simple and less computationally intensive for a real time operation.

(c) How can an improved broadcast ionospheric correction model be implemented on a single-frequency receiver in real-time, to enable better ionospheric delay corrections? From a case study, how accurate can such improved ionospheric model be for a single-frequency receiver in the mid-latitude region, and for a single-frequency receiver in the equatorial region? Ability to generate single-frequency ionospheric model with good level of improvement over the broadcast model would enable significant reduction of the ionospheric divergence effect that limits the use of a long filter length in a single-frequency code-carrier smoothing operation. It will also drastically minimise a single-frequency receiver's dependence on external ionospheric correction that may not even be available and accessible in real time; and it is also envisaged to improve single-frequency ionospheric corrections globally.

(d) How should dual-frequency receivers estimate phase-only-derived ionospheric delay in the presence or absence of cycle slips, and predict same in the event of an observation gap with acceptable level of accuracy and precision? Such a more precise phase-only-derived ionospheric delay could help improve ionospheric modelling even in the presence of observation gaps.

(e) Can an efficient code smoothing or error mitigation algorithm that has capabi-

lity to mitigate the code observation error level(s) on the code observation(s) from a satellite, irrespective of cycle slip occurrences on the phase observation(s), be obtained? Can the algorithm be made robust to observation gap occurrence? Compared to the conventional code-carrier smoothing technique, what level of performance improvement in terms of positioning accuracy and precision would it offer? These are required to enable enhanced positioning in both normal and difficult environments, with or without cycle slip occurrences.

(f) How would a common receiver clock jump or reset value be reliably estimated in non-positioning domain in real-time, irrespective of the receiver oscillator type? This is important to eliminate the impact of receiver clock jumps on cycle slips detection and enable possible receiver clock modelling. It is also required to 'decorrelate' the code and phase observations to generate appropriate covariance matrices in real-time as against formulating covariance matrices under the assumption that the observations are not correlated and usage of conjectured uncertainty values.

(g) How can the algorithms to be developed be made robust to an observation gap occurrence, so as to improve positioning accuracy and precision even in difficult environments such as urban canyons? Can the post-gap convergence time usually associated with ambiguity fixes on phase observations and the usual many-post-gap-epoch observation required for achieving significant code error mitigation be reduced or eliminated at a post-gap epoch? Such a robust algorithm should be able to estimate the relative changes in the ambiguities (cycle slips), ionospheric delay, and in the non-dispersive range components, between a post-gap epoch and a pre-gap epoch, so as to avoid the usual re-initialisation in conventional techniques whenever an observation gap occurs.

(h) Identify the possible limitations, if any, in the developed algorithms or techniques and give appropriate measures or recommendations for use and implementation accordingly.

Successfully achieving these objectives would contribute to improving the performance of single- and multi-frequency GNSS receivers used in different static and kinematic applications. One of such applications is real-time positioning where improved positioning accuracy and precision is desired. For instance, a single-frequency

mobile device would require a simple (reduced computational load and thus fast) cycle slip detection and correction algorithm, which would demand low processing power, thus enabling prolong use of a receiver's battery power; an improved ionospheric correction model; and a cycle-slip-resilient code error mitigation algorithm, to improve its positioning solutions when operating in any environment. Precise Point Positioning (PPP) in all environments is also one of the target applications. Code observation error and cycle slip occurrence are major challenges to PPP, especially when operating in a difficult environment where cycle slips can be prevalent. A simple (fast) and efficient cycle slip detection and correction algorithm coupled with a cycle-slip-resilient code error mitigation algorithm are benefits to PPP. Also, time-critical applications are target of this research. For instance, applications whereby cycle slip detection and correction are performed at a master station of a Wide Area Differential GNSS (WADGNSS), that is, a master station processes all the observations from its network of multi-frequency fixed GNSSs receivers and broadcasts the differential corrections, are considered time-critical, as such networks are often used to support real-time operations. A WADGNSS is a near real-time GNSS application where a maximum latency of a few seconds is allowed for the generation and broadcasting of its differential corrections. It is an application where high dimensions of cycle slip (up to tens of cycle slips at a given time epoch) can occur on phase observations from different satellites observed by the different fixed receivers on a network. A fast and efficient cycle slip fixing algorithm is important for such a time-critical and high dimensions application, so as to improve its reliability and efficiency. Examples of such existing WADGNSS include the Satellite Based Augmentation System (SBAS) of the United States, called Wide Area Augmentation System (WAAS), the European Geostationary Navigation Overlay System (EGNOS), and the Japanese Multifunction Transportation Satellite (MTSAT)-based Satellite Augmentation System (MSAS).

1.4. Methodology

In order to achieve the objectives listed above, the required data sets are the single- and dual-frequency raw phase and code observations from satellites, obtained with both static and moving GNSS receivers. Though the developed algorithms are proposed for any GNSS, only GPS data are used in this research as almost any GNSS receiver is designed compatible with GPS, plus the fact that all the data made available for this research are observations from only GPS satellites. It is important to use real GNSS data obtained by receivers with known 'truth' positions so as to have a reference for comparing positioning results, and examining performance. Consequently, observations from GPS satellites are obtained from different reference stations in different parts of the world and on the network of the IGS, to assess the performance of the new algorithms in static domain. Kinematic data set obtained with a dual-frequency GPS receiver and antenna placed on a docking ship, THV Alert, at a jetty in Harwick, United Kingdom, was provided for use in this research. The truth trajectory for this moving ship was generated using Leica Geo Office software, applying the moving ship data as the rover data, and applying the concurrent data obtained from a fixed nearby station (BASE) on the roof of a building within 1km radius of the moving ship as the reference station data. The available single-frequency data sets had no known truth for reference. As a result, the single-frequency analyses presented in this work are based on the L1 band data of the dual-frequency static and kinematic receivers data used for the dual-frequency analysis. However, additional single-frequency code error levels are simulated for some tests to depict more of a typical single-frequency receiver code error level when necessary.

The developed real-time single- and dual-frequency cycle slip detection and correction (CSDC) algorithms are based on Adaptive Time Differencing (ATD) of a single-satellite phase observation(s). The improved single-frequency ionospheric delay correction (IIC) algorithm is based on adaptive digital filtering of the ionospheric observable obtained from differencing a phase observation from a code observation, both obtained from the same satellite band; whilst the dual-frequency slant ionospheric delay on a given satellite observation is modelled as the sum of a constant and

a varying component, using the observable derived from the difference between the satellite's dual-frequency phase observations. The new algorithm for both single- and dual-frequency code error mitigation is anchored on a band's code-minus-phase observable, after a real-time cycle slip detection and fixing, which enables its resilience to phase cycle slip occurrences. To increase robustness and enable continuity without any need for re-initialisation in the algorithms whenever an observation gap occurs for an observed satellite, the ionospheric variation is predicted from the last pre-gap epoch to a current post-gap epoch; the cycle slips determined with reference to the last pre-gap epoch prior to a current observation gap; and the code errors mitigated, whilst also generating seemingly continuous time series observables for subsequent epochs' cycle slip detection.

With the research objectives in mind, the developed algorithms are tested to determine performance and answers to the research questions. Existing GNSS processing software packages give little or no room for modifications, hence GPS data processing programs are developed in C++ and MATLAB environments to enable processing of the acquired GPS data in real-time mode. The developed programs are to also, by way of simulation, enable the investigation and efficiency of the newly developed cycle slip detection, determination and correction algorithms in real-time mode, using both static and kinematic receivers. The developed programs also enables accessing the impact of code errors on the developed algorithms. The cycle slip simulation involves introducing known cycle slips integer values to actual phase observation from a satellite at known epochs. The developed CSDC algorithms attempt to detect and fix such cycle slips to the correct values in real-time. The designed programs also allows and enables a wider scope of experimentation and comparisons.

Using the newly developed algorithms, static and kinematic mode tests are performed to access performance and identify possible drawbacks in the new algorithms. Point positioning solutions (using only code observations) are obtained and compared with code-positioning solutions acquired with the widely used range-domain code carrier smoothing technique (often called Hatch filter) that re-initialises after an observation gap. The cycle slip detection capability of the new technique is inves-

tigated through cycle slip simulation, to determine the level of efficiency of the CSDC algorithms. Actual positioning results affected by observation gap occurrences and simulated observation gaps, are further analysed to examine the robustness of the new algorithms to observation gap occurrences and period of convergence.

Relevant metrics are used to access the performance of the newly developed algorithms. These metrics include the achieved positioning accuracy and precision obtained for static and moving receivers; the ionospheric model accuracy; the percentages of correctly detected and correctly fixed number of simulated cycle slips, using both static and kinematic data sets; the robustness of the gap-connect technique to observation gap occurrence, which can be accessed by comparing the acquired positioning solutions from the gap-connect technique with the positioning solution obtained with a re-initialising (conventional) positioning technique, over observation epochs with significant presence of observation gap occurrences. Compared to the widely used LAMBDA (Least-squares AMBiguity Decorrelation Adjustment (Chang *et al.*, 2005)) method for cycle slip determination, a simpler and consequently less computationally intensive (i.e. faster) cycle slip determination (repair) algorithm is desired, as it is often the case for time-critical GNSS applications. As such, the suitability of the algorithms to be developed, for real-time applications, is crucial, irrespective of a receiver's clock type - it could be driven by a relatively stable (low-drift) or unstable (high-drift) oscillator.

The new algorithms are intended to be generic - useable for observations from any GNSS; independent of the receiver type/manufacturer. As such, the sets of GPS data used in this research are ensured to be so compliant.

1.5. Thesis Outline

This thesis is presented in ten chapters. This first chapter gives an introduction to GNSS and describes the objectives and methodology of research work. The next two chapters of the thesis review relevant literature around the subject matter.

Chapter 2 introduces most of the errors in GNSS observations and where applicable, discusses the generalized corrective models for some of the errors. Chapter 3

reviews some of the techniques employed in mitigating observation error; it reviews the different methods currently applied for cycle slip detection and determination as well as some available ionospheric models. It further highlights possible limitations in some of the existing techniques.

As a preamble to the newly developed algorithms, Chapter 4 covers the relevant signal processing techniques, and presents the foundational knowledge and hypothesis on which some of the newly developed algorithms are based. It discusses signal domains and energy, digital filtering and Adaptive Time Differencing (ATD). In Chapter 5, the new single-frequency phase-only-derived CSDC algorithm; the Improved Ionospheric Correction (IIC) algorithms; and the code error mitigation algorithm are presented. The method for estimating a receiver clock jump detection is also presented in Chapter 5.

The developed dual-frequency algorithms for dual-frequency cycle slip detection, derivation of the phase-only ionospheric delay, and dual-frequency code error mitigation, are all presented in Chapter 6. The technique, dubbed gap-connect technique, developed to mitigate impacts of observation gaps and to enhance robust positioning, is also covered in Chapter 6.

The testing and performance analyses of the newly developed algorithms are covered in chapters 7 and 8. Chapter 7 covers the tests and analyses of all the single-frequency algorithms developed in Chapter 5; presenting the test results and the discussion of the test results obtained from cycle slip simulation and single-frequency positioning performance, and comparisons. The possible limitation of the single-frequency CSDC algorithm is also discussed. Chapter 8 covers the tests and analyses of all the dual-frequency algorithms developed in Chapter 6. The tests including dual-frequency cycle slip testing by simulation and error-mitigated code positioning performance, are analysed and discussed. The proposed gap-connect technique is also examined with simulated observation gap occurrences, as well as examining the impact of observation gaps on positioning. The possible limitation of the dual-frequency CSDC algorithm is also discussed.

Chapter 9 discusses the modernization on current GNSSs, and the signals to be broadcast by future GNSS. The chapter thereafter discusses the impact of such new

and future signals on the newly developed algorithms.

Chapter 10 Summarises the research process undertaken in this thesis, presenting the relevant conclusions drawn to address the objectives of this research. The recommendations for further research are also presented in the chapter.

The appendix covers topics considered relevant to certain areas or techniques mentioned within the body of the thesis, which include least squares and Kalman filtering.

Chapter 2.

Error Sources and Corrections

The sources of some of the errors manifesting in the GNSS observations are reviewed in this chapter. The chapter also introduces the phase and code observation models, some generalized correction models for the atmospheric induced errors, and mitigation of the common mode errors in differenced observations. A further insight is given on the receiver measurement and origin of multipath error. Also, pre-observation multipath mitigation modalities are also discussed.

2.1. Acquisition, Tracking and Receiver Estimation

The front-end of a receiver (amplifiers, bandpass filters and frequency down-converters) conditions the received analogue satellite signal for processing. An analogue-to-digital converter (ADC) transforms the conditioned signal to its equivalent digital form before the estimation of the chip delay, the transit time, Doppler frequency shift and the carrier phase offset. The first stage in the estimation is the signal acquisition, which is searching for an in-view satellite by employing a defined search space, the approximate chip delay and the Doppler frequency shift, simultaneously. A given GNSS receiver generates replica code for each of the GNSS satellites. The search space is defined by a range of Doppler shift frequencies around the GNSS band transmitted carrier frequency; and the delayed versions of the receiver-generated replica code of a satellite suspected/expected to be in view, enabling the generation of high autocorrelation peak that suggests the detection of the satellite. After

a satellite detection, the receiver continuously tracks the detected satellite through two feedback loops: a code tracking loop called delay lock loop (DLL), and a Phased Locked Loop (PLL) that basically generates a sinusoidal signal to match the frequency and phase of the incoming RF signal from the acquired/detected satellite. The structure of the navigation massage on a satellite's transmitted code (already spread by the navigation message) allows users to have precise and unambiguous measurement of the apparent transit time of the broadcast signal from that GNSS satellite. A detailed description of the acquisition and tracking processes, and the further processing in the receiver leading to the estimation of the transit time, is given in Misra & Enge (2006); Groves (2008). The search range in the acquisition stage differs with receivers. Different receivers have different frequency bin and chip resolutions, and different Doppler frequency shift ranges. For instance, assuming a GPS receiver is designed to accommodate a maximum Doppler frequency shift range within ±6000Hz, apply a frequency bin (interval between any two frequencies in the $f_c \pm 6000$Hz range, f_c being the band nominal carrier frequency) of 500Hz and a chip division of 2 samples per chip, which is a chip bin of $\frac{1}{2}$chip (i.e. each of the 1023 chips long C/A code will be replicated twice within its $\frac{1}{1023}\mu s$ duration). Then, $2 \times 1023 = 2046$-chip bin search space and $\frac{6000}{500} = 24$-frequency bin search space would define the $2046 \times 24 = 49,104$ search spaces to be used by the receiver in the acquisition stage of each PRN or satellite. A receiver's multichannel architecture enables dedicated hardware channels for each satellite, making it possible to perform parallel acquisitions for different satellites. For a defined DLL correlator spacing, d, of say $d \leq 1$, and a discriminator function such as the early-minus-late (Braasch & van Dierendonck, 1999), the DLL can maintain lock with any already acquired satellite, as the PLL does the phase tracking to obtain refined phase offset measurements. For tracking C/A code, the value of d ranges from 1 in low accuracy receivers to as low as 0.1 or less in geodetic receivers. The existing differences in receiver architectures would be one reason why two different receivers simultaneously observing same satellites would produce measurements or observations with different levels of multipath errors. Detailed insight into receiver acquisition and tracking processes can be found in (Misra & Enge, 2006; Groves, 2008; Braasch &

van Dierendonck, 1999). It is only after these processes that the bit synchronization, frame synchronization, and finally the ephemeris and satellite clock data from a satellite is made possible and done.

Irrespective of the receiver complexity/architecture, there seems to be no particular choice of a set of frequency bin, Doppler shift range, correlator spacing, discriminator function, etc, that will always guarantee the correct determination of the transit time, Doppler frequency and the carrier phase offset. The code and phase observations generated by a receiver are not usually free from errors. Moreover, non-receiver dependent errors originating from different GNSS error sources also affect the GNSS code and phase observations.

2.2. GNSS Error Sources

The errors in the observations from a GNSS satellite are from different sources, which include the GNSS control segment, the propagation medium, signal interference due to reflection from objects in the vicinity of the antenna and the receiver itself. Other error sources include jamming, which could be intentional, and signal attenuation (by trees and walls, etc.) that usually lead to a decreased signal-to-noise power ratio of the received signal. A depiction of the interaction of some of these sources with the transmitted signal from a satellite to a receiver, is shown in Figure 2.1. The errors affect both code and carrier phase observations. The quality of the positioning achieved by the observations are also affected by the number of satellites in view and their distribution in space with respect to the receiver antenna - the satellite geometry.

2.2.1. Satellite Ephemeris and Clock Errors

These errors originate from the broadcast navigation message generated by the GNSS control segment. For instance, GPS now has 16 monitoring stations located throughout the world[1], which track the GPS satellites as they pass overhead and

[1] http://www.gps.gov/systems/gps/control/, accessed 13 March 2012

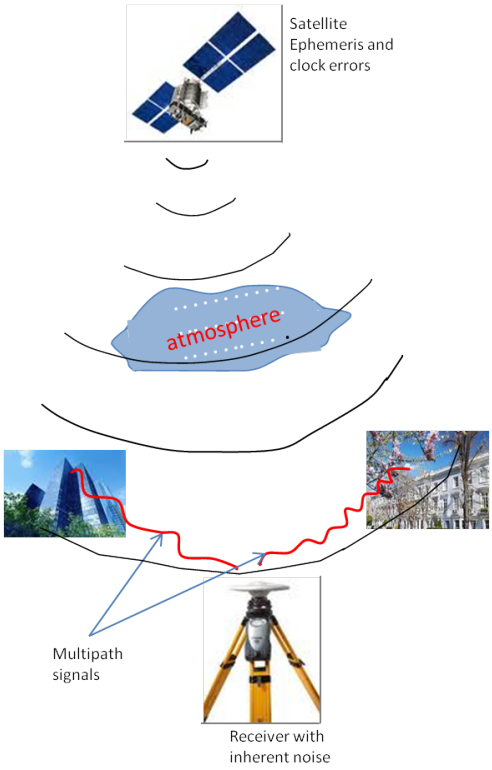

Figure 2.1.: Depiction of the interaction of error sources with the transmitted signal from a satellite to a receiver

channel their observations to the master control station (MCS) in Colorado. The MCS incorporates the observations from the monitoring stations with the models for other effects, to determine and predict the GPS satellites orbits and clocks corrections that are uploaded to the satellites from the current 12 uplink stations. Given a satellite current orbital estimates from an orbit determination (OD) process, the orbit prediction (OP) - the future state (orbital position and clock correction) of the satellite is predicted. The prediction accuracy is influenced by the same effects (errors) that influence the estimation accuracy itself (Tapley *et al.*, 2004). In a GNSS satellite OD process done by the system control segment, the imperfection in the satellite force model could be a principal error source. The force model is determined by using the gravitational (conservative field) parameters (masses of the earth, moon and planets; the geopotential coefficients, etc) and the non-gravitational (non-conservative field) parameters (solar and earth radiation pressure, drag, magnetic field, etc), which are not accurately known or perfectly modelled. However, non-conventional but improved analytical models of the non-conservative fields have been

shown to improve OP of a satellite. Improvement in the OP accuracy of GLONASS satellite has been demonstrated with analytical solar pressure modelling (Ziebart & Dare, 2001); and with combined analytical models of thermal re-radiation and radiation pressure based on given satellite geometry, Ziebart *et al.* (2005) also showed significant improvement (decimetre-level accuracy) in the OP of a GPS block IIR satellite.

Another typical error source in the process is the measurement model. The model is dependent on the employed inertial and terrestrial coordinate systems as well as the ground-based measurements such as the coordinates of tracking station, atmospheric effects, instrument modeling, clock accuracy and tectonic plate motion. Since the predicted values are used to fit set of equations to obtain the fit coefficients that are uploaded as satellite ephemeris and clock parameters in the navigation message, the ephemeris and clock parameters are therefore not error free. The more accurate the estimation and prediction models, and the more frequent upload of new data set to the satellites, the lower would be the satellite ephemeris and clock errors. The level of stability of the satellites' clocks themselves is also a source of clock error and usually varies amongst the satellites of a GNSS.

The ephemeris error can be decomposed to three orthogonal axes: the radial (R) axis, - the direction of a vector from earth centre to the satellite; along-track (AT) axis - the direction of the tangent to the satellite orbital track; and cross-track (XT) axis - the direction perpendicular to the R and AT axes. Of these three, the radial component error is the smallest but it contributes the most error in the range measurement obtained by the ground-based monitoring stations (Warren & Raquet, 2003). The subsequent receiver pseudorange measurement error, being the projection of the satellite position error vector in the satellite-receiver Line of Sight (LoS), is also dominated by the R component of the ephemeris error. The clock error and the 3D ephemeris error of a GPS satellite could be estimated and tracked by the Control Segment in real-time. Before 2006, the magnitude of GPS satellite clock or ephemeris error could be up to 1.5m with the then typical once-a-day data upload (Misra & Enge, 2006). However, the increase from 5 to 16 GPS monitoring stations, which could enable satellite-monitoring capabilities from 97% single-station

coverage to continuous 100% triple-station monitoring of all GPS satellites; and the current number of tracking stations, help improve the quality of the current GPS broadcast ephemeris and clock parameters (Manning, 2005). The IGS specifications updated in 2009, indicate 1-dimensional mean root-mean-square (RMS) accuracy of $\sim 100cm$ over the three XYZ geocentric components for GPS satellite broadcast ephemeris (IGS, 2012).

With reference to a GNSS system time, the broadcast ephemeris and clock parameters (from the prediction) are used by a user receiver to obtain the supposedly 'known' satellite orbit and clock offset. A GPS or Galileo satellite clock offset from its system time since the broadcast data reference time, t_{oc}, is given as in Equation (2.1) where a_0, $a_{1,}$and a_2 are the broadcast clock parameters, t_{sys} is the system time (GPST or GST), and Δt_{rel} is the relativistic correction term dependent on some orbital parameters and speed of light (GALILEOICD, 2008; GPSICD, 1997). This calculated offset is used by the receiver to correct for a satellite clock offset from its system time.

$$\delta t^s = a_0 + a_1(t_{sys} - t_{oc}) + a_2(t_{sys} - t_{oc})^2 + \Delta t_{rel} \tag{2.1}$$

According to the IGS specifications updated 2009, $\sim 5ns$ RMS accuracy with $\sim 2.5ns$ standard deviation relative to the IGS timescale that is linearly aligned to GPS time in one-day segments, can be obtainable with the GPS clock correction broadcast (IGS, 2012). As already mentioned in Section 1.1.4, GPS satellite clock and ephemeris errors can be alternatively corrected by using externally generated corrections such as provided by the IGS. The IGS has a much denser monitoring station network distributed worldwide, and widely accepted as one source providing data for improved satellite clock and ephemeris errors correction.

2.2.2. Atmospheric Errors

A satellite transmitted signal propagates through the atmosphere to a receiver beneath. The atmosphere by refraction, changes the direction and speed of the propagating RF signal from the constant speed of light in a vacuum. The parts of the atmosphere where this phenomenon occurs are the ionosphere and troposphere,

where errors result due to the change in the speed of the transmitted signal.

2.2.2.1. Ionospheric Delay and Scintillation Effects

The ionization caused by the radiation of the sun creates a region of ionized gases resulting to free electrons within a height of about 50-1200km above the earth surface called the ionosphere. The ionosphere comprises the D, E, F1 and F2 layers at different heights and rates of production and loss of electrons. The F2 layer of height range 200-600km has the peak electron density (Opperman *et al.*, 2007) in electrons/m^3 and the satellite signal propagation speed in the ionosphere depends on the number of free electrons per square metre on its path to a receiver, which is defined as the total electron content (TEC) with units of $electrons/m^2$, and $10^{16}TEC = 1TECunit$ (TECU). The intensity of ionization increases with sun intensity in the day and reduces drastically at night when ions and electrons recombine. The ratio of the speed of propagation of the signal in vacuum, c, to the speed in the ionosphere, called the refractive index, is dependent on the transmitted signal frequency (dispersive medium). The refraction (as refractive index is not equal to 1) results in advanced phase observation and delayed code observation, which means the ionospheric delay terms in the phase and code observations would be equal in magnitude but opposite in sign. The ionospheric delay term I, in its first order form, is given as (D. S. Coco *et al.*, 1991)

$$I \simeq \frac{40.3 \times TEC}{f^2} \tag{2.2}$$

where the value 40.3 is a constant with unit $m^3(Hz)^2/electron$. I is seen to be inversely proportional to the square of the GNSS carrier frequency, f, in a given band. The ionospheric path is longer with low elevation satellites and the ionospheric delay is elevation dependent, typically varying from 1-15m and could even exceed 100m in disturbed ionospheric conditions (Klobuchar, 1987).

Apart from the ionosphere diurnal and seasonal variations, the ionosphere is also characterised by significant variability depending upon the solar activity and geomagnetic disturbances. There are also short-term and localized anomalies (travelling

ionospheric disturbances) such as the winter anomaly and the equatorial anomaly (Devi *et al.*, 2008; Bhuyan & Borah, 2007). Rapid electron density variations (Ionospheric irregularities) do occur, and typically develop during and after an anomaly. When severe, these ionospheric irregularities cause signal diffraction (scattering of a GNSS satellite transmitted signal) and refraction that could lead to rapid fluctuations in the signal amplitude and/or phase, an occurrence referred to as ionospheric scintillation. The fluctuation in the amplitude (amplitude scintillation) can be severe enough to result in the received signal amplitude dropping below the GNSS receiver lock threshold, thus driving the receiver to re-acquire lock of the satellite signal; and the rapid carrier phase fluctuations (phase scintillation) can cause cycle slips (Doherty *et al.*, 2000). These ionospheric scintillation effects are common to both single- and dual-frequency receivers, even though it could result to higher positioning error in single frequency receivers (Datta-Barua *et al.*, 2003).

GPS satellites broadcast eight ionospheric delay correction parameters based on the Klobuchar model, to enable single-frequency users to correct for the error in form of ionospheric delay (GPSICD, 1997). This model, on the average, as been reported to correct up to 50-60% of the ionospheric error (de Oliveria Carmago *et al.*, 2000; Feess & Stephens, 1987). For the same ionospheric correction, Galileo satellites will broadcast three parameters based on the NeQuick model (Radicella, 2009). The improved correction capability of the NeQuick model has been reported as well (Aragon-Angel *et al.*, 2005; Somieski *et al.*, 2007). Figure 2.2 depicts satellites propagation paths through the ionosphere to a receiver above the surface of the earth. The half-cosine Klobuchar model, depending on the local time at an IPP (see Figure 2.2), gives the estimated vertical ionospheric delay, I^z, in the zenith direction to an IPP. It uses the corresponding satellite's earth angle, the approximate geodetic latitude, longitude, azimuth of the IPP, and the eight broadcast parameters (Klobuchar, 1987). The I^z is mapped in the LoS direction between the satellite and receiver to generate the path ionospheric delay, I. Thus from Figure 2.2, through laws of sines and the assumption of an ionospheric thin shell height, h (the GPS

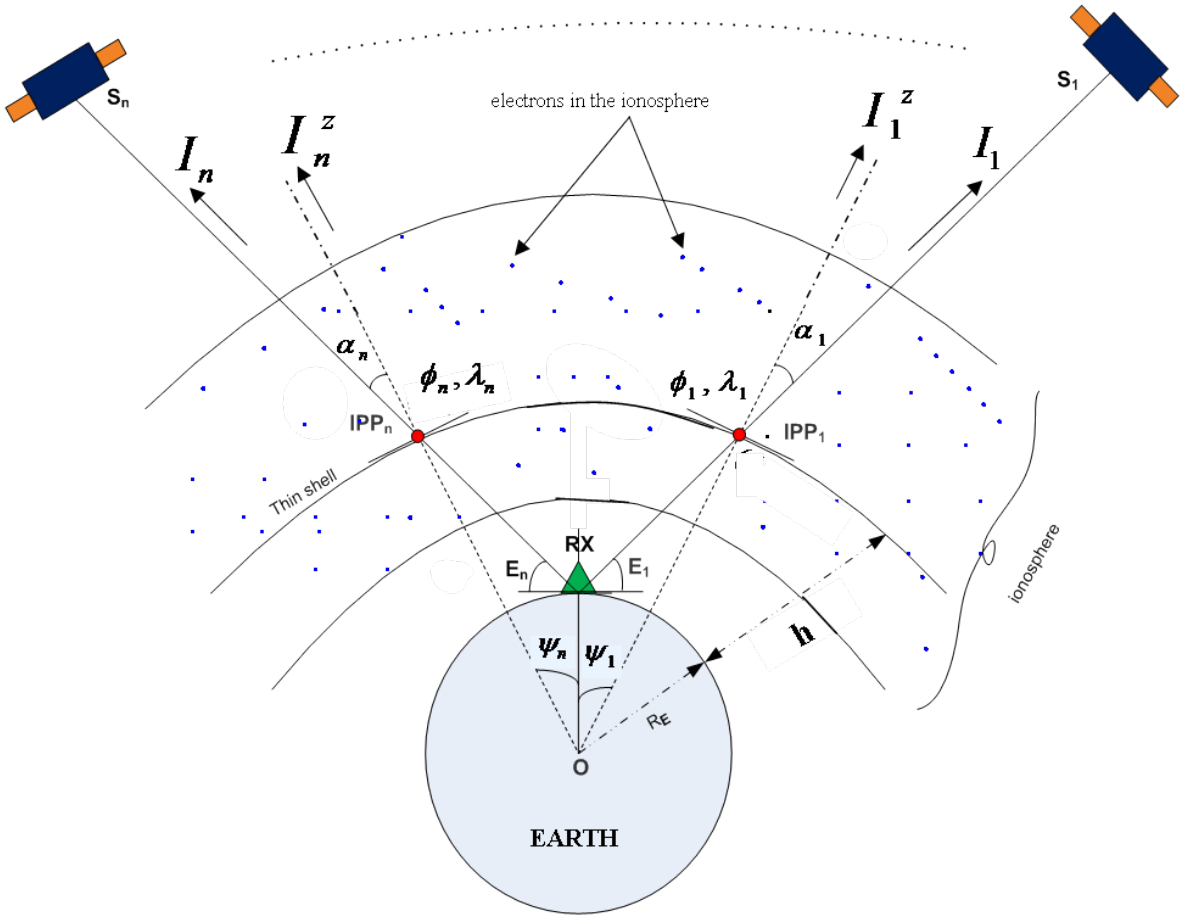

Figure 2.2.: Satellites signal propagation paths through the ionosphere to a receiver. The mean ionosphere height is represented as a thin shell h meters above a spherical earth surface with average radius $R_E = 6378.1363$ (Vallado, 2007). The ionospheric pierce point (IPP) is the point where the LoS signal from a satellite S observed at elevation angle E w.r.t. receiver RX, intersects with the thin shell. Here α, ψ, ϕ and λ are the respective zenith angle, earth angle, latitude and longitude of an IPP corresponding to any of the n observed satellites, in degrees.

Klobuchar model uses $h = 350$km), I is then given as

$$\begin{aligned} I &= I^z \times \frac{1}{cos\alpha} \\ &= I^z \times \left[1 - \left(\frac{R_{E\times} cosE}{R_E + h}\right)^2\right]^{-1/2} \end{aligned} \tag{2.3}$$

The $\frac{1}{cos\alpha} = \left[1 - \left(\frac{R_{E\times} cosE}{R_E+h}\right)^2\right]^{-1/2}$ in Equation (2.3) is an elevation dependent mapping function often referred to as the obliquity factor, zeroth-order or projection

mapping function. The value of I so determined can thus be removed from the single frequency code or phase observation thereby correcting for the ionospheric delay.

It is worth noting that the actual obliquity factor used in GPS is an approximation to the value of $\frac{1}{cos\alpha}$, and it is given as $MF = 1 + 16(0.53 - \frac{E}{180})^3$ where E is the elevation angle of the satellite with respect to the receiver, in degrees. $\frac{1}{cos\alpha}$ or MF is greater than 3 for elevation angles lesser than 5^0. Going by Equation (2.2), and with the same mapping function, we can similarly generate the vertical TEC (vTEC) or slant TEC from the relationship

$$TEC = vTEC \times \left[1 - \left(\frac{R_{E\times} cosE}{R_E + h}\right)^2\right]^{-1/2} \tag{2.4}$$

if either the vTEC or TEC is known. External corrections for single frequency users can also be obtained from external sources like the IGS and the analysis centres such as the Jet Propulsion Laboratory (JPL) and the Centre for Orbit Determination in Europe (CODE), generating the ionospheric model - Global Ionospheric Maps (GIM), in IONEX (IONosphere map EXchange) format. The GIM model is generated from the appropriate IONEX file after interpolation of the TEC values given at geographic grid points in space and time (Schaer *et al.*, 1998). In standard IGS IONEX files, the epoch interval is 2 hours and the spatial grid points spacing is 2.5^0 in latitude and 5^0 in longitude (Ovstedal, 2002).

With a multi-frequency receiver, and based on the first-order ionospheric delay given in Equation (2.2), the ionospheric delay relationship on two different carrier frequencies can be represented as (de Lacey *et al.*, 2011)

$$I_j = I_i \frac{f_i^2}{f_j^2} \tag{2.5}$$

where $i \neq j$, and $\{i, j\} \subset B$; and $B = \{1, 2, 5, \}$ is the set of currently existing frequency bands used by GNSSs and f_i and f_j are two different bands carrier frequencies. For instance, for dual-frequency GPS receiver observations, the term $\gamma_{ij} = f_i^2/f_j^2$ is a constant, which is equal to 1.64695 if $f_1 = 1.57542GHz$ and

$f_2 = 1.2276GHz$ as with GPS. Such multi-frequency observations enable receiver-generated ionospheric error 'elimination' as the dual-frequency observations can be combined to generate observables with almost completely eliminated ionospheric delay (called the ionosphere-free observable (Misra & Enge, 2006)), or differenced to estimate the scaled ionospheric delay that can subsequently be removed from the multi-frequency observations.

2.2.2.2. Tropospheric Delay

The troposphere is an electrically neutral part of the atmosphere below 40km altitude from sea level. It contains dry gases and water vapour. This part of the atmosphere is non-dispersive for GNSS frequencies which are less than 30GHz (Leick, 2004) but has varying refractive index that causes changes in the travel time of the signal, and consequently changes the apparent receiver-satellite range. The code and phase observations at all carrier frequencies from a GNSS satellite experience the same magnitude of tropospheric delay. The tropospheric delay can be over 2m for a satellite at a receiver's zenith direction and over 20m for a satellite at lower elevation angles (Ueno *et al.*, 2001).

The tropospheric delay cannot be determined nor estimated from any broadcast parameters; it can only be estimated and corrected for using models. The zenith total delay (ZTD) in existing models is often separated into a zenith dry or hydrostatic delay (ZD) component that is due to about 90% of the tropospheric delay, and a zenith wet (ZW) component. While the hydrostatic component is caused by the mixture of dry air and water vapour considered to be in hydrostatic equilibrium and proportional only to absolute pressure and temperature, the wet component is caused by the water vapour alone. Again, a mapping function to scale the zenith delay as a function of the elevation angle of the satellite in view of the receiver is also defined. A mapping function such as

$$m(E) = \frac{1}{\sqrt{1 - \left(cos\frac{E}{1.001}\right)^2}} \tag{2.6}$$

is elevation angle dependent (Misra & Enge, 2006) and multiplies the ZTD by a

factor of one for satellites at zenith, to more than five for low elevation satellites. Tropospheric models are built around meteorological parameters (pressure, temperature, humidity profile with altitude, and variations of these with latitude and seasons). Some models like the Saastamoinen and Hopfield models (Xu, 2003) use surface meteorological input data taken at the receiver site and ZTD accuracy of 2.5 - 4cm rms can be achieved. The less accurate global models e.g. the SBAS model that uses receiver latitude and height, temperature and water vapour lapse rates and day of year as input, could achieve ZTD accuracy of 4 - 6cm (van Leeuwen *et al.*, 2004). The implementation of the SBAS tropospheric model and the applied mapping function,

$$m(E)_{SBAS} = \frac{1.001}{\sqrt{0.002001 + sin^2 E}} \tag{2.7}$$

is given in Farah *et al.* (2005) where a comparison between the SBAS tropospheric and the CODE tropospheric models was made, and a maximum of ZTD difference of 5 - 16cm between the two was reported. For elevation angle $E < 5^0$, $m(E)_{SBAS}$ is not valid.

A wide range of mapping functions also exist, and the level of tropospheric delay error in the receiver-satellite LoS direction is also affected by the mapping function used.

2.2.3. Multipath Error

Multipath is a localized effect created by reflective objects on the ground or within the vicinity of a receiver antenna. Such reflective objects include the earth surface and ground water, buildings, sheets on rooftops, etc. This environmental interaction is depicted in Figure 2.1. Multipath refers to a phenomenon where a signal arrives at an antenna via more than one path. This happens as the direct LoS signal and its reflected copies arrive at the antenna forming a composite signal. The consequent impact of multipath depends on the strength, delay and relative phase, all relative to the direct LoS signal. The two extremes (bounds) of multipath effect are from the reflection that arrives in phase, and reflections that arrive 180^0 out of phase with the direct signal (Chang & Juang, 2008). Figure 2.3 shows the error bounds

on the C/A-code observation from multipath amplitude assumed to be about 16 times smaller in magnitude relative to the direct LoS signal. An in-phase multipath increases the magnitude of the observation error (constructive interference) as the errors add up, and an out-of-phase multipath decreases the magnitude of the observation error (destructive interference) as the resulting error becomes the difference between errors. It therefore means that multipath effect will always cause error swing between its upper and lower limits as the relative phase varies from $0^o$to 180^o. The multipath effect on code observations depends among other things, on the code chip rate and generally the pre-correlation bandwidth, which depends on the filtering in the front-end as well as the sample interval used by the front-end. As seen in Figure 2.3, the multipath mitigation is enhanced by small correlator spacing; a correlator spacing of $d = 0.1$ reduces the impact of multipath on a receiver's code observation than $d = 1$. It is observed that with $d = 0.1$, long-delay multipath (where the delay is longer compared to a chip width of 300m and 30m for GPS C/A- and P(Y) respectively), do not result in multipath error as against short-delay multipath that would always create multipath error. The smaller correlator spacing of $d = 0.1$ obviously mitigates the multipath error for both C/A and P(Y) codes. The 10 times higher chip rate of the P(Y) code makes it less affected by multipath.

The multipath effect on the code and phase observations differs widely; the code multipath error is in the typical range of 1-5m while the theoretical maximum phase multipath error amounts to 4.8cm and 6.1cm for the GPS L1 and L2 bands respectively (Rost & Wanninger, 2009).

It is known that lower elevation signals are more vulnerable to multipath. On the receiver code or phase observation, the multipath effect is observed as both low and high frequency variations (Souza & Monico, 2004); it reflects as low frequency variations especially in static domains when reflectors are considerably close to the receiver antenna whilst it could be observed as more of high frequency random 'noise-like' variations in highly dynamic receiver operations (Lau & Cross, 2007). In static observations, the high frequency multipath effect has periods of sub-minute to 2-3min and the low frequency fluctuation is highly dependent on the reflective surfaces in the vicinity of the receiver. Highly reflective surfaces lead to strong multipath

(high amplitude); close objects result in multipath errors with long wavelengths (low frequency); and distant objects cause multipath errors with short wavelength (Ogaja & Satirapod, 2007). The multipath frequency components in a kinematic (moving receiver) operation would be likely dominated by high frequency error/noise components - reflecting more of the antenna changing environment.

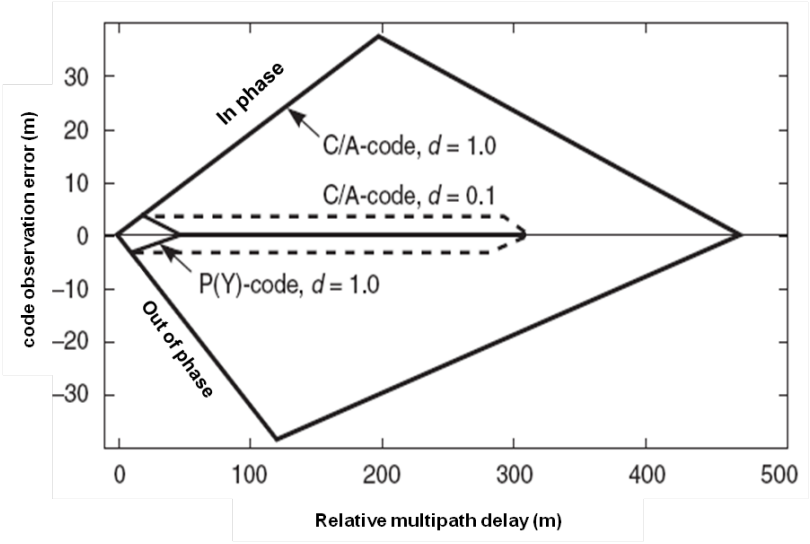

Figure 2.3.: Error bounds on GPS P(Y)- and C/A-code observations due to multipath derived from multipath amplitude of 12dB below the direct signal amplitude. Adapted from Misra & Enge (2006).

There is a subtle difference between multipath contaminated signal and a Non-Line-of-Sight (NLOS) signal. Multipath contaminated signals are reflected signals received by a GNSS receiver via multiple paths. A multipath contaminated signal exists if one or more reflected signals are received together with the direct path (receiver–satellite path) line-of-sight (LoS) signal. On the other hand, a received GNSS satellite signal is considered an NLOS signal when it is the only reflected (indirect) signal received by the receiver, and the direct LoS signal is blocked (Jiang & Groves, 2012). While the error introduced by multipath contaminated signal could be positive or negative, the error on an NLOS signal is always positive due to the extra path delay. The reception of multipath contaminated signals, direct LoS signals and NLOS signals is a common phenomenon in urban environments.

2.2.4. Receiver Noise

Receivers generally are not perfect devices. There is always some noise level contaminating their measurements. The term, receiver noise as used in this work, is a broad term for the random measurement noise on a code or phase observation. It includes the radio frequency (RF) radiation picked up by the antenna in the GNSS band that is not related to the signal; noise introduced by the antenna amplifiers, frequency converters, cables; GNSS multiple-access noise (interference on the CDMA or FDMA system); plus the signal quantization noise (Misra & Enge, 2006). The receiver noise, including also the thermal noise or thermal agitation noise produced by the moving electrons in the electronic components of the receiver, is also proportional to the absolute temperature of the components.

The power of the receiver noise (assuming white noise) occupies the entire GNSS band with constant power spectral density (PSD) $N_0/2$ dBW/Hz over a double-sided bandwidth, B, or N_0 dBW/Hz over a single sided bandwidth B. The noise power spectral density can be approximated as $N_0 = k - T_n$; where the Boltzmann's constant $k = 1.3806 \times 10^{-23} JK^{-1}$ and the effective noise temperature T_n in Kelvin, are assumed converted to dB values. Even without a transmitted GNSS signal, such receiver noise power in the considered bandwidth B in Hz (but assumed converted to dB value here), will always remain as $N = N_0 - B$ [2]. At the RF or Intermediate Frequency (IF) stage of the received signal processing, the carrier power to noise density ratio, C/N_0 [3], is appropriately used to describe the carrier power level to the noise power density level (Langley, 1998). When a signal is transmitted, the ratio of the power of the received signal, S, and the noise power N, called the signal-to-noise ratio, SNR, is usually measured at a given point in the receiver after RF and IF demodulation (i.e. at baseband signal processing stage). The relationship between these two measures of signal quality/strength metrics is given as

[2] N here is the noise power in Watts and not the phase integer ambiguity term. N increases with bandwidth

[3] C/N_o is the ratio of the total signal power to the noise power spectral density (i.e. noise power in a 1Hz bandwidth), which is usually given in dBHz. The SNR is usually given in dB.

$$SNR = C/N_0 - B \tag{2.8}$$

where B is assumed a dB value. As defined by Equation (2.8), B is defined with respect to a point in the receiver where the SNR is determined.

2.2.5. Other Error Sources

Apart from the already discussed error sources, other relatively minor error sources can also be identified. The geometric distance between the satellite antenna phase centre (reference point of the signal emission on the antenna) at the time of the signal transmission, and the receiver antenna phase centre (reference point of the signal reception) at the time of the signal reception, is the receiver-satellite geometric range. Unfortunately, the different satellite and receiver antenna phase centres for the different bands are not exactly known nor fixed. Moreover, the different blocks of GPS satellites have different antenna phase centres, and the phase offset of a receiver varies with the elevation angle of the arriving satellite signal. These unknown phase offsets and variations are error sources in the receiver recorded (raw) observations. The largest receiver antenna phase offset could be up to 10cm (Leick, 2004) while the blocks of GPS satellites phase offsets are within tens of centimeters to more than a meter in the directions of the satellite fixed coordinate system (Xu, 2003). These errors are only mitigated by applying calibration-based models where possible.

The instrumental or hardware delays resulting from the signal processing hardware in the satellite and receiver, constitute biases on the observations. The biases are systematic errors that are different from one frequency carrier channel to the other, and different from the code to the phase observations. These delays can be modelled as constants for a given band carrier frequency over a short period of time (Sardon & Zarraoa, 1997; Gao & Liu, 2002) since the day-to-day variability is negligible (Ma & Maruyama, 2003). In positioning, the correlation between hardware delays and clock offsets results in a biased receiver clock estimate that may not be good enough for timing and time transfer applications when a high precision is required.

Some natural phenomena such as ocean tide - the rise and fall of sea levels, which

results to the displacement of the earth surface (ocean tidal loading), and earth tide - deformation of the elastic body of the earth, are also sources of errors. Tides are caused by the gravitational forces exerted by the Moon and the Sun. The effects of earth tide could reach 60cm worldwide and ocean loading effects could reach deformations in the order of 10cm in near-coast regions while its about 1cm at most continental stations (Jentzsch *et al.*, 2000; Xu, 2003). While air-based GNSS observations without fixed reference on the earth may be free from earth tide effects, static references fixed on the ground especially with long baseline in relative positioning, are not free from tidal effects. Again, the mitigation of the tidal effect is by employing global correction models that are not generally locally effective.

The observed carrier phase depends on the relative orientation of the transmitting and receiving antenna as well as the direction of the LoS between them. A relative rotation between them, even in a fixed position, could change the reference direction and thus the measured phase/accumulated phase (Kim *et al.*, 2006). This effect is called phase wind-up or phase wrap-up and is such that a full rotation of the antenna would generate an error of one wavelength (e.g. 19cm for L1) whose accumulation can be more than the receiver noise or ionospheric variations (Garcia-Fernandez *et al.*, 2008). This effect could also be absorbed along with clock or the float ambiguities estimation.

However, the impact of this errors may be mitigated with differencing across satellites and/or receivers when using more than one receiver for positioning. The effects of these errors, in many cases of single receiver positioning, are often neglected and are only mitigated using applicable corrective models when the desired positioning accuracy is significantly high. The adopted observation model in this study does not include these errors explicitly.

2.3. Observations Models

Before any further discussions on GNSS errors, it is considered appropriate to present the code and phase observation models considered for this research at this point. Considering the measurement process and the errors, the observation functional

models can be generated without any further in-depth to receiver workings, and it is suffice to consider receiver observations simultaneously obtained from several satellites, at the same epoch. Without loss of generality, only GPS single- and dual-frequency observations models are henceforth considered and used, representing a GNSS, for simplicity. Two observations, namely, the code pseudorange and the accumulated carrier phase in cycles can be denoted as P and Φ respectively. The observations made by a GNSS receiver are dependent on the satellite transmit band carrier frequency f_i in Hertz, where $i \in \{1, 2, 5\}$ denotes the subscript for indicating an existing GNSS transmit band. The equivalent carrier phase observation in meters, ψ_i, from an observed GPS satellite s, can be obtained by multiplying the accumulated phase in cycles, Φ_i^s, from the satellite with the wavelength $\lambda_i = c/f_i$, where $c = 299792458$m/sec is the speed of light in vacuum. Functional models for such receiver-satellite code pseudorange, P_i^s, and the associated accumulated carrier phase, ψ_i^s in metres, are

$$P_i^s = r^s + c\delta t^r - c\delta t^s + T^s + I_i^s + d_i^s + d_i^r + S_o^s + m_{P,i}^s + \epsilon_{P,i}^s \tag{2.9}$$

$$\begin{aligned} \psi_i^s &= \lambda_i \Phi_i^s \\ &= r^s + c\delta t^r - c\delta t^s + T^s - I_i^s + b_i^r + b_i^s + \lambda_i N_i^s + S_o^s + m_{\psi,i}^s + \epsilon_{\psi,i}^s \end{aligned} \tag{2.10}$$

where r^s is the true geometric range between the receiver and satellite s in metres; δt^s and δt^r are the satellite and receiver clock offsets from the GPS system time in seconds, respectively. T^s is the tropospheric delay in metres, independent of the carrier frequency; I_i^s is the f_i dependent ionospheric delay in metres, manifesting as a delay in P_i^s and as phase advance in ψ_i^s; and S_o^s is satellite s orbital position error in the receiver-satellite direction, in metres. N_i^s is the carrier phase integer ambiguity in cycles, which can be a positive or negative integer; d_i^r and d_i^s are respectively the receiver and satellite s hardware delays in metres, on P_i^s; while b_i^r and b_i^s are respectively the receiver and satellite s hardware delays in metres, on the carrier phase ψ_i^s. The multipath error on the carrier phase observation is denoted as $m_{\psi,i}^s$ while $m_{P,i}^s$ denotes the multipath error on the code pseudorange observation. $\epsilon_{P,i}^s$ and

$\epsilon^s_{\psi,i}$ represent all other umodelled and/or uncorrected errors on the code observation and on the carrier phase observations respectively, which include, but not limited to the the errors discussed in Section 2.2.5 - receiver random noise, antenna phase centre variation, ocean and earth tide, etc. Unlike the ambiguous (presence of an unknown integer ambiguity term N^s_i) and more precise carrier phase observation ψ^s_i, the code pseudorange observation P^s_i is unambiguous but far less precise. Unlike the code observation that can be used directly for positioning, the N^s_i in phase observation must first be determined or resolved (fix to its integer value) before the phase observation can be used for precise PVT estimation. Though once fixed, the integer N^s_i remains constant as long as satellite s remain tracked by the receiver and without further cycle slips.

As already explained in Section 1.1.4, some of the errors in these observation models can be 'corrected' by using various corrective error models such as discussed in this chapter. However, due to limited accuracy in applied corrective models, correction residual error (CRE), often remains. The combination of the CRE, the multipath error, the receiver noise and clock error, and all other unmodelled errors in any of these functional models given by Equation (2.9) or (2.10) defines the observation error in that functional model that needs to be further mitigated. For instance, the observation error that may be present in a code observation P^s_i would be the combined $c\delta t^r$, S^s_o, $m^s_{P,i}$, $\epsilon^s_{P,i}$ and the CRE that would result if corrective models for I^s_i, T^s, etc, are applied. The level of the observation error in a code observation is significantly higher than the level of the observation error in a phase observation, mostly because of the higher multipath error on a code observation. There is a level of error correlation in P^s_i and ψ^s_i, at least partly due to S^s_o, CRE and the unmodelled errors in P^s_i and ψ^s_i. In each of these observation models, the total observation error level needs to be mitigated for enhanced positioning.

2.4. Impact of Cycle Slip and Receiver Clock Error

The momentary loss of lock of the phase lock loop of the receiver observing a satellite results in a discontinuity in the integer cycle count even though the fractional part

of the phase can be measured continuously. Such a discontinuity causing the phase observation to change by an integer number of cycle(s) is called cycle slip. This could occur due to internal receiver tracking loop problems, a possible interruption in signal reception due to obstacles in the path of the satellite signal to the receiver, or low signal-to-noise ratio. Also, when observation gap occurs for a satellite, there are often cycle slips in the post-gap epoch's phase observations, even though the code observations do not have cycle slips. The magnitude of a cycle slip can vary from one to millions of cycles (de Lacey *et al.*, 2011). When a cycle slip occurs, a new N_i^s ambiguity value has to be determined when the receiver re-locks to the gapped satellite at a post-gap epoch. This is perceived as a drawback in phase observations, as even a short interval lose of lock can cause a slip of a few cycles capable of biasing the phase observation enough to make precise and accurate positioning difficult. Cycle slip is a frequent occurrence in difficult environments such as urban canyon or areas covered by dense foliage.

Cycle slip creates negative impacts; it results in jumps in a phase observation that may not be detected or correctly fixed, and it could result in a receiver spending several minutes (convergence time) before re-gaining a pre-cycle slip acquired level of accuracy and precision. When cycle slip is prevalent, frequent re-initializations in conventional phase ambiguity fixing process or cycle slip value determination is a common impact that is not only inconvenient in real-time applications, but also limits precise positioning accuracy. The error impact would be worse when a cycle slip is not detected, especially if it is a large cycle slip value. However, by certain processing techniques, cycle slips can be detected and corrected as found in Dai *et al.* (2008); Bisnath (2000). A review of cycle slips detection techniques is presented in Chapter 3.

Most receivers endeavour to synchronise their internal clock time to the observed satellite's system time by periodically adjusting the clock - inserting jumps, which is often proprietary to receiver manufacturers. The Ashtech UZ-12 receiver for instance, applies ±1ms resets or jumps (Kim & Langley, 2001). Unlike in differential or relative positioning that depends on at least two different receivers observing the same satellites at the same time, a stand-alone receiver performs positioning based

on its sole observations without recourse to another receiver's observations. Even if such a receiver's time offset with respect to the GNSS system time is known at a previous observation epoch, the receiver clock jumps and its oscillator instability over subsequent epochs, which are usually not known a priori, constitute the receiver clock error. In such a single receiver operation, the receiver clock error is not always eliminated during positioning; it tends to impact as correlating error in the positioning solution, especially on the vertical position component (Weinbach & Schon, 2011); and can also impair cycle slips detection and time transfer.

Even though it has been shown that receiver clock error modelling improves positioning accuracy, such modelling is believed feasible for receivers running only on atomic oscillator, and not quartz crystal oscillator (Weinbach & Schon, 2009) that are more commonly used in receivers. As often the case, especially in kinematic mode positioning, epoch-by-epoch estimation of the clock error/offset is common, and most available receivers' clocks run on crystal oscillators that have very low stability, and not the atomic oscillators that have high stability. The impact of receiver clock error could be 'eliminated' in differential or relative positioning while an adoptable option for stand-alone receiver positioning would be to generate the receiver clock model if possible, or estimate the receiver clock error separately from the positioning domain to enhance decorrelation of the receiver clock error and its positioning solution.

The errors due to cycle slips and receiver jumps could be considered systematic, and they contribute to deteriorate the quality of observations, and consequently, the receiver positioning solutions (Kim & Langley, 2001).

2.5. Common Errors Mitigation

Apart from the errors due to hardware delays, phase wind-up, multipath and the receiver random noise, the most part of other errors are essentially common and equal in magnitude in the phase and code observations from a satellite, in a given observation band. For more than one frequency or band observations, some of these common errors can be eliminated by differencing among the observations obtained

by one receiver or multiple receivers.

2.5.1. Mitigation in Stand-alone Receiver Operation

A single GNSS receiver performs autonomous positioning (single point positioning), based on its sole observations without recourse to another receiver. For such a single-frequency receiver, its autonomous positioning relies on the broadcast or generalized corrective models for some error mitigation. External corrections can be provided by the International GNSS Service (IGS) (IGS, 2012); Satellite Based Augmentation Systems (SBAS) like the American Wide Area Augmentation System (WAAS) and the European Geostationary Navigation Overlay Service (EGNOS) (Rho & Langley, 2005; Beran *et al.*, 2005); or by using NTRIP (Network Transport of the Radio Technical Commission for Maritime (RTCM) via Internet Protocol) (Colombo, 2008). The ionospheric, satellite clock and ephemeris errors mitigation can be improved using the precise IGS routinely produced ionospheric delay maps and precise clocks and orbits as done by Le & Tiberius (2007); Beran *et al.* (2005). Improved corrections can also be obtained from near real-time wide area SBAS broadcast (Ueno *et al.*, 2001; Huang & Yuan, 2007).

A dual-frequency stand-alone receiver can mitigate the error due to the ionosphere by combining the observations from both frequencies. This is a more accurate way of correcting the ionospheric error as it eliminates the frequency-dependent first-order ionospheric error that is more than 99% of the total ionospheric delay in the observation (Klobuchar & Kunches, 2003). The combination, however, results in observables with higher error (combination error) levels when compared to the error level in any one of the observations used in the combination. Moreover, part of the CRE in this type of correction is the residual ionospheric error from the dual-frequency correction that are due to the second and third order ionospheric effects. The second order effect is associated with the geomagnetic field influence and the third order mostly affected by ray bending in non-homogeneous (irregular) ionosphere (Kim & Tinin, 2007a). The second- and third-order effects are typically ~0-2cm, and ~0-2mm in the zenith direction, respectively. The error magnitude from higher order ionospheric effect may not always be neglected in certain stand-

alone receiver operations such as precise point positioning (PPP). PPP is a method that achieves centimeter to sub-decimetre level of positioning accuracy. It involves the processing of a single receiver's phase observations that may be combined with code observations, including the application of appropriate error corrective models to minimize inherent errors (tidal, satellite clocks, orbit and antenna phase offset errors) and ionospheric error. For improved mitigation of the ionospheric error in dual-frequency operation Hoque & Jakowski (2007), based on ionospheric simulations using the Chapman function and a superposed exponential decay for the vertical electron density distribution, generated a correction algorithm for the second-order ionospheric effect, and disclosed that the error from the second-order effects can be mitigated to within 2mm. The effect of the ionospheric irregularities (vertical and horizontal gradients) becomes strong especially at high and low latitudes, and during geomagnetic storms. Kim & Tinin (2007b) proposed the use of a receiver with three-frequency reception for the correction of the resulting higher order effects. The use of triple-frequency, envisaged for modernized GPS and Galileo, was also proposed by Wang *et al.* (2005) for the modelling and mitigation of the higher-order effect of the ionosphere. However, this proposal neglects the increased observation error after such triple-frequency linear combinations of observations.

The tropospheric error can be mitigated from the single- or dual-frequency observations using a generalized model like the SBAS model, or a more accurate model requiring known receiver sight's meteorological parameters. The IGS also produce tropospheric delay grid maps reported to be at the level of 3-6mm in the ZTD (van Leeuwen *et al.*, 2004; IGS, 2012). It is worth mentioning that any differencing between the dual-frequency code and/or phase observations of a stand-alone receiver eliminates the common errors in the resulting observable, though at the expense of increased combination error. An example of such is the geometry free combination used for ionospheric TEC estimation.

The multipath error and receiver noise in the code or phase observation has no corrective model, and thus remains as combined error in a code or phase observation.

2.5.2. Mitigation in Multiple-Receiver Operation

Differential or relative operation involves the use of more than one station (receiver / antenna pair) whereby one or more of them is/are used as reference by another for positioning. This usually involve differencing the observations(s) of the fixed known-location reference station(s) from the observation(s) of the unknown-location rover or user station, observed simultaneously from the same satellites. This kind of positioning operation could be done using the code observation, which is commonly referred to as differential GNSS (DGNSS) (Zhang *et al.*, 2009). Positioning with the phase observation, that could also include the code observation, in such a positioning operation, is often called real-time kinematic (RTK) positioning (Parkins, 2009). RTK relies on the determination of the integer ambiguities in order to use the phase observations for the required precise positioning. Taking the difference of the observations at the user and reference stations at the same epoch gives the single difference (SD), and the differencing between two single differences related to two simultaneously observed satellites produces the double difference (DD) (Ya'acob *et al.*, 2009). By such differencing, common mode errors (errors common to a large extent or the same, in both the reference and rover station's observations) such as a satellite ephemeris and clock errors, the receiver clock error, hardware delays, and atmospheric errors, can be mitigated in DD (Satirapod *et al.*, 2003). This mitigation makes it possible to achieve DGNSS sub-meter accuracy and a RTK accuracy as high as centimeter to millimeter level. The obtained accuracy is dependent on the level of the common mode error mitigation, which in turn depends on the distance between the reference and user station, called the baseline. As usually the case with 'short' baselines, the post-DD resulting tropospheric, ionospheric and ephemeris residual errors are quite small and negligible. The existence of ionospheric gradients; the ionospheric time and spatial decorrelations between a reference station and user station locations - a phenomenon usually common in the equatorial and polar regions; or the presence of ionospheric activities, can however make the residual ionospheric error significant in baselines of a few kilometers (Walter *et al.*, 2004; Lee *et al.*, 2006).

Again, the non-eliminated errors, such as the multipath error in the cumulative

observation error, do not only remain, but increases by a factor of about two and four in the SD and DD observables respectively.

2.6. Pre-Observation Multipath Mitigation

The error contribution of multipath unto a code or phase observation can be suppressed prior to a receiver recording of the raw phase and code observations. 'Pre-observation' mitigation technique is used here to refer to any technique that concentrates on mitigating multipath error, prior to the receiver recording of observations. These pre-observation mitigation techniques include any mitigation technique within the receiver antenna or implemented in the receiver hardware design (e.g. an enhanced DLL), to suppress multipath error on the recorded observations. Such techniques are employed before the receiver finally records the required raw phase and code observations.

A receiver antenna design and configuration is one way in which pre-observation mitigation can be enforced. Extended ground planes, choke rings and microwave absorbing materials added to the antenna hardware can help suppress multipath signals (Bisnath *et al.*, 1997). Many reference stations today employ choke ring antennas. Antenna array has also been shown to have capability in mitigating multipath signals entering a receiver's antenna (Amin & Sun, 2005). Neither of these has however proved to eliminate the multipath error completely. Pre-observation mitigation is also significantly enhanced in the receiver hardware design. The correlators of the DLL plays a significant role in this respect. Narrow correlators have been shown to achieve better mitigation results than the standard correlators of 1chip spacing (Braasch, 2001). The comparison results using correlator spacing of $d = 1$ and $d = 0.1$ shown in Figure 2.3 confirms this for the low chipping rate C/A code. Further improvements acquired through receiver design pre-observation mitigation technique can be found in (Ferreira & Dunes, 2007; Chang & Juang, 2008). The common limitation for receiver hardware mitigation is the incapability to significantly mitigate short-delay multipath (Pany *et al.*, 2005).

One general way of employing a pre-observation mitigation technique when siting

fixed reference stations is by avoiding multipath-prone environments, through careful sites selection. While this approach may be suitable for siting reference stations, it is still difficult to get such sites for all applications, knowing also that a roving user cannot rely on this kind of approach. For example, when siting GNSS antennas for structural monitoring or in oil rig platforms, it may not be possible to have sites not susceptible to multipath.

Also, like with GPS, the geometry relating its satellites and a specific fixed-location antenna repeats every sidereal day, when the antenna environment is 'constant'. The multipath disturbance in such scenarios have periodic characteristic or traits that are repeated between consecutive days, and can therefore be suppressed on daily data sets. Although not employed as a pre-observation but a 'post-observation' multipath mitigation technique, these multipath traits can be used in enabling multipath mitigation as the 'supposed' multipath correction for each satellite signal can be reasonably predicted and applied appropriately (Ge *et al.*, 2000). The limitation is that the method requires continuous monitoring of the antenna environment and could also become unreliable in the presence of ionospheric activities.

While the receiver noise is not mitigated, it can be traded-off against bandwidth, since a decrease in bandwidth results in lower white noise power. A longer correlation interval (reduced bandwidth) in the acquisition stage of the receiver can enable correct satellite signal detection even in the presence of high noise levels.

All these techniques are implemented or used where possible, and their limitations or imperfections manifest as contributory errors to the resulting observation error levels in the receiver's recorded raw code and phase observations. Hence, post-observation mitigation techniques that concentrate on the mitigation of the embedded observation error levels in the recorded (raw) observations are still sought and required.

2.7. Summary

Various error sources do exist, contributing the errors in any GNSS phase or code observations. The errors are associated with the GNSS satellite, the atmosphere which the transmitted satellite signal propagates, the GNSS receiver and the operating environment of the receiving antenna. Corrective error models - with limited accuracy - can be applied to mitigate some of these errors, but the environmentally dependent multipath error, and receiver noise, have no generalized corrective models. Errors can also be mitigated by differencing in relative or differential positioning operations, when more than one receiver is used in positioning; by applying pre-observation mitigation techniques within the receiver/antenna; or by careful siting of fixed stations' antennae. Mitigation of errors aims at improving the PVT solutions obtainable with a GNSS, and GNSS-based parameter estimation.

Chapter 3.

Existing Error Mitigation, Cycle Slip Detection and Correction Techniques for Improving Positioning

GNSS pre-observation mitigation techniques employed prior to a receiver generation of the phase and code observations, aim at suppressing multipath error but do not wholly eliminate the multipath error in the observations. As discussed in Section 1.1.4 and Section 2.6, the recorded code and phase observations remain contaminated with observation error levels that need to be mitigated. The mitigation of the code observation error is a primary objective of this research work. Consequently, this chapter presents a review of some existing observation error mitigation techniques applicable in the position- and range-domain, and their possible limitations. In line with the research objectives, this chapter further reviews different methods currently used for cycle slip detection and determination, as well as applicable ionospheric error mitigation models, for both single- and dual-frequency receivers.

3.1. Position, Velocity and Time Estimations

In 3D-positioning, a stand-alone receiver estimates its unknown position coordinates (usually x, y and z) in a GNSS reference frame coordinate. A global reference frame (realization of a reference system) is described by an ideal earth shape model (ellipsoid). The coordinate system of such a reference frame is usually the earth-centred earth-fixed (ECEF), a geocentric Cartesian coordinate (X, Y, Z); or a curvilinear coordinate (geodetic latitude, longitude, height) system; with origin at the centre of the earth, by which the GNSS satellites' positions and a position of a receiver positioned by the GNSS can be defined. The reference systems for different GNSS are usually different. For example, the World Geodetic System 1984 (WGS84) is the reference system of GPS, while the reference frame of GLONASS, defined by a different ellipsoid, is called PZ 90 (Bykhanov, 1999). Two different positioning coordinates of a receiver, obtained differently, by say GPS and GLONASS, would differ as they are generated on two different reference frames. The GPS refined WGS84 reference frame is currently reported to coincide with the global International Terrestrial Reference Frame (ITRF2000) within a few centimeters at the global level. The ITRF is internationally acclaimed the most precise and accurate reference frame as it is regularly updated to account for the dynamics of the earth (Janssen, 2009). Furthermore, local coordinate systems can be defined by placing a known local position as the origin and other positions defined with respect to this set origin. Example of such a local coordinate is the East (E) pointing to the east, North (N) pointing to the north, and Up (U) coordinate; where the EN plane describes the horizontal plane and the vertical, U, is defined perpendicular to the horizontal plane. Two position coordinates of a receiver would differ if they are generated on different reference frames, say from two different GNSSs. Transformation from one reference frame coordinate to another is do able, but the acquired accuracy depends on the method used, as well as the accuracy and the number of the distributed common points (positions) used to determine the transformation parameters (Janssen, 2009; Xu, 2003).

While all the satellites of a GNSS can be 'synchronised' to the GNSS system time, the receiver clock offset from the GNSS system time remains another unknown.

Consequently, at least four different satellites in the view of a receiver's antenna are required to compute a 3D position of the receiver. Only the observed code observations or both the observed code and phase observations by a receiver, could be used for a receiver positioning. Though different approaches exist for determining a positioning solution, the least squares approach is often used and it is suitable for an over-determined system of equations that arises when the number of observed satellites is greater than four. Least squares approach for GNSS code and phase based positioning can be found in Hegarty (2006); Cross (1983); Misra & Enge (2006).

The user (receiver) velocity can be determined from the Doppler observation (Xu, 2003) or the pseudorange rate. The Doppler shift can be modelled as a projection of the relative velocity vector on the line-of-sight vector from a receiver to a satellite, including the relevant biases. It involves determining the time derivatives of a satellite clock error, the satellite position as well as its velocity from the navigation message (Misra & Enge, 2011). The relativistic effects are also taken into account. A least squares technique for the receiver velocity computation is detailed in Xu (2003).

Timing information for keeping precise time, comparison of remote clocks and synchronisations of multiple nodes (stations), can be obtained with GNSS. After obtaining an unknown receiver clock offset with respect to a GNSS system time, a receiver may further align its time to the Coordinated Universal Time (UTC) - the civil time standard - if the offset between the GNSS system time and UTC is known. For instance, the broadcast GPS navigation message contains parameters to estimate the offset between GPST and UTC at any instant with an rms error of about 10ns (Misra & Enge, 2006). Consequently, a receiver can determine and display UTC time and produce the one pulse per second (PPS) signal for synchronisation with UTC, in precise timing applications. The total error in this mode of time distribution from GPS is within 25ns, making it suitable for time synchronisation such as required in telecommunication networks where accuracy of about 100ns is usually sufficient.

The estimation of a receiver position, velocity and time (PVT) and other parameters such as the ionospheric total electron content (TEC), are all affected by the

magnitudes of the observation errors in the GNSS observations from which such estimations are made. GNSS is applied in many areas mostly because of its capability to provide PVT information. Hence, the use of GNSS in critical applications and estimations of parameters, can be further enhanced when the observation error levels are eliminated or drastically mitigated.

3.2. Observations and Error Mitigation Domains

From Section 2.3, the simultaneously observed and same band's code and phase observations given by Equations (2.9) and (2.10) are repeated here for a current epoch, t, as

$$P_i^s(t) = r^s(t) + c\delta t^r(t) - c\delta t^s(t) + T^s(t) + I_i^s(t) + d_i^s(t) + d_i^r(t) + S_o^s(t) + m_{P,i}^s(t) + \epsilon_{P,i}^s(t) \quad (3.1)$$

and

$$\psi_i^s(t) = r^s(t) + c\delta t^r(t) - c\delta t^s(t) + T^s(t) - I_i^s(t) + b_i^r(t) + b_i^s(t) + \lambda_i N_i^s + S_o^s(t) + m_{\psi,i}^s(t) + \epsilon_{\psi,i}^s(t) \quad (3.2)$$

respectively. $\psi_i^s(t)$ as given by Equation (3.2) assumes that there is no cycle slip at the current t epoch, and so the ambiguity N_i^s is unchanged and remains the same value as in previous epoch(s), if any. It should be recalled that N_i^s can be a positive or a negative integer. This condition is always required by existing phase-dependent code observation error mitigation techniques. There is essentially no difference between the code observation Equations of (2.9) and (3.1), and the phase observation Equations of (2.10) and (3.2), except for the inclusion of the epoch index. As a choice made in this thesis, the observation epoch number, used as an index, could be attached when referring to an epoch observation/observable; and it would be omitted when referring to a time series observation/observable, or could also be omitted for simplicity as may be necessary.

We could assign

$$\rho^s(t) = r^s(t) + c\delta t^r(t) - c\delta t^s(t) + T^s(t) + S_o^s(t) \quad (3.3)$$

to represent the common terms in Equations (3.1) and (3.2), which are carrier frequency or GNSS band independent. As assigned, at epoch t, $\rho^s(t)$ contains the true geometric range and other errors (troposphere, clocks and satellite orbits errors); and differencing between any two observations in the same or different bands from a same satellite s will generate an observable without $\rho^s(t)$ that can be referred to as a geometry-free observable.

As a further simplification to align with the intention of existing code error mitigation or smoothing techniques, and as the primary aim of the code error mitigation algorithm to be developed in this thesis, the combined multipath error and receiver noise, which are the dominant portion of an observation error, can be combined as (Le & Teunissen, 2006)

$$\eta^s_{P,i}(t) = m^s_{P,i}(t) + \epsilon^s_{P,i}(t) \tag{3.4}$$

$$\eta^s_{\psi,i}(t) = m^s_{\psi,i}(t) + \epsilon^s_{\psi,i}(t) \tag{3.5}$$

where $\eta^s_{P,i}$ and $\eta^s_{\psi,i}$ denote the combined multipath error and noise on $P^s_i(t)$ and $\psi^s_i(t)$ respectively. By this definition, $\eta^s_{P,i}$ and $\eta^s_{\psi,i}$ could be assumed the code error and phase error, with negligible differences, thus replacing the whole code observation error and phase observation error in a code and phase observation respectively; and as such are interchangeably used in this thesis. As it turns out, the magnitude of $\eta^s_{\psi,i}$ is orders of magnitude much smaller than the magnitude of $\eta^s_{P,i}$, for both a single- and a dual-frequency receiver, which is the obvious reason why interest is on mitigating the $\eta^s_{P,i}$ code error and not actually the $\eta^s_{\psi,i}$ phase error. A time series of $\eta^s_{P,i}$ and $\eta^s_{\psi,i}$ contain both the low and high frequency components of the multipath error and noise in $\eta^s_{P,i}$ and $\eta^s_{\psi,i}$ respectively. For a single-frequency receiver, it is assumed that $i = 1$ and $i = 1, 2$ for a dual-frequency receiver henceforth.

3.2.1. Error Mitigation Domains

Positioning can be improved through mitigation of the code error and phase error in the code and phase observations. The filtering/smoothing[1] of the raw observations

[1] The terms, filtering and smoothing, are processes that may be interchangeably used in this thesis to refer to a process of error mitigation, for improved estimation of the underlying parameter(s)

in the measurement/observation space is often referred to as measurement- or range-domain filtering (Lee *et al.*, 2005; Paielli & ARC, 1987). Range-domain filtering is usually performed with, and on the observations from a satellite individually, and would thereafter have the smoothed or filtered outputs from individual satellites input into a positioning algorithm to further determine the position of the observing receiver. In position-domain filtering, the observations from all the observed satellites at a given epoch are used in a receiver positioning algorithm, applying relevant weightings to the observations, and thus determining the unknown state variables (at least the receiver position and clock offset). By way of position-domain filtering, the effect of the observation errors on estimated receiver position would be mitigated. Error mitigation can also be done through a combination of both range-domain and position-domain filtering, or by variations of either filtering technique. The main advantage of the range-domain filter is the decreased processing and storage requirements compared to the position-domain filter, while the position-domain filter, compared to the range-domain filter, is negligibly affected with changes in the number of satellites tracked by the receiver over time(Lee & Rizos, 2008; Bisnath & Langley, 2001a).

The filtering algorithms employed in range-domain or position-domain could involve mere weighting of observations, Kalman filtering or least squares process, as done in the existing techniques reviewed in this chapter. While the least squares and Kalman filtering (KF) algorithms are presented in the Appendix of this thesis, (Cross, 1983) and Brown & Hwang (2012) are suitable and extensive reference materials for least squares and Kalman filtering respectively.

from an observation/observable affected by error. In a strict sense, if at current epoch t, the process involves up to the current epoch observation, then filtering is said to be done. If the process involves observation only up to a past epoch, τ, where $\tau < t$, then smoothing is said to be done. In addition, prediction refers to estimation/generation of the parameter(s) for $\tau > t$ (Cross, 1983).

3.3. Improving Positioning via Error Mitigation

This section presents a review of some existing error mitigation and improved positioning techniques applied in a range- or position-domain.

3.3.1. Error Mitigation in Range Domain

Most existing single-receiver (stand-alone receiver) error mitigation techniques in range-domain concentrate on the mitigation of the code error only. To this end, it is a usual practice to assume that the level of the observation error on a phase observation is negligibly small compared to that on the code observation, and as such, advantage is taken of the precision of the ambiguous phase observation to reduce the level of the code error on the more noisy, non-precise but unambiguous code observation. The phase observation in unit of meters given by Equation (3.2) is suitable for use in this regard.

The mitigation of the level of the code error, denoted $\eta^s_{P,i}$ in Equation (3.4), in a code observation, could also be referred to as code smoothing. Some of the existing range-domain techniques for code smoothing are hereby reviewed.

3.3.1.1. Carrier-Smoothing and Its Derivatives

The conventional carrier-smoothing technique for smoothing code observation is a range-domain filter introduced by Hatch (1982). This technique, also called Hatch filtering technique (HFT), is an averaging filter that smooths a code observation using a carrier phase observation. If m is the number of consecutive epoch observation from satellite s since the first observation epoch of s or since the last epoch of cycle slip occurrence on ψ^s_i, the Hatch filter implementation, which is recursive, is given as (Park & Kee, 2005)

$$\bar{P}^s_{i,HFT}(t) = \frac{1}{M}P^s_i(t) + \frac{M-1}{M}[\bar{P}^s_{i,HFT}(t-1) + \psi^s_i(t) - \psi^s_i(t-1)] \tag{3.6}$$

where $\bar{P}^s_{i,HFT}(t)$ and $\psi^s_i(t)$ are respectively the smoothed code observation and raw (unsmoothed) phase observation at a current epoch, t; $\bar{P}^s_{i,HFT}(t-1)$ and $\psi^s_i(t-1)$

are respectively the smoothed code observation and raw phase observation at the previous $t-1$ epoch; and M is a preset or fixed smoothing time constant[2] in samples, which is unitless and could also be referred to as the filter length or smoothing window length. If $m < M$ then $M = m$ in (3.6), otherwise (i.e. for $m \geq M$) M remains as fixed. The m is initialized to 1 whenever a cycle slip occurs on ψ_i^s from s. At the first observation epoch of satellite s, $\bar{P}^s_{i,HFT}(1) = P_i^s(1)$ and $m = 1$. This HFT or carrier-smoothing (CS) technique is widely used. Code error mitigation in the operational Local Area Augmentation System (LAAS) is based on this technique (McGraw *et al.*, 2000). With this technique, the time series ψ_i^s must be continuous without cycle slip occurrence over M observation epochs. As it is, the HFT mitigates the code $\eta^s_{P,i}(t)$, but introduces an HFT-associated error in the smoothed $\bar{P}^s_{i,HFT}(t)$ observable. Following the derivation in Walter *et al.* (2004) for single-frequency operation, and including the impact of the $\eta^s_{\psi,i}$ phase error, the HFT-associated error at current epoch t is thus given as

$$\begin{aligned} \eta^s_{HFT_{P,i}}(t) &= -2\frac{(M-1)}{M}\triangle I_i^s + \frac{1}{M}\eta^s_{P,i}(t) + \frac{(M-1)}{M}\eta^s_{HFT_{P,i}}(t-1) \\ &\quad + \frac{(M-1)}{M}\left[\triangle\eta^s_{\psi,i}(t)\right], \end{aligned} \tag{3.7}$$

where $\triangle I_i^s = I_i^s(t) - I_i^s(t-1)$, $\eta^s_{HFT_{P,i}}(t-1)$ is the HFT-associated error up to the previous $t-1$ epoch, and $\triangle\eta^s_{\psi,i}(t) = \eta^s_{\psi,i}(t) - \eta^s_{\psi,i}(t-1)$. Thus, $\bar{P}^s_{i,HFT}(t)$ contains the HFT-associated error, $\eta^s_{HFT_{P,i}}(t)$, in addition to the other common errors present in $\psi_i^s(t)$ and $P_i^s(t)$ - the troposphere, ionosphere, clocks and satellite orbit errors (see Equation (3.3)). Moreover, $\bar{P}^s_{i,HFT}(t)$ also contains the propagated phase error $\eta^s_{\psi,i}$ that is assumed negligible by the HFT technique.

The HFT performance is dependent on the chosen M; the higher it is, the more precise the smoothed code observation since $\eta^s_{P,i}(t)$ is scaled down by M, as seen in Equation (3.7). However, for single-frequency users, because of the existence of

[2]The time constant of a filter, t_m, has unit of seconds. The smaller it is, the more rapidly the output from the filter resembles the input. The time constant in samples, $M = \frac{t_m}{\triangle t}$, with $\triangle t$ being the inverse of the observation rate, which is the sample interval in seconds. Hence for 1, 2 and 5Hz observation data, a filter with $t_m = 100$seconds will have corresponding time constants in samples as: $M = 100$, 200 and 500 respectively (Ambardar, 1999).

the code carrier divergence - the effect of the opposite signs of the ionospheric error term I_i^s in the code and phase observations (resulting as the first term in Equation (3.7)), the HFT smoothed code observation degrades in accuracy as M increases. Due to this unavoidable ionospheric divergence, the presence of large ionospheric gradients that can result to a rate of change of the ionospheric delay of more than 150mm/sec (Walter *et al.*, 2004) compared to the nominal day value of about 4-6mm/sec, contributes to the degradation of the HFT performance. Such effects could give rise to up to 30m error in the smoothed code observation. A trade-off between precision and accuracy in the smoothed $\bar{P}^s_{i,HFT}$ is automatically set by an 'intelligent' choice of M. For 1Hz data rate (1 second interval between consecutive observations), many experts accept the empirical value of 100 for M, which is also the recommended filter length for LAAS (RTCA, 2004). Zhenggang *et al.* (2008) and Zhao *et al.* (2009) also showed that different code positioning accuracy levels would result for different filter lengths. Consequently, various modifications, being derivatives of the conventional HFT, with either varying or adaptive M, have been unveiled as seen in (Park & Kee, 2005) and (Park *et al.*, 2008) where they obtained DGPS horizontal 2D RMS accuracy of less than 1m from 180m baseline and showed improved code positioning accuracy of about 15%. Proposed algorithm for the reduction of the ionospheric divergence through a non-linear process can be found in Sen & Rife (2008).

Fortunately, with dual-frequency observations, where $i = 1, 2$ for instance, and with the HFT smoothed $\bar{P}^s_{i,HFT}$ code observables generated according to (3.6), the corresponding HFT ionosphere-free code observable at epoch t, can consequently be obtained as (Misra & Enge, 2006)

$$P^{s,IF}_{HFT}(t) = \frac{f_1^2}{f_1^2 - f_2^2}\bar{P}^s_{1,HFT}(t) - \frac{f_2^2}{f_1^2 - f_2^2}\bar{P}^s_{2,HFT}(t) \tag{3.8}$$

Equation (3.8) is presumed unaffected by ionospheric divergence as the first-order ionospheric terms are almost eliminated in such an ionosphere-free observable. Alternatively, the two bands dual-frequency $\bar{P}^s_{i,HFT}$ code observables without the iono-

spheric divergence effect can be generated as (Horemuz & Sjoberg, 2002)

$$\bar{P}^s_{i,HFT}(t) = \frac{1}{t}[\sum_{a=1}^{t} P^s_i(a) + (t-1)(A_i\psi^s_1(t) - B_i\psi^s_2(t) - A_i\sum_{a=1}^{t-1}\psi^s_1(a) + B_i\sum_{a=1}^{t-1}\psi^s_2(t)] \quad (3.9)$$

where $A_1 = (f_1^2 + f_2^2)/(f_1^2 - f_2^2)$ and $B_1 = 2f_2^2/(f_1^2 - f_2^2)$, for generating $\bar{P}^s_{1,HFT}(t)$; and $A_2 = 2f_1^2/(f_1^2 - f_2^2)$ and $B_2 = (f_1^2 + f_2^2)/(f_1^2 - f_2^2)$, for generating $\bar{P}^s_{2,HFT}(t)$. Except for the divergence term $(2\frac{(m-1)}{m}\triangle I^s_i)$, the dual-frequency $\bar{P}^s_{i,HFT}$ observables are still affected by the other HFT-associated error terms given by Equation (3.7). It is worth noting that with dual-frequency code observables such as given by Equations (3.8) and (3.9), there is a choice to either use the increasingly varying filter length ($M = t$, which could make M as large as up to the number of epochs since the very first observation epoch of s if there is no cycle slip in either of the dual-frequency phase observations) as done in Rho & Langley (2005) for dual-frequency static positioning; or fix/set M to a value considered appropriate. In practice, it should be appropriate to fix M to a value not more than a few tens of minutes (for 1Hz data), knowing that the higher-order ionospheric effects that are not eliminated with dual-frequency observations could have significant effect on $\bar{P}^s_{i,HFT}$ when M is excessively large. Dual-frequency HFT techniques can help achieve up to tens of centimetre improvement in positioning compared to solutions obtained with unsmoothed code observations, which is evident in the results of Rho & Langley (2005). Being a range-domain filtering technique, the least square positioning algorithm is often an appropriate choice when using Hatch filtered code observables for positioning.

We can identify some limitations in the HFT. While the ionospheric divergence problem could be presumed eliminated using dual-frequency receivers, it remains a fundamental problem that can only be traded with the positioning accuracy obtainable with a single-frequency receiver, as the applied M is often nothing but an intelligent guess. Again, it is illogical to fix M, as the features of the time series of $\eta^s_{\psi,i}$ are not fixed but varying within a given period of observation. Furthermore, when a large multipath error occurs in the code pseudorange, the effect contaminates the smoothed code observable, not just at that epoch but also at several subsequent epochs - a condition that gives rise to the multipath divergence problem (Kim &

Langley, 2000). Hence, the HFT also suffers from multipath divergence over a short time interval. Due to the nature of the HFT, the raw phase $\eta^s_{\psi,i}$ is also propagated on the smoothed code as an additional error, which can be observed in Equation (3.7). The most critical limitation with the single- and dual-frequency Hatch filtering technique is its inability to smooth the code observations whenever a cycle slip occurs on any or both of the dual-frequency phase observations, or when an outage satellite re-locks to the receiver. In both cases, it re-initialises its smoothing operation, and would only be able to attain a good error mitigation level after a number of epochs, which is analogous to the long convergence time associated with conventional with ambiguity resolution technique.

3.3.1.2. Combination of Code and Phase Observations

Knowing that the ionospheric delay to first order is related to the carrier frequency as given in Equation (2.5), and because of the opposite signs on the ionospheric error (delay) term in the code and phase observations, many existing techniques combine the phase and code observations to mitigate the ionospheric error effect, and consequently generate the smoothed/filtered code observations for a single- or a dual-frequency receiver. It is presumed that the ionosphere-free observable resulting from a dual-frequency LC eliminates the ionospheric divergence problem prevalent in single-frequency operations (Hwang *et al.*, 1999).

Consequently, Gao & Wojciechowski (2004), upon applying external precise satellites clocks and orbits corrections, used a combination of the raw GPS code and phase observations for PPP solutions. The procedure which neglected hardware delays, involved obtaining observables that are considered free of ionospheric error given as

$$P^s_{L1} = 0.5(P^{s*}_1 + \psi^{s*}_1) = r^s + c\delta t^r + T^s + 0.5\lambda_1 N^s_1 + 0.5\eta^s_{P,1} + 0.5\eta^s_{\psi,1} \tag{3.10}$$

$$P^s_{L2} = 0.5(P^{s*}_2 + \psi^{s*}_2) = r^s + c\delta t^r + T^s + 0.5\lambda_2 N^s_2 + 0.5\eta^s_{P,2} + 0.5\eta^s_{\psi,2} \tag{3.11}$$

$$\begin{aligned}\psi^s_{IF} &= \frac{1}{f_1^2 - f_2^2}(f_1^2\psi_1^{s*} - f_2^2.\psi_2^{s*}) \\ &= r^s + c\delta t^r + T^s + F_1\lambda_1 N_1^s - F_2\lambda_2 N_2^s + F_1(\eta^s_{\psi,1}) - F_2(\eta^s_{\psi,2}) \end{aligned} \quad (3.12)$$

The asterisk, $*$, in Equations (3.10) through (3.12) indicate an observable already corrected for satellite clock and orbit errors, and as such, those terms disappear from the observation Equations given by (3.1), and (3.2) and subsequently (3.10) through (3.12). The smoothed new code observables from the L1 and L2 bands are respectively P^s_{L1} and P^s_{L2}, with reduced (halved) code error, while the new ionospheric-free phase observable is ψ^s_{IF}; given that $F_1 = \frac{f_1^2}{f_1^2 - f_2^2} = 2.5467$ and $F_2 = \frac{f_2^2}{f_1^2 - f_2^2} = 1.5467$. These P^s_{L1}, P^s_{L2} and ψ^s_{IF} were the observables used for the PPP solutions in the paper. Assuming equal code error levels on both bands, an obvious observation in Equation (3.10) or (3.11) is that, at best, the code error level in any of these smoothed code observables is only halved, and the technique cannot be used when a cycle slip occurs.

Based on differencing raw phase and code observations from a satellite, many code-minus-carrier (CMC) related techniques are currently used for mitigating code error. CMC techniques are commonly used in dual-frequency operations (Harris & Lightsey, 2009; Bisnath & Langley, 2001b; Bisnath *et al.*, 1997). The basic CMC expressions obtainable from dual-frequency code and phase observations in the L1 and L2 bands, following from Equations (2.10) and (2.9), and neglecting hardware delays, are given as

$$P^s_1 - \psi^s_1 = 2I^s_1 - \lambda_1 N^s_1 + \eta^s_{P,1} - \eta^s_{\psi,1} \quad (3.13)$$

$$P^s_2 - \psi^s_2 = 2\gamma I^s_1 - \lambda_2 N^s_2 + \eta^s_{P,2} - \eta^s_{\psi,2} \quad (3.14)$$

The L1 band ionospheric delay term, I^s_1, is usually obtained from $\frac{(\psi^s_1 - \psi^s_2)}{\gamma - 1}$ and eliminated as in Equations (3.15) and (3.16). As the hardware delays are neglected, the resulting observables are dominated by the different code error levels and the associated scaled ambiguity bias terms:

$$P^s_1 - D_1\psi^s_1 + D_2\psi^s_2 = -D_1\lambda_1 N^s_1 + D_2\lambda_2 N^s_2 + \eta^s_{P,1} - D_1\eta^s_{\psi,1} + D_2\eta^s_{\psi,2} \quad (3.15)$$

$$P_2^s - D_2\psi_2^s + D_1\psi_2^s = -D_2\lambda_1 N_1^s + D_1\lambda_2 N_2^s + \eta_{P,2}^s - D_2\eta_{\psi,1}^s + D_1\eta_{\psi,2}^s \quad (3.16)$$

In Equations (3.15) and (3.16), $D_1 = \frac{\gamma+1}{\gamma-1} = 4.0915$, $D_2 = \frac{1}{\gamma-1} = 3.0915$, knowing that the ambiguity terms remain constant as far as lock is maintained and there is no cycle slips in the time series of ψ_1^s and ψ_2^s. As often done, e.g. in (Bisnath & Langley, 2001b), the mean of the time series of the observable obtained by Equation (3.15), is subtracted from Equation (3.15) to eliminate the constant terms, and the resulting residual is assumed the L1 code error, $\eta_{P,1}^s \equiv \eta_{P,1}^s - D_1\eta_{\psi,1}^s + D_2\eta_{\psi,2}^s$, which is then subtracted from the raw time series of P_1^s to generate the time series smoothed L1 code observable. Similarly, $\eta_{P,2}^s \equiv \eta_{P,2}^s - D_2\eta_{\psi,1}^s + D_1\eta_{\psi,2}^s$, obviously neglecting the impact of the LC phase errors. Alnaqbi (2010) integrated this technique with wavelet decomposition for single-frequency DGPS positioning and reported centimetres range accuracy over short baselines. This algorithm is also limited by a cycle slip occurrence.

Extended forms of the CMC technique, Divergence-Free (DFree) smoothing and Iono-Free (IFree) smoothing, were introduced by (Hwang *et al.*, 1999) for dual-frequency DGPS positioning. The performances of the DFree-smoothing and IFree-smoothing were evaluated and compared in McGraw & Young (2005), Konno *et al.* (2006) and (Konno, 2007). They concluded that DFree-smoothing outperforms the IFree-smoothing under normal ionospheric conditions, and it should be preferable for DGPS because of the presence of lower code error compared to the increased code error in IFree-smoothing. The block diagram for DFree and IFree smoothing, is shown in Figure 3.1. The P^s and θ^s denote the input code-associated and phase-associated observables from satellite s respectively, which are computed as: $P^s = P_1^s$ and $\theta^s = \psi_1^s$, in single-frequency operation; $P^s = P_1^s$ and $\theta = \psi_1^s - \frac{2}{\gamma}(\psi_1^s - \psi_2^s) = D_1\psi_1^s - D_2\psi_2^s$, for the DFree divergence-free smoothing with dual-frequency; and $P^s = F_1P_1^s - F_2P_2^s$ and $\theta^s = F_1\psi_1^s - F_2\psi_2^s$, for the IFree smoothing with dual-frequency. For all three smoothing types, $\epsilon = P^s - \theta^s$. The ϵ includes the difference between the code- and phase-associated errors, and it is filtered by the low pass filter (LPF) usually with a time constant $t_m = 100$seconds, to yield $\bar{\epsilon}$. The smoothed code observable, $\overline{P^s}$ is then obtained by recombining $\bar{\epsilon}$ and θ^s. From Figure 3.1, the DFree

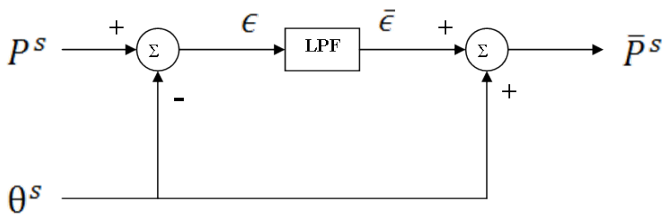

Figure 3.1.: Block diagram of the Divergence-Free and Iono-Free smoothing

smoothed L1 code observable thus becomes

$$\overline{P^s} = \rho^s + I_1^s + d_1^r + d_1^s + \Gamma(\eta_{P,1}) + \Gamma(D_1\eta_{\psi,1} - D_2\eta_{\psi,2}) + D_1\eta_{\psi,1} - D_2\eta_{\psi,2} \quad (3.17)$$

The Γ notation used in Equation (3.17) indicates a term that is filtered (smoothed) by the LPF. It is observed that the ionospheric delay term is still present in the DFree smoothed L1 code observation. Moreover, the smoothed code, and the associated phase combination error terms constituting up to at least 5 times the level of the L1 phase error, are consequently included in the smoothed code observable $\overline{P^s}$ (Equation (3.17)). The IFree-smoothed code observable can be represented as

$$\overline{P^s} = \overline{P^s}_{IF} = \rho^s + d_{IF}^r + d_{IF}^s + \Gamma(F_1\eta_{P,1} - F_2\eta_{P,2}) + \Gamma(F_1\eta_{\psi,1} - F_2\eta_{\psi,2}) \quad (3.18)$$

The IFree smoothed code observable obviously does not have the ionospheric delay term but includes the filtered (smoothed) LC code error and LC phase error. Even though the filter does smooths the ϵ in this case, the level of error in ϵ due to the IFree linear combination is about three times greater than the level of the code error in P_1^s. McGraw & Young (2005), Konno *et al.* (2006) and (Konno, 2007) concluded that the DFree-smoothing outperforms the IFree-smoothing under normal ionospheric conditions, and that the DFree-smoothing would be preferable because of the increased and higher level error in the IFree-smoothed code observable. One of the drawbacks in this DFree- and IFree-smoothing techniques is the use of a fixed time constant. McGraw & Young (2005) also showed that the performance of these techniques depend on the chosen time constant, as it is with the HFT. Moreover, the seemingly preferred DFree-smoothing is not reliable for use under ionospheric

anomalies (Konno *et al.*, 2006). For DFree-smoothing, where the ionospheric delay is still present despite the available dual-frequency observations, it cannot be reliably used for stand-alone receiver positioning without an assisted (possibly external) ionospheric correction. Above all, the three algorithms break down in the presence of a cycle slip.

3.3.1.3. Kalman Filtering and Other Filtering Techniques

Some range-domain error mitigation techniques are built around Kalman filtering and related techniques. In range-domain KF algorithms, assumptions are usually made about the dynamic model of the pseudorange rate, as the true dynamics of the receiver are not known a priori. An exponentially correlated acceleration or velocity, or a white noise acceleration pseudorange rate model is commonly assumed (Paielli & ARC, 1987), which is then incorporated into a designed state transition matrix Φ and a process noise covariance matrix Q. The state vector x often includes the true range and the delta range, and any other parameters that may be of interest, e.g. range rate and range acceleration. Based on a time-correlated multipath and velocity model, Yang *et al.* (2004) presented a KF based technique for mitigating multipath in code observations. Obviously, the applied multipath model cannot be used as a generalized model for multipath. Euler & Goad (1991) employed an exponential model for the pseudorange uncertainty and used a Bayes filter to filter the GPS dual-frequency code observations in range-domain. A common limitation of these techniques is the assumption of the uncertainties in the observation, and the adopted dynamic model where applicable.

A recursive range-domain filtering technique that updates its covariance information was introduced in Lee *et al.* (2005), and based on analytical comparison, concluded that it will be outperformed by a similar position-domain filter. An adaptive finite impulse response (FIR) filter based on a least mean square algorithm was presented in Ge *et al.* (2000), attaining a reduction in the standard deviation of the time series code error by about half. Apart from its limited use for only static positioning, the technique is also dependent on a previously modeled reference signal (obtained from previous days estimated multipath signature of the fixed point),

which has to be used as reference input to estimate the current day's code error.

3.3.2. Error Mitigation and Positioning in Position-Domain

Error mitigation in position-domain are generally based on stochastic models incorporated into a least square or Kalman Filtering positioning algorithm, where the receiver position is determined along side with other unknown parameters/variables that may be of interest. Essentially, position-domain techniques can be considered as techniques that attempt to directly mitigate the effect of the code and phase observation errors on the estimated receiver positioning solution. Position-domain mitigation can be done in both single- and dual-frequency operations.

3.3.2.1. Single-Frequency Position-Domain Mitigation

A lot of position-domain error mitigation techniques are used in single-frequency operation. The so-called phase-adjusted algorithm, where all the raw phase and code observations are used, and the unknown parameters including ambiguities and receiver position parameters are estimated by a recursive LS algorithm, has been used as a position-domain mitigation algorithm in Le & Teunissen (2006); Le & Tiberius (2007). They reported up to 30% improvement in positioning and decimetre to metre level range accuracy, after applying IGS external corrections for satellites clocks and orbits, and the IGS global ionospheric map (GIM) model.

A phase-connected technique (Bisnath & Langley, 2001a), where the code observables and the time differenced phase observables at a given epoch are used in the position-domain algorithm, also exists. After applying external corrections from IGS, Bisnath & Langley (2001a) used the phase-connected technique based on a sequential LS algorithm. Beran *et al.* (2003) also used the phase-connected technique based on a KF algorithm with preset dynamic model. Both reported positioning accuracy up to decimeter-level.

The phase-adjusted and phase-connected position-domain algorithms are limited by the fact that they require more than four satellites to achieve improved positioning solution, especially when it includes real-time estimation of the ionospheric error, thus not making them attractive for use in challenged environments where cycle

slip is prevalent and less than five satellites may be observed at certain epochs. Moreover the covariance matrices of the observables and the the process noise are often preset, not determined in real-time, knowing that different dynamic models generate different levels of accuracy and convergence time.

3.3.2.2. Mitigation in Dual-Frequency or Relative Positioning Operation

Other position-domain error mitigation methods are used, especially in dual-frequency operations and/or in relative positioning operations, where differencing amongst observations almost eliminates the common mode errors leaving a residual that is affected mostly by the differenced phase or code error levels. They include KF-type or stochastic based models (Lee & Rizos, 2008). From the time series multipath variation of a static observation that relates to the carrier phase and signal quality, Rost & Wanninger (2009) developed a mitigation model for only static positioning and reported about 25% reduction in the double differenced (DD) observation residual. Lau & Cross (2006) used a modified SNR-based stochastic model. The model attempts to correct the incorrect SNR-based weighting reported to be due to the orthogonality of the SNR and carrier phase multipath error in multipath contaminated observations (Lau & Cross, 2007). This model was reported to attain more than 26% improvement in DD positioning error. Though may enable improved positioning accuracy, such stochastic models are limited by the usually constrained or generalised statistical behaviour of the phase and code observation/observables. Certainly, mis-specifications in the stochastic model would lead to inaccurate positioning results.

The wavelet transform can be pictured as a signal processing tool that has been identified as a useful tool for mitigating the effect of the observation errors on GNSS observations, as it can simultaneously provide time and frequency information of a signal sequence (Satirapod *et al.*, 2003). It is perceived as an alternative to the classical Fourier transform especially in the analysis of non-stationary signals. More details of wavelet can be found in Mallat (2009). In the GNSS-positioning environment, the technique has only been employed to the DD observation in relative positioning operations where the level of decomposition (the set number of the trans-

form decomposition) is assumed. Quite a lot of phase error mitigation are based on wavelet transformation: (Wang *et al.*, 2009; Satirapod *et al.*, 2003; Zhong *et al.*, 2008; Ya'acob *et al.*, 2009). The wavelet transform was also used in mitigating the high frequency components of the phase error so as to enable monitoring of the 'actual' movement of structures, like bridges (Ogaja & Satirapod, 2007; Roberts *et al.*, 2002b; Souza & Monico, 2004). From using the wavelet transformation technique, relative positioning accuracy improvement of up to tens of a percentage and enhanced integer ambiguity resolution, have been reported in some of these references. Recently, wavelet transformation technique was used for the mitigation of code error (Dammalage *et al.*, 2010). The results indicated between 40-60% improvement in positioning accuracy. While this may appear promising, the choice of the appropriate and suitable level of decomposition, like the choice of a Hatch filter length, remains only an intelligent guess in wavelet transformation technique (Alnaqbi, 2010). Of course the level of accuracy obtainable is highly dependent on the wavelet family and the level of decomposition. A wrong guess would result to less accurate results.

In all these, it is worth mentioning that, in relative positioning, the observation error levels in the double differenced observables can be mitigated by simply averaging over along observation interval of many epochs when both the reference and rover stations are static. This technique only tends to be more accurate over short baselines and on relatively long observation period.

3.4. Cycle Slip Detection, Determination and Correction

Ambiguity resolution or fixing requires the outright determination of the integer ambiguity value on a phase observation. This ambiguity value, when fixed remain constant unless a cycle slip occurs at a subsequent epoch. Cycle slips occurrences on phase observations are not rare, and the frequency of cycle slip occurrence increases in challenging environments such as urban areas, where GNSS signals are intermittently blocked from a GNSS receiver. An undetected and uncorrected cycle slip is a

source of error. When a cycle slip is detected, a new integer ambiguity value associated with a post-cycle-slip phase observation at a current cycle slip epoch, would be determined. If a cycle slip $\triangle N_i^s$ occurs on the ψ_i^s phase observation of satellite s, resulting to a new ambiguity value of $N_i^s + \triangle N_i^s$, at a current epoch t, the observed phase observation can be represented as

$$\psi_i^s(t) = r^s(t) + c\delta t^r(t) - c\delta t^s(t) + T^s(t) - I_i^s(t) + b_i^r(t) + b_i^s(t) + \lambda_i\,(N_i^s + \triangle N_i^s) + S_o^s(t) + m_{\psi,i}^s(t) + \epsilon_{\psi,i}^s(t) \tag{3.19}$$

By this representation, $\triangle N_i^s$ is an integer value, and in the absence of cycle slip $\triangle N_i^s = 0$, and Equation (3.19) becomes the same as Equation (3.2). The conventional PPP ambiguity resolution process requires a convergence time of about 30 minutes to fix the ambiguity values with a high level of confidence, before attaining decimetre-level accuracy (Carcanague *et al.*, 2011b). The convergence time, which begins at every cycle slip epoch, is that prolonged mostly because of the combination of the inherent code errors from the code observations included in such a process. Whatever the error level on a code observation, it cannot be mitigated at a cycle-slip-epoch by code smoothing technique. Such non-mitigated code error leads to degraded positioning accuracy and estimated float ambiguity values that could be subsequently fixed to incorrect integer ambiguity values. Most ambiguity resolution techniques employ the Least-squares AMbiguity Decorrelation Adjustment (LAMBDA) method (Baroni *et al.*, 2009; Teunissen, 1995), which is computationally intensive - requiring a large search space and the determination of a decorrelating transformation matrix (Groves, 2013).

Instead of resolving ambiguities after a cycle slip occurrence, appropriate cycle slip detection, determination and correction techniques can be implemented to eliminate the prolonged convergence time associated with a conventional ambiguity resolution technique. The process of cycle slip detection, determination and correction is different from a typical ambiguity resolution process. The error impact of a cycle slip can only be eliminated when the cycle slip value is detected, accurately determined and corrected for. This involves an accurate determination of the integer change relative to the pre-cycle-slip integer ambiguity value, and the subsequent modification or

update of the pre-cycle-slip phase observations with such determined integer change in number of cycles. To this end, different cycle slip detection and determination techniques have been proposed.

The Melbourne-Wubbena LC is a widely used linear combination for both dual-frequency ambiguity resolution and dual-frequency cycle slip determination. The Melbourne-Wubbena combination is a widelane combination with wavelength, $\lambda_{WL} \simeq 0.86m$. It is a linear combination of dual-frequency carrier phase and code observations. Using the same notations defined earlier, the Melbourne-Wubbena observable, WL_{MW} in cycles, obtained with the raw observations from a GPS satellite s operating on bands $i = 1, 2$ in the presence of dual-frequency cycle slips, $\triangle N_1^s$ and $\triangle N_2^s$, is given as

$$\begin{aligned} WL_{MW} &= \left(\frac{\psi_1^s}{\lambda_1} - \frac{\psi_2^s}{\lambda_2}\right) - \left(\frac{f_1 - f_2}{f_1 + f_2}\right)\left[\frac{f_1}{c}P_1^s + \frac{f_2}{c}P_2^s\right] \\ &= (N_1^s + \triangle N_1^s) - (N_2^s + \triangle N_2^s) + \frac{1}{\lambda_1}(b_1^r + b_1^s) - \frac{1}{\lambda_2}(b_2^r + b_2^s) + \\ &\quad \frac{1}{\lambda_1}(m_{\psi,1}^s + \epsilon_{\psi,1}^s) - \frac{1}{\lambda_2}(m_{\psi,2}^s + \epsilon_{\psi,2}^s) - \left(\frac{f_1 - f_2}{f_1 + f_2}\right)\left[\frac{1}{\lambda_1}(d_1^r + d_1^s)\right] \\ &\quad + \left(\frac{f_1 - f_2}{f_1 + f_2}\right)\left[\frac{1}{\lambda_2}(d_2^r + d_2^s) + \frac{1}{\lambda_1}(m_{P,1}^s + \epsilon_{P,1}^s) + \frac{1}{\lambda_2}(m_{P,2}^s + \epsilon_{P,2}^s)\right] \end{aligned} \quad (3.20)$$

where the geometric range, satellite and receiver clock offsets, and the effect of the ionosphere and troposphere have been eliminated (Horemuz & Sjoberg, 2002). The raw WL_{MW} as given in Equation (3.20), contains the widelane ambiguity, $N_{WL} = (N_1^s + \triangle N_1^s) - (N_2^s + \triangle N_2^s)$ corrupted by the combined phase and code observation error levels, and code and phase hardware biases. The difference between a current epoch's $WL_{MW}(t)$ observable and an immediate past epoch's $WL_{MW}(t-1)$ observable eliminates the constant ambiguity terms to yield the widelane cycle slip,$\triangle N_{WL} = WL_{MW}(t) - WL_{MW}(t-1) = (\triangle N_1^s - \triangle N_2^s)$, if there are cycle slips at the current epoch; and in the the absence of cycle slips, $\triangle N_{WL} = 0$. It is known that the hardware delays are fairly constant producing a fairly constant bias on WL_{MW}, but the biggest drawback in using this WL_{MW} observable is the included combined code error that is only reduced to about 0.71times the code error level on P_1^s or P_2^s (assuming that the code errors on P_1^s and P_2^s are equal and

uncorrelated), which is equivalent to about $0.83\lambda_{WL}$. The WL_{MW} is also unable to indicate cycle slips occurrence when $\triangle N_1^s = \triangle N_2^s$. This equality may be rare but could happen if for instance, after a possible satellite's signal interruption, the difference between the post-interruption and pre-interruption integer ambiguities on the L1 phase observation, i.e. $\triangle N_1^s$, and the difference between the post-interruption and pre-interruption integer ambiguities on the L2 phase observation, i.e. $\triangle N_2^s$, results in the same number of cycles $\triangle N_1^s = \triangle N_2^s$.

Geometry-free observables, which are observables obtained by differencing any two phase or phase and code observables, are also frequently used in many cycle slip detection and determination techniques, as the true geometric term is eliminated in such a differencing.

It is worth mentioning for clarity of purpose, that this research work is restricted to cycle slip detection and determination with a single receiver as required for point or precise point positioning. Relative or differential positioning involves a different procedure for ambiguity or cycle slip determination.

Upon detection of a cycle slip, and followed by the determination or fixing of the cycle slip, the fixed/determined cycle slip is subsequently corrected for in the corresponding satellite phase observation thereby completing a cycle slip detection and correction process for a given cycle-slipped satellite. In this thesis, cycle slip determination or cycle slip fix, are interchangeably used to refer to determining a cycle slip signed magnitude.

3.4.1. Existing Single-Frequency Cycle Slip Detection and Determination Techniques

Considering single-frequency receivers, Ouzeau *et al.* (2007) unveiled two single-frequency cycle slip detection techniques: (i) comparison between Doppler-predicted phase and raw phase observations, requiring pre-fixed variation thresholds; and a comparison between smoothed code and raw code observations. Though (i) is a phase-only-derived method, it is likely limited by the inaccuracy in predicting a phase observation with an assumed constant Doppler frequency over an interval, and also by the use of a threshold value that is a function of false alarm probability

with regards to air flight requirements. Secondly, for (ii), the smoothed and raw code comparison option would only detect large enough cycle slips. Without any proposed complementary cycle slip fixing algorithm, the smallest detectable cycle slips value of 68 and 83cycles were achieved with techniques (i) and (ii) respectively, through simulation.

Polynomial fitting to the phase observation is also one way of detecting and determining cycle slip in single-frequency receivers. It identifies a cycle slip as any large discrepancy between a phase observation and a polynomial model fitted to the phase observation or phase-included observable. For instance, Fath-Allah (2010) used an algorithm based on polynomial fitting to a time series of the change in the single-frequency code-minus-phase ($\triangle CMC$) observable to estimate an expected $\triangle CMC$ observable for a current cycle-slip epoch, which had been detected with a large-enough spike on the $\triangle CMC$ at a current epoch. A detected cycle slip is subsequently fixed by differencing the actual observed $\triangle CMC$ from the expected $\triangle CMC$, and dividing by the corresponding wavelength, before rounding the resulting float solution to an integer. Obviously, the high code error levels in the included code observation affect this method's cycle slip detection and determination performance. Also the use of a recommended a 6th-order polynomial would not be optimal for all single-frequency observations.

Jia & Wu (2001) used a 3rd-order polynomial Kalman filter dynamic model for cycle slip detection, and used wavelet technique for estimation of cycle slip. This method is however designed for post-processing rather real-time processing, and the choice of a 3rd-order may not also be optimal for different data sets. With the receiver oscillator bias estimated and removed, Ren *et al.* (2011) proposed a Doppler-aided cycle slip detection and correction method, based on the assumption that the variation in the atmospheric errors and satellites orbits are negligible, and that the Doppler observations are always available from a receiver. Of course these assumptions are not always the case with single-frequency receivers, and no performance results were given to ascertain reliability of this technique.

3.4.2. Existing Multi-Frequency Cycle Slip Detection and Determination Techniques

Many dual-frequency cycle slip detection and determination algorithms are often built around undifferenced or time differenced linear combinations (LC) of the phase observations and the code observations. These linear combinations include wide-lane phase and narrowlane code LCs, among which is the widely used Melbourne-Wubbena LC.

For instance, the Melbourne-Wubbena observable has been widely used for cycle slip detection and correction Liu (2011). As a cycle slip determination algorithm, (Banville & Langley, 2009) used time differenced phase and code observations in a least square adjustment, and the LAMBDA method, for cycle slip determination for PPP, while Kim & Langley (2001) used triple-differenced observables of phase and code observations in a least square adjustment, and the LAMBDA method, for the determination of cycle slips in relative positioning. While some of these techniques are designed for relative positioning, the common inclusion of the code observations and eventually the code errors, tends to limit the level of correct detection and determination of cycle slips achievable by some of these techniques.

Of special interest is the method of cycle slip detection based on time differencing (between-epoch differencing), where a single-epoch slip can be detected by an amplification in a differenced time series observable (Roberts *et al.*, 2002a). The used time series observable can be a time series of raw phase observable, phase-phase combination or a phase-code combination. The scheme of time differencing usually involves the first-order, second-order, third-order and even up to the fourth-order differencing of an appropriate time series observable, with the higher-order differencing giving the strong indication of the discontinuity (amplification) that is required for the cycle slip detection (Hofmann-Wellenhof *et al.*, 2008). The resulting value (at the single-epoch of the discontinuity) can be differenced from a pre-set cycle slip tolerance to infer a cycle slip (Kleusberg *et al.*, 1993). In single-receiver operation, a drawback with the use of the scheme of differencing method is that the performance of the method can be flawed by the drift of a receiver clock, especially when the

receiver is driven by a crystal oscillator. For relative positioning, Bisnath (2000) employed the same differencing method for cycle slip detection, and used the difference between the first-order difference and the median time difference that is obtained from the first- to the fourth-order time differences, for estimating the size of a cycle slip, if any. The use of third-order differencing is analogous to third-order polynomial curve fitting, which is also commonly used for cycle slip detection, and often for cycle slip correction. By fitting such a curve through the time series of the used observable before and after a cycle slip, cycle slips can be detected, and estimated by the size of the cycle slip from the shift between the two curves (Hofmann-Wellenhof *et al.*, 2008). Polynomial fitting residuals and/or least-squares estimation could also be employed to determine the float values of the detected cycle slips, which can then be rounded up to obtain the integer estimates (Bisnath, 2000). Again, for standalone receiver positioning, the presence of the receiver clock drift impedes the reliability and correctness of this method.

Xiaohong & Xingxing (2011) used a modified phase-only-derived geometry-free ionospheric observable for detecting, and the LAMBDA method for fixing cycle slips. However, the technique would not detect certain cycle slip pairs that result in a phase geometry-free combination magnitude value of less than a few tens of millimetres.

Long ago, Blewitt (1990) developed an algorithm where the geometry-free ionosphere observable and the Melbourne-Wubbena LC filtered by a running average filter, and based on set threshold values, were used to detect and determine cycle slips. With the method, a slip is detected when two consecutive epoch values of the observables are beyond set threshold or confidence level. This algorithm, often called the Turbo Edit, is used in GNSS software packages such as GIPSY and BERNESE for cycle slip detection and fixing (de Lacey *et al.*, 2011), but it is only suitable for post-processing and not for real-time applications.

Polynomial fitting or regression have also been used for dual-frequency cycle slip detection and determination. de Lacy *et al.* (2008) introduced the BICYCLE algorithm where they used discontinuity occurrence in a polynomial regression for the detection of cycle slips that are up to 2 or 3 times larger than the standard error

in the used geometry-free observable. The BICYCLE algorithm is also limited to post-processing applications, and would not be able to detect cycle slip pairs that result in small combination values in metres.

Kalman filter based detection and determination techniques do exist, where significant discrepancies between the successive KF estimated ambiguity values may be used to indicate cycle slips (detection), whilst the determination is usually based on the statistical properties of the difference between two successive epochs' KF estimates of an integer ambiguity values (Kamimura *et al.*, 2011). The accuracy of this technique is based on the assumed dynamic model in the KF.

The techniques anchored on the Melbourne-Wubbena LC, and the LAMBDA method, often resolve the widelane (with wavelength of 86.2cm, which is greater than $\lambda_1 = 19.03$cm or $\lambda_2 = 24.4$cm) cycle slip before resolving a narrowlane (less than $\lambda_1 = 19.03$cm) cycle slip or $\triangle N_1$ directly, using the LAMBDA method. Examples of different widelane and narrowlane combinations exist (Collins, 1999). The LAMBDA method is quite computationally intensive as already mentioned, and most dual-frequency cycle slip determination techniques involve either the LAMBDA method or a similarly complex formulation, to fix cycle slip values. This complexity could be a serious drawback when cycle slips are prevalent just as it is in difficult environments. Apart from the technique presented in Xiaohong & Xingxing (2011), all other existing cycle slip detection and fixing techniques discussed, breakdown in the presence of an observation gap, thus re-initializes and become ambiguity resolution processes, instead of remaining as cycle slip detection and determination processes to eliminate the usual long convergence time at a post-observation gap.

Though identified for the future, triple-frequency cycle slip detection and determination algorithms have also been proposed based on certain defined geometry-free LCs that are considered to have minimum phase and ionospheric errors. Xu & Kou (2011) and Dai *et al.* (2009) used such LCs and the LAMBDA method in detecting and fixing cycle slips. With slightly different LCs, and based on least squares algorithm combined with the LAMBDA method, de Lacey *et al.* (2011); Dai *et al.* (2008) also proposed other cycle slip detection and fixing algorithms for triple-frequency receivers, involving geometry-free combinations that include the code observations.

The performance of these triple-frequency based algorithms are also dependent on preset uncertainty levels assumed for the respective phase and code observations. The performance of these triple-frequency algorithm would only be established at the berth of a fully operational civilian triple-frequency GNSS, which is anticipated in the near future.

3.5. Ionospheric Modelling and Correction

The ionospheric error in the code or phase observation has to be mitigated by using a broadcast correction, external correction or a real-time ionospheric model. This mitigation is implemented differently in single- and dual-frequency receivers.

In a single-frequency operation, the broadcast Klobuchar and the NeQuick models can be used for the mitigation of the ionospheric error in the observations from GPS and Galileo satellites respectively. The GIM model is an external correction model obtainable from the IGS and its processing centres, which can be used mostly by single-frequency receivers to eliminate ionospheric error (Andrei *et al.*, 2009; Choy *et al.*, 2008). However the GIM model is affected by a latency of less than 24 hours (rapid version) or about 11 days (final version), and it is limited to an accuracy of $\sim 2-9$ TECU (i.e. $\sim 0.32-1.44$m accuracy on the L1 band observation(s)) (IGS, 2012). This makes the GIM model not quite appropriate for real-time applications, assuming a receiver, in the first place, has real-time access to the external correction, and the limited accuracy can be tolerated. A method commonly referred to as GRAPHIC (Group And Phase Ionospheric Correction), which is halving the sum of the single-frequency code and phase observations, thereby generating an observable 'without' the ionspheric error (Choy, 2011; Chen & Gao, 2005), can be used to mitigate the ionospheric error. Perhaps, due to the high code error, and the introduced integer ambiguity term that makes single-epoch positioning impractical, coupled with its associated long convergence time, GRAPHIC is not widely used for single-frequency operation despite its good ionospheric error mitigation. Other single-frequency methods model the ionospheric error in real-time from the single-frequency code and phase observations. This modeling could include deterministic

and stochastic ionospheric parametisation (Shi *et al.*, 2012), which will require at least five satellites for a position fix; fitting a piecewise linear ionospheric gradient model to the ionospheric observable generated from the difference between the code and phase observations (Sen & Rife, 2008); or a linear model where the vertical ionospheric delay parameters are jointly estimated with other unknown parameters by Kalman filtering (Beran *et al.*, 2005), requiring also at least 5 satellites for positioning.

Dual-frequency receivers have capacity to mitigate the ionospheric error without recourse to external corrections. Ionosphere observables are often generated and used when the increased error level in such LC is acceptable or has been mitigated. Dual-frequency ionospheric models also help in ionospheric predictions; the time series geometry-free ionospheric observable is often used for modeling the relative ionospheric variation or prediction at cycle slips epochs. With such observable, (Momoh, 2012) assumed a linear variation and temporal correlation of the ionospheric error to predict the relative ionospheric delay, to aid error mitigation at a post-gap epoch. On converting the ionospheric observable to TEC rate, Liu (2011) predicted the TEC variation at every epoch, making it also suitable for cycle slip detection. Xiaohong & Xingxing (2011) adopted a linear model of the ionospheric observable to model and predict the relative ionospheric delay using Kalman filtering algorithm, which was also used for cycle slips detection and fixing. As for positioning with a dual-frequency receiver, the ionospheric error is often eliminated by generating and using ionosphere-free observables of the phase and code observations, as done in Carcanague *et al.* (2011a); Momoh (2012).

3.6. Existing Techniques and Limitations

The error mitigation techniques reviewed in this chapter are generally used for static and kinematic domains positioning, to achieve various levels of accuracy and precision. Some limitations can however be identified. Some of these limitations, as already highlighted, include the fixed filter length for in the HFT, the assumed uncertainty values in weighting observations for positioning, and the assumed and

preset dynamic models for a Kalman filtering (KF) positioning algorithm, etc.

The common practice of assuming the raw observations from same and different satellites have statistically independent errors, and the use of preset values of uncertainties for the raw observations, is certainly not realistic (Wang *et al.*, 2002). This is the major limitation of error mitigation techniques based on KF and similar techniques. In reality, receivers movement/trajectory are not fully known in advance and a stochastic model would marginally predict such. KF based techniques are strongly dependent on the consistency between the assumed dynamic model and the receiver's true motion (Lee *et al.*, 2004). Moreover, the PPP solutions obtained by most of the techniques relying on external corrections often fail to consider the correlation introduced to the corrected observables (Shi *et al.*, 2012).

The reviewed techniques have no means of smoothing or mitigating code error whenever cycle slips or observation gaps occur at any given epoch. The code smoothing techniques result to re-initialisation of the smoothing process, thereby unable to mitigate code errors at post-cycle-slip epochs. Many of these existing cycle slip detection, determination and correction techniques are usually multi-satellite based; quite computationally intensive; and are often marred by the inherent code errors on the included code observations. Moreover, they essentially degenerate to become ambiguity resolution techniques whenever an observation gap occurs.

Therefore, there exist the need to define an error mitigation technique resilient to cycle slip occurrence and independent of filter length; and suitable for mitigating code error on a code observation obtained by a single- or dual-frequency receiver operating in static or kinematic mode. Furthermore, efficient cycle slip correction and determination algorithms - essentially independent of the code observations and robust to observation gap occurrences - are required for robust positioning in different environments.

3.7. Summary

The observation error, which is essentially the combination of multipath error and receiver noise, on a phase or code observation from a satellite, remains the largest

source of error on a phase or code observation subsequent to applying corrective error models or improved receiver/antenna design techniques. As such, various error mitigation techniques - especially met to mitigate the larger code error on a code observation - designed to be applied in the range- or position-domains, have been reviewed in this chapter. Existing techniques for detection and determination of cycle slips on a phase observation from a satellite observed by a single- or dual-frequency receiver, have also been reviewed. Various single- and dual-frequency ionospheric delay correction methods have also been reviewed. While these techniques may be as efficient as they are, they are also limited one way or the other; the code error mitigation or smoothing techniques breakdown whenever cycle slip occurs, and most of the cycle slip detection and correction techniques become ambiguity resolution techniques that require longer convergence time in the presence of an observation gap. The motivation for this research is sequel to these limitations, and as such, new algorithms are developed in this thesis to overcome some of these limitations.

Chapter 4.

Relevant Signal Processing Background and Preambles

Having reviewed some existing techniques used for error mitigation and cycle slip detection and correction, this chapter presents a background of relevant signal processing techniques, and the preambles considered necessary to create a better understanding of the premise on which some of the newly developed algorithms presented and used in the subsequent chapters of this thesis are based. As a preparation, both terminologies and notations relevant for the algorithms developed in the following chapters, are also introduced.

4.1. Background on Signal Domains

The well-known Fourier analysis reveals that a time domain signal can be represented by summing together basic sinusoids - sine waves having frequencies equal to the harmonics of a fundamental frequency (the inverse of the period of the signal). This points to the existence of a dual nature for a signal representation- the time domain (TD) and frequency domain (FD) representations. While the TD representation gives the value(s) of the signal over a time series, the FD representation gives the harmonic content of the signal at every frequency. Generally, for a continuous time domain signal (analogue signal), the equivalent representation in the frequency domain can be obtained by a Fourier transform (Shin & Hammond, 2008). The TD

representation can likewise be obtained from the FD representation by an inverse Fourier transform. The dual representations of the signal ensures that either representation can be constructed from the other. Spectrum is a shorter way of referring to the FD representation (Stein, 2000). While a signal TD representation shows the signal amplitude variation with time, the FD representation shows the contribution in amplitude of the frequency components in the signal, and its FD absolute magnitude values versus frequency plot is often called the signal magnitude spectrum. The square of the FD magnitude values gives the power density (periodic signals) or energy density (aperiodic signals), which describes the power/energy per unit bandwidth called the Power Spectral Density (PSD) or Energy Spectral Density (ESD), as the case may be. The PSD or ESD is a measure of the decomposition of the energy of the signal over different frequencies.

Sampling a time-continuous signal, $x(t)$[1], at specific instants converts the signal into a discrete-time sequence suitable for digital signal processors and computers to handle. The inverse of the sampling interval (time between any two samples of the signal) is referred to as the sampling frequency, f_{samp}. The minimum sampling frequency, called the Nyquist frequency, is required to be at least twice the highest frequency component present in the signal. For instance, 30second-interval GPS observations are assumed sampled at 30 second interval, corresponding to an $f_{samp} = \frac{1}{30} = 0.0333$Hz while 1second-interval observations will correspond to an $f_{samp} = 1$Hz. Assuming sampling at a Nyquist frequency (twice the maximum frequency component in the signal, or twice the bandwidth of the signal), the one-sided spectrum of a discrete signal ranges from 0 to $\frac{f_{samp}}{2}$Hz while the two-sided would range within $-\frac{f_{samp}}{2}$ to $\frac{f_{samp}}{2}$Hz. The FD representation of a discrete-time signal is called the Discrete-Time Fourier Transform (DTFT). If the discrete-time signal in the TD is periodic, its spectrum is also discrete and periodic, and describes the Discrete Fourier Transform (DFT), whose computation is sped up by the so-called Fast Fourier Transform (FFT) algorithms (Ambardar, 1999). Essentially, the DFT is actually the DTFT evaluated at a finite number of discrete frequencies, and it is

[1]For purpose of clarity, t is used as a continuous time variable only in this chapter. In other chapters, t is use as a variable to indicate the epoch number of discrete observations.

periodic. While the DFT can be used to approximate the spectrum of a discrete-time TD signal, another transform also exists for discrete-time signals, called z-transform, which is essentially the discrete version of the Laplace transform (Ambardar, 1999) for analogue signals. The Parseval's theorem showed that the energy/power of the signal can be obtained from either the TD or FD representation of a signal.

Noise, especially white noise, is usually observed random in the TD representation but depicts a uniform noise power density in its FD representation. The presence of such noise in a zero-mean signal often results in the noisy signal having increased energy or power level, as the noise energy adds up to the energy of the zero-mean signal. Consequently, for two identical signals affected by different levels of observation noise/error, the more noisy signal is likely to have more total power/energy than the less noisy one, even though they both exist within the same frequency range in their FD representations.

4.1.1. The DFT and Parseval's Theorem

A GNSS raw code and phase observations are usually discrete in time as the recorded measurements are done at certain intervals. An intention to process the observables derived from these observations in the FD would require a transformation to the FD by the DFT.

The DFT of a length-L time domain sequence $x[\tau]$, where $\tau = 1, 2, ..., L$ is the discrete TD index of the x sequence, is defined as

$$X(K) = \sum_{\tau=1}^{L} x[\tau] e^{-j\frac{2\pi\tau K}{L}}, \qquad 1 \leq K \leq L \tag{4.1}$$

The DFT coefficients of the FD X, that is $X(K)$ with the index $K = 1, 2, ..., L$, are in general complex numbers even when x is real. Since X is also a length-L sequence in the FD, it is often referred to as the L-point DFT (Mitra, 2006). The absolute values $|X(K)|$ and $|X(K)|^2$ for all K give the magnitude spectrum and PSD respectively. The DFT can be regarded as the sampled version of the continuous Fourier transform at the equivalent frequencies, which are at $f_K = K\triangle f = K\frac{f_s}{L}$. The inverse DFT (IDFT) given by (4.2) is used to transform X back to the TD

sequence as

$$x[\tau] = \frac{1}{L}\sum_{K=1}^{L} X(K)e^{j\frac{2\pi\tau K}{L}}, \qquad 1 \leq \tau \leq L \tag{4.2}$$

For real-valued x, the negative and positive frequency parts of the double-sided spectrum obtained by DFT are equal in magnitude and symmetrical about the zero frequency (also called DC). Hence an easy one-sided magnitude spectrum equivalent representation can be obtained just by doubling the corresponding magnitude values associated with some positive frequency components from 0 to $\frac{f_{samp}}{2}$Hz. The one-sided (only positive frequency axis) discrete frequency values can be obtained as

$$f(K) = \frac{(K-1)f_{samp}}{L}; \quad 1 \leq K \leq L_{half} \tag{4.3}$$

where $L_{half} = \frac{L+1}{2}$ when L is odd or $L_{half} = \frac{L+2}{2}$ when L is even. The associated magnitude values, describing the one-sided magnitude spectrum over the L_{half} discrete frequencies can be obtained: for odd L, all L_{half} magnitude values except magnitude value at $K = 1$ (DC component), are doubled; and for even L, all L_{half} magnitude values except magnitude values at $K = 1$ (DC component) and $K = L_{half}$, are doubled. The L_{half}-discrete frequencies one-sided PSD can be obtained in the same way: by doubling the magnitudes associated with a two-sided PSD accordingly for odd or even L.

The Parseval's theorem can be used to compute the total energy of a finite length sequence in both the FD and TD. By the theorem, the total energy is computed from the FD by summing the squares of the absolute values of the X sequence, and dividing by L, or from the TD by summing the squares of the absolute values of x; that is,

$$\sum_{\tau=1}^{L} |x[\tau]|^2 = \frac{1}{L}\sum_{K=1}^{L} |X(K)|^2 \tag{4.4}$$

The Parseval's theorem makes it possible to compute, from the FD representation of a signal, the amount of the signal's energy within a certain bandwidth (frequency range) occupied by the signal. For instance, one can compute the amount of energy of the signal within the zero frequency component to a certain discrete frequency. Such computation flexibility is apparently not possible from the TD representation

of a signal. This is essentially why the FD representation obtained by a DFT is considered in this thesis, providing a means for bandwidth energy computation that is used in the adaptive frequency determination presented in Chapter 5.

4.2. Spectrum and Energy of a Noisy Signal

To put the impact of 'noise-like' (rapidly-varying) errors on a slowly-varying (low-frequency) signal into perspective, it will be useful to examine the characteristic of the spectrum of a discrete-time noisy signal. Assume a true real-valued discrete-time noiseless signal sequence, s, contaminated by real-valued additive noise-like error sequence, η, such that it results in the observed real-valued TD noisy signal sequence, $x[\tau] = s[\tau] + \eta[\tau]$ with $\tau = 1, 2, ..., L$. The energy of x, deduced from the TD application of the Parseval's theorem given in (4.4), is

$$\begin{aligned} E_t &= \sum_{\tau=1}^{L} |x[\tau]|^2 = \sum_{\tau=1}^{L} |s[\tau] + \eta[\tau]|^2 \\ &= \sum_{\tau=1}^{L} \left| s^2[\tau] + \eta^2[\tau] + 2s[\tau]\eta[\tau] \right| \\ &= \sum_{\tau=1}^{L} |s[\tau]|^2 + \sum_{\tau=1}^{L} |\eta[\tau]|^2 + 2\sum_{\tau=1}^{L} s[\tau]\eta[\tau] \end{aligned} \tag{4.5}$$

The first and second summations in (4.5) are the energies of the true signal s and the embedded noise η, respectively. The last summation can result in a positive or negative value, but for long enough L with either s or η having a zero mean and both uncorrelated, the expectation (denoted $\boldsymbol{E}$) of the last summation in (4.5) would be zero, and consequently, the energy of x can be approximated as

$$E_t = \boldsymbol{E}(E_t) = \sum_{\tau=1}^{L} |s[\tau]|^2 + \sum_{\tau=1}^{L} |\eta[\tau]|^2 \tag{4.6}$$

Thus, when an observed signal is uncorrelated with the contaminating measurement noise/error, the total energy of the resulting noisy signal is the sum of the energies of the true noiseless signal and that of the contaminating noise, as given by (4.6). The Parseval's theorem expresses the principle of conservation of energy in TD and

FD, hence this total energy can also be computed from the FD representation of the signal.

Additive white noise is known to have uniformly distributed energy density across a signal's spectrum. It covers from zero frequency to the entire spectrum range (bandwidth) defined for a noisy signal. For instance, sampling a noisy analogue signal of maximum frequency component of say 10Hz at $f_{samp} = 100$Hz, the consequent spectrum (the FD representation) obtained by DFT would contain the uniformly distributed noise energy density in the defined bandwidth from 0 to $\frac{f_{samp}}{2} = 50$Hz, even though the maximum frequency component in the signal is 10Hz. Hence, for a low frequency signal embedded in noise (noisy signal), the actual energy of the true signal is concentrated in the lower frequency region of the defined spectrum bandwidth (0 to $\frac{f_{samp}}{2}$Hz) while the energy within the high frequency region of the bandwidth is dominated by the energy of the contaminating noise. As the noise level increases, the signal-to-noise ratio, SNR, decreases and the noise energy over the defined bandwidth increases. This characteristic is further illustrated by a simulation. By sampling the continuous time t dependent analogue signal, $s(t) = 2 + 10sin2\pi 1t + 20sin2\pi 0.5t$, with an $f_{samp} = 20Hz$, the discrete-time sampled signal resulting in a sequence, s, contains $L = 40$ samples ($\tau = 1, 2, ..., 40$) at intervals of $1/20 = 0.05s$, over the analogue signal period of 2s. As possible observations of this signal, two noisy forms of s are generated: x, affected by low zero-mean noise of standard deviation $\sigma = 1.4$ (i.e. $(\mu = 0, \sigma = 1.4)$); and z, affected by six times the level of noise in x (i.e. $(\mu = 0, \sigma = 8.4)$). The TD plots of these three signal sequences are shown in Figure 4.1. The effect of the different noise levels is obvious; the higher level noise causes wider fluctuation/alternation on the true signal than the lower level noise. This effect, by (4.6), prompts that though same frequency components may exist in both noisy signals, the more noisy z will contain more noise energy and would have higher magnitudes in the FD than the less noisy signal, especially at the higher frequency regions of the signals spectra. The one-sided spectra of all three TD signals contain $K = 1, 2, ..., 21$ discrete frequencies equally spaced by the discrete frequency spacing, $\triangle F = \frac{f_{samp}}{L} = 0.5$Hz. The corresponding one-sided magnitude spectrum, and the accumulating bandwidth

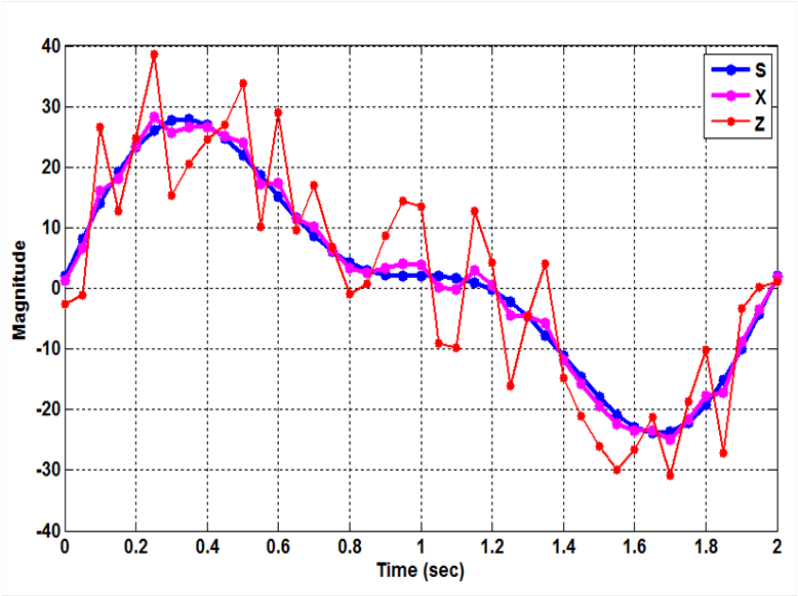

Figure 4.1.: TD plots of the true signal, S; the less noisy signal, X; and the more noisy signal, Z.

energy, E_{BW}, as frequency (or K) increases, are shown in Figure 4.2, for each of the three TD signals. E_{BW} is an accumulating spectrum energy accumulated within a bandwidth starting from 0Hz to a given discrete frequency on the one-sided FD representation of a TD signal, and at the end of the defined spectrum (here at $K = 21$), it accumulates to equal the total energy (accumulated PSD) of the corresponding TD signal. From this figure, the magnitude spectra of all three sequences, s, x and z, represented respectively as S_f, X_f and Z_f, where subscript f indicates FD, reveal peaks roughly at 0 (DC), 0.5 and 1Hz, thus indicating the true presence of those frequency components in the sampled analogue signal. The FD disparities between the true noiseless signal, S_f, and the noisy signals, X_f and Z_f, become wider and obvious as the frequency increases. While the true signal, S_f, shows a typical diminishing magnitude characteristic - tending to zero-magnitude at higher frequencies, the noisy signals, X_f and Z_f, do not exhibit such a characteristic. The magnitude spectra show, as expected, that the effect of the noise is dominant in the higher frequency range of the defined bandwidth while the true signal energy is concentrated in the lower frequency region. The higher the noise level in the signal the more the disparity between a noisy signal and the true noiseless signal in magnitude at higher frequency components. The FD representation of a signal enables the computation of the signal energy within a given bandwidth, i.e. E_{BW}.

Again, from figure 4.2, where the accumulating bandwidth energies have been nor-

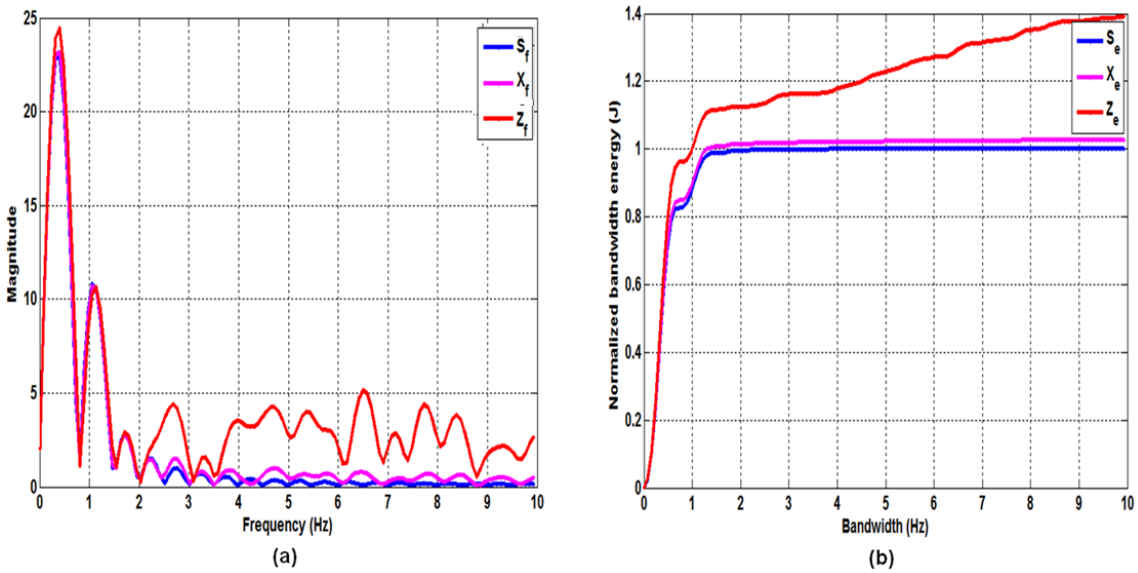

Figure 4.2.: FD plots of the signals S, X and Z, showing the dominant effect of noise at higher frequencies: (a) the one-sided magnitude spectra of the true noiseless signal, S_f; the less noisy signal, X_f; and the most noisy signal, Z_f. (b) The corresponding normalized accumulating bandwidth energies denoted S_e, X_e and Z_e.

malized by the total energy of the true noiseless S_f signal, the disparities among the energies of S_e, X_e and Z_e widen after about 1Hz; S_e shows no noticeable increase beyond 1Hz as the energy is concentrated on the lower region (recall its maximum frequency component is 1Hz); X_e shows a slightly noticeable increase beyond 1Hz; and Z_e shows significant increase and with highest increase rate (ramps) after 1Hz. The increasing energy trend in X_e and Z_e, due to their additional noise levels, is envisaged, as already predicted by (4.6). Since the interest is in the true signal without noise, it is therefore necessary to seek a 'way' to eliminate the higher frequency components from the observed noisy signals, knowing that the true noiseless signal's energy is concentrated on the lower frequency region of the defined spectrum, and the unwanted noise is the dominant source of energy in the higher frequency region. This premise is adopted in filtering the ionospheric observable in Section 5.3.

4.3. Filters and Filtering

In signal processing, filters are devices or processes that remove unwanted component(s) from an observed composite signal. Most often, as is the case in this work, filters are used for the attenuation (reduction of the amplitude) of some frequency components and not others, in a signal. The cut-off frequency, f_c, is essentially a boundary frequency in the FD representation of the signal at which the magnitude spectrum of the signal predominantly initializes attenuation. Two fundamental types of filters are the lowpass filter (LPF) and the highpass filter (HPF). An LPF amplifies or maintains the magnitudes of a signal frequency components that are lower than f_c and attenuates the magnitudes of the frequency components of the signal that are greater than or equal to f_c. The HPF is the opposite of the LPF as it amplifies or maintains the magnitudes of a signal frequency components greater than f_c and attenuates the magnitudes of the frequency components lower than or equal to f_c. An example of a Butterworth LPF with normalized frequency magnitude response is shown in Figure 4.3(a). A filter's frequency magnitude response is an FD representation of the filter's impulse response, indicating the filter's interaction with input signals' frequencies. The LPF frequency response in Figure 4.3(a) has $f_c = 60$Hz, and as such, would attenuate (reduce the gain) magnitudes associated with frequencies greater than 60Hz in an input signal; while the HPF in Figure 4.3(b) with f_c= 30Hz, would attenuate the magnitudes associated with frequencies less than 30Hz in an input signal, and at the same time maintain (unity gain) the magnitude levels associated with frequencies greater than 30Hz in a signal. From these given examples, the LPF can be described as having a bandwidth (passband) of 0 to f_c, and the HPF as having a bandwidth of f_c to 100Hz. The cascade of an HPF and an LPF produces a band pass filter (BPF) that maintains or amplifies the magnitudes of frequency components of a signal within a certain frequency range (bandwidth), and attenuates the others. Filters can be implemented in analogue or digital form, and could be formed from any of the filter classes that include Butterworth, Chebyshev, Elliptic or Bessels.

The Butterworth classes of filters, as typical characteristic, achieves the desired maximally flat magnitude gain (unity gain) for frequency components of a signal

within a passband, as can be observed in Figure 4.3. This is the obvious reason why a Butterworth class filter is often chosen for filtering a noisy low-frequency signal whose frequency components are essentially within the passband defined by 0 to f_c. Between the passband and the stopband of a filter, a transition band exists where the gain in magnitude drops off smoothly. The frequencies f_s and f_p, respectively called the passband edge frequency and stopband edge frequency, are defined for a particular filter. The f_c is usually given as the frequency where the maximum gain reduces by a factor of $1/\sqrt{2}$ (-3dB) in magnitude or by a factor of $1/2$ $(-3dB)$ in the maximum energy density. The steepness of the transition band is determined by the filter order, R; the higher the value of R, the steeper and smaller the transition region becomes (Proakis & Manolakis, 1996), and the higher the time lag in generating a filtered output.

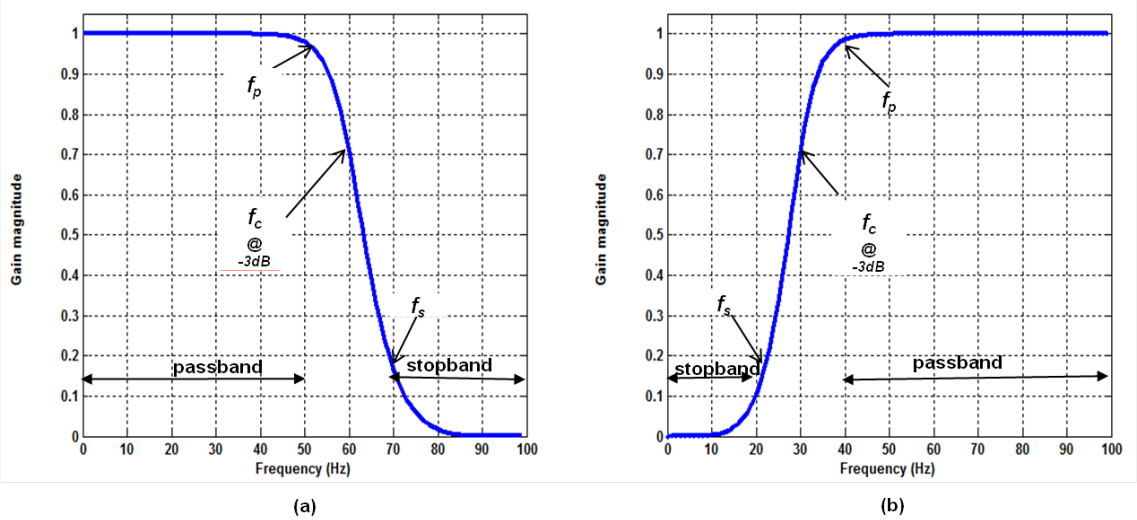

Figure 4.3.: Normalized frequency magnitude response of low- and high-pass 5th-order Butterworth filters (a) LPF with cut-off frequency of 60Hz (b) HPF with cut-off frequency of 30Hz

An analogue filter can be described in TD as a function of continuous time t, by $h(t)$ called the filter impulse response. The Laplace transform[2] (Ambardar, 1999) of $h(t)$ produces the transfer function, $H(s)$, that can be evaluated at the complex frequency variable, $s = j2\pi f$, and thus gives the filter frequency response (plot of

[2]The Laplace transform is an integral transform like the Fourier transform, which also translates TD signals to the complex FD equivalent. It converts integral and differential equations into algebraic equations.

the gain magnitude versus frequency, f) such as the ones shown in Figure 4.3. A TD filtered output signal, $y(t)$, is equivalent to a TD convolution of $h(t)$ and $x(t)$ - the input analogue signal. In the FD, the output is just a multiplication of the Laplace transformed input, $X(s)$, and the transfer function, $H(s)$, that is, $Y(s) = H(s)X(s)$. It is therefore obvious that it is easier to obtain $y(t)$ from the inverse of the FD $Y(s)$, than $y(t)$ directly from TD convolution.

It is worth noting that filters are not applicable only in FD but also in TD. The concept of a lowpass filter exists in many different forms not exclusive to electronic circuits. Lowpass filters play the same role in signal processing that moving averages do in some other fields, such as finance, providing a smoother form of a signal by removing the short-term oscillations and leaving only the long-term trend(s). The carrier-smoothing technique, also called the Hatch filtering, covered in Chapter 2, is a TD LPF as it results in attenuation of the high frequency components in a code observation. Systems for the processing of discrete-time signals are also called digital filters (Ambardar, 1999). Digital filters, implemented in digital processors by adders, multipliers and registers, or as algorithms, are also used for interpolation and decimation, smoothing, and prediction processes in different fields.

In digital signal processing, the digital filters are implemented either in the form of a Finite Impulse Response (FIR) filter that is basically an averaging filter where no previous filtered output contributes to the current filtered output, or as an Infinite Impulse Response (IIR) filter where past filtered output(s) contribute(s) to the current filtered output. Digital filters essentially involve using shift registers, multipliers and adders. The digital filter can be described by the impulse response $h(\tau)$ in the discrete-time domain, and by the transfer function, $H(z)$, obtained by a z-transform[3] of $h(\tau)$, in the complex z-plane. If we assume a discrete-time signal is observed from $\tau = 1$ and a causal system, the z-transform of such a discrete-time

[3]The z-transform can be considered as a discrete equivalent of the Laplace transform. The z-transform permits simple algebraic manipulations and it is an important tool in digital filter designs Mitra (2006).

signal, say of x expressed as $X(z)$, is defined as (Smith, 2007)

$$X(z) = \sum_{n=0}^{\infty} x[n+1]z^{-n} \tag{4.7}$$

where z is a complex variable. From the analogue filter design parameters primarily specified by f_c and R, the equivalent digital IIR filter transfer function can be generated by using an appropriate transformation, such as the bi-linear transformation, to transform the s-domain $H(s)$ to the complex plane z-domain $H(z)$ that is needed for a digital filter implementation (Ambardar, 1999). For a basic digital filter, the filter order R defines the number of past inputs and outputs that can be used to compute the current input. As with a FD $Y(s)$, $Y(z) = H(z)X(z)$ in the z-domain, and the convolution of $h(\tau)$ and x produces y in the discrete-time domain, whilst the inverse transform relationship also hold. MATLAB has optimized functions for generating digital and analogue filters for different types and classes of filters, provided the design parameters are specified in addition to the f_{samp} required for a digital filters.

4.3.1. Filtering with IIR Butterworth LPF

The scope of the filtering done in this thesis is limited to only digital filtering, at least for the easy integration to present-day digital signal processors. The desired lowpass filter is implemented as an IIR rather than an FIR. This is mainly because a large delay (time lag) is usually associated with an FIR filter compared to an IIR filter, even though the FIR is a linear phase filter - exhibits a constant change in phase angle as a function of frequency and can thereby achieve the cancellation of the usual phase shift between input x sequence and a filtered output y sequence. Detailed comparison of FIR and IIR filters can be found in (Lyons, 2011). Although, an IIR filter has a non-linear phase response, it can still be used to achieve a zero-phase shifted y output with respect to the phase of the input x sequence by employing the same IIR filter twice bi-directionally as shown in Figure 4.4 (Lyons, 2011). The time reversal is implemented as a straight left-right flipping of a sequence, A is the first stage filtered output sequence that is phase shifted with respect to the input x,

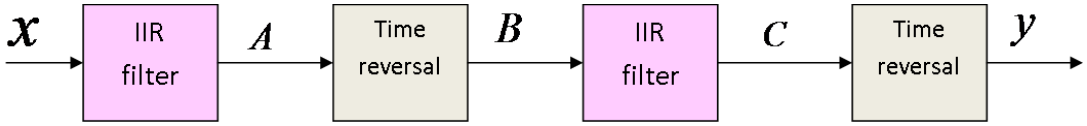

Figure 4.4.: Zero-phase filtering with an IIR filter

B is the time-reversed A, C is the second stage filtered output of sequence B now having the same phase shift but in the opposite direction compared to the phase shift direction of A. This results in a summed phase shift equal to zero in sequence C relative to the phase of the initial x input sequence. The last time reversal is to align the output y sequence in time, with the input x. As it is, the aim of this bi-directional or forward-backward filtering with an IIR is to just cancel the non-linear phase effect, producing the filtered y output without the usual filter-induced phase distortion, knowing that the required filtering is already achieved after the first IIR filtering stage. This bi-directional filtering however requires a set of sampled data at once (block processing) where the required L samples of x are already acquired.

The z-domain $H(z)$ transfer function can be obtained from the continuous $H(s)$ transfer function in the Laplace-domain, by a simple bi-linear transform which requires the substitution for

$$s = 2f_{samp}(\frac{1 - z^{-1}}{1 + z^{-1}}) \tag{4.8}$$

in $H(s)$ to get $H(z)$. For the discrete-time filter input x sequence and filtered output y sequence, with their respective z-transforms as $X(s)$ and $Y(s)$, the $H(z)$ is defined, and can be expressed in the form

$$H(z) = \frac{Y(z)}{H(z)} = \frac{\sum_{k=0}^{R} a_k z^{-k}}{1 - \sum_{k=1}^{R} b_k z^{-k}} \tag{4.9}$$

While different and elaborate digital filter design methods can be find in many digital signal processing books (Lyons, 2011; Proakis & Manolakis, 1996; Ambardar, 1999), a brief and simplified illustration here will put the design and implementation of an IIR filter into perspective. For instance, we may want to design an IIR lowpass filter with filter order $R = 1$ and cut-off frequency of $f_c = 0.1$Hz (0.2πrad/s) set at

where the filter magnitude response is $\frac{1}{\sqrt{2}}$ (-3dB magnitude attenuation frequency), for filtering observation data sampled at $f_{samp} = 1$Hz. From the generally known 1st-order Butterworth lowpass prototype transfer function $H_P(s) = \frac{1}{1+s}$ formulated for a cut-off frequency at 1rad/s (Ambardar, 1999), we get the s-domain transfer function $H(s) = \frac{0.2\pi}{0.2\pi+s}$ that defines the required filter with required cut-off frequency at 0.2πrad/s and not 1rad/s, by substituting $s = \frac{s}{\omega_c} = \frac{s}{2\pi f_c}$ in the prototype $H_P(s)$. We note that the magnitude of $H(s = j2\pi f_c)$ is $\frac{1}{\sqrt{2}}$ as required. By substituting for s in $H(s)$ using the bi-linear transformation equation given by (4.8), and subsequently simplifying to the form such as given in Equation (4.9), the $H(z)$ results as

$$H(z) = \frac{0.2391 + 0.2391z^{-1}}{1 - 0.5219z^{-1}} \tag{4.10}$$

with $a_0 = 0.2391$ and $a_1 = 0.2391$ being the numerator coefficients, and $b_0 = 1$ and $b_1 = -0.5219$ being the denominator coefficients of the required 1st-order IIR Butterworth lowpass filter with $f_c = 0.1$Hz. We can generate the filter frequency response of this LPF, shown in Figure 4.5, after substituting $z = e^{j2\pi F}$ in Equation (4.10), and evaluating the resulting $H(e^{j2\pi F})$ at enough discrete values of frequency, F, within 0 and $\frac{f_{samp}}{2} = 0.5$Hz. We can notice that the transition band of this 1st-order filter is not as steep as the transition of the 5th-order Butterworth LPF shown in plot(a) of 4.3; the higher a filter's order the steeper the transition region but at the expense of increased time lag in generating filtered output. Following from Equations (4.9) and (4.10), the z-transform of the filtered output is

$$\begin{aligned} Y(z) &= H(z)X(z) \\ &= a_0X(z) + a_1X(z)z^{-1} - b_1Y(z)z^{-1} \end{aligned} \tag{4.11}$$

It should be noted that because the filter order $R = 1$, the least power of z is -1; for an $R = 3$ filter, additional coefficients for z^{-2} and z^{-3} will be obtained as part of the $H(z)$ given by Equation (4.10). By taking the inverse z-transform of Equation (4.11), usually by inspection, we obtain the discrete-time filtered output from the IIR filter as

$$y(\tau) = a_0x[\tau] + a_1x[\tau - 1] - b_1y[\tau - 1] \tag{4.12}$$

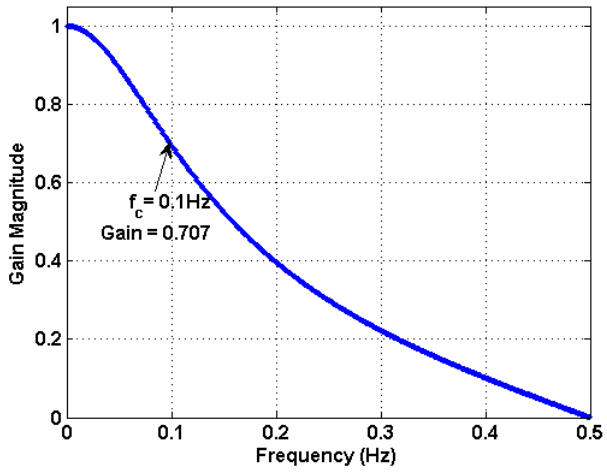

Figure 4.5.: Frequency response of a 1st-order IIR Butterworth LPF with $f_c = 0.1$Hz

with $y[1] = x[1]$. Equation (4.12) gives the simple implementation of the IIR filter, indicating that we need the last and current input samples of sequence x and the immediate past output sample of y. The numerator and denominator coefficients of $H(z)$ multiply the input samples of x and past output sample of y respectively. As an example, for up to a current $100th$ input sample of x, $\tau = 100$. The $x[99]$ and $x[100]$ samples of x multiplied by a_0 and a_1 respectively, and the last $y[99]$ sample of the filtered y sequence multiplied by b_1, are summed to obtain the current $100th$ filtered sample, $y[100]$, of the output y from the IIR filter. For the bi-directional (zero-phase) filtering discussed above, L samples of the input x sequence including a current sampled value are processed to give the same L samples of filtered output y sequence, in both the forward and time-reversed directions.

IIR Butterworth filtering is employed in generating the improved single-frequency ionospheric model presented in Chapter 5.

4.4. Adaptive Time Differencing

Time differencing, as a technique for cycle slip detection, has been used in many cycle slips detection techniques such as reviewed in Section 3.4.2. However, the maximum orders of differencing used in these techniques are pre-fixed orders that can be described as orders determined by intelligent-guess. Here in this thesis, the

adaptive time differencing is designed to adaptively determine the maximum order of differencing, which makes it useful for determining cycle slips in phase observations that are obtained at different rates, and for estimating the energy of the noise level in a time series low-frequency noise-contaminated signal (see Section 5.3.1).

To describe this adaptive time differencing technique, we can recall some facts. It is known that the time differencing of a noise-like sequence with standard deviation σ_o produces a more noisy sequence with standard deviation σ_1, where $\sigma_o < \sigma_1 \leq 2\sigma_o$ (Hamming, 1973). It is also known that the successive time differencing of a noiseless slowly-varying sequence or function such as a polynomial-like sequence, results in a constant-value differenced sequence after a certain number of differencing, d, at which point the underlying noiseless slowly-varying component gets 'eliminated'. For instance, it is known that if we successively difference a noiseless quadratic sequence, we get a constant-value sequence after $d = 2$ order of differencing. To illustrate the central idea of the time differencing concept consider the behaviour of an observable that is essentially quadratic in time defined as $y = ax^2 + bx + c_0$ where x is time in seconds and y is a time series of measurements. If four samples of y are obtained at discrete time $x[\tau]$, where index $\tau = 1, 2, 3, 4$, the resulting sequence will be

$$y = \{a + b + c_0,\ 4a + 2b + c_0,\ 9a + 3b + c_0,\ 16a + 4b + c_0\}$$

For discrete data, the time differenced y is formulated as

$$\triangle y(\tau) = \frac{[y(\tau) - y(\tau - 1)]}{[x(\tau) - x(\tau - 1)]}$$

where, unlike in conventional differencing, the value of the denominator, $[x(\tau) - x(\tau - 1)]$, is always equal to 1 as $\tau - 1$ and τ are consecutive time indices of consecutive samples, and the value of $[x(\tau) - x(\tau - 1)]$ is not dependent nor equal to the data sample interval. Thus, the 1-st order difference is generated as $\triangle^1 y = \{3a + b,\ 5a + b,\ 7a + b\}$, and the 2nd-order difference, which is obtained by differencing the already obtained $\triangle^1 y$ sequence as though it is also a sequence of consecutive samples, yields $\triangle^2 y = \{2a,\ 2a\}$. A 3rd-order differencing to generate $\triangle^3 y$ will treat the already obtained $\triangle^2 y$ sequence as a sequence of consecutive samples, and

so on. We observe that the $d = 2$ order of differencing is a constant-value sequence of $2a$. On the other hand, when such a slowly-varying sequence is contaminated with some noise levels, the same $d = 2$ order of differencing of the noisy sequence will result in a varying noise-like differenced sequence and not a constant-value sequence anymore, because of the rapid changes introduced by the non-slowly-varying noise. Simply put, such successive time differencing could be described as analogous to highpass filtering where the low-frequency (slowly-varying) components of an un-differenced noisy sequence are suppressed and the high-frequency (rapidly-varying) components are not.

This background knowledge of successive differencing and the change in the 1-sigma value (standard deviation) of a differenced sequence suggests that a time series code or phase observation from a GNSS satellite, which normally includes noise-like errors can be successively differenced to 'eliminate' the underlying slowly-varying large geometric range and other slowly-varying parameters in the raw phase or code observation, thereby detecting sharp transitions such as indicated by a cycle slip on phase observation. For illustrative purposes and clarity, the statistics of successively differenced actual phase observations obtained by a static MBAR receiver, at different data rates of 1 and $\frac{1}{30}$Hz on day 170 of 2009, are presented in Tables 4.1 and 4.2 respectively. A trend can be observed in the mean values and 1-sigma values of the sequences presented in both tables; the mean and sigma values continuously decrease until at a certain order of differencing at which the decreasing sigma values change from decreasing-to-increased (DIS) sigma value and thereafter (on further differencing) the different sigma values increase subsequently by a factor less than 2, confirming the $\sigma_{j-1} < \sigma_j \leq 2\sigma_{j-1}$ relationship given in Hamming (1973) where σ_j and σ_{j-1} denote the 1-sigma of the sequence at the j^{th}-order of differencing and the 1-sigma of the sequence at the$(j-1)^{th}$-order differencing respectively. The differencing order at which a DIS value occurs in a successive differencing is referred to as the adaptive-order of differencing in this thesis. As indicated in the tables, $d = 3$ and $d = 4$ are the different adaptive orders of differencing for the 1-second and 30-second interval phase data respectively.

Table 4.1.: Statistics obtained for an undifferenced sequence of 30-epoch consecutive phase observations and for the successively differenced sequences, phase observations at 1Hz from PRN2 observed by MBAR.

Order of differencing *j*	Mean of differenced sequence (m)	1-sigma of difference sequence (m)	Adaptive order of differencing, *d*
0	$2.40\text{x}10^{7}$	$1.92\text{x}10^{3}$	-
1	$-2.17\text{x}10^{2}$	$6.14\text{x}10^{-1}$	-
2	$7.33\text{x}10^{-2}$	$2.83\text{x}10^{-2}$	-
3	$1.33\text{x}10^{-4}$	$5.02\text{x}10^{-2}$	3
4	$4.27\text{x}10^{-3}$	$9.33\text{x}10^{-2}$	-
5	$7.06\text{x}10^{-3}$	$1.75\text{x}10^{-1}$	-
6	$1.29\text{x}10^{-2}$	$3.29\text{x}10^{-1}$	-

decreasing sigma

Decreasing-to-Increased Sigma (DIS)

increasing sigma

Table 4.2.: Statistics obtained for an undifferenced sequence of 30-epoch consecutive phase observations and for the successively differenced sequences, phase observations at $\frac{1}{30sec} = 0.0333$Hz from PRN2 observed by MBAR.

Order of differencing *j*	Mean of differenced sequence (m)	1-sigma of difference sequence (m)	Adaptive order of differencing, *d*
0	$2.40\text{x}10^{7}$	$4.94\text{x}10^{3}$	-
1	$-5.61\text{x}10^{3}$	$5.40\text{x}10^{2}$	-
2	$6.34\text{x}10^{1}$	$1.32\text{x}10^{0}$	-
3	$-1.44\text{x}10^{-1}$	$5.49\text{x}10^{-1}$	-
4	$-1.84\text{x}10^{-2}$	$1.04\text{x}10^{0}$	4
5	$1.80\text{x}10^{-2}$	$2.00\text{x}10^{0}$	-
6	$4.69\text{x}10^{-2}$	$3.91\text{x}10^{0}$	-

decreasing sigma

Decreasing-to-Increased Sigma (DIS)

increasing sigma

We can observe that at an adaptive-order of differencing, the mean of the differenced sequence is within a few millimetres compared to the thousands of metres range in the mean value of an undifferenced phase sequence; and the 1-sigma value (millimetre range for 1Hz data or a metre range for the 0.033Hz data) is so small compared to the hundreds of metres range of the 1-sigma value of an undifferenced phase sequence. These results further indicate that the slowly-varying underlying parameters

in consecutive phase observations (sequence) are highly suppressed (mitigated) at an adaptive-order differencing. We can also notice that further differencing beyond d produces increasing 1-sigma values, and changing mean values that are fairly close to the mean value at d^{th}-order differencing, thus indicating noise-dominated sequences as a result of excess number of differencing.

The new Adaptive Time Differencing (ATD) technique is predicated on the hypothesis that an adaptive-order differencing of a sequence enables the 'elimination' of the underlying slowly-varying parameters and reveals sharp/rapid transitions in the undifferenced sequence. An undifferenced sequence or time series observation for an ATD process should be made up of consecutively obtained samples of the observable, and such an undifferenced sequence must contain a minimum number of samples, which for this research is set to ten samples. The output of an ATD process is an Adaptively Differenced Sequence (ADS). An ADS is hereby defined as the differenced sequence obtained at the d^{th} adaptive-order differencing of an undifferenced time series observable or sequence. This d^{th}-order of differencing can be considered as an appropriate order of differencing required to 'eliminate' the slowly-varying parameters in an undifferenced sequence or a time series of an observable. The adaptive time differencing ensures that the accepted adaptive-order is 'optimum' in some sense; it is not lower than d to ensure that the underlying slowly-varying parameters in the undifferenced sequence are well-mitigated; and it is not allowed greater than d to ensure that increasing error-sequences originating from over-differencing are not generated and used for further processing or estimation or estimation that may be required. The d adaptive-order is affected by the levels of noise/error in an undifferenced sequence. Further successive differencing beyond the d^{th}-order will successively produce differenced sequences with increasing 1-sigma as can be observed in tables Tables 4.1 and 4.2. Apart from the presented results in these tables, results from other tests done by contaminating slowly-varying sequences with different levels of randomly generated noise have also been used to validate the hypothesis on which the ATD technique is predicated.

By way of graphical illustration with actual GNSS code and phase observations, the resulting phase and code ADSs obtained by successively differencing the undif-

ferenced (raw) time series phase ψ_1^s and code P_1^s observations from a satellite s, are shown in Figure 4.6, where a 30-epoch time series of ψ_1^s without cycle slip, and a 30-epoch time series of P_1^s have been used. The DIS values occurred for both the code and phase sequences at the 3rd-other of differencing, as can be observed in the inserted sigma values for code and phase sequences in the figure. As such, the phase and code ADSs are the adaptively differenced phase and code sequences obtained at the $d_s = 3$, which are shown at the bottom of Figure 4.6. As expected, the higher code error levels in the code observations compared to the phase observation, is indicated in the higher 1-sigma (0.19m) of the code ADS compared to the 1-sigma (0.05m) of the phase ADS. It should also be observed that an ADS is lesser in length by d_s when compared to the length of the undifferenced sequence, as each successive differencing results in a differenced sequence reduced in length by 1.

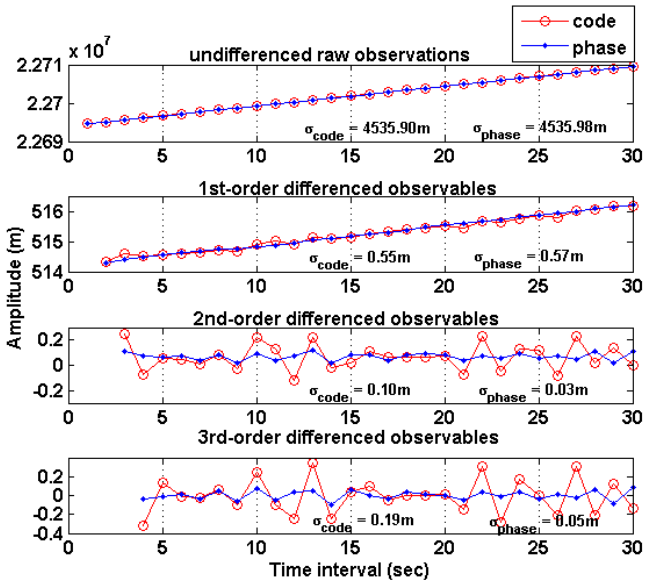

Figure 4.6.: Undifferenced code and phase 1second- interval observations and the successive differenced sequences, from PRN 20 observed by MBAR receiver.

Figure 4.7 shows similar plots to the plots in Figure 4.6, but for an observation interval of 30 seconds. The occurrence of the DIS values for both code and phase sequences, indicating the phase and code ADSs, is seen attained at the adaptive-order $d_s = 4$. Again, the higher code error levels in the code observations compared to the phase observation, is also indicated in the higher 1-sigma (3.32m) of the code ADS compared to the 1-sigma (1.05m) of phase ADS.

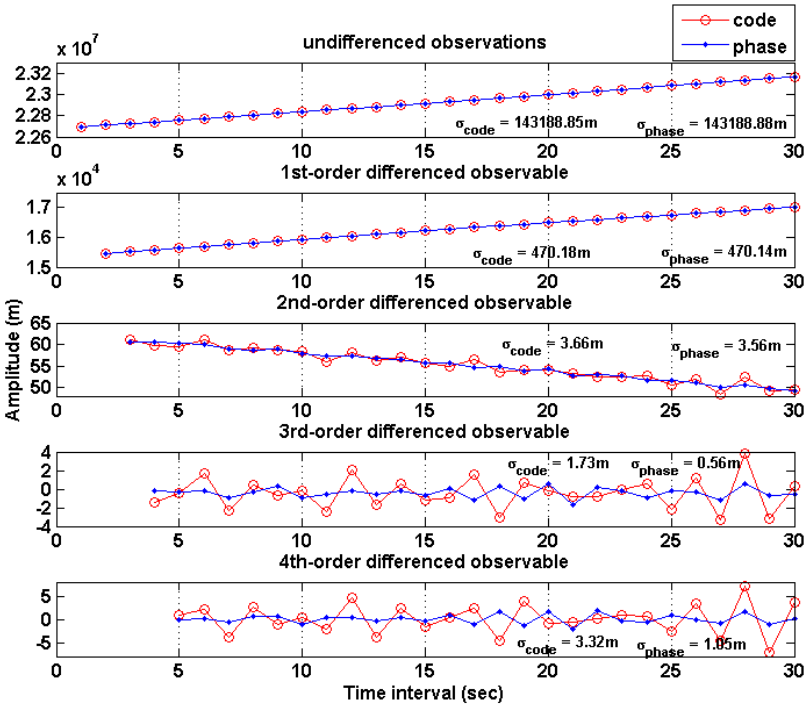

Figure 4.7.: Undifferenced code and phase 30-second interval observations and the successive differenced sequences, from PRN 20 observed by MBAR receiver.

To generate the phase or code ADS from the phase or code observations from a given satellite s, it was observed through extensive test results that $d_s \geq 2$ and it is usually higher for lower data rate, as can be noticed in the statistics presented in Tables 4.1 and 4.2; and from the $d_s = 3$ and $d_s = 4$ adaptive-orders obtained for the two different observation data at 1-second and 30-second intervals respectively. Actually, a d_s adaptive-order, though always made same for a given satellite phase and code ADSs, is preferably determined with the time series phase observation and not with the time series code observation from s. This is primarily because the interest is on the phase observation which could have cycle slips that can be detected as sharp transitions via an ATD process. Moreover, the level of code errors in a time series code observation may produce, via an ATD process, a code-based adaptive-order that may be different from that obtainable with the phase observation, and that will not be beneficial to the intended purpose of cycle slip detection if that code-based adaptive order is used to generate a phase ADS. There is no need to use different order of differencing for code and phase observations from the same satellite

s, as the underlying common parameters would not be completely eliminated after a linear combination of the resulting phase and code ADSs; for instance, and an attempt to estimate a common parameter from the two ADSs would be flawed.

Although an uncommon condition, a constrain is included in determining d_s and consequently, the code and phase ADSs, prior to the occurrence of a DIS value. The constrain is applied only if prior to the occurrence of a DIS value, the condition

$$0 < \sigma_{j-1} - \sigma_j \leq 0.01 \tag{4.13}$$

is satisfied, where σ_j is the 1-sigma value of the differenced sequence at the j^{th}-order of differencing before a DIS value occurs, and σ_{j-1} is the 1-sigma value of the differenced sequence at the $(j-1)^{th}$-order of differencing. When (4.13) is satisfied prior to the occurrence of a DIS value, then constrain $d_s = j$ is applied. This constrain is to help stop any further unnecessary differencing, bearing in mind that the sought-after sharp/rapid variation in an adaptively differenced sequence should be well above a centimetre. It should be noted that prior to the occurrence of a DIS value, $\sigma_{j-1} > \sigma_j$. The 0.01m value is used here for 1Hz data since the difference between 1-sigma values of ADSs after an adaptive-order of differencing is usually less than 1cm (as found from test results) and as can been observed from Table 4.1 above. This constrain may not be employed for 30-second interval observations as the mean of the differenced sequences after an adaptive-order of differencing would usually be in the range of a metre.

As may be inferred from the foregoing discussion in this section, the ADSs and their corresponding 1-sigma values are to be used for the new cycle slip detection and estimation algorithm developed in this thesis.

4.5. Cycle Slip Simulation

The Equations given in (2.10) and (3.19) are the used functional model for a satellite phase observation with and without cycle slips, respectively. A cycle slip, which manifests as an unknown integer number of cycles added to the functional model of the accumulated carrier phase observation in cycles, from a given satellite, can

be easily simulated to perform a cycle slip test for that satellite. As done in this work, to simulate a cycle slip occurrence of x cycles on the phase observation from a satellite at a current observation epoch, where x is either a positive or negative integer, x is first added to a previously accumulated cycle slips sum including the first simulated cycle slip to the last simulated cycle slip for that satellite. The currently accumulated integer sum that includes x at the current epoch, becomes the integer value added to the current epoch's phase observation in cycles, from that satellite, thereby simulating x cycle slips on the current epoch's phase observation from that satellite. The cycle slip value at the first observation epoch for any satellite is always set to zero, and the x cycle slip value at a current epoch could be a randomly generated or selected integer value but known as the true cycle slip value. The cycle slipped phase observation in metres, for the cycle-slipped satellite, can then be obtained as the product of the resulting current epoch's cycle slipped phase observation in cycles, and the corresponding wavelength of the transmission band. The simulation of x cycle slips can be done on any phase observation obtained from any band(s), as may be desired.

This way of simulating cycle slips presumes that the integer ambiguity value at the first observation epoch of a continuously observed satellite remains constant and does not change; any cycle slip occurrence or simulated at subsequent observation epochs after the first observation epoch of the satellite are only reflected in the accumulated cycle slip sum.

In this thesis, for a given simulation epoch interval, τ_{slip}, a cycle-slip-only test or combined cycle slip and code error tests by simulation, are done for selected satellites in either of two ways: (i) the simulated cycle slips and code errors (in the case of combined cycle slip and code error tests) are applied to the respective phase and code observations from the satellites selected for test at same observation epochs (test epochs) separated by τ_{slip}; or (ii) the simulated cycle slips and code errors (where applicable) are applied to the respective phase and code observations from the satellites selected for test at different observation epochs (test epochs), for the different selected satellites. In option (ii), the first test epoch, t_{slip}^{PRN}, at which the GPS satellite indicated by its PRN, is tested for only cycle slips (cycle-slip-only

test) or combined cycle slip and code error, is chosen as $t_{slip}^{PRN} = \tau_{slip} + PRN$, and the subsequent test epochs are the epochs where:

$$mod(t,\, t_{slip}^{PRN}) = 0 \tag{4.14}$$

According to (4.14), these are the epochs where a current epoch t is a multiple of t_{slip}^{PRN}, as *mod* represents the modulo operation of t modulo t_{slip}^{PRN}. In this way, it will be rare to find any two satellites tested for cycle slips at a same observation epoch (test epoch). In option (i) or (ii), for combined cycle slip and code error test where code errors as well as cycle slips are simulated for a given satellite at a given test epoch, the simulated code error(s) and cycle slip(s) are respectively applied to code and phase observations (from the satellite) at that same test epoch.

4.6. Summary

The representation of a noisy and noiseless signal in both time and frequency domains, and the procedures for determining the energies of such signals - obtainable from either domain - has been presented, based on the fundamental theories underlying such procedures. Filtering of a low-frequency signal affected by noise/errors, with specific interest on digital Butterworth IIR lowpass filtering; and how such a filtering process can be implemented for real-time filtering, have been presented. The FD representation of a noisy signal can be exploited to estimate the energy of the less-noisy part of its spectrum, which can subsequently be used to determine the cut-off frequency of an IIR filter that can be used to 'filter-off' the noise from the noisy signal. The introduced adaptive time differencing (ATD) technique can be applied to generate adaptively differenced sequences (ADSs) that are suitable for the detection of cycle slips on the phase observation(s) from a satellite. This chapter also presented some terminologies and notations to be used henceforth, and ends with the description of the cycle slip simulation procedure used in this thesis.

Chapter 5.

New Single-Frequency Cycle Slip and Ionospheric Correction Algorithms

This chapter presents a new phase-only Cycle Slip Detection and Correction (CSDC) algorithm, as well as an Improved Ionospheric Correction (IIC) algorithm, for a single-frequency GNSS receiver, to address some of the objectives of this research. The CSDC algorithm is done with adaptively differenced sequences (ADSs) generated from an adaptive time differencing (ATD) process, while the IIC algorithm involves filtering an ionospheric observable using modified first-order IIR Butterworth filter, both introduced in Chapter 4. This chapter, in addition, unveils a receiver clock jump detection and estimation algorithm, which is required for an effective phase-only cycle-slip detection algorithm; and also, a cycle-slip-resilient code error mitigation algorithm.

5.1. Time Series Phase and Code Sequences for ATD

For a GNSS, the $i = 1$ (L1 band) is used here as the representative observation band for the considered single-frequency receiver in this chapter. The ATD process is applied to observations from any satellite which must have been observed for at

least ten consecutive epochs. From the tenth observation epoch of satellite s, the ATD technique can process the short time series or sequence of raw phase or code observation from s, that includes l^s consecutive epoch observation, where ($10 \leq l^s \leq W_L$). W_L is a set sliding window length for all observed satellites, suitably within 10 to 60 epochs (i.e. 10 to 60seconds observation for 1Hz data), which ensures a long enough sequence of data that can be successively differenced to indicate a DIS value, and consequently, an ADS from an ATD process. Though different values of W_L from within 10-60 epochs range were tested and similar ADS results were obtained, as a common fixed value for this research, the sliding window length is set to 30epochs (equivalent to 30seconds for 1-second interval data). That is, $W_L = 30$ and it is so fixed for the 1Hz observation data used for the research work presented in this thesis. Too large values of W_L create unnecessary extra computations without any additional improvement or gain from an ATD process. When L^s, the total number of observation epochs since the first observation epoch from s, exceeds W_L, the last W_L observables from s then form the current time series observation (the undifferenced sequence) processed to generate an ADS, and subsequently $l^s = W_L$.

The time series or sequence of phase observable used for the ATD process for cycle slip detection is required to be free from cycle slip up to the last $(L^s-1)^{th}$ observable but not the current $(L^s)^{th}$ observation, $\psi_1^s(L^s)$, from s that may be affected by cycle slip. Hence, the l^s-length time series phase observable for an ATD process contains the previous (l^s-1)-length cycle-slip-free phase observables, $\overline{\psi_1^s}(L^s-l^s+1 : L^s-1)$[1], and the current raw phase observation of s, being $\psi_1^s(L^s)$. That is, the l^s-length undifferenced time series phase observable, $\psi_{TS,1}^s$, and the l^s-length undifferenced time series code observation, $P_{TS,1}^s$, for the $i = 1$ single-frequency ATD are always generated as:

$$\psi_{TS,1}^s = \left[\overline{\psi_1^s}(L^s - l^s + 1 : L^s - 1),\ \psi_1^s(L^s)\right] \tag{5.1}$$

$$P_{TS,1}^s = [P_1^s(L^s - l^s + 1 : L^s)] \tag{5.2}$$

[1] In this thesis, the notation $x(a : b)$ is used to specify a new sequence/vector containing the values in the a^{th} to the b^{th} index of an existing sequence x, where the number of samples in x is more than or equal to the number of samples, $b - a + 1$, in $x(a : b)$. $x(a)$ is a single value denoting the a^{th} index value of sequence x.

where $\overline{\psi_1^s}$ is the cycle-slip-free phase observable in metres. The the last $(l^s - 1)$ values from a time series of $\overline{\psi_1^s}$ must have been corrected for cycle slips prior to the current observation epoch of s, if cycle slips existed. In the absence of cycle slips, $\overline{\psi_1^s}(1 : L^s - 1) = \psi_1^s(1 : L^s - 1)$, meaning that all the previous $(L^s - 1)$ raw phase observations from s are used as the $(L^s - 1)$ cycle-slip-free phase observables in (5.1) As an example, for satellite s continuously observed without cycle slip up to a current 20^{th} epoch, $l^s = L^s < W_L$, and as such, the $\psi_{TS,1}^s = \psi_1^s(1 : 20)$ sequence contains the first 1 to 20 epochs phase observations from s: the $\left[\overline{\psi_1^s}(L^s - l^s + 1 : L^s - 1)\right] = \left[\overline{\psi_1^s}(1 - 1 + 1 : 20 - 1)\right] = \left[\overline{\psi_1^s}(1 : 19)\right]$ part of the $\psi_{TS,1}^s$ sequence contains the past 19 cycle-slip-free phase observables and the current epoch's raw phase observation, $\psi_1^s(20)$, that may have a cycle slip. For the same s continuously observed without cycle slip up to a current 40^{th} epoch, $L^s > W_L$ and as such $\psi_{TS,1}^s = \psi_1^s(11 : 40)$ is a 30-length sequence containing the 11^{th} to the 40^{th} epochs' phase observations from s, recalling that the set maximum length of data for the ATD process is $W_L = 30$.

For this single-frequency observation processing, when an observation gap (temporary loss of a satellite) occurs for s, the time series lengths, l^s and L^s, are reset to 1, i.e. $l^s = L^s = 1$, which is equivalent to treating s as a new entrant satellite without any previous observation records whenever the observing receiver re-locks to s.

Following from Equation (3.19) with $i = 1$ and $\triangle N_1^s$ denoting the cycle slip value between a current epoch and the immediate past epoch phase observation from s, the phase ADS denoted as $\Delta^{d_s}\overline{\psi_1^s}$ can be obtained by applying the ATD technique (described in Section 4.4) on a corresponding undifferenced $\psi_{TS,1}^s$ phase sequence. The resulting $\Delta^{d_s}\psi_1^s$ sequence can be represented as:

$$\begin{aligned}
\Delta^{d_s}\overline{\psi_1^s} &= \Delta^{d_s}\psi_{TS,1}^s = \triangle^{d_s} r^s + c\triangle^{d_s}\delta t^r + \lambda_1 \triangle^{d_s} N_1^s - \triangle^{d_s} I_1^s + \triangle^{d_s} m_{\psi,1}^s \\
&\quad + \triangle^{d_s}\epsilon_{\psi,1}^s + \triangle^{d_s}(-c\delta t^s + T^s + b_1^r + b_1^s + S_o^s) \\
\Delta^{d_s}\overline{\psi_1^s} &\simeq c\triangle^{d_s}\delta t^r + \lambda_1 \triangle N_1^s + \triangle^{d_s} e_{\psi,1}^s
\end{aligned} \tag{5.3}$$

where $\triangle^{d_s}(\centerdot)$ is used to denote the adaptive-order (d_s) differencing of the $(\centerdot)$ sequence. It is intentional representing $\triangle^{d_s} N_1^s$ with $\triangle N_1^s$ in (5.3) as an ADS would

reveal a $\triangle N_1^s$ cycle slip by the amplitude of $\triangle^{d_s} N_1^s$. At the d_s^{th} adaptive-order of differencing, the values of $\triangle^{d_s} r^s$, $\triangle^{d_s} I_1^s$, and $\triangle^{d_s}(-c\delta t^s + T^s + b_1^r + b_1^s + S_o^s)$ are negligibly small compared to the wavelength value $\lambda_1 = 19.02$cm, recall that the mean of an ADS is usually within a few millimetre range and with a 1-sigma value under a few centimetres (see the mean and sigma values of ADSs given in Table 4.1 and Figure 4.6) - and knowing that $\lambda_1 \triangle N_1^s \geq 19.02$cm when a cycle slip occurs. Even then, these assumptions for an ADS could also be considered valid for the following reasons: the adaptive-order differencing of the slowly-varying parameters, T^s, b_1^r, b_1^s, and S_o^s, in a $W_L = 30$-length 1Hz phase or code observation would result in only few millimetres amplitude variation values as they are not known to vary rapidly over short intervals; $\triangle^d \delta t^s \approx 0$ since a satellite clock is a highly stable atomic clock usually modelled as a quadratic variation, and usually $d_s \geq 2$; the value of $\triangle^{d_s} I_1^s$ is negligible for $d_s \geq 2$, under mild ionospheric conditions; and $\triangle^{d_s} r^s$ is negligibly small going by the statistics of an ADS; for instance the 1Hz data have values under a few centimetres with millimetre-level mean and centimetre level 1-sigma values. As such, each value of the $\Delta^{d_s}\overline{\psi_1^s}$ sequence can be accepted as the sum of the common receiver clock high-order (since $d_s \geq 2$) variation that indicates a receiver clock jump/reset or a large drift; the integer cycle slip equivalent in metres, at the current epoch; and of the combined adaptively-differenced phase error terms denoted as $\triangle^{d_s} e_{\psi,1}^s$ in (5.3). In the same way, by applying ATD on $P_{TS,1}^s$, we get the code ADS denoted as $\Delta^{d_s} P_1^s$ and given as

$$\begin{aligned} \Delta^{d_s} P_1^s &= \Delta^{d_s} P_{TS,1}^s \\ &\simeq c\triangle^{d_s}\delta t^r + \triangle^{d_s} e_{P,1}^s \end{aligned} \tag{5.4}$$

where $\triangle^{d_s} e_{P,1}^s$ denotes a time series of the combined adaptively-differenced code error terms. Equations (5.3) and (5.4) presume the typical scenario where the receiver clock jump/reset/drift affects the code and phase observations from all observed satellites at a given epoch in the same way and simultaneously too. For a stable receiver clock without jumps/resets, $c\triangle^{d_s}\delta t^r \approx 0$ in (5.3) and (5.4). When there is no cycle slip at a current t epoch phase observation from s, the corresponding value

in the phase ADS, i.e. $\Delta^{d_s}\overline{\psi_1^s}(l^s)$, will contain only the common receiver high-order clock variation $c\triangle^{d_s}\delta t^r(l^s)$ and the combined differenced error $\triangle^{d_s}e^s_{\psi,1}(l^s)$, as can be observed in (5.3).

5.2. Single-Frequency Phase-Only Cycle Slip Detection

The single-frequency CSDC algorithm is a single-satellite phase-only based algorithm; it is implemented for each individual satellite using only the phase ADS obtained for the satellite through an ATD process. The ADSs for all n observed satellites with $10 \leq l^s \leq W_L$ $(s = 1, 2, .., n)$ at the current epoch are first generated. The CSDC algorithm uses the last value of the phase ADS generated for satellite s at a current epoch t, i.e. $\Delta^{d_s}\overline{\psi_1^s}(l^s - d_s)$, to determine if a cycle slip exist on the phase observation from s at the current epoch or not. It should be recalled that the ADS, which is the $\Delta^{d_s}\overline{\psi_1^s}$ sequence, is shorter in length by d_s compared to the undifferenced $\psi^s_{TS,1}$. The CSDC process block diagram is depicted in Figure 5.1.

A cycle slip is indicated or detected on ψ_1^s when

$$\left|\Delta^{d_s}\overline{\psi_1^s}(l^s - d_s)\right| \geq \lambda_1 \tag{5.5}$$

while a cycle slip is considered not to exist at the current epoch if otherwise - that is, when $\left|\Delta^{d_s}\overline{\psi_1^s}(l^s - d_s)\right| < \lambda_1$. The limitation in this criterion is that very small cycle slip values of 1 or 2 cycles may not always be detected with Equation (5.5) since $c\triangle^{d_s}\delta t^r + \triangle^{d_s}e^s_{\psi,1}$ could add up destructively with a cycle slip of less than or equal to two cycles to result in $\left|\Delta^{d_s}\overline{\psi_1^s}(l^s - d_s)\right| < \lambda_1$. However in single-frequency code positioning, assuming a cycle slip of 2 cycles (about 38cm) gets undetected and translates to error, it is still smaller than the typical single-frequency code error magnitude.

Although d_s may not be the same adaptive-order for all observed n satellites at a current epoch, for simplicity and convenience, the common receiver clock high-order variation, henceforth denoted as ε_c as indicated in Figure 5.1, can be used to replace

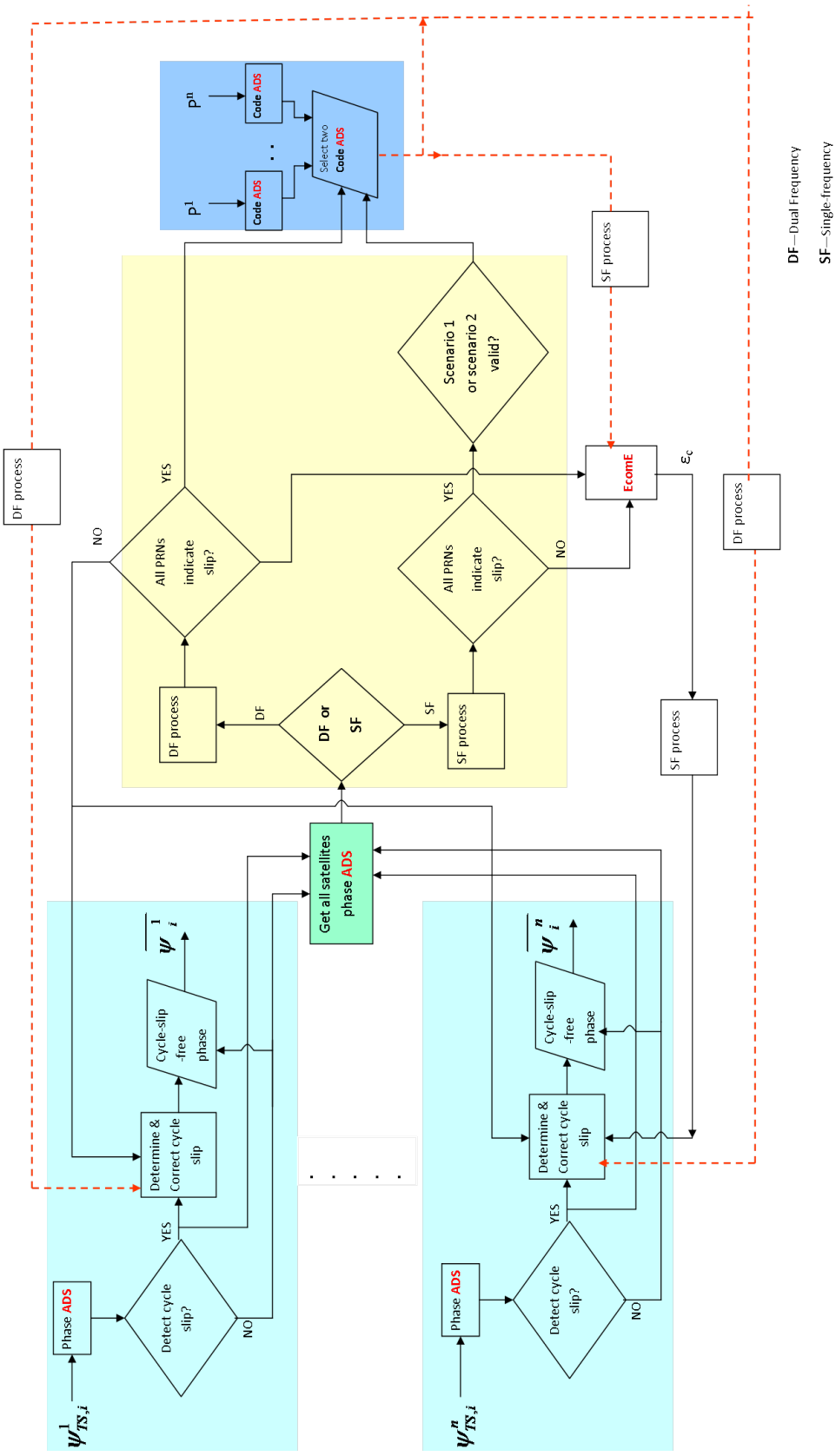

Figure 5.1.: The process diagram of the Cycle Slip Detection and Correction (CSDC) algorithm

the $c\triangle^{d_s}\delta t^r$ terms in Equations (5.3) and (5.4) with negligible error contribution: meaning then that $\Delta^{d_s}\overline{\psi_1^s}(l^s - d_s) = \varepsilon_c(t) + \lambda_1 \triangle N_1^s + \triangle^{d_s} e^s_{\psi,1}(l^s - d_s)$, and $\Delta^{d_s} P_1^s(l^s) = \varepsilon_c(t) + e^s_{p,1}(l^s - d_s)$. The estimated value of $\varepsilon_c(t)$ can be used as the indicator for a receiver clock jump/reset or drift. The plots in Figure 5.2 are the obtained phase

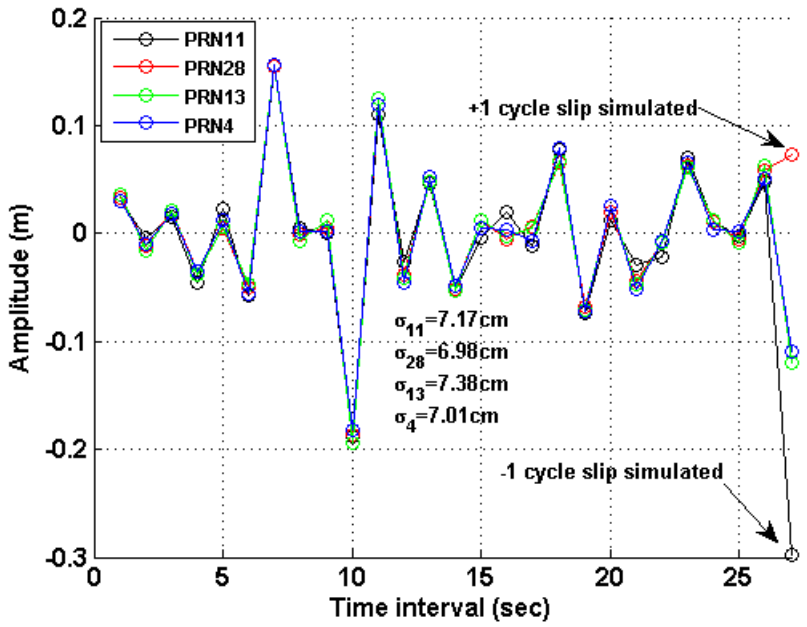

Figure 5.2.: Plots of different single-frequency phase adaptively differenced sequences (ADSs) from different satellites, with a common simulated cycle slip of 1cycle at current epoch

ADSs for 4 different satellites (PRN 11, 28, 13 and 4) observed by a static station (MBAR) on day 170 of 2009, presented for insight and clarity to the CSDC algorithm and the common receiver clock high-order variation ε_c. The 1-sigma value of the different ADSs are also inscribed in the figure. The undifferenced W_L-length time series phase observation for each of the satellites contained the 871^{th} to the 899^{th} epochs phase observations without cycle slips occurrence, and the current 900^{th} epoch observation. At the current 900^{th} epoch cycle slip was simulated for only PRN 28 and PRN 11. The same adaptive-order $d = 3$ resulted for all the four satellites, and the resulting 27-length time series ADSs plotted in Figure 5.2 indicate a high correlation among the ADSs, especially over the no-cycle-slip epochs and no-cycle-slip satellites, even though the satellites were observed at widely different elevation angles. This time series correlation is assumed due mainly to the common receiver

clock variation that has been adaptively differenced up to the adaptive-order $d = 3$. The ε_c value, which can be estimated for each and every epoch, is thus the estimated value of this correlation among all the observed satellites at a given epoch. The responsiveness of Equation (5.5) to cycle slip can be observed at the current 900^{th} epoch - the 27^{th} value of the ADS; only the satellites with simulated cycle slip values of $+1$ (PRN 28) and -1 (PRN 11) indicating ADSs values of 0.074m and -0.297m respectively, vary widely from the amplitudes of the no-cycle-slipped satellites (PRN 4 and PRN 13) with respective ADSs values of 0.110m and 0.121m. These values include the common receiver clock high-order variation, that is the ε_c value at the 900^{th} epoch, which has to be estimated and removed prior to estimating the cycle slip float values and fixing them. The cycle slip detection based on Equation (5.5) will only be able to detect the cycle slip on PRN 11 and not the cycle slip on PRN 28, simply because the current ε_c and the combined differenced error $\triangle^{d_{11}} e^{11}_{\psi,1}$ summed up constructively for PRN 11 resulting in an absolute value of $0.297m > \lambda_1$ whilst the current ε_c and the combined differenced error $\triangle^{d_{28}} e^{28}_{\psi,1}$ summed destructively for PRN 28 resulting in an absolute value $0.074m < \lambda_1$. Of course, for larger cycle slip values, Equation (5.5) becomes more effective in detecting cycle slips. The procedures used for estimating the current $\varepsilon_c(t)$ value and cycle slips float values when cycle slips are detected, are presented next.

5.2.1. Receiver Clock Jump Detection

A receiver clock jump/reset could hinder accurate phase-only cycle slip detection if it is not detected, estimated and considered in the CSDC algorithm. As such, a simple test is performed to instantaneously detect receiver clock jumps at any current epoch provided a minimum of ten epochs' observations have been recorded by the receiver from some satellites. The receiver clock jump detection is done prior to the CSDC; using the raw undifferenced code observations from all the n observed satellites with $10 \leq l^s \leq W_L$ at the current epoch, and their respective adaptive-order. A receiver clock jump is detected based on the satisfaction of Equations (5.6) and (5.7) given as

$$d_s(L^s) < d_s(L^s - 1)\,; \quad s = 1, .., k\,; \;\; 1 < k \leq n \tag{5.6}$$

$$|P_1^s(L^s) - P_1^s(L^s - 1)| \geq |P_1^s(L^s - 1) - P_1^s(L^s - 2)| + 200\,; \;\; s = 1, 2, ..., n \tag{5.7}$$

It should be observed that not all of the n satellites observations may satisfy Equation (5.6) but all n satellites code observations must satisfy Equation (5.7). If no satellite observation satisfies (5.6), and (5.7) is valid, it means the clock jump/reset would ordinarily not affect the phase-only CSDC algorithm of the n satellites. Equation (5.7) implies that the current change in the observed code pseudorange must be greater than the immediate past change in pseudorange by at least two-third of the maximum theoretical error possible on P_1 (maximum error is ∼300m), meaning such change, equivalent to about $\frac{200}{c} \simeq 0.67$microsecond of clock jump can be detected. When a clock jump is detected at a current epoch, a clock jump flag is set and the already generated phase ADS for each of the k satellites that satisfied Equation (5.6) is then further differenced in time to reach the adaptive-order, $d_s(L^s - 1)$, obtained at the last epoch, so as to maintain consistency in the CSDC algorithm for the k satellites.

It should be noted that if the total observed satellites with observation records at an epoch is s_{total}, the $(s_{total} - n)$ satellites with $l^s = L^s < 10$ observations are not considered in the clock jump detection algorithm neither is the CSDC algorithm implemented for such satellites. These $(s_{total} - n)$ satellites would either be new entrant satellites or gapped satellites recovered after observation gaps.

5.2.2. Estimating Cycle Slip Float Values and Common Receiver Clock High-order Variation

In a bid to estimate the value(s) of unknown parameter(s), which could be for instance, cycle slip float value(s) or a receiver's position coordinates, an over-determined system of equations formed from different observations/observables contaminated with different errors is often encountered. It can be assumed that the observation errors on the different observations are uncorrelated and that the distribution of the observation errors can be described by a normal distribution. As such, a suitable

estimator can be a maximum likelihood estimator, such as the least squares estimator (Bromiley, 2008). In this research, the raw code and phase observations or the derived observables from the raw code and phase observations, are assumed corrupted by observation errors that fit into these assumptions. Since the least squares estimator is identified as a suitable estimator when estimating unknown parameters from such observables/observations, the least squares algorithm is used in this section and other relevant areas of this thesis, for the estimation of cycle slip float values and receivers' position coordinates. It was unveiled in Bromiley (2008) that a least squares estimator is a derivative of both maximum likelihood and Best Linear Unbiased Estimator (BLUE) estimators. For a BLUE estimator, the observation errors are assumed uncorrelated, having a symmetric distribution of zero mean, and that the errors are homoscedastic (equal-variance space). This also justifies the use of least squares even if the observation errors have symmetric distribution of zero mean and are homoscedastic.

On obtaining the ADS - the $\Delta^{d_s}\overline{\psi_1^s}$ sequence - for each of the n observed satellites with $l^s \geq 10$, at a current epoch, and determining the cycle slip status using Equation (5.5), meeting one of three broad conditions determines how the float values of the inferred/detected cycle slips and the receiver clock high-order variation, $\varepsilon_c(t)$, at the current epoch are estimated for a single-frequency receiver. When a clock jump or reset is not detected at a current epoch, the estimated $\varepsilon_c(t)$ is assumed to represent the high-order drift of the receiver clock at that epoch, and it is presumed common to all the observed satellites at that epoch. When a clock jump or reset is detected at a current epoch, the estimated current epoch $\varepsilon_c(t)$ is taken as the clock jump value and denoted $\varepsilon_{c,jump}(t) = \varepsilon_c(t)$. The processing block for the estimation procedure for $\varepsilon_c(t)$ is represented as the **EcomE** in Figure 5.1. The three conditions and the corresponding estimation procedure for the unknown cycle slips float values and $\varepsilon_c(t)$ are:

(a) **The condition when cycle slips are not detected on all n satellites.** Under this condition, the cycle slip value for all n satellites is zero, but we estimate the common receiver clock high-order variation as the weighted average of all $\Delta^{d_s}\overline{\psi_1^s}(l^s - d_s)$ where $(s = 1, 2, .., n)$. The weight on $\Delta^{d_s}\overline{\psi_1^s}(l^s - d_s)$ is $w_s = \left(1/\sigma_{d_s}^s\right)^2$,

where $\sigma_{d_s}^s$ is the standard deviation of the phase ADS - the $\Delta^{d_s}\overline{\psi_1^s}$ sequence. That is,

$$\varepsilon_c(t) = \frac{\sum_{s=1}^{n} w_s \Delta^{d_s}\overline{\psi_1^s}(l^s - d_s)}{\sum_{s=1}^{n} w_s} \tag{5.8}$$

It should be noted that the computation of $\sigma_{d_s}^s$ does not involve the last value of the corresponding ADS.

(b) **The condition when cycle slip is detected on at least one but not all n satellites**. Under this condition, each $\Delta^{d_s}\overline{\psi_1^s}(l^s - d_s)$ value $(s = 1, 2, .., j)$ from each of the j satellite(s) that indicated no cycle slips and with corresponding weight $w_s = \left(1/\sigma_{d_s}^s\right)^2$, are used to compute $\varepsilon_c(t)$ as

$$\varepsilon_c(t) = \frac{\sum_{s=1}^{j} w_s \Delta^{d_s}\overline{\psi_1^s}(l^s - d_s)}{\sum_{s=1}^{j} w_s} \tag{5.9}$$

Subsequently the cycle slip float values of the $(n-j)$ cycle-slipped satellites are thus computed using a no-clock-effect observable, $Y_1^s = \Delta^{d_s}\overline{\psi_1^s}(l^s - d_s) - \varepsilon_c(t)$, obtained for all of the $(n-j)$ cycle-slipped satellites, $(s = 1, 2, ..., n-j)$. The matrix equation is thus :

$$\begin{array}{ccccc}
\begin{bmatrix} Y_1^1 \\ \vdots \\ \vdots \\ \vdots \\ Y_1^{n-j} \end{bmatrix} & = & \begin{bmatrix} \lambda_1 & 0 & \cdots & 0 & 0 \\ 0 & \ddots & 0 & 0 & \vdots \\ \vdots & 0 & \lambda_1 & 0 & \vdots \\ \vdots & 0 & 0 & \ddots & 0 \\ 0 & \cdots & \cdots & 0 & \lambda_1 \end{bmatrix} & \begin{bmatrix} \triangle N_1^1 \\ \vdots \\ \vdots \\ \vdots \\ \triangle N_1^{n-j} \end{bmatrix} & + & \begin{bmatrix} \triangle^{d_1} e_{\psi,1}^1(l^1 - d_1) \\ \vdots \\ \vdots \\ \vdots \\ \triangle^{d_{n-j}} e_{\psi,1}^{n-j}(l^{n-j} - d_{n-j}) \end{bmatrix} \\
Y & = & A & \triangle N & + & \triangle e_{\psi,1}
\end{array} \tag{5.10}$$

where Y is an $(n-j)\mathbf{x}1$ vector of observables; A is an $(n-j)\mathbf{x}(n-j)$ diagonal design matrix; $\triangle e_{\psi,1}$ is the $(n-j)\mathbf{x}1$ error vector containing the corresponding error values on each of the observables in Y, which are assumed uncorrelated; and $\triangle N = \left[\triangle N_1^1, \cdots, \triangle N_1^{n-j}\right]^T$ is an $(n-j)\mathbf{x}1$ vector of the cycle slips float values, which is thus estimated as

$$\triangle N = A^{-1}Y \tag{5.11}$$

(c) **The condition when all n satellites are detected to have cycle slips**. Here, $\triangle Y_\psi = \left[\triangle^{d_1}\overline{\psi_1^1}(l^1 - d_1), ..., \triangle^{d_n}\overline{\psi_1^n}(l^n - d_n)\right]^T$, the vector of phase cycle slip observables is first defined, the error vector, $\triangle^d e_{\psi,1} = \left[\triangle^{d_1} e^s_{\psi,1}(l^1 - d_1), ..., \triangle^{d_n} e^s_{\psi,n}(l^n - d_n)\right]^T$, and the respective weights, $w_s = \left(1/\sigma^s_{d_s}\right)^2$, for all $s = 1, 2, ..., n$. The estimations are then performed consequent on the outcome of three different scenarios.

Scenario 1: When the difference between the minimum and maximum values of $\triangle Y_\psi$ are within a set threshold of 3 wavelengths:

$$max(|\triangle Y_\psi|) - min(|\triangle Y_\psi|) <= 3\lambda_1 \tag{5.12}$$

The threshold of $3\lambda_1$ is set to accommodate a possible spread range of all the n combined differenced errors $\triangle^d e_{\psi,1}$. For this scenario, $\varepsilon_c(t)$ is computed as in Equation (5.8), and the $n\mathbf{x}1$ vector of no-clock-effect observables, $Y = \triangle Y_\psi - \varepsilon_c(t)$, can be obtained. The matrix equation then becomes:

$$Y = \begin{bmatrix} \lambda_1 & 0 & \cdots & 0 & 0 \\ 0 & \ddots & 0 & 0 & \vdots \\ \vdots & 0 & \lambda_1 & 0 & \vdots \\ \vdots & 0 & 0 & \ddots & 0 \\ 0 & \dots & \dots & 0 & \lambda_1 \end{bmatrix} \begin{bmatrix} \triangle N_1^1 \\ \vdots \\ \vdots \\ \vdots \\ \triangle N_1^n \end{bmatrix} + [\triangle e_{\psi,1}] \tag{5.13}$$

where A is the same $(n)\mathbf{x}(n)$ diagonal design matrix and $\triangle^d e_{\psi,1}$ is the $(n-j)\mathbf{x}1$ error vector containing the corresponding error values on each of the observables of Y, in (5.10); and $\triangle N = \left[\triangle N_1^1, \cdots, \triangle N_1^{n-j}\right]^T$ is an $(n-j)\mathbf{x}1$ vector of the cycle slip float values, which can be obtained as

$$\triangle N = A^{-1}Y \tag{5.14}$$

Scenario 2: When a receiver clock jump has been detected and all values in the $\triangle Y_\psi$ vector have the same sign, but scenario 1 (Equation (5.12)) above is not valid. In this case, any possible outlier, which is any observable in $\triangle Y_\psi$ that satisfies the condition

$$\left|\Delta^{d_s}\overline{\psi_1^s}(l^s - d_s)\right| > |\langle \triangle Y_\psi \rangle| + \sigma_{\triangle Y_\psi} \tag{5.15}$$

is removed from $\triangle Y_\psi$ to get $\triangle Y_{\psi,R}$, before estimating $\varepsilon_c(t)$ as the mean of $\triangle Y_{\psi,R}$. In this thesis, $\langle\bullet\rangle$ indicates the mean of the operand, $\bullet$, i.e. $\langle\triangle Y_\psi\rangle$ and $\sigma_{\triangle Y_\psi}$ in (5.15) are the mean and standard deviation of $\triangle Y_\psi$ respectively. Consequently, with $Y = \triangle Y_\psi - \varepsilon_c(t)$, the matrix equation given by (5.13) holds and the vector of cycle slips can then be obtained as in (5.14).

Scenario 3: This scenario is the last resort when both scenarios 1 and 2 above are not valid. The solution employed here is to include the last two values of two code ADSs, $\Delta^{d_\alpha}P_1^\alpha(l^\alpha - d_\alpha)$ and $\Delta^{d_\beta}P_1^\beta(l^\beta - d_\beta)$, which are the last two values from the two code ADSs having the least standard deviations, $\sigma_{d_\alpha}^\alpha$ and $\sigma_{d_\beta}^\beta$, from among the set of all code ADSs, $\Delta^{d_s}P_1^s$, for $\{\alpha,\beta\} \in s = 1,2,...,n$ at the current epoch. The computation of the sigma value of an ADS does not involve the last value of the ADS sequence. The possible code involvement in estimating $\varepsilon_c(t)$ is indicated by the dotted red arrow in Figure 5.1. The corresponding weights on the two additional code observables are obtained as $w_\alpha = \left(1/\sigma_{d_\alpha}^\alpha\right)^2$ and $w_\beta = \left(1/\sigma_{d_\beta}^\beta\right)^2$. As a result, a joint $(n+2)\mathbf{x}1$ vector of observables, $\triangle Y = \left[\triangle^{d_1}\overline{\psi_1^1}(l^1 - d_1), ..., \triangle^{d_n}\overline{\psi_1^n}(l^n - d_n), \Delta^{d_\alpha}P_1^\alpha(l^\alpha - d_\alpha), \Delta^{d_\beta}P_1^\beta(l^\beta - d_\beta)\right]^T$, and an appropriate $(n+2)\mathbf{x}(n+2)$ diagonal weight matrix, W, defined as

$$W = \begin{bmatrix} w_1 & 0 & \cdots & 0 & 0 & 0 \\ 0 & w_2 & \vdots & 0 & 0 & 0 \\ \vdots & \cdots & \ddots & \cdots & \vdots & \vdots \\ 0 & 0 & \vdots & w_n & 0 & 0 \\ 0 & 0 & \vdots & 0 & w_\alpha & 0 \\ 0 & 0 & \cdots & 0 & 0 & w_\beta \end{bmatrix} \tag{5.16}$$

can be formed. The resulting matrix equation is thus given by

$$\begin{bmatrix} \triangle^{d_1}\overline{\psi_1^1}(l^1-d_1) \\ \triangle^{d_2}\overline{\psi_1^2}(l^2-d_2) \\ \vdots \\ \triangle^{d_n}\overline{\psi_1^n}(l^n-d_n) \\ \Delta^{d_\alpha}P_1^\alpha(l^\alpha-d_\alpha) \\ \Delta^{d_\beta}P_1^\beta(l^\beta-d_\beta) \end{bmatrix} = \begin{bmatrix} \lambda_1 & 0 & \cdots & 0 & 1 \\ 0 & \lambda_1 & \vdots & 0 & 1 \\ \vdots & \cdots & \ddots & \cdots & \vdots \\ 0 & 0 & \vdots & \lambda_1 & 1 \\ 0 & 0 & \vdots & 0 & 1 \\ 0 & 0 & \cdots & 0 & 1 \end{bmatrix} \begin{bmatrix} \triangle N_1^1 \\ \triangle N_1^2 \\ \vdots \\ \triangle N_1^n \\ \varepsilon_c(t) \end{bmatrix} + \begin{bmatrix} \triangle^{d_1}e_{\psi,1}^1(l^1-d_1) \\ \triangle^{d_2}e_{\psi,1}^2(l^2-d_2) \\ \vdots \\ \triangle^{d_n}e_{\psi,n}^n(l^n-d_n) \\ \triangle^{d_\alpha}e_{P,1}^\alpha(l^\alpha-d_\alpha) \\ \triangle^{d_\beta}e_{P,1}^\beta(l^\beta-d_\beta) \end{bmatrix} \quad (5.17)$$

$$\triangle Y \quad = \quad H \quad \triangle X \quad + \quad \triangle e$$

where $\triangle e$ is the resulting $(n)\mathbf{x}1$ error vector containing the corresponding error values in each of the observables in $\triangle Y$. A weighted least square is used to solve for $\triangle X = [\triangle N, \varepsilon_c(t)]^T$, being the $(n+1)\mathbf{x}1$ vector containing the n unknown cycle slips float values and $\varepsilon_c(t)$, as (Cross, 1983)

$$\triangle X = \left[H^T W H\right]^{-1} H^T W \triangle Y \quad (5.18)$$

The estimated $\varepsilon_c(t)$, as wanted, absorbs the common receiver clock high-order variation plus the common error (correlation among the observables in $\triangle Y$), hence a diagonal W matrix is used and the H matrix includes a last column of '1's. Under condition (c) where all n satellites indicate cycle slips, a final check is put in place to determine whether to null or accept the estimated n float cycle slip values in $\triangle N$. Under condition (c) above, the estimated float cycle slip values are nulled (made equal to zero) if $max(|\triangle N|) < 5$, and are accepted as true cycle slips if otherwise. This tolerance of 5cycles$\approx$ 95cm is set to compensate for: the error on the two values from the code ADSs that are used; the error due to possible phase wind-up effects; the error effect of the n combined differenced errors (the impact of $\triangle e_{\psi,1}$ or $\triangle e$ given in (5.10) or (5.17) respectively); and the error due to possible limitation in the cycle slip detection and float values estimation processes. It is however presumed that the probability of having cycle slips on all satellites at a single epoch with the highest cycle slip magnitude less than 5cycles is low; and when this results, the algorithm assumes that it is more likely to be due to errors in the estimation process or as a result of receiver's clock drift, rather than actual occurrence of all n cycle slips with

magnitudes under 5cycles.

5.2.3. Handling the Limitation of the Single-Frequency CSDC Algorithm

The single-frequency CSDC algorithm is not assumed a perfect algorithm; it could be limited by the magnitude of the adaptive-order differenced error, $\triangle^{d_s} e^s_{\psi,1}$, in the detection process. The ATD process for the cycle slips detection is also quite sensitive to receiver clock drifts or variations, and possibly also to receiver antenna dynamics. As such, the ATD process could indicate cycle slips for satellites when actually there are no cycle slips at certain epochs of high clock drifts or antenna dynamics. The effect of $\triangle e_{\psi,1}$ or $\triangle e$ in the cycle slips float values estimation process given by (5.10) or (5.17) respectively, or a wrong estimation of an $\varepsilon_c(t)$ value, could also be significant to flaw the estimation of cycle slips float values, especially when the sensitive ATD detection process indicates cycle slips on all satellites at a given epoch and code ADSs are then involved. Any falsely detected cycle slip would be fixed to a false integer value, and if falsely corrected for in the phase observation, it would result to decreasing positioning accuracy and precision.

As a possible solution to minimise the impact of this limitation in the single-frequency CSDC algorithm, some checks are done, which can result in Nulling of Fixed Cycle Slip (NFCS) prior to correcting for the fixed (not nulled) cycle slip on the phase observation of a cycle-slipped satellite. The single-frequency checks for a given satellite s whose detected cycle slip has already been fixed/determined at the current epoch, are:

(a) Check the immediate past epoch cycle slip status of s - the estimated cycle slip float value, and the fixed cycle slip value - if there was. The nulling at a current epoch can be done based on the status of the estimated float or fixed integer value at the last epoch of s, and this can happen if: (i) there was an estimated cycle slip float value nulled at the last epoch for s, probably due to its magnitude lower than a set threshold in the float value estimation, and the difference in metres between it and the current epoch's estimated cycle slip float value is less than 0.5m, that is $\lambda_1 \left| \triangle N^s_1(L^s) - \triangle N^s_1(L^s - 1) \right| \leq 0.5m$; (ii) there was a detected and

fixed cycle slip at the last epoch that was nulled after previously applying NFCS checks. If there was, and the difference between the current epoch's fixed cycle slip value and the last epoch's nulled fixed cycle slip is not more than 3cycles, i.e. $\left|\triangle N^s_{1,int}(L^s) - \triangle\overline{Ns}_{1,int}(L^s-1)\right| \leq 3$. If either (i) or (ii) is satisfied, then the fixed cycle slip at the current epoch is nulled, otherwise the fixed cycle slip is accepted and corrected for in the corresponding phase observation. This implies that if a cycle slip was detected but not accepted based on the condition given by Equation (5.20), or it was fixed but was nulled after NFCS checks at the immediate past epoch, the current epoch's detected or fixed cycle slip value can only be accepted and corrected for if it differs from the last epoch's nulled cycle slip by more than 3 cycles.

(b) Check if cycle slips were fixed and corrected for in the last two consecutive epoch observation from s. A fixed integer cycle slip is denoted $N^s_{1,int}$. If the fixed cycle slip at the current epoch is a multiple of the last epoch cycle slip value or $\left|\triangle N^s_{1,int}(L^s) - \triangle N^s_{1,int}(L^s-1)\right| = \left|\triangle N^s_{1,int}(L^s-1) - \triangle N^s_{1,int}(L^s-2)\right|$, the current epoch's fixed cycle slip is nulled. The NFCS under this condition helps in eliminating repeatedly inferred cycle slips that may be due, for instance, to false detection of a cycle slip or possible antenna dynamics among other possible reasons that may not have been identified in this research.

5.2.4. Single-Frequency Cycle Slip Correction

The estimated satellite s cycle slip float value, $\triangle N^s_1$, for each of the $k \leq n$ cycle-slipped satellites, must first exceed a certain minimum threshold, $x^s_{1,min}$, to be actually accepted as a true cycle slip occurrence. From the sequence of the no-clock-effect observable generated as $Y^s_1 = \Delta^{d_s}\overline{\psi^s_1}(1 : l^s - d_s - 2) - \varepsilon_c(t - l^s - d_s + 1 : t - 2)$ for s, and its standard deviation $\sigma_{Y^s_1}$, the minimum threshold $x^s_{1,min}$ is derived as

$$x^s_{1,min} = \lambda_1 - \sigma_{Y^s_1} \tag{5.19}$$

for each of the k satellites detected to have cycle slips. The last two epochs are not included in generating the Y^s_1 vector used for determining $\sigma_{Y^s_1}$ so as to exclude the impact of the current epoch that may have a slip and to make Y^s_1 independent of

the last epoch's cycle slip that may not have been correctly corrected for. If

$$|\lambda_1 \triangle N_1^s| > x_{1,min}^s \tag{5.20}$$

then the estimated cycle slip float value is valid and accepted, and can therefore be fixed to an integer value, otherwise the estimated cycle slip float value is nulled (assigned zero value and not treated as a cycle slip any further) even though the satellite was indicated to have cycle slip. The fixing of the cycle slips float values to integers is a trivial process of rounding-up the estimated and accepted cycle slips float values in $\triangle N$ vector to integers. The fixed integer cycle slip, $\triangle N_{1,int}^s$, can be obtained for the $s = 1, .., k$ cycle-slipped satellites as

$$\triangle N_{1,int}^s = round(\triangle N_1^s) \tag{5.21}$$

and they are the fixed cycle slips integers at the current epoch that corresponds to the ${L_s}^{th}$ epoch of $s = 1, .., k$. The phase observation sequence from a given s is subsequently corrected for the current epoch's fixed cycle slip value. The correction is applied by adding the determined/fixed cycle slip equivalent value in metres to the pre-cycle-slip observables in metres, thereby able to generate a current cycle-slip-free phase observable, $\overline{\psi_1^s}(L^s)$, with 'no' cycle slip relative to the past $\overline{\psi_1^s}(1 : L^s - 1)$ observables. This is done for each of the k cycle-slipped satellites at the current observation epoch. For a given s, the L_s-length time series or sequence of cycle-slip-free phase observables in metres, is corrected as

$$\overline{\psi_1^s}(1 : L^s) = \left\{ \overline{\psi_1^s}(1 : L^s - 1) + \lambda_1 \triangle N_{1,int}^s,\ \psi_1^s(L^s) \right\} \tag{5.22}$$

As given by Equation (5.22), the cycle slip correction involves adding the product of the determined cycle slip value and the corresponding wavelength, to the previous $(L^s - 1)$-length cycle-slip-free phase observables from s, i.e. $\overline{\psi_1^s}(1 : L^s - 1)$, and appending the current epoch's raw phase $\psi_1^s(L^s)$ observation that is affected by cycle slip as the last value of the cycle-slip-free phase sequence. In this way, the previous phase observables are updated with the current cycle slip value, and the

resulting integer ambiguity value at any such epoch of cycle slip will thus be changing accordingly. The previous $\overline{\psi_1^s}(1 : L^s - 1)$ values must have been corrected for cycle slips if there were detected, accepted and determined cycle slips. The sliding window observables - the last W_L-length observables from the current L^s-length cycle-slip-free phase sequence - are what are used for the ATD process for the phase cycle slip detection on the next $(L^s + 1)^{th}$ observation epoch of s, as earlier described in Section 5.1. As such, only the last W_L number of observables are actually required to be updated since the maximum length of an undifferenced phase sequence is W_L. In this way, the receiver does not need to store more than W_L past phase and code observables in real time processing.

5.3. Single-Frequency Improved Ionospheric Correction Model

The Klobuchar model is the ionospheric delay correction model for single-frequency users of GPS. Currently, each GPS satellite broadcasts eight time-varying coefficients required by a single-frequency receiver in a given location, which are used for generating the ionospheric delay correction for a given receiver-satellite path. The Klobuchar model assumes an ideal smooth behaviour of the ionosphere. The NeQuick model is the ionospheric model proposed to be used by Galileo system for single-frequency ionospheric correction (GALILEOICD, 2008). Three world-wide coefficients (to be computed at the Galileo system level, using a set of world-wide distributed monitoring stations to evaluate slant TEC needed to determine the coefficients on a current day for use on the following day) are to be broadcast to the user (Radicella, 2009). In addition to a receiver-determined MODIP - a geomagnetic coordinate, the effective ionisation and subsequently, the slant TEC and ionospheric delay on the satellite-receiver path can be computed. It has been claimed that the NeQuick model, compared to the Klobuchar model, would achieve better ionospheric correction accuracy (see (Angrisano *et al.*, 2011)). However, because of the current unavailability of the Galileo broadcast coefficients, and the use of GPS data for the testing and validation of the algorithms proposed in this thesis, the Klobuchar mo-

del has been adopted and used as the reference ionospheric model for the correction of single-frequency ionospheric delay in this thesis.

The process diagram for the proposed improved ionospheric correction (IIC) model is shown in Figure 5.3. The process involves the last l^s_{iono} $(1 \leq l^s_{iono} \leq W_{iono})$ time

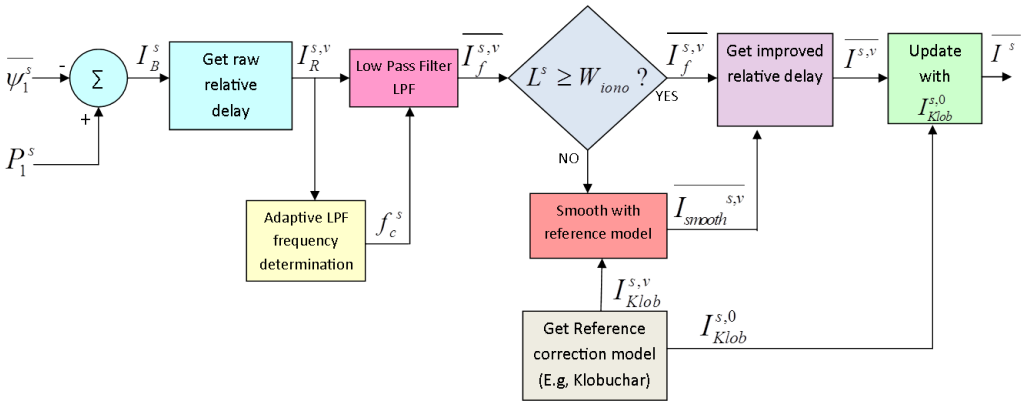

Figure 5.3.: Process diagram for improving ionospheric correction

series code observations and phase observables where $W_{iono} = 600$ (600seconds for 1Hz data) is the set ionospheric window length for all observed satellites. This set window length assumes a quiet ionosphere with relatively low ionospheric variations over a 600seconds interval. The window length may vary for different data rates. The true ionospheric delay can be represented as the sum of an unknown constant initial ionospheric delay value, $I^{s,0}$, and a time-varying relative delay component, $I^{s,v}$ (Momoh, 2012).

$$I^s = I^{s,0} + I^{s,v} \tag{5.23}$$

The varying $I^{s,v}$ at any epoch, is the relative ionospheric delay with respect to the ionospheric delay at the first observation epoch of s, with $I^{s,v}(1) = 0$. In other words, at the first observation epoch of s, $l^s_{iono} = L^s = 1$, $I^s(1) = I^{s,0}$, and $I^{s,v}(1) = 0$. Neglecting higher-order ionospheric effects, the difference between an l^s_{iono}-length time series of raw code observation, $P^s_1(L^s - l^s_{iono} + 1 : L^s)$, and an l^s_{iono}-length time series of cycle-slip-free phase observable, $\overline{\psi^s_1}(L^s - l^s_{iono} + 1 : L^s)$, gives a time series ambiguity-biased ionospheric observable, $I^s_B(L^s - l^s_{iono} + 1 : L^s)$, given as

$$\begin{aligned} I_B^s &= (P_1^s - \overline{\psi_1^s})/2 \\ &= I^s - \frac{1}{2}\lambda_1 N_1^s + \frac{1}{2} b_1^s d_1^s + \frac{1}{2} e_{iono} \\ I_B^s &= I^{s,0} + I^{s,v} - \frac{1}{2}\lambda_1 N_1^s + \frac{1}{2} D_1^s + \frac{1}{2} e_{iono} \end{aligned} \tag{5.24}$$

where $D_1^s = d_1^s + d_1^r - b_1^s - b_1^r$ and $e_{iono} = (m_{P,1}^s + \epsilon_{P,1}^s - m_{\psi,1}^s - \epsilon_{\psi,1}^s)$ are used to represent the combined hardware delays and the combined code and phase errors respectively. Assuming within the time series, that the hardware delays are constants, and cycle slips do not occur or are detected and corrected for when they occur, the initial ambiguity-biased ionospheric delay value, $I_B^{s,0} = I_B^s(1) \approx I^{s,0} - \frac{1}{2}\lambda_1 N_1^s + \frac{1}{2} D_1^s + \frac{1}{2} e_{iono}(1)$, remains constant. As such, a time series of the time-varying relative ionospheric delay observable, $I_R^{s,v}$, is generated as

$$I_R^{s,v} = I_B^s - I_B^{s,0} = I^{s,v} + \frac{1}{2} e_{iono} \tag{5.25}$$

Equation (5.25) presents a sequence of ionospheric observables, which includes a true time-varying relative ionospheric delay and a contaminating error of $0.5 e_{iono}$, where $I_R^{s,v}(1) = 0$. The aim here is to mitigate the $0.5 e_{iono}$ error component in the $I_R^{s,v}$ sequence by adaptive lowpass filtering so as to better estimate the sought-after underlying $I^{s,v}$. By this ionospheric modelling approach, the update

$$I_B^{s,0} = I_B^{s,0} - \frac{1}{2}\lambda_1 \triangle N_1^s \tag{5.26}$$

has to be done whenever a cycle slip, $\triangle N_1^s$, occurs between the current epoch's phase observation and last epoch's phase observable. This important update preludes the use of $I_B^{s,0}$ in Equation (5.25) for generating the $I_R^{s,v}$ sequence, and it is done once a cycle slip is detected, accepted and determined on the phase observation from s, at a current epoch.

5.3.1. Adaptive Lowpass Frequency Determination

Since the time-varying relative ionospheric variation is presumed slowly-varying, a lowpass filter (LPF) (see Figure 5.3), can be used to mitigate the error level on the $I_R^{s,v}$ sequence. As seen in the figure, a suitable LPF cut-off frequency is adaptively determined after adaptive time differencing of the undifferenced $I_R^{s,v}$ ionospheric sequence.

The ATD of $I_R^{s,v}$ follows the earlier description of ATD process in Section 4.4, done to yield the ionospheric adaptively differenced sequence (ADS), $\Delta^{d_{s,iono}} I_R^{s,v}$, as

$$\Delta^{d_{s,iono}} I_R^{s,v} = \Delta^{d_{s,iono}} I^{s,v} + \frac{1}{2}\Delta^{d_{s,iono}} e_{iono} \tag{5.27}$$

where $d_{s,iono}$ is the adaptive-order of the ionospheric ADS. The resulting ADS is assumed the high frequency error/noise signature in $I_R^{s,v}$. A constrain is applied in determining $d_{s,iono}$ if the 1-sigma of the $I_R^{s,v}$ sequence is smaller than the 1-sigma (standard deviation) of the ionospheric ADS. Hence,

$$d_{s,iono} = \begin{cases} j_{s,iono}\,; & if \;\; \sigma_{j_{s,iono}} \leq \sigma_{I_R^{s,v}} \\ j_{s,iono} - 1\,; & if \;\; \sigma_{j_{s,iono}} > \sigma_{I_R^{s,v}} \end{cases} \tag{5.28}$$

where $\sigma_{j_{s,iono}}$ is the 1-sigma value of the ionospheric ADS obtained at the $j_{s,iono}^{th}$-order of differencing. This constrain is necessary because of the relatively large magnitude of $\frac{1}{2}\Delta^{d_{s,iono}} e_{iono}$ (see Equation (5.27)) that could make the 1-sigma value of an ionospheric ADS greater than the 1-sigma value of the undifferenced $I_R^{s,v}$ ionospheric sequence. The $\sigma_{d_{s,iono}}$ is consequently obtained as the standard deviation of $\Delta^{d_{s,iono}} I_R^{s,v}$ sequence. It should be observed that this constrain is not required for the adaptive-order, d_s, determined for a phase or code ADS. If the constrain on $d_{s,iono}$ results in $d_{s,iono}$ equal to zero, It means there is no need of performing ATD on $I_R^{s,v}$, and as such, $\sigma_{d_{s,iono}} = \sigma_{I_R^{s,v}}$; implying that the undifferenced ionospheric $I_R^{s,v}$ sequence becomes the ionospheric ADS. Getting the variance of the undifferenced ionospheric $I_R^{s,v}$ sequence as $var_R^s = (\sigma_{I_R^{s,v}})^2$, we estimate the variance of the

embedded error/noise, var^s_{noise}, as

$$var^s_{noise} = \begin{cases} (d_{s,iono}.\sigma_{d_{s,iono}})^2\,; & if \;\; d_{s,iono} \neq 0 \\ var^s_R\,; & if \;\; d_{s,iono} = 0 \end{cases} \tag{5.29}$$

The error variance estimation given by (5.29) presumes that $\sigma_{d_{s,iono}}$ is the standard deviation of the high-frequency error components in $I^{s,v}_R$, and the multiplication by $d_{s,iono}$ compensates for the low-frequency error components that would have been mitigated by the $d_{s,iono}$-order differencing. When $d_{s,iono}$ is zero, it is interpreted as $I^{s,v}_R$ is dominated by $0.5e_{iono}$ (analogous to a very low signal-to-noise ratio), and as such, the error variance is assumed the variance of the undifferenced ionospheric $I^{s,v}_R$ sequence, i.e. $var^s_{noise} = var^s_R$. Assuming $I^{s,v}$ is not correlated with e_{iono}, the variance of $I^{s,v}$, var^s_v, is thus

$$var^s_v = var^s_R - var^s_{noise} \tag{5.30}$$

Obviously, when $var^s_{noise} = var^s_R$, $var^s_v = 0$. The estimated var^s_v is used to adaptively determine the required LPF cut-off frequency, f^s_c, which is needed to filter the error-contaminated $I^{s,v}_R$ sequence.

The developed technique for determining f^s_c from an estimated var^s_v follows from a derived relationship between a signal variance and the signal energy. Proceeding to establish this relationship, one can imagine a discrete-time domain sequence, $x[\tau]$ where $\tau = 1, 2, ..., l^s_{iono}$, and its frequency domain equivalent, $X(K)$ where $K = 1, 2, ..., l^s_{iono}$; both x and X containing the same l^s_{iono} number of values. Then, as with the Parseval's theorem given in Equation (4.4), it holds that

$$\sum_{\tau=1}^{l^s_{iono}} |x(\tau)|^2 = \frac{1}{l^s_{iono}} \sum_{K=1}^{l^s_{iono}} |X(K)|^2 \tag{5.31}$$

If the x sequence is a zero-mean (x minus mean of x) sequence, then its variance, var_{sig}, is known simply as

$$var_{sig} = \frac{\sum_{\tau=1}^{l^s_{iono}} (x[\tau])^2}{(l^s_{iono} - 1)} \tag{5.32}$$

Following from equations (5.31) and (5.32), the energy, E_f, computed from the FD X; the energy, E_t, computed from the TD x; and the variance of x, can be related thus:

$$E_f = \frac{1}{l^s_{iono}} \sum_{K=1}^{l^s_{iono}} |X(K)|^2 = E_t = var_{sig} \times (l^s_{iono} - 1) \tag{5.33}$$

Deductively, Equation (5.33) reveals that once the variance of an l^s_{iono}-length 'noiseless' and zero-mean relative ionospheric delay sequence is known or estimated, its energy can be obtained as the product $var^s_{sig} \times (l^s_{iono} - 1)$. To achieve this, the zero-mean $I^{s,v}_R$ sequence, denoted $I^{s,v}_{R,zm}$, is obtained as

$$I^{s,v}_{R,zm} = I^{s,v}_R - \langle I^{s,v}_R \rangle \tag{5.34}$$

followed by generating the equivalent one-sided energy spectrum of $I^{s,v}_{R,zm}$ as described in Section 4.2. The total energy, E^s_{total}, of $I^{s,v}_{R,zm}$, is the energy of the zero-mean components - the underlying zero-mean noiseless $I^{s,v}_{zm}$ and the zero-mean embedded error sequence - going by Equation (4.6). However, the interest is on the energy of $I^{s,v}_{zm}$, being a low-frequency (slowly-varying) component of $I^{s,v}_{R,zm}$, and whose energy, E^s_{BW}, is predominantly within the bandwidth from 0Hz to the required cut-off frequency f^s_c. The required energy of the 'noiseless' $I^{s,v}_{zm}$ is estimated as the bandwidth energy E^s_{BW}, which is the accumulated energy from $K = 1$ - the 0Hz frequency - through to a critical $K = K_c$ at which the accumulated energy equals or is just less than $var_x \times (l^s_{iono} - 1)$. As a mathematical expression,

$$E^s_{BW} = \sum_{K=1}^{K_c} |X_{iono}(K)|^2 \approx var_x.(l^s_{iono} - 1)\,;\ \ K_c \leq L_{half} \tag{5.35}$$

where $L_{half} = \frac{l^s_{iono}+1}{2}$ when l^s_{iono} is odd or $L_{half} = \frac{l^s_{iono}+2}{2}$ when l^s_{iono} is even. Thus, following from Equation (4.3), the required cut-off frequency, f^s_c, is obtained as

$$f^s_c = (K_c - 1)\triangle F \tag{5.36}$$

in Hertz, where $\triangle F = \frac{f_{samp}}{l^s_{iono}} = \frac{1}{l^s_{iono}}$ since $f_{samp} = 1$Hz - the sampling frequency or observation rate of the data used in this research. However, as the ionospheric

variation is presumed slowly-varying, it is expected that f_c^s should not increase with increasing $l_{iono}^s < W_{iono}$. As such, at a current epoch t, if the estimated f_c^s increases relative to the estimated f_c^s value at the last $t-1$ epoch, the current epoch's f_c^s value is then constrained to the f_c^s value obtained at the last $t-1$ epoch, that is $f_c^s(L^s) = f_c^s(L^s - 1)$.

It should be noted that for a satellite with very few observation epochs available (usually within $2 \leq l_{iono}^s < 10$), or when $var_{sig}^s = 0$, the cut-off frequency is simply obtained as $f_c^s = \triangle F = \frac{1}{l_{iono}^s}$Hz. When an observation gap occurs, l_{iono}^s is re-initialised to 1.

5.3.2. Performing the Lowpass Filtering

The digital LPF employed to filter each satellite's $I_R^{s,v}$sequence is an IIR Butterworth LPF of order $R = 1$ and cut-off frequency f_c^s, which is similar to the Butterworth filter illustrated in Section 4.3.1. As depicted in Figure 5.3, the LPF filters individual satellite's $I_R^{s,v}$ sequence using its estimated f_c^s. Depending on the number of available L^s epoch observations from s, the filtered output, $\overline{I_f^{s,v}}$, is further either combined or initialised with the GPS broadcast Klobuchar ionospheric model that is used as the reference ionospheric model here. The lowpass filtering is implemented in either of these two ways:

(a) When $L^s < W_{iono}$. In this case $l_{iono}^s = L^s$ and a zero-phase (bi-directional filtering) Butterworth lowpass filtering described in Section 4.3.1 is implemented to ensure a zero-phase shift between the filtered output $\overline{I_f^{s,v}}$ sequence and the filter input $I_R^{s,v}$ sequence, in addition to mitigating the high-frequency (rapidly-varying) error components in the $I_R^{s,v}$ sequence. The time series (sequence) of the filtered output $\overline{I_f^{s,v}}$ could still be 'noisy' especially when l_{iono}^s is small compared to W_{iono}. To address this, further smoothing of the filtered output with the smoother referenced Klobuchar ionospheric model is done whilst $L^s < W_{iono}$. With the time-varying Klobuchar model relative ionospheric delay, $I_{Klob}^{s,v}$, obtained as

$$I_{Klob}^{s,v} = I_{Klob}^s - I_{Klob}^{s,0} \tag{5.37}$$

where I^s_{Klob} and $I^{s,0}_{Klob}$ are respectively the Klobuchar model slant ionospheric delay and the Klobuchar model initial slant delay at $l^s_{iono} = 1$, which is constant for a given satellite as far as it is continuously observed, the further smoothed relative ionospheric delay, $\overline{I^{s,v}_{smooth}}$, at the current epoch (corresponding to L^s) is generated as

$$\overline{I^{s,v}_{smooth}}(L^s) = \frac{(W_{iono} - l^s_{iono})}{W_{iono}} I^{s,v}_{Klob}(L^s) + \frac{l^s_{iono}}{W_{iono}} \overline{I^{s,v}_f}(L^s) \tag{5.38}$$

The improved relative ionospheric delay (the estimate of the actual underlying $I^{s,v}$) at the current epoch is gotten as $\overline{I^{s,v}}(L^s) = \overline{I^{s,v}_{smooth}}(L^s)$, noting that $\overline{I^{s,v}}(1) = \overline{I^{s,v}_{smooth}}(1) = I^{s,0}_{Klob}$. Subsequently, by updating $\overline{I^{s,v}}(L^s)$ with the reference Klobuchar model initial slant delay, the improved slant ionospheric delay

$$\overline{I^s} = \overline{I^{s,v}}(L^s) + I^{s,0}_{Klob} \tag{5.39}$$

to be used for the single-frequency improved ionospheric delay correction when $L^s < W_{iono}$, is thus acquired.

(b) When $L^s \geq W_{iono}$. In this case a slight modification to the typical Butterworth LPF given by Equation (4.12) is implemented so as to reduce the computational burden involved with filtering a whole W_{iono}-long undifferenced ionospheric sequence in addition to mitigating the embedded error. The modification of the IIR Butterworth LPF to generate a current epoch's filtered output $\overline{I^{s,v}_f}(L^s)$ value is implemented as follows

$$\overline{I^{s,v}_f}(L^s) = a_0 I^{s,v}_R(L^s) + a_1 \overline{I^{s,v}_f}(L^s - 2) - b_1 \overline{I^{s,v}_f}(L^s - 1) \tag{5.40}$$

Comparing Equation (4.12) to (5.40), the modification is seen on the second term, and it is such that instead of using the last epoch value of the input, $I^{s,v}_R(L^s - 1)$, it is replaced by $\overline{I^{s,v}_f}(L^s - 2)$ - the next to the last epoch value of the already filtered output. The improved relative ionospheric delay (the estimate of the actual underlying $I^{s,v}$) at the current epoch is then acquired as $\overline{I^{s,v}}(L^s) = \overline{I^{s,v}_f}(L^s)$; and the subsequent update of $\overline{I^{s,v}}(L^s)$ with the reference Klobuchar model initial slant

delay yields the improved slant ionospheric delay

$$\overline{I^s}(L^s) = \overline{I^{s,v}}(L^s) + I^{s,0}_{Klob} \tag{5.41}$$

This modification enhances better smoothness of $\overline{I^{s,v}_f}$.

It should be noted that, irrespective of the ionospheric model that may be used for single-frequency ionospheric correction - either the Klobuchar, NeQuick or even the IONEX GIM model - the generation of a receiver-satellite slant ionospheric delay with any of these models involves the use of an elevation-dependent mapping function. This proposed IIC model estimates the relative slant ionospheric delay without making use of a mapping function. It is however dependent on the initial ionospheric delay value that is determined from the chosen reference model, which in this case is the Klobuchar model.

5.4. Code Error Mitigation

The simple code error mitigation process is depicted in Figure 5.4. At a current

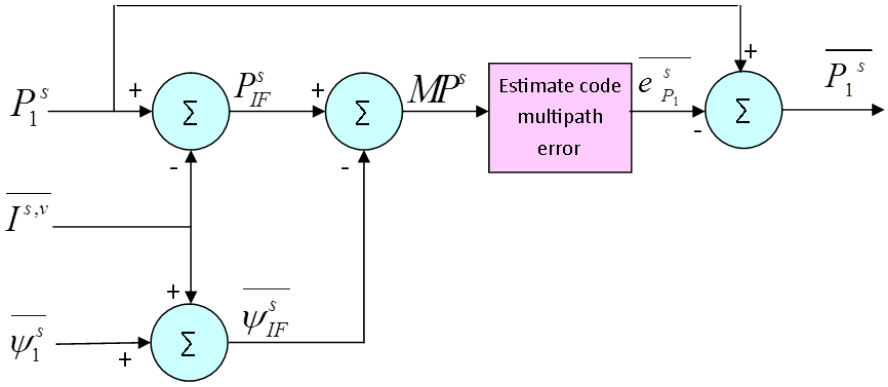

Figure 5.4.: Code error mitigation process

epoch, the estimated value of the varying relative ionospheric delay is first eliminated from the current epoch's code observation and from the current epoch's cycle-slip-free phase observation, for each of the total S_{total} observed satellite at the current epoch. This helps generate pseudo-iono-free code and phase observables represented as $P^s_{IF}(L^s) = P^s_1(L^s) - \overline{I^{s,v}}(L^s)$ and $\psi^s_{IF}(L^s) = \overline{\psi^s_1}(L^s) + \overline{I^{s,v}}(L^s)$ respectively. By taking the difference between P^s_{IF} and ψ^s_{IF}, a code multipath observable at the

current epoch is obtained as

$$\begin{aligned} MP^s(L^s) &= P^s_{IF}(L^s) - \psi^s_{IF}(L^s) \\ &= 2I^{s,0} - \lambda_1 N^s_1 + d^s_1 + d^r_1 - b^s_1 - b^r_1 + m^s_{P,1} + \epsilon^s_{P,1} - m^s_{\psi,1} - \epsilon^s_{\psi,1} \\ &= 2I^{s,0} - \lambda_1 N^s_1 + D^s_1 + e^s_{p_1} \end{aligned} \tag{5.42}$$

The $MP^s(L^s)$ is observed to consist of constants - $I^{s,0}$ and $\lambda_1 N^s_1$; the combined fairly constant hardware delays denoted as $D^s_1 = d^s_1 + d^r_1 - b^s_1 - b^r_1$; and the combined phase error and dominant code error, denoted as $e^s_{p_1} = m^s_{P,1} + \epsilon^s_{P,1} - m^s_{\psi,1} - \epsilon^s_{\psi,1}$. Assuming the phase error is negligibly small compared to the code error as usual, the whole error, $e^s_{p_1}$ in Equation (5.42), is treated as the code error. Also, assuming the time series error, $e^s_{p_1}$, approaches a zero-mean sequence as the number of observation epochs increase, a zero-mean code error value can be estimated. It can easily be shown, as done in Section A.1, that the updated mean value, $\langle MP^s \rangle$, at a current epoch, that is $\langle MP^s(L^s) \rangle$, is given by

$$\langle MP^s(L^s) \rangle = \frac{1}{L^s} \left[(L^s - 1) \left\{ \langle MP^s(1 : L^s - 1) \rangle - \lambda_1 \triangle N^s_{1,int} \right\} + MP^s(L^s) \right] \tag{5.43}$$

where $\triangle N^s_1$ is the determined value of the cycle slip that may have occurred between the current epoch's phase observation and the last epoch's phase observable. $\triangle N^s_{1,int}$ is equal to zero if a cycle slip was not detected and determined for s at a current epoch. The zero-mean code error, $\overline{e^s_{p_1}(L^s)}$, is subsequently computed as $\overline{e^s_{p_1}(L^s)} = MP^s(L^s) - \langle MP^s(L^s) \rangle$; and finally, the smoothed or error-mitigated code observable, $\overline{P^s_1}$, is obtained after subtracting the estimated zero-mean code error value from the current epoch's code observation. That is, for a current epoch,

$$\overline{P^s_1}(L^s) = P^s_1(L^s) - \overline{e^s_{p_1}(L^s)} \tag{5.44}$$

and $\overline{P^s_1}(L^s)$ is the smoothed or error-mitigated code observable used for code positioning at a current epoch. This code error mitigation algorithm thus leads to mitigation of the code error (mostly composed of the multipath error and noise on the code observation) level. Like the Hatch filter, it follows that $\overline{P^s_1}(1) = P^s_1(1)$ at the very first observation epoch of s. Unlike the Hatch filter, this algorithm is obser-

ved to be based on the prior determination of a cycle slip value, and the 'elimination' of the relative ionospheric delay. In that way, the algorithm is cycle-slip-resilient and almost unaffected by ionospheric divergence, unlike the many existing code smoothing or error-mitigation techniques that are limited by cycle slip occurrence and ionospheric divergence.

It is worth mentioning that for an NLOS signal from a satellite, the code and phase observations experience the same path delay, and as such, the code and phase errors, which are essentially range errors, are more or less the same. Consequently, any code carrier-smoothing technique or a filtering/smoothing technique that depends on the phase observation from a satellite to smooth/filter the code observation from the same satellite, will not mitigate the code errors. The proposed code error mitigation technique in this thesis is only suitable and recommended for mitigation of the code error mainly due to multipath and noise on the code, and not designed to mitigate the code range error in an NLOS signal.

5.5. Updating Past Observables with a Clock Jump Value

Recalling that the ATD process requires an undifferenced sequence obtained from consecutive epochs observables for cycle slip detection, a clock jump occurrence at a current epoch creates a huge difference between the immediate past epoch observables and the current epoch observable, which has capacity to mar the cycle slip detection with ATD. To avoid this possibility, the past code and phase observables are updated with an estimated clock jump value, $\varepsilon_{c,jump}(t)$, at a current epoch where a clock jump/reset has been detected according to Equations (5.7) and (5.6). The updates done as

$$\overline{\psi_1^s}(1:L^s) = \left\{\overline{\psi_1^s}(1:L^s-1) + \varepsilon_{c,jump}(t),\ \psi_1^s(L^s)\right\} \tag{5.45}$$

$$P_1^s(1:L^s) = \left\{P_1^s(1:L^s-1) + \varepsilon_{c,jump}(t),\ P_1^s(L^s)\right\} \tag{5.46}$$

shows that the estimated clock jump at a current epoch is added to the previous phase observables and code observations. In this way, ATD at subsequent epochs after a clock jump will be independent of the clock jump at a previous epoch. Again, only the last W_L number of observables are really required to be updated as the required maximum length of an undifferenced sequence for an ATD process is W_L.

5.6. Summary

Following the generation of adaptively differenced sequences (ADSs) acquired through an adaptive time differencing (ATD), a phase-only-derived cycle slip detection, determination and correction algorithm has been developed for a single-frequency receiver. Suitable equations for clock jump detection and estimation; cycle slips float values and common receiver clock high-order variation estimation; and appropriate equations for cycle slip and clock jump corrections, have been presented. The simple procedure for fixing or determining the integer value of a cycle slip, as well as the nulling of a 'falsely' detected and fixed cycle slip - a measure to address the envisaged limitation of the single-frequency CSDC algorithm - are also given. A new approach involving adaptive determination of a lowpass filtering frequency and energy estimation, to obtain an improved broadcast ionospheric model for single-frequency receivers, is also introduced. Lastly, a proposed cycle-slip-resilient code error mitigation algorithm is introduced, to enable continuous code smoothing even in the presence of cycle slip occurrence.

Chapter 6.

Dual-Frequency Cycle Slip Correction and Observation Gap Impacts Mitigation

Firstly, this chapter presents the dual-frequency CSDC algorithm for detecting, determining and correcting cycle slips that may occur on phase observations from a dual-frequency GNSS receiver. Secondly, this chapter unveils procedures for generating a phase-only-derived ionospheric observable and dual-frequency code error mitigation. In most cases, the occurrence of an observation gap/discontinuity - a short duration outage of a satellite being observed by a receiver - creates two identified negative impacts: (i) it decreases positioning accuracy at a post-gap epoch and at few epochs following a post-gap epoch, as observation errors are not mitigated, and (ii) it introduces a convergence time that is required to resolve post-gap dual-frequency ambiguities and/or achieve significant code smoothing. Thus, this chapter finally introduces a novel technique for mitigating these impacts of observation gaps, with a view to enhancing positioning and achieving more robust positioning even in challenged environments.

6.1. The Dual-Frequency Observables

The notation set out in Section 5.1 is also adopted here, except that for the dual-frequency processing, when an observation gap occurs for satellite s, the time series observation lengths, l^s and L^s, are only reset to 1 if the gap duration, l^s_{gap}, occurring for s exceeds the set gap duration limit, L_{gap}. It is only when $l^s_{gap} > L_{gap}$ that the number of observations from s is reset to 1, i.e. $l^s = L^s = 1$, which thereby results in treating s as a new entrant satellite without recourse to its previous observation records.

Also, for dual-frequency bands, $i = 1, 2$ for the L1 and L2 bands of GPS, are used here as the representative dual-frequency bands of a GNSS. These bands correspond to the wavelengths $\lambda_1 = 19.03cm$ and $\lambda_2 = 24.42cm$ respectively. The dual-frequency phase and code observables are thus the corresponding observables for $i = 1, 2$. As such, ψ^s_1 and ψ^s_2 denote the raw phase observations observed on the L1 and L2 bands respectively; the L1 and L2 cycle-slip-free phase observables denoted as $\overline{\psi^s_1}$ and $\overline{\psi^s_2}$ respectively; the L1 and L2 bands raw code observations denoted as P^s_1 and P^s_2 respectively; and the L1 and L2 bands error-mitigated code observables denoted as $\overline{P^s_1}$ and $\overline{P^s_2}$ respectively. Similar to Equations (5.1) and (5.2) given for single-frequency receiver, the sequences of the l^s-length undifferenced time series dual-frequency observables used for ATD are obtained as:

$$\psi^s_{TS,1} = \left[\overline{\psi^s_1}(L^s - l^s + 1 : L^s - 1),\ \psi^s_1(L^s)\right] \tag{6.1}$$

$$\psi^s_{TS,2} = \left[\overline{\psi^s_2}(L^s - l^s + 1 : L^s - 1),\ \psi^s_2(L^s)\right] \tag{6.2}$$

$$P^s_{TS,1} = [P^s_1(L^s - l^s + 1 : L^s)] \tag{6.3}$$

$$P^s_{TS,2} = [P^s_2(L^s - l^s + 1 : L^s)] \tag{6.4}$$

Continuous observation of satellites throughout the period they are within the view elevation angle of a receiver may not be practical as satellite outages do occur - a common occurrence in urban canyons. Practically, occurrence of an observation gap or observation discontinuity, which is a short duration outage of a satellite being observed by a GNSS receiver, is not an uncommon phenomenon. When a receiver

re-locks to a gapped satellite at a post-gap epoch, the technique for mitigating the impact of the observation gap - presented in later sections of this chapter - utilises the observations prior to the observation gap and the observations at the post-gap epoch. Therefore, to help distinguish between continuously observed observations, the post-gap-adjusted phase and code observables for a gap satellite s are denoted as $\hat{\psi}_i^s$ and $\hat{P}_i^s$ respectively. .

6.2. Dual-Frequency Phase and Code ADSs

Following the procedure set out in Section 5.1, the dual-frequency phase and code ADSs for a given satellite s are given thus:

$$\Delta^{d_s}\overline{\psi_1^s} \simeq c\triangle^{d_s}\delta t^r + \lambda_1\triangle N_1^s + \triangle^{d_s}e_{\psi,1}^s \tag{6.5}$$

$$\Delta^{d_s}\overline{\psi_2^s} \simeq c\triangle^{d_s}\delta t^r + \lambda_2\triangle N_2^s + \triangle^{d_s}e_{\psi,2}^s \tag{6.6}$$

$$\Delta^{d_s}P_1^s \simeq c\triangle^{d_s}\delta t^r + \triangle^{d_s}e_{P,1}^s \tag{6.7}$$

$$\Delta^{d_s}P_2^s \simeq c\triangle^{d_s}\delta t^r + \triangle^{d_s}e_{P,2}^s \tag{6.8}$$

It is re-emphasized here that Equation (6.5) through (6.8) assume the typical scenario where the receiver clock jump/reset/drifts affects the dual-frequency code and phase observations from all observed satellites in same way and at the same receiver observation epoch, and as such it suffice to replace the common $c\triangle^{d_s}\delta t^r$ with ε_c - the receiver clock high-order variation - as previously done for single-frequency ADSs. For clarity and illustrative purposes, Figure 6.1 shows plots of the phase ADSs obtained for two observed GPS satellites (PRN 2 and PRN 7), simultaneously observed during the first 30 observation epochs by a static MBAR receiver. These first 30 observations from both satellites had no cycle slips. We can observe the high correlation amongst the phase ADSs obtained for the satellites. Defining κ_b^{sat} as the correlation coefficient between two phase ADSs obtained from the band(s) in the set b and for the PRN(s) in the set sat, the correlation coefficients obtained for any two ADSs associated with PRN2 and PRN7 are $\kappa_{L1,L1}^{2,7} = 0.98467$, $\kappa_{L1,L2}^{2,7} = 0.98172$, $\kappa_{L2,L2}^{2,7} = 0.98175$ and $\kappa_{L2,L1}^{2,7} = 0.98463$; and for same satellite, $\kappa_{L1,L2}^{2} = 0.99996$ and

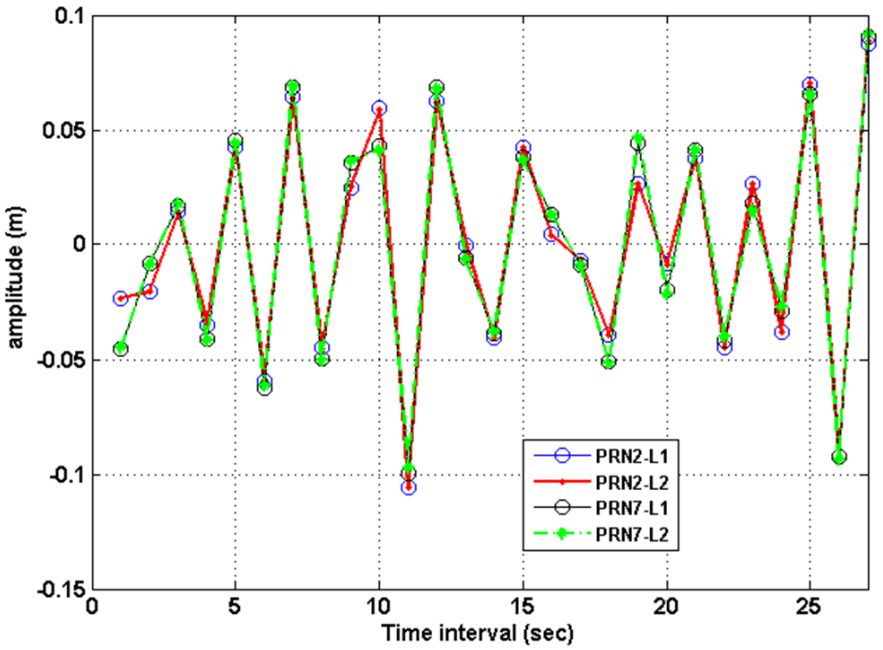

Figure 6.1.: Dual-Frequency phase ADSs obtained for two PRNs observed by a static MBAR receiver

$\kappa^{7}_{L1,L2} = 0.99966$, as obtained from the ADSs plotted in Figure 6.1. The small differences (within a few millimetres) in the amplitudes can be traceable to the various differenced error levels -$\triangle^{d_s} e^{s}_{\psi,i}$ - in the different phase ADSs, whilst the high correlation (observed in the correlation coefficients) is presumed largely due to the common receiver clock high-order variation within the considered time series interval. From the lots of tests done, this high-level correlation was always observed amongst satellites' dual-frequency phase ADSs when the W_L-length time series phase observations of the satellites indicate no cycle slip occurrences.

Between the L1 and L2 bands phase observations, the L1 band $\overline{\psi^{s}_{1}}$ observable is theoretically considered as the observable with the least level of error, and as such, its time series observable is used in an ATD process to determine a satellite's adaptive-order, d_s. This L1-phase derived d_s is consequently used as the order of differencing in generating the L2 phase ADS from the ATD of the L2 phase observables, and the ADSs of L1 and L2 code observations if necessary. That is, once ATD has been done with the l^s-length time series $\psi^{s}_{TS,1}$ to determine $\Delta^{d_s}\overline{\psi^{s}_{1}}$ and d_s, then $\psi^{s}_{TS,2}$, and $P^{s}_{TS,1}$ and $P^{s}_{TS,2}$ if necessary, are then successively differenced to the d^{th}_{s}-order to

obtain their corresponding ADSs denoted as $\Delta^{d_s}\overline{\psi_2^s}$, $\Delta^{d_s}P_1^s$ and $\Delta^{d_s}P_2^s$ respectively.

6.3. Dual-Frequency Phase-Only Cycle Slip Detection

The CSDC algorithm process block diagram given in Figure 5.1 is applicable to the dual-frequency cycle slip detection and correction algorithm presented here. The detection and correction algorithms are different from single-frequency CSDC algorithm, and the dual-frequency CSDC algorithm is designed to involve the dual-frequency phase observations of a given satellite. In other words, the generated L1 and L2 phase ADSs are the only required inputs for detecting the occurrence of cycle slip(s) on either one or both of ψ_1^s and ψ_2^s observed from satellite s. Dual-frequency phase-only cycle slip detection is not affected by the level of error associated with detection algorithms that are based on linear combinations (LC) of the phase observables and, code and phase observables (e.g. Blewitt (1990); Kim & Langley (2001); Liu (2011)). Though a dual-frequency phase-only detection based on a phase-only geometry-free LC observable is presumed more reliably accurate, it could be hampered by high ionospheric variations, plus the fact that such a LC is also unable to detect certain cycle slips pairs that can result in a difference or combination magnitude $\lambda\triangle N = \lambda_1\triangle N_1^s - \lambda_2\triangle N_2^s = 0$, or a difference magnitude lower than the set threshold for a given detection algorithm. A cycle slip pair which can result in a combination/difference magnitude value less than 5.38cm - the difference magnitude in unit of length for $\triangle N_1 = 1$ and $\triangle N_2 = 1$ cycle slip pair - is regarded as a *special slip pair* in this thesis. Figure 6.2 shows the values of all the possible dual-frequency cycle slip pairs from within 1 to 100cycles that can result in difference magnitudes less than 5.38cm. A special slip pair of $\triangle N_1$ and $\triangle N_2$ are indicated by an asterisk, and the corresponding value of the difference magnitude, $\lambda\triangle N = N_1^s\lambda_1 - N_2^s\lambda_2$, is indicated by the blue dot vertically aligned with the asterisk. It can been seen from the figure that different values of combination/difference magnitude exist for different cycle slips pairs. For instance $\lambda\triangle N$ is 0cm for $\triangle N_1 = 77$ and $\triangle N_2 = 60$; 0.38cm for $\triangle N_1 = 9$ and $\triangle N_2 = 7$; 2.54cm for $\triangle N_1 = 5$ and $\triangle N_2 = 4$; 2.85cm for

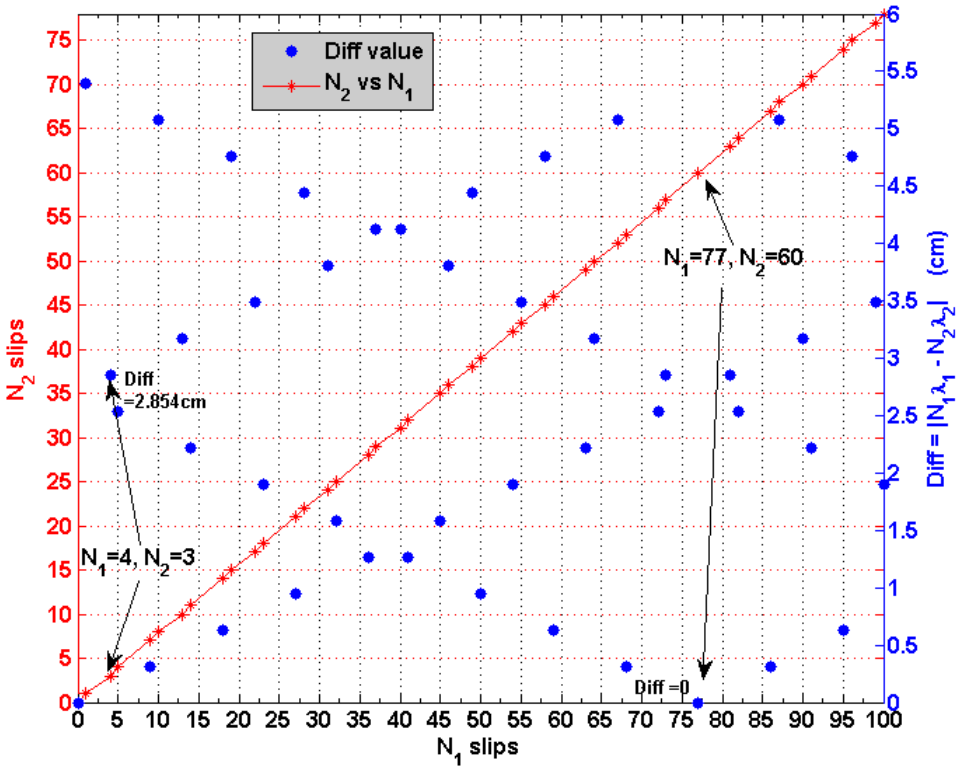

Figure 6.2.: Plots of cycle slip values between 1 to 100 cycles and their combination results, assuming zero ionospheric variation.

$\triangle N_1 = 4$ and $\triangle N_2 = 3$, and so on. The difference magnitude, $\lambda\triangle N$, of a special slip pair is close to the theoretical error level on a raw phase observation, making the detection of a special slip pair difficult, especially in the presence of significant phase errors. Though only positive pairs are shown in Figure 6.2, it is worth mentioning that the same difference magnitudes will result if the special slip pairs were negative cycle slip values. The $\triangle N_1 = \pm 4$ and $\triangle N_2 = \pm 3$ cycle slip pair is the first of the special slip pairs whose absolute difference magnitude of 2.85cm is less than 5.38cm as can be seen in Figure 6.2. Probably because the probability of occurrence of a special slip pair is considered low, some existing phase-only detection techniques such as presented in Xiaohong & Xingxing (2011), do not consider the special slip pair occurrence, and as such have no proffered solution for their occurrence. A more useful phase-only cycle slip detection should include detection of all possible cycle slip pairs - including the special slip pairs - with little or no ionospheric variation and receiver clock impediments. The new phase-only cycle slip detection that is

presented here seeks to achieve this goal.

6.3.1. The New Phase-Only Cycle Slip Detection

The new dual-frequency cycle slip detection algorithm applies set thresholds based on the anticipated adaptively-differenced phase error level, $\triangle^{d_s} e^s_{\psi,i}$; and uses the error-bound-adjusted for $\triangle N_1 = 4$ and $\triangle N_2 = 3$ and its difference magnitude for dual-frequency cycle slip detection. The error-bound-adjusted values $\triangle N_1 = 4$ and $\triangle N_2 = 3$ pair is used as the detection threshold because the $\triangle N_1 = 4$ and $\triangle N_2 = 3$ pair is the first pair with the least cycle slip values from among the special slip pairs. To determine the error thresholds, it is considered that the maximum theoretical phase multipath error is $\frac{\lambda_1}{4} \simeq 4.8$cm and $\frac{\lambda_2}{4} \simeq 6.1$cm on the L1 and L2 bands respectively (Rost & Wanninger, 2009); while an additional 1-sigma phase noise level of 5mm on each band's phase observation, as in Liu (2011), can be assumed, which results in a 3σ noise level of 1.5cm. Consequently, the maximum differenced phase error levels achieved from differencing the combined multipath error and noise on consecutive epochs of phase observations, could be doubled; reaching $2(0.048 + 0.015) = 0.126$m (0.66cycles) and $2(0.061 + 0.015) = 0.152$m (0.62cycles) for the L1 and L2 bands phase ADSs respectively. As such, the absolute values of $\triangle^{d_s} e^s_{\psi,1} = 0.126$m and $\triangle^{d_s} e^s_{\psi,2} = 0.152$m are set as the possible maximum values of error on the time series L1 and L2 phase ADSs generated for a given s as given by Equations (6.5) and Equation (6.6) respectively.

The dual-frequency CSDC algorithm is a single-satellite CSDC algorithm which involves detection of cycle slip on a given satellite's phase observation using only the satellite's l^s-length $\psi^s_{TS,i}$ observables. From the generated $\Delta^{d_s}\psi^s_i$ sequence, the two corresponding values for $i = 1, 2$ at a current epoch t, which correspond to the values $\Delta^{d_s}\psi^s_i(l^s - d_s)$, are used to determine the occurrence of cycle slips at the current epoch. Cycle slip(s) is/are detected or inferred to have occurred if either of two tests, test 1 given by Equation (6.9), or test 2 given by (6.10), is satisfied.

$$\left|\Delta^{d_s}\psi_1^s(l^s-d_s)-\Delta^{d_s}\psi_2^s(l^s-d_s)\right| \geq 0.0285 \tag{6.9}$$

$$\left|\Delta^{d_s}\psi_1^s(l^s-d_s)-\Delta^{d_s}\psi_2^s(l^s-d_s)\right| < 0.0285\,; \quad if \quad \left|\Delta^{d_s}\psi_1^s(l^s-d_s)\right| \geq 3.34\lambda_1 \;\&\; \left|\Delta^{d_s}\psi_2^s(l^s-d_s)\right| \geq 2.38\lambda_2 \tag{6.10}$$

The used difference magnitude threshold value of $0.0285m$ (equivalent to 0.178TECu) in the detection is a large deviation from the nominal ionospheric variation value usually of a few millimetres per second, and as such the test equations are also expected to sustain accurate cycle slip detection under 'mildly' disturbed ionospheric conditions. Liu (2011) used a conjectured threshold value of 0.15TECu and reported good cycle slip detection under high ionospheric activities, and by deduction, a 0.178TECu threshold is expected to perform even better under similar ionospheric conditions. A destructive combination of the L1 and L2 adaptively-differenced phase error thresholds (derived above) with the $\triangle N_1 = 4$ and $\triangle N_2 = 3$ cycle slips respectively, would result to a minimum of $4-0.66 = 3.34$ cycles and $3-0.62 = 2.38$ cycles respectively; whilst a constructive combination of same would result to a maximum of $4+0.66 = 4.66$ cycles and $3+0.62 = 3.62$ cycles respectively. That explains why the error-bound-adjusted values of 3.34 and 2.38 are used for the cycle slip detection with test 2 - Equation (6.10). This error-bound-adjusted values are to ensure that the level of the adaptively-differenced phase errors would not result to a false cycle slip detection, but to allow the detection of special slip pairs that include the $\triangle N_1 = 4$ and $\triangle N_2 = 3$ pair, even under a destructive phase error combination with cycle slip values. A cycle slip is presumed not to exist if neither of the two tests is satisfied. It should be noted that (6.9) for test 1 is equivalent to the current epoch's value of an adaptively differenced time series of a geometry-free phase observable with negligible ionospheric variation.

The detection with test 2 is primarily met to detect special slip pairs, and can be impaired by the receiver clock high-order variation. As such, receiver clock jumps are also detected as given in by Equations (5.6) and (5.7) in Section 5.2.1, for a reliable dual-frequency CSDC process. The detection with both test 1 and test 2

seek to enable detection of all cycle slip pairs using only the dual-frequency phase observables from a single satellite.

6.3.2. Estimating Dual-Frequency Cycle Slips Float Values and Receiver Clock High-Order Variation

As already discussed in Section 5.2.2, the least squares algorithm is used in the relevant part of this section, recalling that the derived observables from the raw code and phase observations are assumed corrupted by observation errors that are uncorrelated and conform to a normal distribution.

Once satellite s is detected to have cycle slip the CSDC algorithm proceeds to estimate the cycle slip float value. The set out procedures for the estimation of dual-frequency cycle slip float values and the common receiver clock high-order variation different from the set out procedures for single-frequency estimation presented in Section 5.2.2, plus it includes the involvement of the L2 band phase ADS - $\Delta^{d_s}\overline{\psi_2^s}$. From Equations (6.5) and (6.6), and using the same notation for the terms already defined and used in Section 5.2.2, two sequences,

$$\begin{aligned} A_\psi^s &= \Delta^{d_s}\overline{\psi_1^s} - \Delta^{d_s}\overline{\psi_2^s} \\ &= \lambda_1 \triangle N_1^s - \lambda_2 \triangle N_2^s + \Delta^{d_s} e_{\lambda_{1,2}} \qquad (6.11) \\ B_\psi^s &= \frac{\Delta^{d_s}\overline{\psi_1^s}}{\lambda_1} - \frac{\Delta^{d_s}\overline{\psi_2^s}}{\lambda_2} \\ &= \triangle N_1^s - \triangle N_2^s - \frac{\varepsilon_c}{\lambda_{WL}} + \Delta^{d_s} e_{\lambda_{WL}} \\ \lambda_{WL} B_\psi^s &= \lambda_{WL}(\triangle N_1^s - \triangle N_2^s) - \varepsilon_c + \lambda_{WL}\Delta^{d_s} e_{\lambda_{WL}} \qquad (6.12) \end{aligned}$$

where $\Delta^{d_s} e_{\lambda_{1,2}} = \Delta^{d_s} e_{\psi,1} - \Delta^{d_s} e_{\psi,2}$; $\Delta^{d_s} e_{\lambda_{WL}} = \frac{\Delta^{d_s} e_{\psi,1}}{\lambda_1} - \frac{\Delta^{d_s} e_{\psi,2}}{\lambda_2}$; $\frac{1}{\lambda_{WL}} = \frac{1}{\lambda_1} - \frac{1}{\lambda_2}$; and $\varepsilon_c = c\triangle^{d_s}\delta t^r$, can be defined. Though A_ψ^s and $\lambda_{WL} B_\psi^s$ are time series linear combinations of the two bands' phase ADSs, they are synonymous to the ADSs obtainable via ATD of the satellite's geometry-free phase and widelane phase observables respectively, and as such, they are referred to as the phase-geometry-free ADS and the phase-widelane ADS respectively. We note that $\lambda_{WL} \simeq 0.86$m, which is a known widelane wavelength; and because of the high positive corre-

lation between phase ADSs (such as seen from Figure 6.1 and the accompanied correlation coefficients), $\Delta^{d_s} e_{\lambda_{1,2}} \ll \triangle^{d_s} e^s_{\psi,1}$ in magnitude and it is negligibly small compared to the combination magnitude $\lambda \triangle N = \lambda_1 \triangle N^s_1 - \lambda_2 \triangle N^s_2$ in (6.11). Also, based on the set error thresholds, the adaptively-differenced phase-widelane error, $\lambda_{WL} \Delta^{d_s} e_{\lambda_{WL}} < \lambda_{WL} \sqrt{\left(\frac{0.126}{\lambda_1}\right)^2 + \left(\frac{0.152}{\lambda_2}\right)^2} \approx 0.78$m, may be significantly less than 0.78m in (6.12), since $\triangle^{d_s} e^s_{\psi,1}$ and $\triangle^{d_s} e^s_{\psi,2}$ are usually positively and highly correlated, as indicated in Section 6.2. However, as in Equation (6.12), an error range of 0.78m on $\lambda_{WL} B^s_\psi$ is capable of introducing up to 4 or 3 cycles error on the estimated L1 or L2 band's cycle slip values, respectively. The 1-sigma values of A^s_ψ and $\lambda_{WL} B^s_\psi$ are respectively obtained as $\sigma^s_{A_\psi}$ and $\sigma^s_{B_\psi}$, being the standard deviation values of A^s_ψ and $\lambda_{WL} B^s_\psi$ sequences respectively. The computation of σ^s excludes the last value of the corresponding sequence. For a given s, the last value of the A^s_ψ sequence and the last value of the $\lambda_{WL} B^s_\psi$ sequence, given as

$$a^s_\psi = A^s_\psi (l^s - d_s) \tag{6.13}$$

$$b^s_\psi = \lambda_{WL} B^s_\psi (l^s - d_s) \tag{6.14}$$

correspond respectively to the last values of the phase-geometry-free and phase-widelane ADSs at the current receiver observation epoch t, which are required for the estimation of a current epoch's pair of cycle slips float values on s, and $\varepsilon_c(t)$. The errors associated with a^s_ψ and b^s_ψ are thus $e^s_{a,\psi} = \Delta^{d_s} e_{\lambda_{1,2}} (l^s - d_s)$ and $e^s_{b,\psi} = \Delta^{d_s} e_{\lambda_{1,2}} (l^s - d_s)$ respectively. The associated weights are computed as $w^s_{A_\psi} = \left(1/\sigma^s_{A_\psi}\right)^2$ and $w^s_{B_\psi} = \left(1/\sigma^s_{B_\psi}\right)^2$.

Subsequently, the procedure for the dual-frequency estimation of cycle slip float values and $\varepsilon_c(t)$, at a current t epoch, is set out as as follows, recalling that n is the number of satellites with $l^s \geq 10$, at a current epoch.

(a) **The condition when cycle slips are not detected on all n satellites**. Under this condition, the cycle slip value for all n satellites is zero, but we estimate the common receiver clock high-order variation, $\varepsilon_c(t)$, as the weighted average of all b^s_ψ where $(s = 1, 2, .., n)$ since ε_c is only found in the phase-widelane ADS sequence

-$\lambda_{WL}B^s_\psi$. Thus,

$$\varepsilon_c(t) = \frac{\sum_{s=1}^{n} w^s_{B_\psi} b^s_\psi}{\sum_{s=1}^{n} w^s_{B_\psi}} \tag{6.15}$$

(b) **The condition when cycle slips are detected on at least one but not all n satellites**. Under this condition, if j of the n satellites indicated cycle slips and the rest $n-j$ satellites indicated no cycle slips, the j pairs of a^k_ψ and b^k_ψ observables ($k = 1, 2, ..., j$) from the j cycle-slipped satellites; and the $n-j$ number of b^J_ψ observables ($J = j+1, j+2, ..., n$) from the $n-j$ non-cycle-slipped satellites, are used for the estimation of the cycle slip float values and $\varepsilon_c(t)$. Following from Equations (6.11), (6.12), (6.13) and (6.14), the resulting matrix equation is given as

$$\begin{bmatrix} a^1_\psi \\ b^1_\psi \\ \vdots \\ a^j_\psi \\ b^j_\psi \\ b^{j+1}_\psi \\ b^{j+2}_\psi \\ \vdots \\ b^n_\psi \end{bmatrix} = \begin{bmatrix} \lambda_1 & -\lambda_2 & \cdots & 0 & 0 & 0 \\ \lambda_{WL} & -\lambda_{WL} & \cdots & 0 & 0 & 1 \\ \vdots & \vdots & \ddots & \vdots & \vdots & \vdots \\ 0 & 0 & \cdots & \lambda_1 & -\lambda_2 & 0 \\ 0 & 0 & \cdots & \lambda_{WL} & -\lambda_{WL} & 1 \\ 0 & 0 & \cdots & 0 & 0 & 1 \\ 0 & 0 & \cdots & 0 & 0 & 1 \\ \vdots & \vdots & \cdots & \vdots & \vdots & \vdots \\ 0 & 0 & \cdots & 0 & 0 & 1 \end{bmatrix} \begin{bmatrix} \triangle N^1_1 \\ \triangle N^1_2 \\ \vdots \\ \triangle N^j_1 \\ \triangle N^j_2 \\ \varepsilon_c(t) \end{bmatrix} + \begin{bmatrix} e^1_{a,\psi} \\ e^1_{b,\psi} \\ \vdots \\ e^j_{a,\psi} \\ e^j_{b,\psi} \\ e^{j+1}_{b,\psi} \\ e^{j+1}_{b,\psi} \\ \vdots \\ e^n_{b,\psi} \end{bmatrix} \tag{6.16}$$

$$\triangle Y \quad = \quad H \quad\quad \triangle X \quad + \quad \triangle e_\psi$$

where H is the $(j+n)\times(2j+1)$ design matrix, $\triangle e_\psi$ is the $(j+n)\times 1$ error vector containing the corresponding error values in each of the $(j+n)$ observables in $\triangle Y$, which are assumed uncorrelated. With a corresponding $(j+n)\times(j+n)$ diagonal weight matrix defined as

$$W = \begin{bmatrix} w^1_{A_\psi} & 0 & \cdots & 0 & 0 & 0 & 0 & 0 & 0 \\ 0 & w^1_{B_\psi} & \cdots & 0 & 0 & 0 & 0 & 0 & 0 \\ \vdots & \cdots & \ddots & \cdots & \vdots & \vdots & \vdots & \vdots & \vdots \\ 0 & 0 & \cdots & w^j_{A_\psi} & 0 & 0 & 0 & 0 & 0 \\ 0 & 0 & \cdots & 0 & w^j_{B_\psi} & 0 & 0 & 0 & 0 \\ 0 & 0 & \cdots & 0 & 0 & w^{j+1}_{B_\psi} & 0 & 0 & 0 \\ 0 & 0 & \cdots & 0 & 0 & 0 & w^{j+2}_{B_\psi} & 0 & 0 \\ \vdots & \vdots & \cdots & \vdots & \vdots & \vdots & \vdots & \ddots & \vdots \\ 0 & 0 & \cdots & 0 & 0 & 0 & 0 & 0 & w^n_{B_\psi} \end{bmatrix} \tag{6.17}$$

a weighted least square is used to solve for $\triangle X = \left[\triangle N_i^k\,, \varepsilon_c(t)\right]^T$, being the $(2j+1)\times 1$ vector containing the $2j$ unknown cycle slips float values and unknown $\varepsilon_c(t)$. That is (Cross, 1983)

$$\triangle X = \left[H^T W H\right]^{-1} H^T W \triangle Y \tag{6.18}$$

contains the estimated cycle slips float values for all j cycle-slipped satellites, and $\varepsilon_c(t)$, for the current epoch. A diagonal weight matrix, W, is used and the common part amongst the observables in $\triangle Y$ are assumed absorbed by the last column of '1's in the H design matrix. The uncertainties in the estimated cycle slips float values and $\varepsilon_c(t)$ can be obtained from the variance-covariance matrix of the estimated $\triangle X$, which is given as (Morujao & Mendes, 2008)

$$Q_{estm} = \left[H^T W H\right]^{-1} \tag{6.19}$$

The uncertainty on an estimated cycle slip float value for each cycle-slipped satellite can be determined. The square root of each of the diagonal elements of Q_{estm} estimates the level of uncertainty (standard error) on a corresponding estimated parameter in $\triangle X$. In this way, it is possible to generate real-time uncertainty values on estimated cycle slips float values and $\varepsilon_c(t)$. Figure 6.3 shows the estimated uncertainties on $\triangle N_1$ and $\triangle N_2$ for two satellites (PRN4 and PRN7) when cycle slips were simulated for different satellites at different test epochs as described in Section 4.5, for an observation interval of 1 hour (3600 epochs). It can be observed that of the 124 pairs of tested cycle slip pairs for PRN4, the standard errors on $\triangle N_1$ and $\triangle N_2$ are highly positively correlated but higher on $\triangle N_1$ than on $\triangle N_2$,

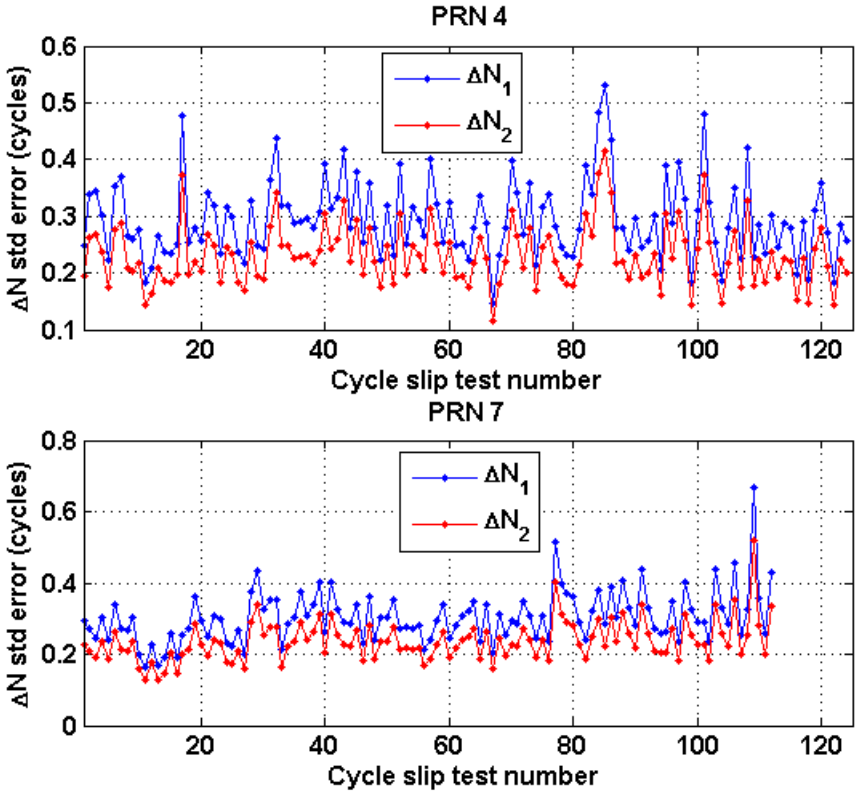

Figure 6.3.: Plots showing uncertainty values obtained for PRN4 and PR7 observed by MBAR (day 170 of year 2009). Cycle slips simulated for at least one but not simultaneously for all satellites, and at different test epochs.

over the test interval. The same interpretation can be drawn from the 112 pairs of simulated cycle slips for PRN7. The uncertainties could exceed 0.5 cycles even though this condition does not include any adaptively-differenced code observable in the estimation, suggesting that a simple rounding-up of estimated float values cannot be appropriate for fixing the cycle slips float values to their integer values. For this illustration, the estimated uncertainty levels for the common receiver high-order variation, ε_c, over the 3600 epochs, are given in the plot shown in Figure 6.4. The standard error can be observed to be under half a centimetre for this condition when cycle slips 'occur' at different epochs for different satellites.

(c) **The condition when all n satellites indicate cycle slips**. The procedure, as it could be for the single-frequency operation, is to include two code observables, $\alpha_P = \Delta^{d_\alpha} P_1^\alpha (l^\alpha - d_\alpha)$ and $\beta_P = \Delta^{d_\beta} P_1^\beta (l^\beta - d_\beta)$, which are the two last values from the two code ADSs having the least standard deviations, $\sigma_{d_\alpha}^\alpha$ and $\sigma_{d_\beta}^\beta$, from among

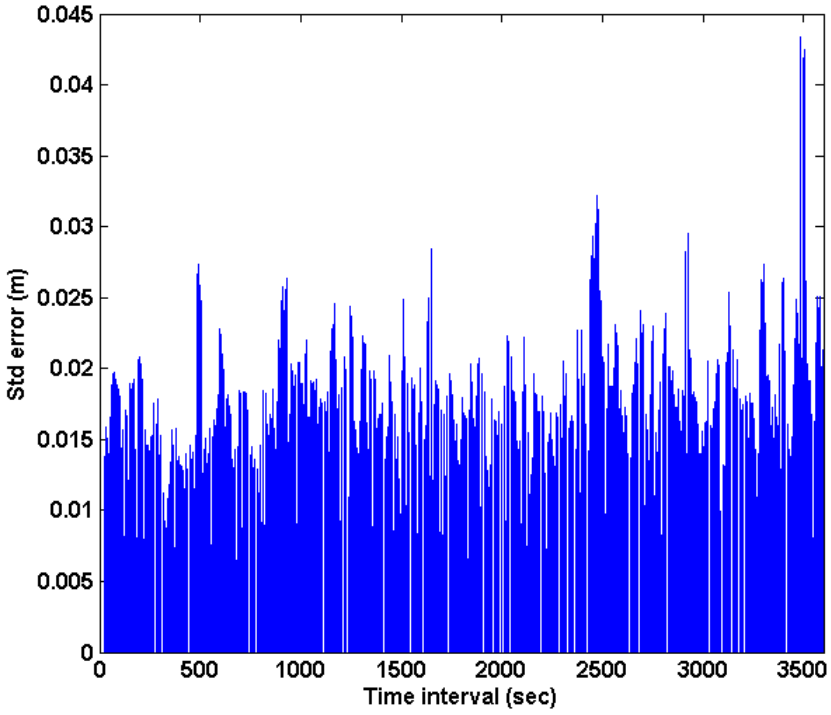

Figure 6.4.: Plots of the uncertainty values estimated for ε_c. Cycle slips simulated for at least one but not all satellites, at different epochs.

the set of all code ADSs, $\Delta^{d_s} P_i^s$ where $\{\alpha, \beta\} \in \{s = 1, 2, ..., n\}$, knowing that α and β could be the same satellite, at a current epoch. The corresponding errors on α_P and β_P are denoted e_P^α and e_P^β, while the weighting values are $w_{P,\alpha} = \left(1/\sigma_{d_\alpha}^\alpha\right)^2$ and $w_{P,\beta} = \left(1/\sigma_{d_\beta}^\beta\right)^2$ respectively. As a result, the matrix equation

$$\begin{bmatrix} a_\psi^1 \\ b_\psi^1 \\ \vdots \\ a_\psi^n \\ b_\psi^n \\ \alpha_P \\ \beta_P \end{bmatrix} = \begin{bmatrix} \lambda_1 & -\lambda_2 & \cdots & 0 & 0 & 0 \\ \lambda_{WL} & -\lambda_{WL} & \cdots & 0 & 0 & 1 \\ \vdots & \vdots & \ddots & \vdots & \vdots & \vdots \\ 0 & 0 & \cdots & \lambda_1 & -\lambda_2 & 0 \\ 0 & 0 & \cdots & \lambda_{WL} & -\lambda_{WL} & 1 \\ 0 & 0 & \cdots & 0 & 0 & 1 \\ 0 & 0 & \cdots & 0 & 0 & 1 \end{bmatrix} \begin{bmatrix} \triangle N_1^1 \\ \triangle N_2^1 \\ \vdots \\ \triangle N_1^n \\ \triangle N_2^n \\ \varepsilon_c(t) \end{bmatrix} + \begin{bmatrix} e_{a,\psi}^1 \\ e_{b,\psi}^1 \\ \vdots \\ e_{a,\psi}^n \\ e_{b,\psi}^n \\ e_P^\alpha \\ e_P^\beta \end{bmatrix} \quad (6.20)$$

$$\triangle Y \quad = \quad H \quad \triangle X \quad + \quad \triangle e_{\psi,P}$$

where H is a $(2n+2)\times(2n+1)$ design matrix, $\triangle e_{\psi,P}$ is a $(2n+2)\times 1$ error vector

containing the corresponding error values in each of the n observables in $\triangle Y$, which are assumed uncorrelated. With a corresponding $(2n+2)\times(2n+2)$ diagonal weight matrix defined as

$$W = \begin{bmatrix} w^1_{A_\psi} & 0 & \cdots & 0 & 0 & 0 & 0 \\ 0 & w^1_{B_\psi} & \cdots & 0 & 0 & 0 & 0 \\ \vdots & \cdots & \ddots & \cdots & \vdots & \vdots & \vdots \\ 0 & 0 & \cdots & w^n_{A_\psi} & 0 & 0 & 0 \\ 0 & 0 & \cdots & 0 & w^n_{B_\psi} & 0 & 0 \\ 0 & 0 & \cdots & 0 & 0 & w_{P,\alpha} & 0 \\ 0 & 0 & \cdots & 0 & 0 & 0 & w_{P,\beta} \end{bmatrix} \tag{6.21}$$

a weighted least squares solution for $\triangle X = \left[\triangle N^k_i\,, \varepsilon_c(t)\right]^T$, being the n $\times 1$ vector containing the $2n$ unknown cycle slips float values and the unknown $\varepsilon_c(t)$, is thus obtained as

$$\triangle X = \left[H^T W H\right]^{-1} H^T W \triangle Y \tag{6.22}$$

Again, a diagonal weight matrix is used and the common part amongst the observables in $\triangle Y$ are assumed absorbed by the last column of '1's in the H design matrix. The estimated $\varepsilon_c(t)$ absorbs the common error in all the observables in $\triangle Y$ plus the actual receiver clock high-order variation at the current epoch.

Again, we can determine the uncertainty on an estimated cycle slip float value, for each of the n cycle-slipped satellites, under this condition when code ADSs values are included in the estimation because all observed satellites at a given epoch indicate cycle slips. Obtaining Q_{estm} as given by Equation (6.19) and the square root of each of the diagonal elements of Q_{estm}, we can obtain the level of uncertainty (standard error) on the estimated parameters in $\triangle X$. Figure 6.5 shows the estimated uncertainties on $\triangle N_1$ and $\triangle N_2$ for the same two satellites (PRN4 and PRN7) when cycle slips were simulated for all satellites at same test epochs as described in Section 4.5, for an observation interval of 1 hour (3600 epochs). It should be recalled that since all n satellites indicate cycle slip at same test epochs two code ADSs values will be used at such test epochs for estimation of $\triangle X$. It can be observed that, of the 144 cycle slips pairs simulated for each of PRN4 and PRN7, the standard errors on $\triangle N_1$ and $\triangle N_2$ are highly positively correlated but still higher on a PRN's $\triangle N_1$ than on

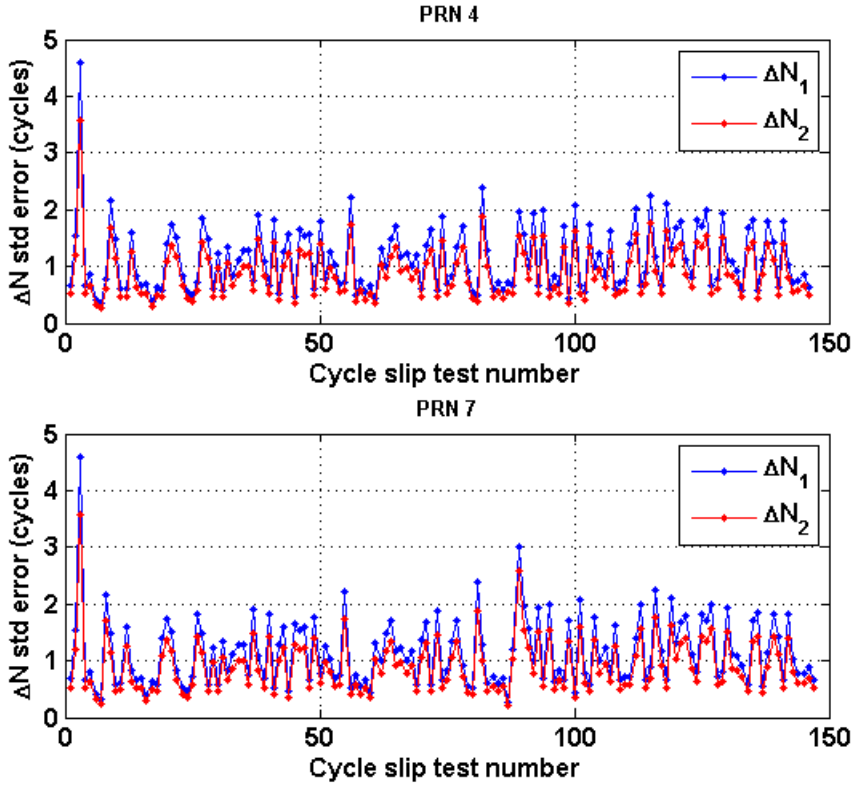

Figure 6.5.: Plots showing uncertainty values obtained for PRN4 and PR7 observed by MBAR (day 170 of year 2009). Cycle slips simulated simultaneously for all satellites, and at same test epochs.

$\triangle N_2$. Furthermore, the standard errors among all $\triangle N_i$ for all cycle-slipped satellites are also positively correlated, as can be observed for PRN 4 and PRN7. In contrast to the uncertainty levels obtained for condition (b) above (Figure 6.3), the uncertainty levels for $\triangle N_1$ and $\triangle N_2$ under this condition (c), as revealed in Figure 6.5, often exceed 1 cycle and could even exceed 3 cycles. For this illustrated condition, the estimated uncertainty levels for the common receiver high-order variation, ε_c, over the 3600 epochs, are given in the plot shown in Figure 6.6. The standard error can be observed up to tens of centimetres because of the involvement of two code ADSs values and possible correlation between the cycle slip values on satellites at a test epoch. We can insinuate from these results that the estimated cycle slips float values and $\varepsilon_c(t)$ when all satellites experience cycle slips would be less accurate, which can possibly flaw a cycle slip fixing process.

Under condition (c) when all n satellites indicate cycle slips, threshold values

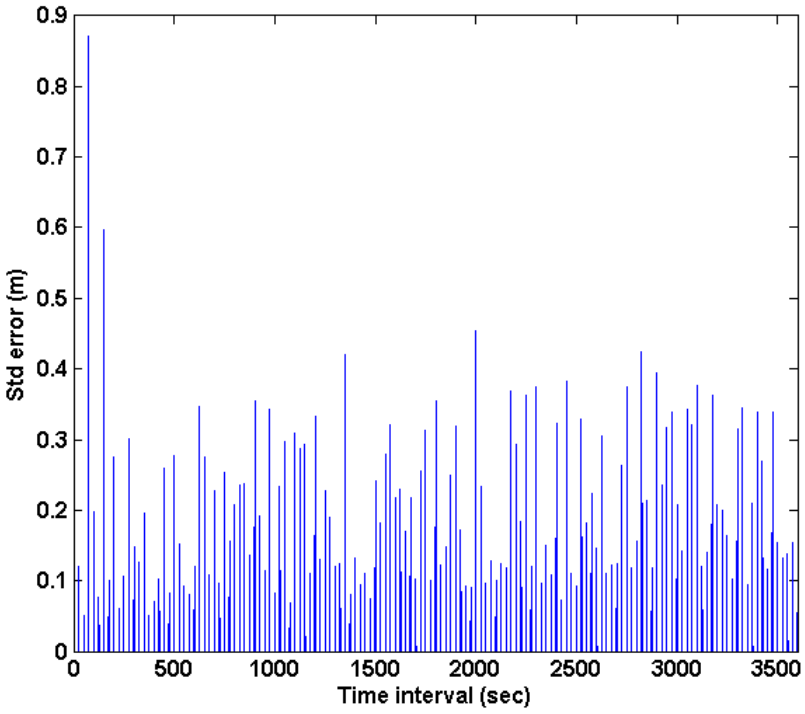

Figure 6.6.: Plots of the uncertainty values estimated for ε_c. Cycle slips simulated for all satellites, at same test epochs.

are set for making a decision, as in the single-frequency case, to enable nulling or acceptance of the cycle slips float values, mostly because of the possible adaptively-differenced error levels in a^s_ψ, b^s_ψ and in the two included code ADSs values. The cycle slips float values are nulled if Equations (6.23) and (6.24) below are satisfied simultaneously, otherwise the float values are accepted as true cycle slips float values for a given s.

$$\underset{s\in\{1,2,..,n\}}{max}(|\lambda_1 \triangle N^s_1 - \lambda_2 \triangle N^s_2|) \leq 0.0285 \tag{6.23}$$

$$\underset{s\in\{1,2,..,n\}}{max}(|\triangle N^s_1 - \triangle N^s_2|) < 5 \tag{6.24}$$

The reasons behind using these thresholds for nulling estimated cycle slips float values when all satellites indicate cycle slip at a given epoch are: (i) the occurrence of cycle slips on all satellites at same epoch whereby all the dual-frequency cycle slips pairs result in special slip pairs, is considered rear; and, (ii) the occurrence may be more likely due to a receiver clock drift/jump value that is common to all satellites

observations or due to the adaptively-differenced code errors from the two included code ADSs that could affect the estimated cycle slips float values - produce small cycle slip values of $\triangle N_1$ and $\triangle N_2$. The first few pairs of special slip combination pairs: $\triangle N_1 = \pm 4$ and $\triangle N_2 = \pm 3$; $\triangle N_1 = \pm 5$ and $\triangle N_2 = \pm 4$; $\triangle N_1 = \pm 9$ and $\triangle N_2 = \pm 7$; and $\triangle N_1 = \pm 14$ and $\triangle N_2 = \pm 11$, produce $|\triangle N_1^s - \triangle N_2^s| \leq 3$. However, because an estimated cycle slip pair result in a float value of $|\triangle N_1^s - \triangle N_2^s|$, the threshold <5 is used in (6.24). The set threshold of 0.0285m in (6.23) can be recognised as the value of the difference magnitude, $\lambda\triangle N$, for the $\triangle N_1 = 4$ and $\triangle N_2 = 3$ special slip pair; and by a least squares estimation, the effect of $\triangle e_{\psi,P}$ is likely to be almost equally impacted on $\triangle N_1^s$ and $\triangle N_2^s$ of a given s (see Figure 6.5), and as such, when truly there is no cycle slip, the $|\lambda_1\triangle N_1^s - \lambda_2\triangle N_2^s|$ value is likely to be smaller than 0.0285m.

As in the single-frequency case, when a clock jump or reset is not detected at a current epoch, the estimated $\varepsilon_c(t)$ is assumed to represent the high-order drift of the receiver clock at that epoch, which is common to all observed satellites. When a clock jump or reset is detected at a current epoch, the estimated current epoch $\varepsilon_c(t)$ value is taken as the clock jump value and denoted $\varepsilon_{c,jump}(t) = \varepsilon_c(t)$.

6.4. Dual-Frequency Cycle Slip Fixing, Validation and Correction

The whole CSDC algorithm for dual-frequency involves the already described dual-frequency detection procedure for $k \leq n$ cycle-slipped satellites; a procedure for determining/fixing the cycle slips float values to integers; and a process of validation of the fixed (integer) cycle slip values. Thereafter, the k pairs of phase observations from the k cycle-slipped satellites are corrected for such cycle slips. The dual-frequency cycle slip fixing process at a current epoch are based on the current epoch's estimated values of the difference magnitude difference, $\lambda\triangle N^s = \lambda_1\triangle N_1^s - \lambda_2\triangle N_2^s$, and the widelane phase cycle slip $\triangle N_{WL}^s = \triangle N_1^s - \triangle N_2^s$, for a given cycle-slipped satellite s. The real-time estimated uncertainty levels in $\lambda\triangle N^s$ and $\triangle N_{WL}^s$ are consequently considered.

Upon obtaining Q_{estm} as given by Equation (6.19), the variances of the estimated $\triangle N_1^s$ and $\triangle N_2^s$ float values, and the covariance between them can be extracted for any s where $s = 1, 2, .., k$. If we denote the variance of $\triangle N_1^s$ as $Q_{estm}(\triangle N_1^s)$, variance of $\triangle N_2^s$ as $Q_{estm}(\triangle N_2^s)$ and their covariance as $Q_{estm}(\triangle N_1^s, \triangle N_2^s)$ then we can estimate the variance of $\lambda\triangle N^s = \lambda_1\triangle N_1^s - \lambda_2\triangle N_2^s$, denoted $\left(\sigma^s_{\lambda\triangle N}\right)^2$, and the variance of $\triangle N^s_{WL} = \triangle N_1^s - \triangle N_2^s$, denoted $\left(\sigma^s_{WL}\right)^2$, respectively as:

$$\left(\sigma^s_{\lambda\triangle N}\right)^2 = \lambda_1^2 Q_{estm}(\triangle N_1^s) + \lambda_2^2 Q_{estm}(\triangle N_2^s) - 2\lambda_1\lambda_2 Q_{estm}(\triangle N_1^s, \triangle N_2^s) \quad (6.25)$$

$$\left(\sigma^s_{WL}\right)^2 = Q_{estm}(\triangle N_1^s) + Q_{estm}(\triangle N_2^s) - 2Q_{estm}(\triangle N_1^s, \triangle N_2^s) \quad (6.26)$$

The square root of $\left(\sigma^s_{\lambda\triangle N}\right)^2$ gives the standard error (uncertainty) in $\lambda\triangle N^s$ and the square root of $\left(\sigma^s_{WL}\right)^2$ gives the standard error (uncertainty) in $\triangle N^s_{WL}$.

An insight into the levels of uncertainty in $\lambda\triangle N^s$ and $\triangle N^s_{WL}$ can obtained for the condition (b) under Section 6.3.2 above - when at least one but not all observed satellites are affected by cycle slips at given epochs, and also the condition (c) above - when all satellites experience cycle slip at the same epochs. Figure 6.7 shows the different uncertainty levels for $\lambda\triangle N^s$ and $\triangle N^s_{WL}$ over 3600 epochs of observation, for different satellites (each uncertainty value is for any randomly selected satellite at a given test epoch), where cycle slips are simulated for all satellites at different test epochs separated by 25 epochs interval. In this case, no code ADS values are involved as all satellites do not experience cycle slip at a test epoch, as in condition (b) above. The uncertainty level on $\lambda\triangle N^s$ can be observed to be in the range of a few millimetres, while the uncertainty level for $\triangle N^s_{WL}$ can be observed to be less than 0.2 cycles. Figure 6.8 shows the different uncertainty levels for $\lambda\triangle N^s$ and $\triangle N^s_{WL}$ over the same 3600 epochs of observation, for different satellites (each uncertainty value is for any randomly selected satellite at a given test epoch), where cycle slips are simulated for all satellites at same test epochs separated by 25 epochs interval. The estimation of the float cycle slip values involved two code ADSs values as all satellites experience cycle slip at same test epochs, as in condition (c) above.

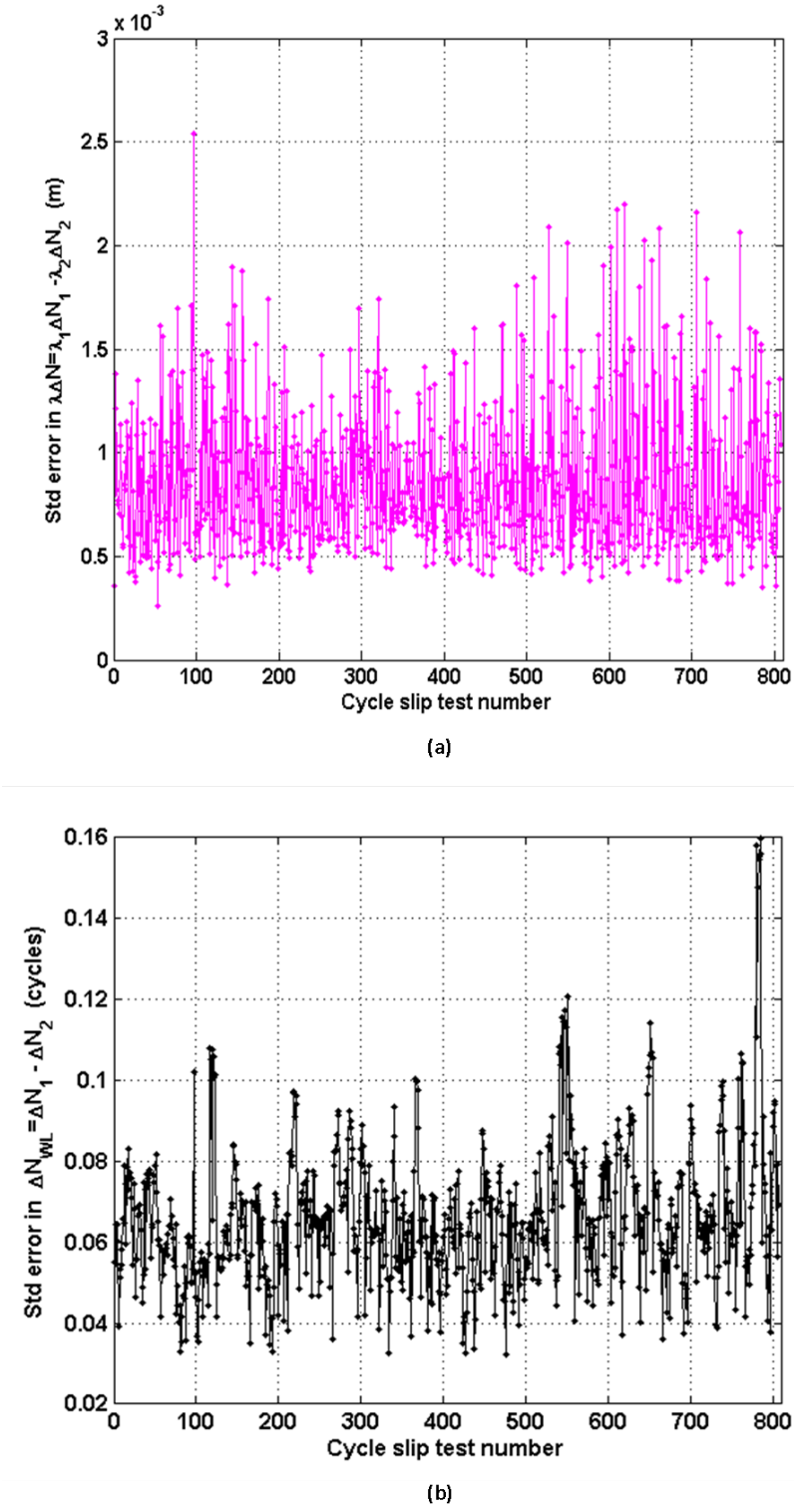

Figure 6.7.: Plots of uncertainty levels on (a) $\lambda \triangle N^s = \lambda_1 \triangle N_1^s - \lambda_2 \triangle N_2^s$ observable and (b) on $\triangle N_{WL}^s = \triangle N_1^s - \triangle N_2^s$ observable, obtained with estimated dual-frequency cycle slips float values, for different satellites observed by MBAR (day 170 of year 2009), with cycle slips simulated for all satellites at different test epochs.

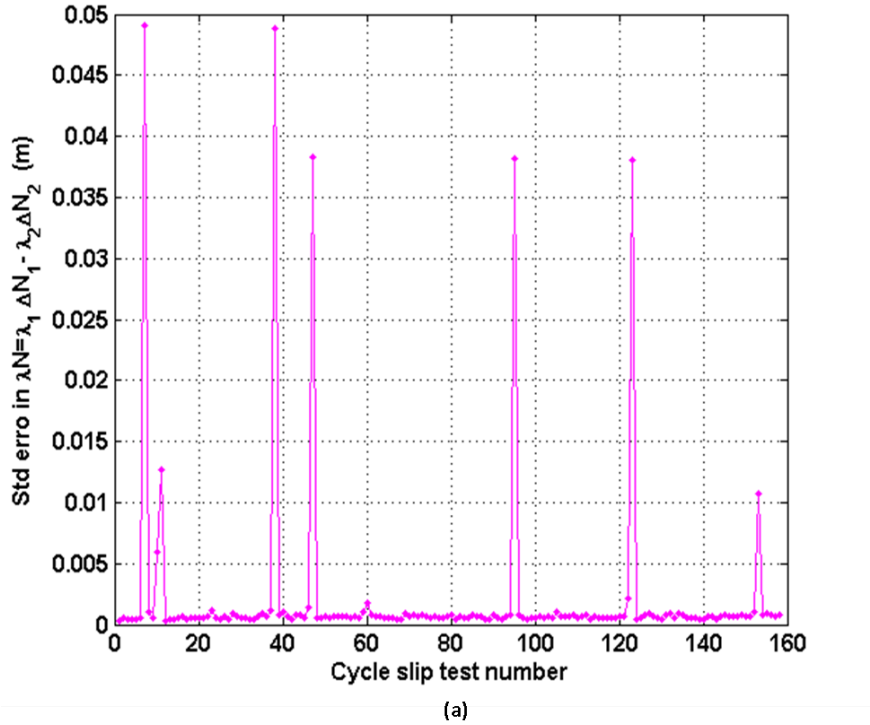

Figure 6.8.: Plots of uncertainty levels on (a) $\lambda\triangle N^s = \lambda_1\triangle N_1^s - \lambda_2\triangle N_2^s$ observables and (b) on $\triangle N_{WL}^s = \triangle N_1^s - \triangle N_2^s$ observables, obtained with estimated dual-frequency cycle slips float values, for different satellites observed by MBAR (day 170 of year 2009), with cycle slips simulated for different satellites at same test epochs.

The uncertainty on $\lambda\triangle N^s$ can be observed to be in the range of a few millimetres for most test epochs of simulated cycle slips but could reach up to about 5cm (possibly at test epochs when the code adaptively-differenced error levels were significantly high). The uncertainty level for $\triangle N^s_{WL}$ also increased compared to the values shown in Figure 6.7- varying within 0.1 cycle (8.6cm) to 0.4 cycle (34cm) at most simulated cycle slip test epochs, but reached more than 1 cycle (86cm) at one test epoch. When such large uncertainty levels are associated with estimated $\lambda\triangle N^s$ and $\triangle N^s_{WL}$, fixing the cycle slips float values to the correct integers becomes more doubtful - envisaged whenever all satellites indicate cycle slips at a given epoch.

For the real-time cycle slip determination procedure presented next, the $3\sigma^s_{\lambda\triangle N}$ value and the $3\sigma^s_{WL}$ value are used for setting the thresholds values in the cycle slip fixing procedure.

6.4.1. Dual-Frequency Cycle Slip Determination

As shown in Section 6.3.2, the estimated error range of 0.78m on $\lambda_{WL}B^s_\psi$ alone is capable of causing up to 4 cycles and/or 3 cycles of error on the estimated cycle slips float values on the L1 and L2 bands phase observables respectively. This can also be insinuated from the level of uncertainty that can be associated with an estimated $\triangle N^s_1$ or $\triangle N^s_2$ float value, as can be observed from Figure 6.5. As such, the dual-frequency cycle slip fixing process is initiated by first generating, a set of cycle slip integer values that are within $r_{slip} = \pm 4$ cycles around and including the two boundary integers for the estimated float value $\triangle N^s_i$, for each of the $k \leq n$ cycle-slipped satellites. The two boundary integers here refer to the integer just lower than the $\triangle N^s_i$ float value and the integer just greater than the $\triangle N^s_i$ float value. For instance for $\triangle N^s_1 = 3.06$, the boundary integers are 3 and 4. While a wider than ± 4 cycles range can be used, the ± 4 cycles range is chosen to minimize computation, and also because of the thought that the true cycle slip integer would not likely exceed ± 4 cycles from the boundary integers, especially when code observables are not included in the cycle slip float values estimation. This inference can be drawn from the plots in Figures 6.3 and 6.5. A lesser cycle slip range is considered too optimistic and may result in more wrong cycle slip fixes. This defined $r_{slip} = \pm 4$

cycles range results in a set of 10 cycle slip integers for any estimated $\triangle N_i^s$ value, and such a set of integers is here referred to as the set of cycle slip candidates, C_i^s, for such $\triangle N_i^s$. The lengths of C_1^s and C_2^s are therefore equal for any cycle slip occurrence on a phase observation from s, irrespective of whether cycle slip occurred in one or both bands. As such, $C_i(z) \in \mathbb{Z}$ with the index $z = 1, 2, ..., 10$. For instance, for an estimated cycle slip float value of $\triangle N_1^s = 2.2$ cycles and $\triangle N_2^s = 4.2$ cycles, the corresponding $C_1 = \{-2, -1, 0, 1, 2, 3, 4, 5, 6, 7\}$ with the range of $r_{slip} = \pm 4$ cycles round about the integer boundary values of 2 and 3 in the middle of C_1, while the corresponding $C_2 = \{0, 1, 2, 3, 4, 5, 6, 7, 8, 9\}$ with the range of $r_{slip} = \pm 4$ cycles round about the integer boundary values of 4 and 5. Both C_1 and C_2 thus contain 10 values each.

The second step is to form the two vectors of aligned cycle slip candidates. The two vectors of aligned cycle slip candidates are obtained as

$$V_{C_1}^s(10z - 9 : 10z) = \left\{C_1^s(z),\ C_1^s(z), ..., C_1^s(z)\right\} \tag{6.27}$$

$$V_{C_2}^s(10z - 9 : 10z) = \left\{C_2^s(1),\ C_2^s(2), ..., C_2^s(2 + 2\,|r_{slip}|)\right\} \tag{6.28}$$

$$z = 1, 2, .., (2 + 2\,|r_{slip}|)$$

where the $(2 + 2\,|r_{slip}|)^2 = 100$-length vector, $V_{C_i}^s$, contains $(2 + 2\,|r_{slip}|) = 10$ times replication of each element of C_i^s. As an example, for the $C_1 = \{-2, -1, 0, 1, 2, 3, 4, 5, 6, 7\}$ and $C_2 = \{0, 1, 2, 3, 4, 5, 6, 7, 8, 9\}$ sets, the corresponding

$$V_{C_1}^s = \{-2, -2-2, -2, -2, -2, -2, -2, -2, -2, -1, ..., 6, 7, 7, 7, 7, 7, 7, 7, 7, 7, 7\}$$

$$V_{C_2}^s = \{0, 1, 2, 3, 4, 5, 6, 7, 8, 9, 0, ..., 9, 0, 1, 2, 3, 4, 5, 6, 7, 8, 9\}$$

Thirdly, a 100-length slip combination vector, v_{slip}^s, for each of the k cycle-slipped satellites is then generated as

$$v_{slip}^s = \lambda_1 V_{C_1}^s - \lambda_2 V_{C_2}^s \tag{6.29}$$

where each value of v_{slip}^s is the difference magnitude of a cycle slip pair in metres, and contains such possible difference magnitudes of index-to-index pairs of all the

integers in C_1^s and C_2^s. The estimated difference magnitude for a cycle-slipped satellite s is computed using the estimated cycle slip float values at the current epoch as given in Equation (6.30) below.

$$v_{estm}^s = \lambda_1 \triangle N_1^s - \lambda_2 \triangle N_2^s \tag{6.30}$$

A vector of squared residuals, being the vector of the square of the difference between all values in the v_{slip}^s vector and the estimated v_{estm}^s, is thus obtained:

$$v_{resid}^s = \left(v_{slip}^s - v_{estm}^s\right)^2 \tag{6.31}$$

The 100-length v_{resid}^s vector thus contains only positive values, and defines the $(2 + 2\,|r_{slip}|)^2 = 100$-value search space to search for the two smallest values in v_{resid}^s, which are required for fixing the dual-frequency cycle slips.

Fourthly, we search for the two smallest values, from amongst the 100 values in v_{resid}^s vector, and subsequently obtain the corresponding indices of the two minimum values in the v_{resid}^s vector. The index of the least of the two smallest values from v_{resid}^s is the τ^{th} index such that $v_{resid}^s(\tau)$ is the minimum value of v_{resid}^s, defined mathematically as

$$v_{resid}^s(\tau) = min\left\{v_{resid}^s\right\}\ ; \quad \tau \in \left\{1, 2, ..., (2 + 2\,|r_{slip}|)^2\right\} \tag{6.32}$$

The index, κ, corresponding to the larger of the two smallest values from v_{resid}^s is obtained as the index κ, such that

$$v_{resid}^s(\kappa) = min\left\{v_{resid}^{s*}\right\}\ ; \tag{6.33}$$

where the vector v_{resid}^{s*} is the remaining part of the v_{resid}^s vector after removing $v_{resid}^s(\tau)$, containing $(2 + 2\,|r_{slip}|)^2 - 1$ values. Both $v_{resid}^s(\tau)$ and $v_{resid}^s(\kappa)$ are each associated to a pair of integer values from $V_{C_1}^s$ and $V_{C_2}^s$; $v_{resid}^s(\tau)$ is associated to the τ^{th}-index integers of $V_{C_1}^s$ and $V_{C_2}^s$, and $v_{resid}^s(\kappa)$ is associated to κ^{th}-index integers of $V_{C_1}^s$ and $V_{C_2}^s$. These two pairs of integer values are the two pairs of integer values

considered as the most likely integer solutions for the estimated float cycle slip values for the cycle-slipped satellite s, which are consequently considered for a validation process.

It should be noted that this dual-frequency CSDC algorithm defines and uses a search space of 100 values, which are the $(2+2\,|r_{slip}|)^2$ values defined for each cycle cycle-slipped satellite, and as such the cycle slip fixing for one satellite is independent of another. This is a totally different approach from many of the existing cycle slip fixing algorithms where the algorithms usually involve a much wider search space defined for all cycle-slipped satellites at a current epoch that often leads to intensive computations. The LAMBDA method, used in Xiaohong & Xingxing (2011); Banville & Langley (2009), is known as one of such computationally intensive algorithms (Parkins, 2009).

6.4.1.1. Relative Potential Performance of the Cycle Slip Determination Algorithm

The initial step in repairing, fixing/determining cycle slips is usually the estimation of the float values of the cycle slips, which can be achieved from time-differenced observables, by obtaining polynomial fitting residuals, etc. The determination of the integer values of the cycle slips from these estimated float values includes various methods ranging from simple rounding-up of the estimated float values to integer values, down to the more reliable but complex techniques primarily used for ambiguity resolution, which include the popular LAMBDA method. The LAMBDA method is arguably the most acceptable and widely used method for cycle slip or ambiguity fixing (Joosten & Tiberius, 2002), especially in relative positioning operations. For single-receiver operations such as considered in this thesis, a lot of cycle slip determination techniques have also employed the LAMBDA method (e.g. (Liu, 2011; Xu & Kou, 2011; Banville & Langley, 2009; de Lacey *et al.*, 2011; Dai *et al.*, 2009)). However, the LAMBDA method is computationally intensive; it involves the two stages of reduction (generation of a transformation matrix used to reduce the cross-correlation between any two of the estimated cycle slips float values), and a search in a pre-defined search space (Hofmann-Wellenhof *et al.*, 2008). The in-

tensive computational load of the LAMBDA method does not make the method attractive for real-time applications with high dimensions and where computational speed is crucial (Chang *et al.*, 2005). A modification to the LAMBDA method, called MLAMBDA, was proposed in Chang *et al.* (2005), for improved speed of computation, even though the MLAMBDA method also involves the two stages of the LAMBDA method. For high dimensions, the average elapsed time for the reduction stage may be comparable to the average search time (within tens of a millisecond to a few seconds), going by the performance and comparison plots given in Chang *et al.* (2005) for the LAMBDA and MLAMBDA methods. The total elapsed time of computation with the LAMBDA/MLAMBDA method is the combination of the reduction time and the search time, which could exceed a second for high dimensions (say for ≥ 10 cycle slips). Processing high dimensions cycle slips is likely for a multi-frequency receiver, such as a master station of a network of receivers that are observing different GNSSs.

In terms of relative potential performance, this newly developed dual-frequency cycle slip determination algorithm would drastically increase computational speed compared to the widely used LAMBDA method, since it has relatively lower computational load for high dimensions, and does not involve the reduction stage required by the LAMBDA method. To put this in perspective, one can assume a dual-frequency receiver detected cycle slip on 5 observed satellites. If the range to be searched for each estimated cycle slip float value is 10cycles (i.e. an uncertainty of ± 5 cycles, which could easily exceed this range for methods that include code observations in the estimation of the cycle slips float values) after the reduction stage of the LAMBDA method, the sets of integer combinations to test in the search stage of the LAMBDA method is $10^{10} = 100$ billion. On the other hand, this newly proposed dual-frequency cycle slip determination algorithm will only have to search a total of $5 \times 100 = 500$ sets of combinations. To get an idea of the elapsed search time for these two computational loads, one can further assume, for illustrative purposes, that the average elapsed time for processing a set of combination of integer cycle slips with a possible high-speed processor on a dual-frequency receiver is 10picoseconds. Consequently, it would take $10^{10} \times 10 \times 10^{-12} = 1$ second and $500 \times 10 \times 10^{-12} = 5$

nanoseconds for the LAMBDA method and the new dual-frequency cycle slip determination algorithm respectively. This illustration portrays the significant reduction in the search speed of the LAMBDA method. Recalling that additional time will also be spent on the reduction stage of the LAMBDA method, the relative decrease in computational speed, achievable by this newly proposed dual-frequency cycle slip determination algorithm, is a measure of improved performance that is desired for time-critical applications with high dimensions. However, the comparison of the percentages of correct fixes or success rate achievable by the LAMBDA method and this newly proposed algorithm needs to be further investigated to extensively evaluate relative performance.

6.4.2. Dual-Frequency Cycle Slip Validation

The first pair of integer values associated with $v^s_{resid}(\tau)$ are

$$\begin{aligned} \triangle N^{s,\tau}_{1,int} &= V^s_{C_1}(\tau) \\ \triangle N^{s,\tau}_{2,int} &= V^s_{C_2}(\tau) \end{aligned} \tag{6.34}$$

while the second pair of integer values associated with $v^s_{resid}(\kappa)$ are

$$\begin{aligned} \triangle N^{s,\kappa}_{1,int} &= V^s_{C_1}(\kappa) \\ \triangle N^{s,\kappa}_{2,int} &= V^s_{C_2}(\kappa) \end{aligned} \tag{6.35}$$

The validation process described here helps to choose which of the two pairs of integers above ((6.34) or (6.35)) can be accepted as the correct pair, based on certain metrics; and if the first pair is considered incorrect, the second pair is subsequently the most likely to be correct; and if the second pair is also considered incorrect, the float values are adopted and the cycle slip is not fixed to integer values. The simple validation process involves decision made based on two deviation values computed

from the first and the second pairs of integers as follows:

$$\begin{aligned} \Omega^s_\tau &= \left|(\triangle N^s_1 - \triangle N^s_2) - (\triangle N^{s,\tau}_{1,int} - \triangle N^{s,\tau}_{2,int})\right| \\ \Omega^s_\kappa &= \left|(\triangle N^s_1 - \triangle N^s_2) - (\triangle N^{s,\kappa}_{1,int} - \triangle N^{s,\kappa}_{2,int})\right| \end{aligned} \tag{6.36}$$

where Ω^s_τ and Ω^s_κ are measures of how wide the first and second pairs of integer cycle slip values deviate from the estimated cycle slip float values, respectively. A correct Ω^s_τ or Ω^s_κ is expected to be lesser than 1 because the maximum expected error on the $\triangle N^s_{WL} = \triangle N^s_1 - \triangle N^s_2$ widelane cycle slip value estimated as 0.78m, is less than a widelane wavelength of $\lambda_{WL} = 0.86$m, going by the assumptions made in Section 6.3.2. The smaller any one of Ω^s_τ or Ω^s_κ is, the higher the confidence on the correctness of its associated integer pair. An expected validation deviation threshold, which is obtained as the ratio of the expected maximum error of 0.78m on $B^s_\psi \lambda_{WL}$ to the widelane wavelength of $\lambda_{WL} = 0.86$m, i.e. $\Omega_{expt} = \frac{\lambda_{WL} \Delta^{d_s} e_{\lambda_{WL}}}{\lambda_{WL}} = \frac{0.78}{0.86} \simeq 0.90$, can be set. This value of Ω_{expt} suggests that up to 0.9 widelane cycle slip error can be contributed to an estimated widelane cycle slip float value when an observable from the $B^s_\psi \lambda_{WL}$ sequence is used for the estimation of cycle slip float value. The values of the uncertainty levels of $\triangle N^s_{WL}$ obtained and plotted in Figure 6.8 and Figure 6.7 are observed to be well below this 0.9 threshold at nearly all epochs. Also, an estimated validation deviation threshold, which is obtained as 3 times σ^s_{WL}- the post-float-estimated uncertainty value of $\triangle N^s_{WL}$ at a current epoch - to the widelane wavelength of $\lambda_{WL} = 0.86$m, i.e. $\Omega^s_{estm} = \frac{3\sigma^s_{WL}}{\lambda_{WL}}$. The value of Ω^s_{estm} would vary at each cycle-slip epoch for s and would also be different for different cycle-slipped satellites, as can be inferred from Figure 6.8 and Figure 6.7.

Hence, the first pair of integers is accepted as the correct cycle slip pair if Ω^s_τ is less than the minimum between the expected and estimated deviation ratios, Ω_{expt} and Ω^s_{estm}; and if otherwise, only then is the second deviation threshold Ω^s_κ examined, and it is only when Ω^s_κ is also less than the minimum between Ω_{expt} and Ω^s_{estm} that the second pair of integers is accepted as the correct cycle slip pair, but also rejected if otherwise. Consequently, for $\Omega^s_\tau \geq min\left\{\Omega_{expt}, \Omega^s_{estm}\right\}$ and $\Omega^s_\kappa \geq min\left\{\Omega_{expt}, \Omega^s_{estm}\right\}$, the float cycle slip pair is not fixed and the float cycle

slip values, $\triangle N_1^s$ and $\triangle N_1^s$, are retained. Summarily, the fixed dual-frequency cycle slips integer values, $\triangle N_{1,int}^s$ and $\triangle N_{2,int}^s$ are

$$\begin{aligned} \triangle N_{1,int}^s &= \triangle N_{1,int}^{s,\tau} \\ \triangle N_{2,int}^s &= \triangle N_{2,int}^{s,\tau} \\ & \quad if \;\; \Omega_\tau^s < min\left\{\Omega_{expt},\, \Omega_{estm}^s\right\} \end{aligned} \tag{6.37}$$

$$\begin{aligned} \triangle N_{1,int}^s &= \triangle N_{1,int}^{s,\kappa} \\ \triangle N_{2,int}^s &= \triangle N_{2,int}^{s,\kappa} \\ & \quad if \;\; \Omega_\kappa^s < min\left\{\Omega_{expt},\, \Omega_{estm}^s\right\} \end{aligned} \tag{6.38}$$

or are not fixed but assigned to the float values

$$\begin{aligned} \triangle N_{1,int}^s &= \triangle N_1^s \\ \triangle N_{2,int}^s &= \triangle N_2^s \\ & \quad if \;\; \Omega_\tau^s < min\left\{\Omega_{expt},\, \Omega_{estm}^s\right\} \;\&\; \Omega_\kappa^s < min\left\{\Omega_{expt},\, \Omega_{estm}^s\right\} \end{aligned} \tag{6.39}$$

The Ω_τ^s and Ω_κ^s deviation values were carefully examined via simulation of known cycle slip values or pairs of cycle slips on phase observations, for different data sets. The value of Ω_τ^s or Ω_κ^s was found to be usually less than 0.8 for correctly determined cycle slip pairs. It was also discovered that, the first integer pair (Equation (6.34)) was often found to be the correct pair of simulated cycle slips integers. Only in very rare cases were Ω_τ^s and Ω_κ^s simultaneously found greater than Ω_{expt} resulting in non-fixed cycle slip values as in (6.34).

This new single-satellite phase-only validation algorithm is quite different from the known F-ratio and W-ratio tests (Wang *et al.*, 2000) that are used for multiple-satellite cycle slip validation.This new procedure is a validation algorithm for individual cycle slip satellites.

6.4.3. Handling the Limitation of the Dual-Frequency CSDC Algorithm

The dual-frequency CSDC algorithm is not assumed a perfect algorithm; it could be limited by the magnitude of the adaptively-differenced errors, $\triangle^{d_s} e^s_{\psi,i}$, in the detection process. Furthermore, the ATD process for cycle slips detection is quite sensitive to receiver clock drifts or variations, and possibly also to receiver antenna dynamics. As such, it could indicate cycle slips for satellites when actually there are no cycle slips at certain epochs of high clock drifts or antenna dynamics. The impact of $\triangle e_\psi$ or $\triangle e_{\psi,P}$ in the cycle slips float values estimation process given by (6.16) or (6.20) above, or poor estimation of an $\varepsilon(t)$ value, could also be significant to flaw an accurate-enough estimation of cycle slip float values, especially when the sensitive ATD detection process indicates cycle slips on all satellites at a given epoch, and code ADSs are then involved. Falsely detected cycle slip values will be fixed to false integer values, and if corrected for in the phase observations, the correction would result to decreasing positioning accuracy and precision, rather than the intended improvement.

As measures to minimise the impact of this limitation or imperfection in the dual-frequency CSDC algorithm, two checks are done, which can result in the Nulling of Fixed Cycle Slip (NFCS), prior to finally correcting for fixed cycle slips on the phase observations of the cycle-slipped satellites. The dual-frequency checks for a given s whose cycle slip pair has already been fixed at the current epoch, are:

(a) Check if $\left|\triangle N^s_{1,int} - \triangle N^s_{2,int}\right| < 3$, and if the estimated change in the ionospheric delay is greater than expected. The $\left|\triangle N^s_{1,int} - \triangle N^s_{2,int}\right| < 3$ criterion is used because when false detection of cycle slips occur, the cycle slips estimation and fixing procedure would usually result in close $\triangle N^s_1$ and $\triangle N^s_2$ values such as: $\triangle N_1 = 2$ and $\triangle N_2 = 1$; $\triangle N_1 = 3$ and $\triangle N_2 = 2$; $\triangle N_1 = 4$ and $\triangle N_2 = 3$; $\triangle N_1 = 5$ and $\triangle N_2 = 4$; $\triangle N_1 = 9$ and $\triangle N_2 = 7$, etc, mainly because of the error present in the observables that are used for cycle slips float values estimation. The big challenge here is to determine the expected change in the ionospheric delay. The applied technique to address this challenge is to compare the change in ionospheric delay estimated in

the presence of the fixed cycle slip pair, to the change in the ionospheric delay in the absence of cycle slips.

Assuming cycle slips actually occurred at the current epoch for s, then the ambiguous change in the ionospheric delay, $\triangle I^s_{1,ambg}$, computed from the raw phase observations of s at a current epoch is

$$\begin{aligned} \triangle I^s_{1,ambg} &= \left[\psi^s_1(L^s) - \psi^s_2(L^s) - (\psi^s_1(L^s-1) - \psi^s_2(L^s-1))\right]/(\gamma-1) \\ &= \left[\triangle I^s_1 + \lambda_1 \triangle N^s_1 - \lambda_2 \triangle N^s_2 + \triangle b + \triangle \epsilon_\psi\right]/(\gamma-1) \end{aligned} \tag{6.40}$$

where $\triangle b$ and $\triangle \epsilon_\psi$ indicate the change in phase hardware delays and phase error respectively, between the current epoch's phase observable and the immediate past epoch's phase observation. Substituting the fixed integer values $\triangle N^s_{1,int}$ and $\triangle N^s_{2,int}$ for $\triangle N^s_1$ and $\triangle N^s_2$ in (6.40) gives the estimated change in ionospheric delay, $\triangle I^s_{1,slip}$, in the presence of the cycle slips; and substituting zero values for $\triangle N^s_1$ and $\triangle N^s_2$ in (6.40) gives the change in ionospheric delay in the absence of cycle slips, $\triangle I^s_{1,zeros}$; both affected by the negligible $\triangle b$ and $\triangle \epsilon_\psi$. The idea here is that $\left|\triangle I^s_{1,slip}\right|$ should be greater than $\left|\triangle I^s_{1,zeros}\right|$ if there were no cycle slips, and smaller if there is/are cycle slip(s). But by what margin? To figure out a suitable margin, we recall that the error impact of $\triangle b$ and $\triangle \epsilon_\psi$ are expected to be within a few millimetres because the change in the fairly constant hardware delays is negligible over consecutive epochs and the high correlation between dual-frequency phase observations makes $\triangle \epsilon_\psi$ quite small. Secondly, we recall that the $\triangle N^s_1 = \pm 9$ and $\triangle N^s_2 = \pm 7$ cycle slip pair has the least difference magnitude amongst the first few pairs of the special slip pairs, with a difference magnitude of $\lambda \triangle N^s = \lambda_1 \triangle N^s_1 - \lambda_2 \triangle N^s_2 = 3.17$mm, which is also within the millimetres level of ionospheric rate of change. However, it is also possible to estimate, in real-time, the uncertainty, $\sigma_{\lambda \triangle N}$, in the $\lambda \triangle N^s$ difference magnitude, such as done and shown in plot (a) of Figure 6.7, and consider its 3-sigma value, $3\sigma^s_{\lambda \triangle N}$, as a threshold. In the sequel, the minimum between $3\sigma^s_{\lambda \triangle N}$ and 3.17mm is used as the set margin by which $\left|\triangle I^s_{1,slip}\right|$ should at least be greater than $\left|\triangle I^s_{1,zeros}\right|$ if there were no cycle slip occurrence at a current epoch. The fixed cycle slips are nulled (made equal to zero) if this set margin is exceeded for a given cycle-slipped

s. That is, the already fixed cycle slip

$$\begin{aligned} \triangle N^s_{1,int} &= 0 \\ \triangle N^s_{2,int} &= 0 \\ & if \quad \left|\triangle I^s_{1,slip}\right| > \left|\triangle I^s_{1,zeros}\right| + min\left\{3\sigma_{\lambda\triangle N},\, 0.00317\right\} \end{aligned} \tag{6.41}$$

Summarily, the first check is: if $\left|\triangle N^s_{1,int} - \triangle N^s_{2,int}\right| < 3$ and (6.41) is satisfied, NFCS is done, otherwise the already fixed cycle slips are accepted and corrected for.

(b) Check if cycle slips were fixed and corrected for in the immediate past observation epoch of s, where s is not a gap-recovering satellite. A satellite is considered to be a gap-recovering satellite if it has not been observed by the receiver in more than two consecutive epochs after the last post-gap epoch. The NFCS is done only if any of these two criteria further hold: (i) the fixed cycle slips integer values at the current epoch are multiples of the last epoch's fixed cycle slips integer values, or (ii) $\left|\lambda_1\triangle N^s_{1,int} - \lambda_2\triangle N^s_{1,int}\right| \leq 0.0285$ and $\left|\triangle N^s_{1,int} - \triangle N^s_{2,int}\right| \leq 4$. These two criteria are to null the possible manifestations of inaccurately corrected or falsely fixed cycle slips at an immediate past epoch, in the current epoch. The assumption in criterion (ii) is that the consecutive epochs occurrence of special slip pairs of difference magnitudes less than 0.0285m on s is assumed rare, and when it does occur, it is likely due to a false detection or an inaccurately fixed cycle slip in the immediate past epoch. If neither of (i) nor (ii) holds, the already fixed cycle slips are accepted and corrected for.

However, these assumptions may not always hold, but to a great extent, are good enough measures to address the possible limitations of this new dual-frequency CSDC algorithm, as observed in the several cycle slips test scenarios. Above all, it is also worth mentioning that there may be other factors contributing to the imperfection of this newly-developed dual-frequency CSDC algorithm that may not have been mentioned as they are currently unknown to the author.

6.4.4. Dual-Frequency Cycle Slip Correction

The raw ψ_i^s phase observations are subsequently corrected for the determined/fixed cycle slip values, thereby generating a sequence of cycle-slip-free phase observable, $\overline{\psi_i^s}$, for each s of the k cycle-slipped satellites at a current observation epoch. Similar to single-frequency operation, each of the dual-frequency phase observation sequences is subsequently corrected for the current epoch's fixed cycle slip value. The correction is applied by adding the determined cycle slip value equivalent in metres to the pre-cycle-slip observables in metres, thereby able to generate a current cycle-slip-free phase observable, $\overline{\psi_i^s}(L^s)$, with 'no' cycle slip relative to the past $\overline{\psi_i^s}(1:L^s-1)$ observables. This is done for each of the dual-frequency phase observations detected to have a cycle slip, for the k cycle-slipped satellites at the current observation epoch. For s, the dual-frequency L_s-length time series or sequences of cycle-slip-free phase observables in metres, are corrected as

$$\overline{\psi_1^s}(1:L^s) = \left\{\overline{\psi_1^s}(1:L^s-1) + \lambda_1 \triangle N_{1,int}^s,\ \psi_1^s(L^s)\right\} \tag{6.42}$$

$$\overline{\psi_2^s}(1:L^s) = \left\{\overline{\psi_2^s}(1:L^s-1) + \lambda_2 \triangle N_{2,int}^s,\ \psi_2^s(L^s)\right\} \tag{6.43}$$

Each band's cycle slip correction involves adding the product of the determined cycle slip value and the corresponding wavelength, to the previous (L^s-1)-length cycle-slip-free phase observables from s, i.e. $\overline{\psi_i^s}(1:L^s-1)$, and appending the current epoch's raw phase observation, $\psi_i^s(L^s)$, as the last value of the cycle-slip-free phase sequence. In this way, the previous phase observables are updated with the current cycle slip value, and the resulting integer ambiguity value at any epoch of cycle slip will thus be changing accordingly. The previous $\overline{\psi_i^s}(1:L^s-1)$ values must have been corrected for cycle slips if there were detected and determined cycle slips. The sliding window observables - the last W_L-length observables from the current L^s-length cycle-slip-free phase sequences - are what are used for the ATD process for the dual-frequency phase cycle slips detection on the next $(L^s+1)^{th}$ observation epoch of s, as earlier described in Section 5.1. As such, only the last W_L number of observables are actually required to be updated since the maximum length of an undifferenced phase sequence is W_L. In this way, the receiver does not need to store

more than W_L past phase and code observables in real time processing.

6.5. The Dual-Frequency Ionospheric Delay

The ionospheric observable on the L1 band and consequently on the L2 band, are estimated from the dual-frequency raw phase observations. The ionospheric correction on the L1 band of satellite s can be modelled as

$$I_1^s = I_1^{s,0} + I_1^{s,v} \tag{6.44}$$

where, as already defined for Equation (5.23), $I_1^{s,0}$ is an unknown constant initial ionospheric delay value while $I_1^{s,v}$ is the time-varying relative ionospheric delay component at a given epoch. Simply put, I_1^s is a slant ionospheric delay from s to the receiver; the varying $I_1^{s,v}$ is a relative ionospheric delay with respect to the ionospheric delay at the first observation epoch of s or at the last observation epoch when $l^s = L^s = 1$, where $I_1^{s,v}(1) = 0$; and the unknown constant $I^{s,0}$ is the ionospheric delay at the observation epoch when $l^s = L^s = 1$. For this dual-frequency operation, $I_1^{s,v}$ is a phase-only derived observable obtained for the current t epoch (corresponding to the $(L^s)^{th}$ observation of s).

For a continuously observed s up to the current epoch, that is when s is observed without an observation gap between the last observation epoch and the current observation epoch, $I_1^{s,v}$ is estimated from a geometry-free phase observable generated with the cycle-slip-free phase observables $\overline{\psi_1^s}$ and $\overline{\psi_2^s}$ as

$$I_1^{s,v}(L^s) = \frac{\overline{\psi_1^s}(L^s) - \overline{\psi_2^s}(L^s) - (\overline{\psi_1^s}(L^s - l^s + 1) - \overline{\psi_2^s}(L^s - l^s + 1))}{(\gamma - 1)} + I_1^{s,v}(L^s - l^s + 1) \tag{6.45}$$

where $\gamma = (f_1/f_2)^2 = 1.64694$, $\overline{\psi_1^s} = \psi_1^s$ and $\overline{\psi_2^s} = \psi_2^s$ in the absence of cycle slips; but in the presence of cycle slips, $\overline{\psi_1^s}$ and $\overline{\psi_2^s}$ are observables obtained after the dual-frequency cycle slip correction described in Section 6.4.4. It should be noted in Equation (6.45) that $\overline{\psi_1^s}(L^s) - \overline{\psi_2^s}(L^s)$ is the geometry-free phase observable at the current epoch while $\overline{\psi_1^s}(L^s - l^s + 1) - \overline{\psi_2^s}(L^s - l^s + 1)$ is the geometry-free phase observable at the $L^s - l^s + 1$ observation epoch of s. The relative ionospheric

variation and ionospheric delay on the L2 band are obtained as $I_2^{s,v} = \gamma I_1^{s,v}$ and $I_2^s = I_2^{s,0} + I_2^{s,v} = \gamma I_1^s$ respectively. A time series $I_1^{s,v}$ generated with Equation (6.45) contains neither N_1^s nor N_2^s ambiguity term, but includes differenced phase differential hardware delay values that are scaled by $1/(\gamma - 1)$, and differences between combined phase error levels. These inclusions are presumed negligible and as such, $I_1^{s,v}$ is assumed a true time varying ionospheric delay.

6.6. Dual-Frequency Code Error Mitigation

The dual-frequency code error mitigation algorithm is the same as that employed for single-frequency code error mitigation already presented in Section 5.4, except that in this case, it is applied to the dual-frequency code observations. At a current epoch, the estimated relative ionospheric delay is first eliminated from a current epoch's raw code observation and from the current epoch's cycle-slip-free phase observable, for each of the total S_{total} observed satellite at the current epoch. In this way, pseudo-iono-free code and phase observables given as $P_{IF,i}^s(L^s) = P_i^s - I_i^{s,v}(L^s)$ and $\psi_{IF,i}^s(L^s) = \overline{\psi_i^s}(L^s) + I_i^{s,v}(L^s)$ respectively, are generated for dual-frequency $i = 1, 2$. By taking the difference between $P_{IF,i}^s(L^s)$ and $\psi_{IF,i}^s(L^s)$, the code multipath observables at the current epoch are obtained as

$$MP_1^s(L^s) = P_{IF,1}^s(L^s) - \psi_{IF,1}^s(L^s) = 2I_1^{s,0} - \lambda_1 N_1^s + D_1^s + e_{p_1}^s \quad (6.46)$$

$$MP_2^s(L^s) = P_{IF,2}^s(L^s) - \psi_{IF,2}^s(L^s) = 2I_2^{s,0} - \lambda_2 N_2^s + D_2^s + e_{p_2}^s \quad (6.47)$$

The $MP_i^s(L^s)$ is observed to consist of constants - $I_i^{s,0}$ and $\lambda_i N_i^s$; the fairly constant combined hardware delays denoted as $D_i^s = d_i^s + d_i^r - b_i^s - b_i^r$; and the combined phase error and dominant code multipath/error, denoted $e_{p_i}^s = m_{P,i}^s + \epsilon_{P,i}^s - m_{\psi,i}^s - \epsilon_{\psi,i}^s$. Assuming phase errors are negligibly small compared to the code errors, as usual, the included $e_{p_1}^s$ and $e_{p_2}^s$ errors in (6.46) and (6.47) are treated as the respective code errors on P_1^s and P_2^s respectively. Also, assuming the time series errors, $e_{p_i}^s$, approach zero-mean sequences as the number of observation epochs increases, zero-mean code error values can be estimated. The updated mean value, $\langle MP_i^s \rangle$, as given in (5.43)

for a current epoch, are thus

$$\langle MP_1^s(L^s)\rangle = \frac{1}{L^s}\left[(L^s-1)\left\{\langle MP_1^s(1:L^s-1)\rangle - \lambda_1 \triangle N_{1,int}^s\right\} + MP_1^s(L^s)\right] \quad (6.48)$$

$$\langle MP_2^s(L^s)\rangle = \frac{1}{L^s}\left[(L^s-1)\left\{\langle MP_2^s(1:L^s-1)\rangle - \lambda_2 \triangle N_{2,int}^s\right\} + MP_2^s(L^s)\right] \quad (6.49)$$

where $\triangle N_i^s$ are the determined values of the cycle slips that may occur between the current epoch's Li band phase observation and the last epoch's Li phase observable. The $\triangle N_{i,int}^s$ values are equal to zero if cycle slips are not detected and determined for s at the current epoch. The zero-mean code errors, $\overline{e_{p_i}^s(L^s)}$, are subsequently computed as $\overline{e_{p_i}^s(L^s)} = MP_i^s(L^s) - \langle MP_i^s(L^s)\rangle$; and finally, the smoothed or error-mitigated dual-frequency code observables, $\overline{P_i^s}$, are obtained after subtracting an estimated zero-mean code error from its corresponding current epoch's raw code observation. That is, for a current epoch,

$$\overline{P_1^s}(L^s) = P_1^s(L^s) - \overline{e_{p_1}^s(L^s)} \quad (6.50)$$

$$\overline{P_2^s}(L^s) = P_2^s(L^s) - \overline{e_{p_2}^s(L^s)} \quad (6.51)$$

where $\overline{P_i^s}(L^s)$ are the resulting smoothed or error-mitigated dual-frequency code observables used for code positioning at a current epoch. As with single-frequency operation, this dual-frequency code error mitigation algorithm thus leads to mitigation of the code error (mostly composed of the multipath error and noise on the code observation) level. Like the Hatch filter, it follows that $\overline{P_1^s}(1) = P_1^s(1)$ and $\overline{P_2^s}(1) = P_2^s(1)$ at the very first observation epoch of s or when $L^s = l^s = 1$. Unlike the Hatch filter, this algorithm is observed to be based on the prior determination and correction of cycle slip values. In that way, the algorithm is cycle-slip-resilient, unlike the many existing code smoothing or error-mitigation techniques that are limited by cycle slip occurrence.

6.7. Updating Dual-Frequency Past Epochs Observables with a Clock Jump Value

A receiver clock jump or reset at a current epoch t, would impede the ATD process as already discussed in Section 5.5 for single-frequency operation. The dual-frequency code and phase observables prior to the current epoch are thus updated to nullify the impact of a current clock jump with value $\varepsilon_{c,jump}(t)$, on the ATD process at subsequent epochs. The update of the dual-frequency code and phase observables is thus

$$\overline{\psi_1^s}(1:L^s) = \left\{\overline{\psi_1^s}(1:L^s-1) + \varepsilon_{c,jump}(t),\ \psi_1^s(L^s)\right\} \tag{6.52}$$

$$\overline{\psi_2^s}(1:L^s) = \left\{\overline{\psi_2^s}(1:L^s-1) + \varepsilon_{c,jump}(t),\ \psi_2^s(L^s)\right\} \tag{6.53}$$

$$P_1^s(1:L^s) = \left\{P_1^s(1:L^s-1) + \varepsilon_{c,jump}(t),\ P_1^s(L^s)\right\} \tag{6.54}$$

$$P_2^s(1:L^s) = \left\{P_2^s(1:L^s-1) + \varepsilon_{c,jump}(t),\ P_2^s(L^s)\right\} \tag{6.55}$$

This update shows that the estimated clock jump at a current epoch is added to the previous phase observables and code observations, and it is only required when a clock jump has been detected. In this way, ATD at subsequent epochs will be independent of a clock jump at a previous epoch. Again, only the last W_L number of observables are really required to be updated as the required maximum length of a time series undifferenced sequence is W_L.

6.8. The Technique for Mitigating Impacts of Observation Gap

Very often, an observation gap or observation discontinuity, which is a short duration outage of a satellite being observed by a GNSS receiver, impacts negatively on the positioning accuracy of a GNSS receiver. Such a satellite is here dubbed a gapped satellite. A decreased positioning accuracy at a post-gap epoch, and existence of a convergence time necessary to resolve post-gap ambiguities, are two possible

impacts of an observation gap occurrence. This is because, as with a conventional ambiguity resolution or cycle slip detection and fixing technique, and conventional code smoothing technique, the procedures require re-initialisation whenever the receiver re-achieves lock to a gapped satellite at a post-gap observation epoch. As cycle slips nor ambiguities cannot be determined and code observations cannot be smoothed at such post-gap epochs of re-initialistion, the computed positioning solutions at such epochs of re-initialistion are often marred, leading to poorer accuracy compared to the level of accuracy obtained prior to an observation gap. Moreover, the re-initialisation usually introduces long convergence time in a conventional ambiguity resolution process, which is undesired in positioning. The period (or number of post-gap epochs) required for a re-initialised code smoothing algorithm, such as the HFT, to achieve significantly improved positioning accuracy after an observation gap occurrence can be likened to the convergence time in a conventional ambiguity resolution technique. As a proposed solution for continuously improving positioning after a receiver re-locks to a gapped satellite, a technique which involves generating seemingly continuous observables for a gap satellite, when the gap duration is less than a few minutes, is introduced, which avoids re-initialisation at a post-gap epoch. This new technique is hereafter referred to as 'gap-connect technique'.

In this research a maximum gap duration of four minutes was set and used, even though no satellite outage or gap was found to last for more than 2.5minutes in all processed data sets. The gap-connect technique involves estimating for a gapped satellite, the relative ionospheric delay, the cycle slip values on the dual-frequency phase observations, and subsequent generation of the error mitigated dual-frequency code observables, at a post-gap epoch (re-lock epoch) for the gapped satellite; all relative to the last observation epoch from the gapped satellite prior to its outage. The final step in the technique involves adjusting the observations acquired prior to the observation gap in such a way as to create the impression that the observations up to the current post-gap epoch are observed consecutively - a requirement by the ATD process that will be used to detect cycle slips occurrence in subsequent post-gap epochs of the gapped satellite. It should be noted that this gap-connect technique does not, nor attempt to, 'fill-in' the missing (gap) epoch observations, but com-

putes the relative changes in the ambiguities (i.e. cycle slips) and in ρ at a post-gap epoch. It should be recalled that ρ is the common non-dispersive range components in all code and phase observations from a satellite. As there is no re-initialisation in the gap-connect technique, cycle slips are determined and corrected for, and code error mitigation is also performed, which together should result in improving the positioning solution at a post-gap epoch instead of the worsening positioning solution via the re-initialisation undergone by conventional ambiguity/cycle slip determination and correction, and code smoothing techniques. The detailed algorithm of this technique is presented in subsequent sections.

Once an observation gap is observed for satellite s, the 'adjusted' dual-frequency phase and code observables are then denoted as $\hat{\psi}_i^s$ and $\hat{P}_i^s$ respectively. Prior to the first observation gap of s, when $L^s - 1$ observations of s have been acquired by the receiver, $\hat{\psi}_i^s(1 : L^s - 1) = \overline{\psi_i^s}(1 : L^s - 1)$ while $\hat{P}_i^s(1 : L^s - 1) = \overline{P}_i^s(1 : L^s - 1)$. To mitigate the negative impacts associated with an observation gap occurrence via the gap-connect technique, the estimation of the post-gap relative ionospheric delay, determination of the dual-frequency cycle slips, if any, and the mitigation of the dual-frequency code errors, are paramount.

6.8.1. Predicting Post-Gap Relative Ionospheric Delay

Consider a re-locked gap satellite s at a current (post-gap) epoch, whose observation gap occurred at the $(t_{gap} + 1)^{th}$ observation epoch of the receiver. This pre-gap epoch, t_{gap}, corresponds to the $(L^s - 1)^{th}$ observation epoch of s. At the post-gap epoch, the omitted and current epochs (totaling m epochs) relative ionospheric delay values are predicted. As such, at a current t receiver observation epoch, the total $m = t - t_{gap} - 1$ value(s) of $I_1^{s,v}$ are predicted from a maximum of l^s-length immediate past ionospheric observables estimated from s, as

$$I_1^{s,v}(L^s - 1 + \tau) = I_1^{s,v}(L^s - 1);\ if\ t_{gap} = 1$$

$$I_1^{s,v}(L^s - 1 + \tau) = \tau \left\langle \triangle^1 I_1^{s,v}(L^s - l^s : L^s - 1) \right\rangle + I_1^{s,v}(L^s - 1),\ if\ t_{gap} > 1 \qquad (6.56)$$

where $\tau = \triangle t, 2\triangle t, .., m\triangle t$, and $\triangle t$ is the observation interval. This prediction is done provided the gap duration is not greater than the set gap limit, that is, $l^s_{gap} \leq L_{gap}$. The $\triangle^1$indicates a first order differencing of the $I_1^{s,v}(L^s - l^s : L^s - 1)$ sequence. In this way, the relative ionospheric delay of the current epoch, $I_1^{s,v}(L^s) = I_1^{s,v}(L^s - 1 + m\triangle t)$, and the omitted or gap epochs are predicted values. Equation (6.56) is based on the assumption that over a short L_{gap} interval, the ionospheric variation is low within the interval, and could be modelled to be linearly varying with time (Kim *et al.*, 2007). As given by Equation (6.56), we note that only a maximum of W_L-length immediate past relative ionospheric delay observables are used in the ionospheric prediction. The ionospheric prediction algorithm allows for a set maximum of $L_{gap} = 4$ minutes interval between the pre-gap epoch and the post-gap epoch of a gapped satellite, in this research. The algorithm assumes fresh observation of s if the gap interval exceeds L_{gap} and thus resets the observations lengths $L^s = l^s = 1$. The prediction of the relative ionospheric delay values for the m epochs is useful in the subsequent estimation of the cycle slips that may occur due to the observation gap. It also ensures that the estimated $I_1^{s,v}$ value at any epoch is obtained with reference to the unknown constant initial ionospheric delay value $I_1^{s,0}$ obtained at the $l^s = L^s = 1$ observation epoch of s, irrespective of observation gaps.

6.8.2. Determination of Post-Gap Dual-Frequency Cycle Slips

After predicting the relative ionospheric delay value at a post-gap epoch for a gapped satellite s, the next step towards mitigating the impact due to the observation gap is to estimate the float values of the dual-frequency phase cycle slips, $\triangle N_1^{s,gap}$ and $\triangle N_2^{s,gap}$, rather than re-initialising to solve for new ambiguity values of N_1^s and N_2^s. The cycle-slip-free phase $\overline{\psi_i^s}$ and the error-mitigated code observables $\overline{P_i^s}$ with $i = 1, 2$, that were already generated at the last $(L^s - 1)^{th}$ epoch prior to the current observation gap of s, are required. $\hat{\psi}_i^s$ and $\hat{P}_i^s$ are used in place of $\overline{\psi_i^s}$ and $\overline{P_i^s}$ if the immediate past observation gap is not the first for s. The current epoch's (the $(L^s)^{th}$observation) raw phase and code observations, ψ_i^s and P_i^s, are also involved in generating the six required observables that are simultaneously used to estimate the dual-frequency cycle slips float values and the change in $\triangle\rho^s$ - the change in

the combined true geometric range and other common parameters as defined by Equation (3.3). The change in the L1 relative ionospheric delay between these two epochs is

$$\triangle I_1^{s,v}(L^s) = I_1^{s,v}(L^s) - I_1^{s,v}(L^s - 1) \tag{6.57}$$

The six observables are thus generated as

$$\begin{aligned}
\triangle y_{\overline{\psi_1}} &= \psi_1^s(L^s) - \overline{\psi_1^s}(L^s - 1) + \triangle I_1^{s,v}(L^s) \\
\triangle y_{\overline{\psi_2}} &= \psi_2^s(L^s) - \overline{\psi_2^s}(L^s - 1) + \gamma \triangle I_1^{s,v}(L^s) \\
\triangle y_{\overline{P_1}} &= P_1^s(L^s) - \overline{P_1^s}(L^s - 1) - \triangle I_1^{s,v}(L^s) \\
\triangle y_{\overline{P_2}} &= P_2^s(L^s) - \overline{P_2^s}(L^s - 1) - \gamma \triangle I_1^{s,v}(L^s) \\
\triangle y_{P_1} &= P_1^s(L^s) - P_1^s(L^s - 1) - \triangle I_1^{s,v}(L^s) \\
\triangle y_{P_2} &= P_2^s(L^s) - P_2^s(L^s - 1) - \gamma \triangle I_1^{s,v}(L^s)
\end{aligned} \tag{6.58}$$

The difference between two epochs' code observables or two epochs' phase observables on the same band eliminates the unknown constant $I_1^{s,0}$ and $I_2^{s,0} = \gamma I_1^{s,0}$; while the subtraction and addition of $\triangle I_1^{s,v}$ and $\gamma \triangle I_1^{s,v}$ to the differenced code and phase observables 'eliminate' the varying relative ionospheric delay on the L1 and L2 bands observables respectively, in Equation (6.58). The six observables are broken down to their constituent parameters in the matrix equation given by Equation (6.59)

$$\begin{bmatrix} \triangle y_{\overline{\psi_1}} \\ \triangle y_{\overline{\psi_2}} \\ \triangle y_{\overline{P_1}} \\ \triangle y_{\overline{P_2}} \\ \triangle y_{P_1} \\ \triangle y_{P_2} \end{bmatrix} = \begin{bmatrix} 1 & \lambda_1 & 0 \\ 1 & 0 & \lambda_2 \\ 1 & 0 & 0 \\ 1 & 0 & 0 \\ 1 & 0 & 0 \\ 1 & 0 & 0 \end{bmatrix} \begin{bmatrix} \triangle \rho^s \\ \triangle N_1^{s,gap} \\ \triangle N_2^{s,gap} \end{bmatrix} + \begin{bmatrix} \triangle e_{\overline{\psi_1}} \\ \triangle e_{\overline{\psi_2}} \\ \triangle e_{\overline{P_1}} \\ \triangle e_{\overline{P_2}} \\ \triangle e_{P_1} \\ \triangle e_{P_2} \end{bmatrix}$$

$$\triangle Y = H \quad \triangle X + \triangle e_{\psi,P} \tag{6.59}$$

Equation (6.59) clearly reveals that only the determination of the three parameters, $\triangle \rho^s$, $\triangle N_1^{s,gap}$ and $\triangle N_2^{s,gap}$, are required in the gap-connect technique. The

technique does not attempt to determine and fill-in the gap epoch observation(s). Assuming the errors in the observables are uncorrelated (as already stated in Section 5.2.2), the 6×6 diagonal weight matrix used is defined as

$$W = \begin{bmatrix} w^s_{\psi 1} & 0 & 0 & 0 & 0 & 0 \\ 0 & w^s_{\psi 2} & 0 & 0 & 0 & 0 \\ 0 & 0 & w^s_{P1} & 0 & 0 & 0 \\ 0 & 0 & 0 & w^s_{P2} & 0 & 0 \\ 0 & 0 & 0 & 0 & w^s_{P1} & 0 \\ 0 & 0 & 0 & 0 & 0 & w^s_{P2} \end{bmatrix} \tag{6.60}$$

where $w^s_{\psi i}$ and w^s_{Pi} are the inverse of the square of the standard deviation values of the corresponding ADSs obtained upon applying ATD on the pre-gap sequences of $\overline{\psi^s_i}(L^s - l^s - 1 : L^s - 1)$ and $\overline{P^s_i}(L^s - l^s - 1 : L^s - 1)$, respectively. The $\triangle N^{s,gap}_1$ and $\triangle N^{s,gap}_2$ values to be estimated are the cycle slips float values, which respectively represent the changes in the N^s_1 and N^s_2 ambiguity values in the phase observations of s at a current $(L^s)^{th}$ and $(L^s - 1)^{th}$ observation epochs of s; whilst $\triangle \rho^s$ is a change in metres, of the constituent parameters between the two epochs; $\triangle e_{\psi,P}$ is the $6{\times}1$ differenced error vector containing the errors in the corresponding observables in the $6{\times}1$ observable vector, $\triangle Y$; and H being a $6{\times}3$ design matrix. Consequently, the vector of unknowns, $\triangle X = [\triangle \rho^s, \triangle N^{s,gap}_1, \triangle N^{s,gap}_2]^T$, is estimated via least squares as

$$\triangle X = \left[H^T W H\right]^{-1} H^T W \triangle Y \tag{6.61}$$

thus providing the needed estimate of the cycle slips float values, $\triangle N^{s,gap}_1$ and $\triangle N^{s,gap}_2$. For a geodetic grade receiver, each error element in the $\triangle e_{\psi,P}$ error vector could be under 5 metres, and such error range affects the accuracy of the estimated $\triangle X$ vector.

Having estimated the post-gap dual-frequency cycle slip float values, the dual-frequency cycle slip fixing and validation are done as already presented in Subsections 6.4.1 and 6.4.2 above, to determine $\triangle N^{s,gap}_{1,int}$ and $\triangle N^{s,gap}_{2,int}$. NFCS is only implemented if condition (a) alone, and not (b), in Section 6.4.3 is satisfied. The (b)

condition is not considered because of the observation gap(s) between the current epoch and the last epoch prior to the gap. Finally, the phase observables are then corrected for the determined cycle slips as

$$\hat{\psi}_1^s(1:L^s) = \left\{\hat{\psi}_1^s(1:L^s-1) + \lambda_1 \triangle N_{1,int}^{s,gap},\ \psi_1^s(L^s)\right\} \quad (6.62)$$

$$\hat{\psi}_2^s(1:L^s) = \left\{\hat{\psi}_2^s(1:L^s-1) + \lambda_2 \triangle N_{2,int}^{s,gap},\ \psi_2^s(L^s)\right\} \quad (6.63)$$

6.8.3. Dual-Frequency Post-Gap Code Error Mitigation

Mitigating the code errors becomes a trivial process once the relative ionospheric delay and the cycle slip values have been determined. The procedure towards obtaining the error-mitigated code observables is just as presented in Section 6.6. That is, we first eliminate $I_1^{s,v}(L^s) = I_1^{s,v}(L^s - 1 + m\triangle t)$ and $\gamma I_1^{s,v}(L^s)$ from the current post-gap epoch's L1 and L2 raw code observations and cycle-slip-free phase observables of the gap satellite s, to generate the pseudo-iono-free code and phase observables, $\hat{P}_{IF,i}^s(L^s) = P_i^s - I_i^{s,v}(L^s)$ and $\hat{\psi}_{IF,i}^s(L^s) = \hat{\psi}_i^s(L^s) + I_i^{s,v}(L^s)$ respectively. By taking the difference between $\hat{P}_{IF,i}^s(L^s)$ and $\hat{\psi}_{IF,i}^s(L^s)$, the code multipath observables, $\hat{MP}_1^s(L^s) = \hat{P}_{IF,1}^s(L^s) - \hat{\psi}_{IF,1}^s(L^s)$ and $\hat{MP}_2^s(L^s) = \hat{P}_{IF,2}^s(L^s) - \hat{\psi}_{IF,2}^s(L^s)$ are obtained. The updated mean values $\langle MP_1^s(L^s)\rangle$ and $\langle MP_2^s(L^s)\rangle$ at the current epoch are computed as in Equations (6.48) and (6.49), giving

$$\langle MP_1^s(L^s)\rangle = \frac{1}{L^s}\left[(L^s-1)\left\{\langle MP_1^s(1:L^s-1)\rangle - \lambda_1 \triangle N_{1,int}^{s,gap}\right\} + \hat{MP}_1^s(L^s)\right] \quad (6.64)$$

$$\langle MP_2^s(L^s)\rangle = \frac{1}{L^s}\left[(L^s-1)\left\{\langle MP_2^s(1:L^s-1)\rangle - \lambda_2 \triangle N_{2,int}^{s,gap}\right\} + \hat{MP}_2^s(L^s)\right] \quad (6.65)$$

where $\triangle N_{1,int}^{s,gap}$ and $\triangle N_{1,int}^{s,gap}$ are the determined values of the cycle slips that may have occurred between the current post-gap epoch's phase observations and the phase observables at the pre-gap epoch. The zero-mean code errors, $\overline{e_{p_i}^s(L^s)} = \hat{MP}_i^s(L^s) - \langle MP_i^s(L^s)\rangle$, are computed; and finally, the smoothed or error-mitigated dual- frequency code observables, $\hat{P}_i^s$, are obtained after subtracting the estimated

zero-mean code error from the post-gap epoch's raw code observations, giving

$$\hat{P}_1^s(L^s) = P_1^s(L^s) - \overline{e_{p_1}^s(L^s)} \tag{6.66}$$

$$\hat{P}_2^s(L^s) = P_2^s(L^s) - \overline{e_{p_2}^s(L^s)} \tag{6.67}$$

where $\hat{P}_1^s(L^s)$ and $\hat{P}_2^s(L^s)$ are the resulting post-gap smoothed or error-mitigated dual-frequency code observables included in the code positioning of the receiver at the current post-gap epoch.

6.8.4. Generating Post-Gap Dual-Frequency Observables for ATD

The ATD process expects an undifferenced sequence with consecutively observed observable values, as input. A continuously observed satellite naturally enables the generation of an undifferenced time series of an observable from consecutive epochs, as needed by the ATD process. For a gap satellite s, this need by the ATD process is only met by 'adjusting' observables, i.e. generating seemingly continuous dual-frequency code and phase observables, to enable the use of the ATD process for cycle slips detection on subsequent observation epochs of s when it re-locks to the receiver after an observation. The steps for adjusting the code and phase observables are:

(a) Take the current l^s-length phase observables, which includes the current post-gap epoch's raw phase observations, that is,

$$\Upsilon_i^s(1:l^s) = \left\{\hat{\psi}_i^s(L^s - l^s + 1 : L^s - 1),\ \psi_i^s(L^s)\right\} \tag{6.68}$$

ATD is applied to the $\Upsilon_i^s(1:l^s)$ sequence with $d_s = d_s(L^s - 1)$, the adaptive-order of differencing determined at the last pre-gap epoch. The ATD process yields the phase ADSs, $\triangle^{d_s}\Upsilon_1^s$ and $\triangle^{d_s}\Upsilon_2^s$.

(b) Estimate the update values, υ_1 and υ_2, to be added to the past epochs L1 and

L2 band observables of s, respectively. These are obtained as

$$\upsilon_1 = \triangle^{d_s}\Upsilon_1^s(l^s - d_s) - \varepsilon_c^*(t) \tag{6.69}$$

$$\upsilon_2 = \triangle^{d_s}\Upsilon_2^s(l^s - d_s) - \varepsilon_c^*(t) \tag{6.70}$$

where $\triangle^{d_s}\Upsilon_1^s(l^s - d_s)$ and $\triangle^{d_s}\Upsilon_2^s(l^s - d_s)$ correspond to the last value of the Υ_1^s and Υ_2^s sequences respectively. The values, $\Upsilon_1^s(l^s - d_s)$ and $\Upsilon_2^s(l^s - d_s)$, indicate in metres, the difference between the current post-gap adaptively-differenced value and the pre-gap epoch's adaptively-differenced value. When a clock jump or reset is not detected at the current epoch, $\varepsilon_c^*(t) = \varepsilon_c(t)$, where $\varepsilon_c(t)$ is estimated for the current epoch from the observables of the continuously observed satellites at the current epoch (see Equations (5.6) and (5.7)), assuming that all satellites do not experience observation gap at the same current epoch. If a clock jump is detected, $\varepsilon_c(t) = \varepsilon_{c,jump}(t)$ and $\varepsilon_c^*(t) = 0$. This subtraction of $\varepsilon_c^*(t)$ in Equations (6.69) and (6.70) to obtain υ_i is necessary to ensure that the common receiver high-order variation value at the current epoch is maintained in subsequent ADSs to be obtained for the gapped satellite s in subsequent post-gap epochs.

(c) Finally the past epochs L1 and L2 phase and code observables are adjusted by adding the υ_1 and υ_2 values respectively, and subsequently, the L^s-length time series observables from s are generated thus

$$\hat{\psi}_1^s(1:L^s) = \left\{\hat{\psi}_1^s(1:L^s-1) + \upsilon_1,\ \psi_1^s(L^s)\right\} \tag{6.71}$$

$$\hat{\psi}_2^s(1:L^s) = \left\{\hat{\psi}_2^s(1:L^s-1) + \upsilon_2,\ \psi_2^s(L^s)\right\} \tag{6.72}$$

$$\hat{P}_1^s(1:L^s) = \left\{\hat{P}_1^s(1:L^s-1) + \upsilon_1,\ P_1^s(L^s)\right\} \tag{6.73}$$

$$\hat{P}_2^s(1:L^s) = \left\{\hat{P}_2^s(1:L^s-1) + \upsilon_2,\ P_2^s(L^s)\right\} \tag{6.74}$$

This adjustment completes the final step of this new gap-connect technique and the resulting time series $\hat{\psi}_i^s$ and $\hat{P}_i^s$ given by (6.71) through (6.74) are seemingly continuous observables obtained from a 'continuously' observed s. It is the last l_s- or W_L-length observables from the time series of $\hat{\psi}_i^s$ that are used in the ATD

process for cycle slips detection on s in the next epochs phase observations. Hence, in real-time processing, only the last W_L number of observables are really required to be updated and stored by the receiver.

6.9. Summary

Following the generation of dual-frequency adaptively differenced sequences (ADSs) acquired through an adaptive time differencing process, a dual-frequency phase-only-derived cycle slip detection, determination and correction - CSDC algorithm, is proposed. The algorithm is designed to detect all possible dual-frequency cycle slip pairs, even under a fairly active ionospheric condition. The cycle slip fixing and validation are simple procedures, requiring a 100-value search space and implemented for each individual cycle-slipped satellite, unlike the more computationally intensive LAMBDA method. The effect of the limitation of the dual-frequency CSDC algorithm is minimised by nulling of falsely detected and fixed cycle slips when possible. The introduced dual-frequency cycle-slip-resilient code error mitigation algorithm enables continuous code smoothing even in the presence of cycle slip occurrence. In addition, the proposed gap-connect technique - for use during an observation gap occurrence - makes the dual-frequency CSDC and code error mitigation algorithms robust to observation gap occurrences.

Chapter 7.

Single-Frequency Tests, Results and Discussion

This chapter presents single-frequency tests results obtained with the newly developed algorithms (cycle slip detection and fixing, improved ionospheric correction, and code observation error mitigation) presented in Chapter 5, and the discussion of the results based on some performance metrics. The tests are performed with single-frequency observations from GPS receivers in both static and kinematic modes. The tests include investigation of the performance of the single-frequency CSDC algorithm under simulated cycle slip conditions; and examining the positioning performance of the new error-mitigated code observables with and without simulated cycle slips. Accuracy of the developed single-frequency improved ionospheric model is also examined a receiver in the equatorial region and a receiver in the the mid-latitude region. Except stated otherwise, the tests were done with the software developed in C++ and MATLAB environments, at University College London (UCL).

Under the cycle slips tests in this chapter, the comparison of the positioning results from the newly developed algorithms (NEW) and the conventional code-carrier smoothing (Hatch filter (HFT)) methods, is only aimed at revealing the possible improvements achievable with the NEW method. The NEW method here, integrates the proposed simple cycle slip fixing and code error mitigation algorithms, and its improvement in positioning is measured relative to the standalone Hatch filter, which

does not integrate any cycle slip fixing method. As such, the comparison results from the methods should be so interpreted. It is envisaged that, if a conventional single-frequency cycle slip fixing algorithm is used alongside the Hatch filter, the positioning results to be obtained with such an integration, are bound to be more improved than the standalone HFT results presented in the cycle slip test sections of this chapter.

7.1. Single-Frequency Test Data

The static data used for the test were downloaded from ftp://cddis.gsfc.nasa.gov, as provided by NASA/JPL, for station MBAR - an IGS station in Uganda in the equatorial region. The 1Hz downloaded data were recorded by an Ashtech UZ-12 GPS receiver at MBAR on day 170 of 2009, starting from the 468000^{th} second of GPS week 1536. Though the downloaded data recorded dual-frequency GPS code and phase observations, only the L1 band phase and code observations are used for the single-frequency tests and analyses involving MBAR in this chapter.

The kinematic data was collected in May 2008 in a marine environment to enable analysis of such data with regards to the International Maritime Organisation (IMO) positioning requirements for future GNSS constellations (Parkins, 2009). The GPS observation data were recorded from onboard a vessel, THV Alert, hereafter referred to as SHIP, that navigated into Harwich Habour, United Kingdom. The SHIP made several approaches to the jetty, recreating port approach and docking, thereby making many turns during the observation period. The SHIP, which was moving at less than 4km/hr, had a Topcon GR-3 GPS receiver mounted on the stern of it for dual-frequency GPS code and phase observations. Done on day 122 of 2008, the recorded 1Hz data started from the 412328^{th} second of GPS week 1477. Again, though the dual-frequency code and phase observations were recorded with this receiver in kinematic mode, the single-frequency tests involving SHIP in this chapter are performed using only the L1 single-frequency phase and code observations.

For all the days of observations, the corresponding GPS broadcast navigation files, obtainable from any of the IGS centre's website, were used where necessary.

7.2. Performance of the new Single-Frequency CSDC Algorithm

The performance of the CSDC algorithm for cycle slip detection, determination and correction, was tested with the L1 single-frequency phase observations recorded by the static MBAR and the moving SHIP. The test involved simulation of cycle slip values randomly generated from between -100 to +100 cycles, and adding them to the L1 single-frequency phase observation at every τ_{slip} =20 epochs interval. At a 20-epoch cycle slip simulation interval, and at same test epochs, a total of 1080 cycle slips were simulated for six selected satellites observed by MBAR, while a total of 900 cycle slips were simulated for five selected satellites observed by SHIP. The average number of satellites observed by MBAR was greater than SHIP's.

For the static MBAR, the CSDC algorithm attained a 100% correct detection (detected all 1080 simulated cycle slips) of which 1038 (96.1%) were correctly fixed to their integer values. The result from one of the satellites (PRN 7) from among the six satellites observed by MBAR that were selected for cycle slip test, is shown in Figure 7.1.

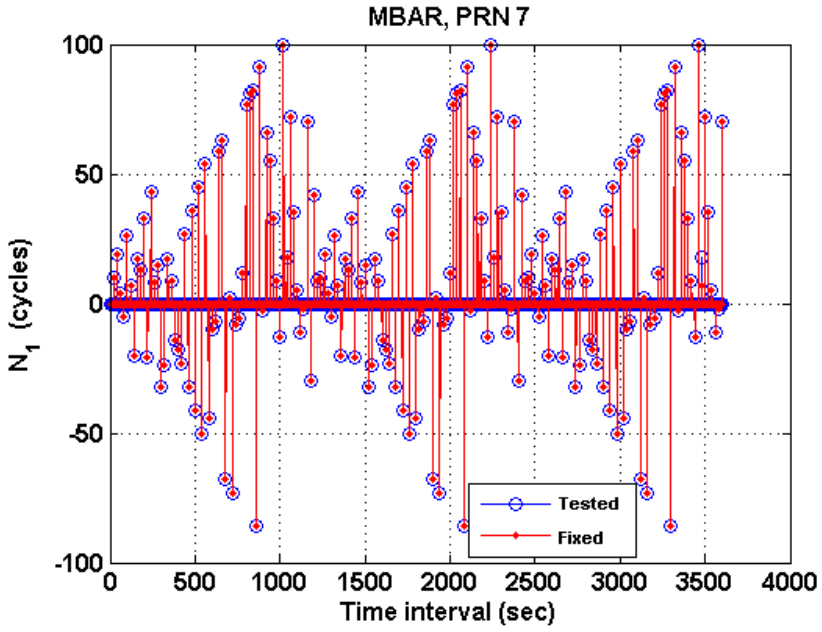

Figure 7.1.: Tested and fixed single-frequency cycle slips on static MBAR receiver

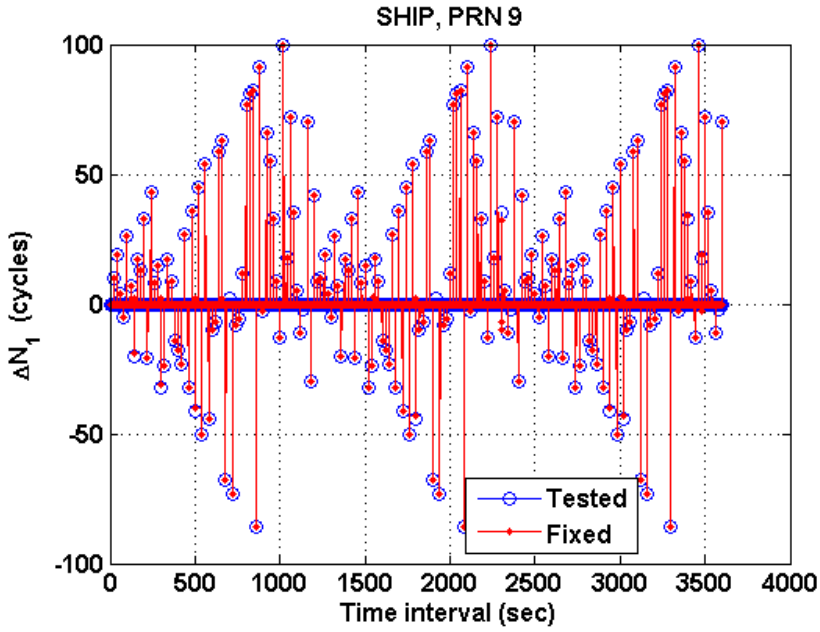

Figure 7.2.: Tested and fixed single-frequency cycle slips on moving SHIP receiver

The results from SHIP cycle slip simulation given in Figure 7.2 also indicated a 100% detection (detected all 900 simulated cycle slips) and attained 91.9% (828 of 900) correct fix. From the results, it was observed that most of the wrongly fixed cycle slips occurred at the same test epochs across all satellites observed by MBAR or SHIP, or were wrongly fixed with a maximum difference of 2cycles error. The imperfection in the cycle slip fixing could be as a result of out-of-range estimated cycle slip float values due to errors on the ADSs at such test epochs, or possibly due to wrongful nulling of fixed cycle slips (NFCS). It was also realised that the single-frequency CSDC algorithm generally achieves better cycle slip fixing performance with a static receiver than with a moving (SHIP) receiver even with different or the same cycle slip values. The average correct detection and average correct fix of cycle slips obtained from repeated tests via simulation were more than 98% and 92% respectively, for both the static MBAR and kinematic SHIP receiver.

7.3. Accuracy of the Improved Ionospheric Correction

The accuracy obtained with the algorithm for the improved ionospheric correction (IIC) model was investigated with the static MBAR station in the equatorial region and the moving SHIP in the mid-latitude region. The availability of the dual-frequency observation from both MBAR and SHIP receivers enabled the generation of the dual-frequency phase-only relative ionospheric delay that is only used as a 'truth' model to examine the accuracy of the IIC. The dual-frequency phase-only relative ionospheric delay is the ionospheric delay computed from using only the time series dual-frequency phase observations, as in Momoh (2012). Figure 7.3 shows the relative ionospheric correction plots for PRN 4 and PRN 15 observed by MBAR and SHIP respectively, each satellite decreasing in elevation angle with respect to its observing receiver. PRN 4 was observed by the MBAR receiver in the equatorial region, and it was selected, as an example, to reveal the possible degradation in ionospheric correction accuracy in the Klobuchar model that employs an elevation-dependent mapping function. PRN 15 was observed by the SHIP receiver in the mid-latitude, and it was selected, also as an example, to reveal a possible decrease in accuracy when using the same model for a decreasing-elevation satellite in mid-latitude. We can observe the improvement of the IIC model over the broadcast Klobuchar model for both the receiver at the equatorial and the receiver at mid-latitude regions. As expected, the Klobuchar model provided lower accuracy correction for the MBAR satellite observed by the receiver in the equatorial region; with the error increasing as the satellite elevation decreases, to over 1m within the 1hour observation interval. Though the Klobuchar model achieved a better ionospheric correction accuracy for the satellite observed by the mid-latitude SHIP receiver when compared to the correction accuracy for PRN4 observed by MBAR, but it was still accompanied with up to 0.75m error within the 1hr observation interval.

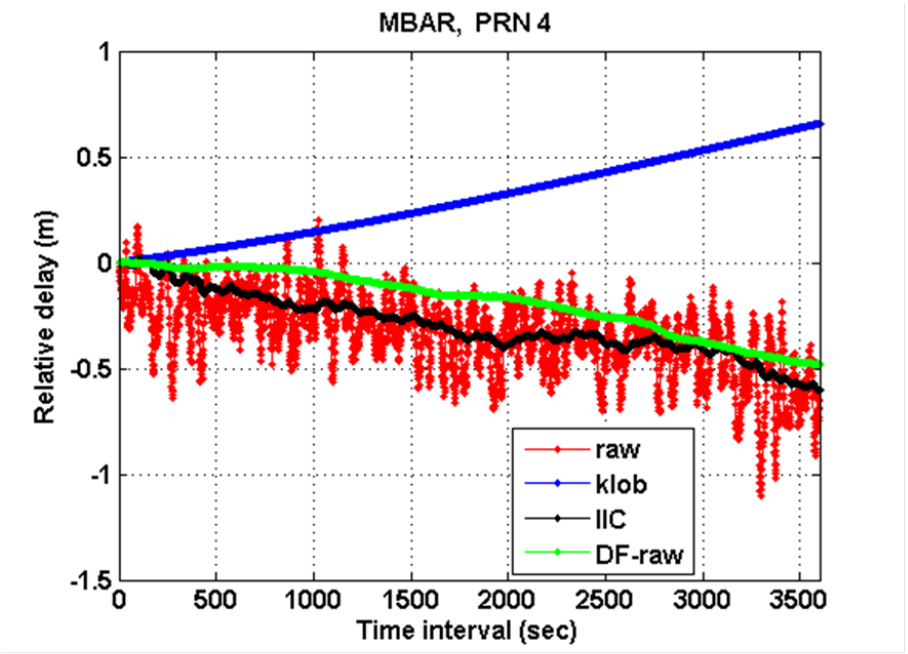

(a)

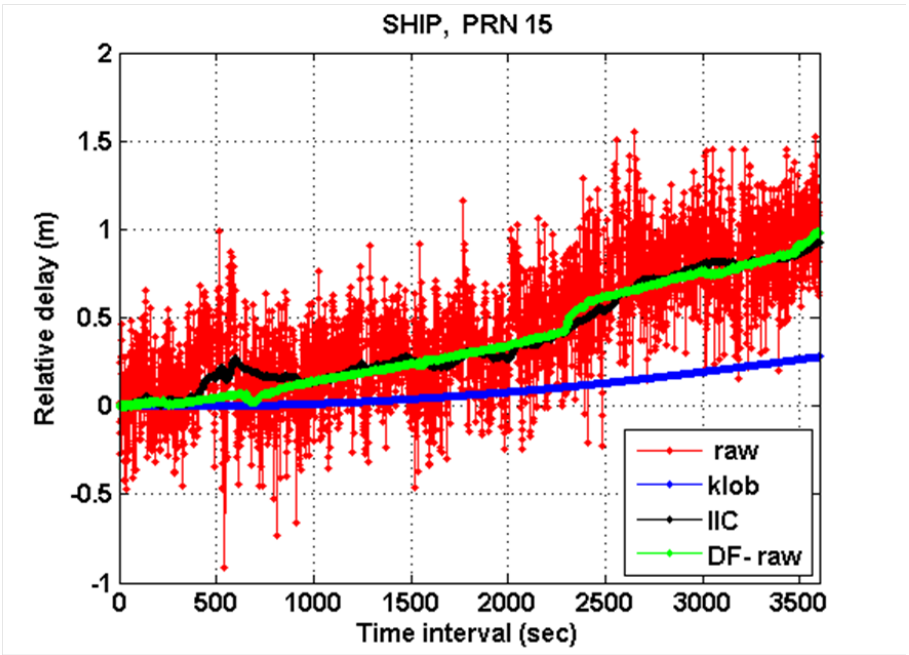

(b)

Figure 7.3.: Comparison of relative ionospheric corrections (a) correction plots for PRN4 observed by MBAR in the equatorial region; (b) correction plots for PRN15 observed by SHIP receiver in the mid-latitude region. The '**raw**' is the raw ionospheric observable, '**klob**' is the broadcast Klobuchar model, '**IIC**' is the improved ionospheric correction and model '**DF-raw**' is the raw dual-frequency phase-only ionospheric observable. All plots are the relative ionospheric delays relative to the first epoch ionospheric delay value, hence they all start at zero delay.

The IIC model achieved a higher correction accuracy for both satellites observed by MBAR and SHIP, giving less than 0.2m error in the 1hr observation interval of both satellites. The IIC model's improvement over the Klobuchar model is believed to be due to its independence on satellite elevation by way of a mapping function, unlike the Klobuchar model that uses an elevation dependent mapping function. Also the applied filtering technique shows good mitigation capability of the error levels in a generated single-frequency ionospheric observable, $I_R^{s,v}$. Similar performance results were also observed for some of the other satellites observed by MBAR, and by SHIP.

7.4. Single-Frequency Positioning Performance

The positioning performance of the new method which integrates the algorithms for single-frequency CSDC, IIC model and code error mitigation, all presented in Chapter 5, was evaluated using single-frequency observations recorded by the static MBAR and moving SHIP receivers. The point positioning (using only code observables) with and without known (simulated) cycle slips occurrences, were examined. Essentially, single-frequency point positioning is done using range-domain smoothed code observations in a least square algorithm or via a Kalman filter implementation. Since the newly developed code error mitigation algorithm is employed in the range domain, the least squares (Cross, 1983) point positioning results are compared to the point positioning results obtained with the widely used range domain single-frequency carrier-smoothed (Hatch filter) code observables, so as to examine and compare their performances. Following from Section 5.2.2, it is assumed that the residual errors on the code observations/observables after filtering or smoothing the raw code observations/observables, are uncorrelated and homoscedastic. Hence, in the least squares positioning algorithm, a diagonal (unity) weight matrix is used. As already discussed, the Hatch filter technique (HFT) is simple and it is implemented with a fixed filter length M, as given by Equation (3.6), to generate the HFT code observables.

The 'truth' position of the static MBAR receiver was obtained as the nominal

position given in the header of its rinex file. However, it is known that this position is essentially an approximated true position and not really the known true position of the receiver on the said day. The 'truth' trajectory of the moving SHIP receiver was obtained with Leica GeoOffice processing software. Using the dual-frequency data obtained with a fixed master receiver that was installed within a few kilometres from the moving SHIP during the data collection, and treating the moving SHIP's receiver as the rover receiver, dual-frequency relative positioning with Leica GeoOffice processing software was performed to determine the 'truth' trajectory of the SHIP.

The positioning solutions denoted as 'HFT' in this chapter, are the single-frequency code positioning solutions obtained by using the Hatch filtered (carrier smoothed) code observables that have been further corrected for the ionospheric delay on the HFT code observable using the broadcast Klobuchar ionospheric model, for each of the observed satellites at a given epoch, prior to using the resulting code observables in the least squares positioning code-only algorithm. The positioning solutions denoted 'RAW' are the single-frequency positioning solutions obtained with the raw (unsmoothed) code observations that are only corrected for ionospheric delay using the broadcast Klobuchar ionospheric model, for each of the observed satellites at a given epoch, prior to the least squares code-only positioning. The positioning solutions denoted 'NEW' (the new method) in this chapter, are the single-frequency code positioning solutions obtained by using the error mitigated code observables that have been further corrected for ionospheric delay using the IIC model, for each of the observed satellites at a given epoch, prior to the least squares code-only positioning. It should be recalled that an error-mitigated code observable is generated subsequent to CSDC.

7.4.1. Single-Frequency Static Positioning Results

Firstly, the new method was used in obtaining positioning solutions for the static MBAR receiver using the true data - the actual receiver recorded observations without any alterations through simulation of cycle slips or code errors, and without any prior processing to correct possible presence of cycle slips in the data. For

an observation period of one hour, using the raw (RAW) - unsmoothed code observations from the true data; the HFT smoothed code observables obtained with different Hatch filter lengths of $M = 50, 100, 200$; the respective RAW and HFT code positioning results were also obtained for comparison with the positioning results from the new (NEW) method. The obtained 2D and 3D positioning solutions using the raw (RAW) - unsmoothed code observations; the Hatch smoothed code (HFT) observables; and the new (NEW) method, are shown in Figure 7.4. The statistics of the solutions are presented in Table 7.1. The table reveals the up to 24% improvement in the NEW solutions over the RAW solutions, and the different filter lengths HFT smoothed code solutions achieved between 2-4% improvement over the RAW solutions. The NEW solutions are also observed to be more accurate than the HFT solution, with the most improvement observed in the height (Up) component. It is fairly obvious that all the three positioning solutions indicate offsets from the assumed truth position of the static MBAR receiver. This offset could be due to the low accuracy of the initial ionospheric delay correction value, $I^{s,0}_{Klob}$, for each observed satellite at the very first receiver observation epoch, which was obtained from the broadcast Klobuchar model and was used as the reference (first observation epoch ionospheric delay for any of the satellites) for all three positioning solutions; the impact of possible code errors on satellites' code observations at the very first receiver observation epoch, which is not mitigated in $\overline{P^s_{1,hft}}$ nor in $\overline{P^s_1}$; and/or the possibility that the assumed truth position of the MBAR receiver as obtained from the rinex file was not accurate enough. Improvement in the positioning accuracy of the NEW method is evident in the divergence towards zero error (especially in the Up component), unlike in the solutions of the other methods. Two possibilities may be identified for this divergence that indicates improvement. Firstly, the achieved ionospheric correction improvement of the IIC model used in the NEW method, especially for low elevation or decreasing-elevation satellites such as PRN 4 (see Figure 7.3(a)), translates to significant improvement in the positioning solution. Secondly, it is believed that there were actual cycle slips between the 950-3600th observation epochs of the actual raw data (see Figure 7.5), which would have been detected and fixed by only the NEW method, as it has the capability to do so. The divergence,

more pronounced in the height component, contributed to the achieved 3.23m RMSE in the Up direction as against the 4.41m achieved by the RAW method, which is shown in Table 7.1.

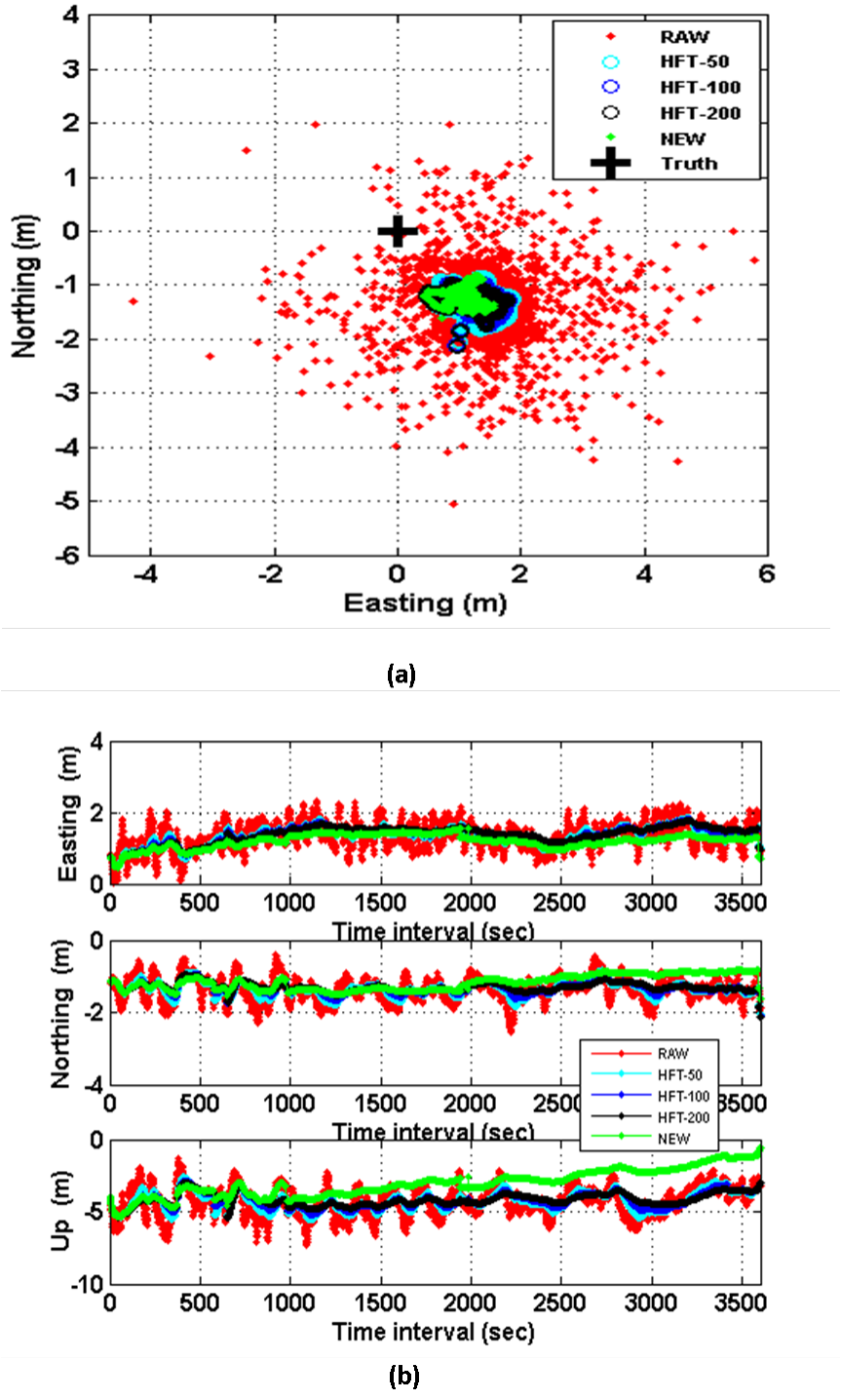

Figure 7.4.: MBAR positioning solutions using the true data - without simulated cycle slips and code errors applied: (a) 2D positioning and (b) 3D positioning

Table 7.1.: Statistics for the MBAR positioning solutions in Figure 7.4

Type	East (m)		North (m)		Up (m)		Combined RMSE improvement over ' RAW'
	RMSE	sigma	RMSE	sigma	RMSE	sigma	
RAW	1.39	0.37	1.41	0.33	4.41	0.99	-
HFT_50	1.37	0.25	1.37	0.20	4.34	0.66	2%
HFT_100	1.38	0.25	1.34	0.16	4.28	0.54	3%
HFT_200	1.40	0.25	1.31	0.12	4.20	0.44	4%
NEW	1.21	0.19	1.20	0.22	3.23	1.00	24%

For single-frequency code smoothing, the HFT with $M = 100$ is highly recommended and used (e.g. for LAAS) as it is presumed a good enough filter length to achieve acceptable trade-off between resulting ionospheric divergence effect and the smoothness of the HFT smoothed code observable. Moreover, since the $M = 100$ filter length HFT presents a lesser ionospheric divergence effect than the $M = 200$ HFT, and based on their comparable positioning results seen in Figure 7.4 and the statistics on Table 7.1, subsequent HFT positioning results in this chapter are processed with $M = 100$ filter length.

The d adaptive-order of differencing was observed to vary between 2 to 4 for all satellites in the 1hour MBAR observations used, even though 3 was found to be the modal value. The estimated MBAR receiver's clock high-order variation, ε, for the 1hr observation interval is shown in Figure 7.5. The receiver clock at MBAR was a crystal oscillator clock. There was no clock jump or reset detected within the 1hr observation interval used, and the high-order variations are estimated and found to be under half a meter with a 1-sigma of $\sigma_\varepsilon = 5.43$cm and mean $\mu_\varepsilon = 0.02$mm, within the 3600 observation epochs. On further investigation, it was found that there were eight observation epochs, some of which are indicated with arrows in Figure 7.5, where the single-frequency CSDC algorithm indicated cycle slips for all the observed satellites at those epochs; and the estimated ε was greater than 0.2m at each of those eight epochs. Of course a 0.2m between-epoch drift on the receiver clock can trigger a false detection of cycle slip on all satellites, going by the detection threshold of one wavelength (see Equation (5.5)), even though some or all of the eight cycle slip detected epochs may not be false cycle slip epochs.

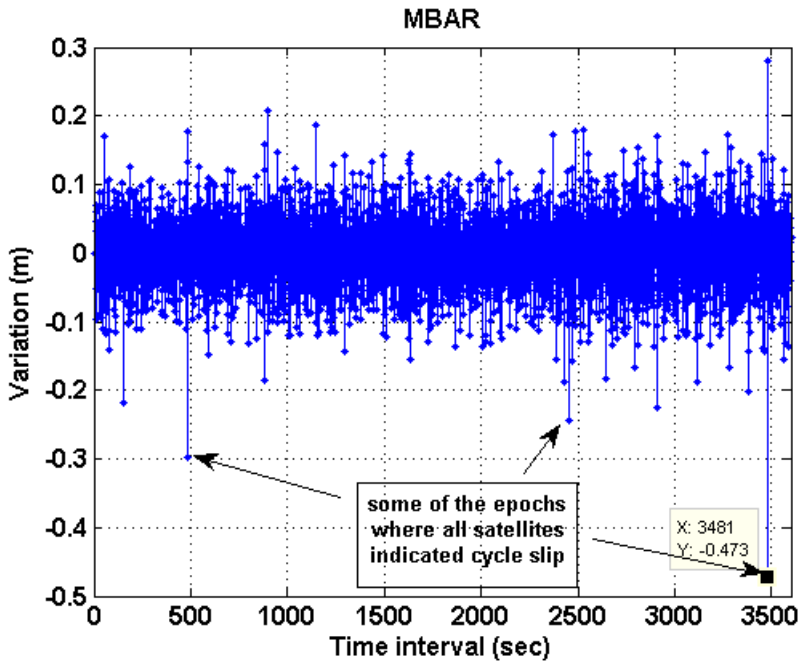

Figure 7.5.: Estimated common receiver clock high-order variation for MBAR receiver

The code error impact on estimated $\varepsilon(t)$ is expected since the code observations and consequently the code errors would have been included in determining $\varepsilon(t)$ whenever all satellites indicate cycle slip occurrence at a given epoch. At such epochs, $\varepsilon(t)$ may not be accurately determined and consequently, all satellites' cycle slips may not also be accurately fixed. For instance, the clock drift of -0.473m at the 3481 observation epoch, shown in Figure 7.5 is suspicious; chances are that both the $\varepsilon(t)$ and some, if not all of the satellites cycle slips, if there were, may have been fixed incorrectly.

7.4.1.1. Single-Frequency Static Positioning in the Presence of Cycle Slips

The performances of the single-frequency CSDC algorithm under frequent cycle slip occurrence and possible higher code error on the code observations, which are typical with single-frequency positioning especially in a challenged environment, were investigated. The performance tests were done by introducing, by way of simulation, known cycle slips on the phase observation, and code error values when intended, on the code observation, for different satellites at known test epochs (see Section 4.5 for the simulation procedure).

For the following cycle slip test scenarios, the comparison of the positioning results with the conventional code-carrier smoothing technique, which is the Hatch filter, is only intended to reveal the level of performance improvement of the new method over the standalone Hatch filter that has no cycle slip fixing capability. The NEW method integrates the proposed code error mitigation algorithm and the simple single-frequency cycle slip fixing algorithm, without significant additional computational load.

The cycle-slip-only test for the static MBAR receiver here, involved the use of known cycle slip values randomly generated from between -100 to 100cycles at certain observation epochs selected for the cycle slip test on different satellites. The cycle slips were simulated for all the single-frequency phase observations from all but one observed satellite by the MBAR receiver. The one satellite (PRN28 that was observed throughout the 1 hour observation period) was excluded so as to minimise the number of epochs that the common receiver clock high-order variations would be estimated without involving any code observations. The cycle slips were simulated at the same epochs (test epochs separated by 20-epochs) for all cycle-slip-test satellites, within the 1hour observation period of 3600 epochs. Figure 7.6 shows the 2D Easting-Northing horizontal positioning results while the statistics are presented in Table 7.2. The offsets in Figure 7.6 can be attributed to the same reasons initially given in Section 7.4.1 for the offsets in Figure 7.4(a). The test results show that, of the total 1768 simulated cycle slips, the single-frequency CSDC algorithm correctly detected 1766 (99.9%) cycle slips and fixed correctly 1710 (96.7%) cycle slips, consequently achieving 29% improvement over the HFT positioning solutions. It should be noted that the simulation procedure indicates a cycle slip flag to the HFT algorithm whenever a cycle slip is simulated but the new single-frequency CSDC algorithm detects and corrects for cycle slip on its own.

Since the MBAR receiver is actually a dual-frequency geodetic receiver, the code error values on the raw code observations from the observed satellites are relatively lower than the typical error range on actual single-frequency receiver's code observation. Hence, a combined cycle slip and code error test was further done using the same MBAR single-frequency data. The additional code error values to the satel-

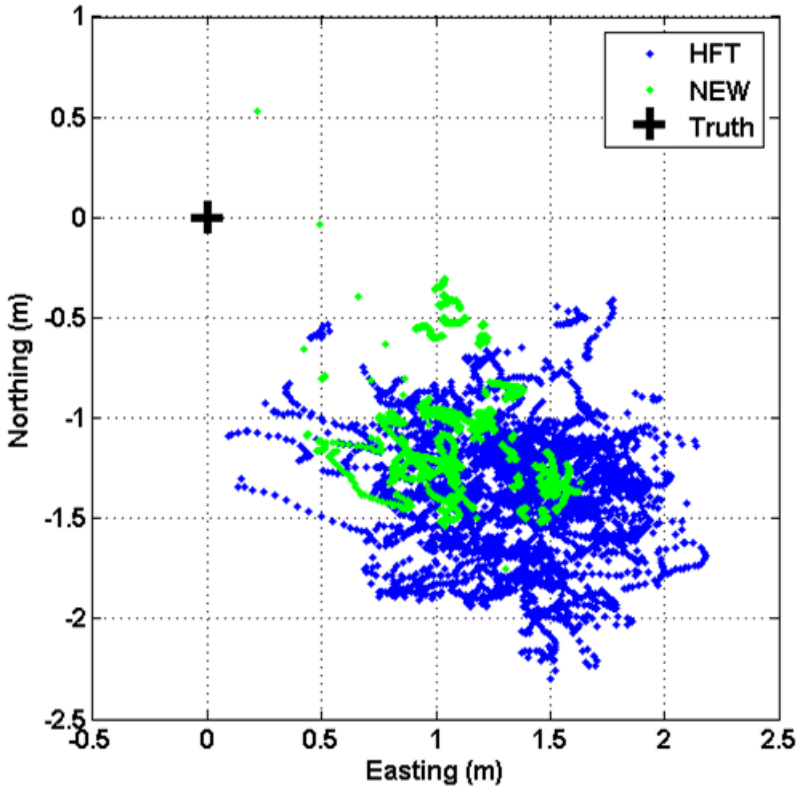

Figure 7.6.: MBAR 2D positioning, with simulated cycle slips applied to all but one satellite at same epochs

lites code observations was done to simulate more realistic code error values such as could be associated with a single-frequency receiver; and to enable the investigation of the improvement of the new method's CSDC and code error mitigation capability in the presence of both cycle slips and high code errors, which are very likely in a relatively difficult environment. The simulated cycle slip values were randomly chosen from between -100 to 100cycles and the code errors were randomly chosen from between -20m to 20m, and respectively applied to the phase and code observations observed at same test epochs, for each of the cycle-slip-test satellites. The test involved all but one satellite (PRN28 as before). The obtained positioning solutions are presented in Figure 7.7 while the corresponding statistics are presented in Table 7.3. The results indicate that the same 99.9% of the total 1768 simulated cycle slips were detected correctly and 96.5% (1706) of the total cycle slips were correctly fixed, obviously because the ATD cycle slip detection process is independent of the code observation. Compared to the previous results from the cycle-slip-only test above,

Table 7.2.: Statistics for the MBAR positioning solutions in Figure 7.6 with simulated cycle slips within ±100cycles for all satellites, at the same epochs

Type	East (m)		North (m)		Up (m)		Simulated slips			Combined RMSE improvement of 'NEW' Over HFT
	RMSE	sigma	RMSE	sigma	RMSE	sigma	Not available			
HFT	1.38	0.35	1.40	0.32	4.40	0.94				29%
NEW	1.23	0.25	1.13	0.31	3.01	1.04	Total slips 1768	Detected 99.9%	Fixed 96.7%	

$1710 - 1706 = 4$ more cycle slips were not fixed correctly, and that was traceable to epoch 3480 where all observed satellites indicated cycle slips via an ATD process, and as such, two code observations were included in estimating ε_c. As seen in Figure 7.5, a large $\varepsilon_c(3481) = -0.473$m was estimated without code errors nor cycle slips simulation, leading to the perception that the two used code observations with the additional simulated code errors affected the cycle slips float values and ε_c, and consequently impaired the correct fixing of the 4 cycle slips that occurred on four out of the nine satellites simulated for cycle slip at the 3480^{th} epoch. The performance of the new method however resulted in 42% improvement in positioning accuracy over the HFT with $M = 100$ filter length, as it never had to re-initialise the code error mitigation process but continuously detected and corrected for cycle slips whenever cycle slip occurred. The most improvement over the HFT is observed in the height component (by 42.4%). The level of divergence in the positioning solution of NEW in Figure 7.7(b) can be traceable to the same reasons initially given in Section 7.4.1 for the divergence of the NEW solutions shown in Figure 7.4(b), while the offsets in Figure 7.7(a) can be attributed to the reasons initially given in Section 7.4.1 for the offsets in Figure 7.4(a). It can also be observed from the 2D plots of Figure 7.7 that the HFT produces almost the same positioning solutions as with RAW at every 20-epoch test interval when cycle slips were simulated for all but one satellite. This indicate the low performance level improvement achievable with the HFT in a frequent cycle slip scenario. The HFT positioning solutions are also observed to have produced the worst statistical results (Table 7.3) among the three positioning solutions compared in this case.

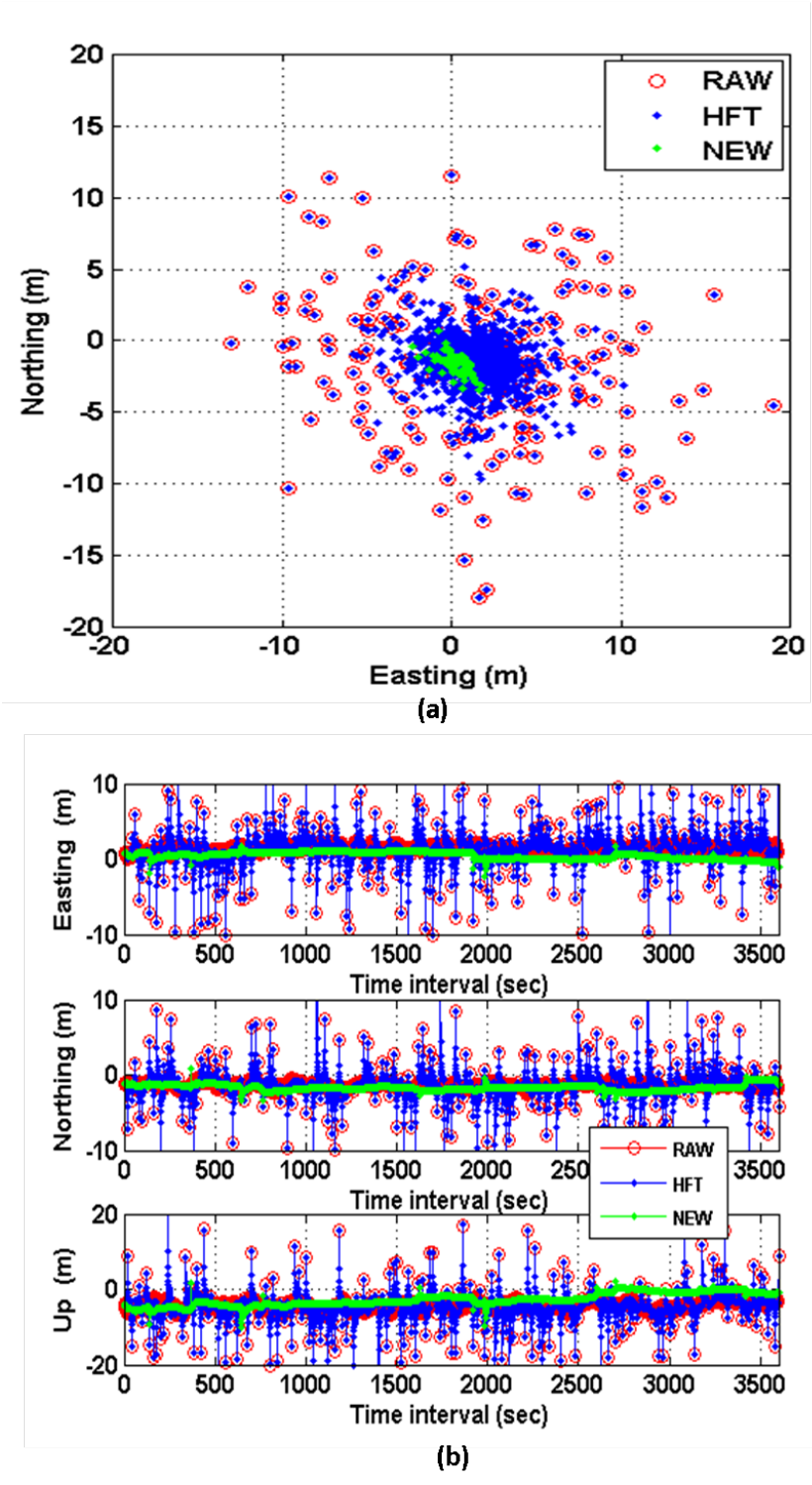

Figure 7.7.: MBAR 2D (top) and 3D (bottom) positioning solutions, with simulated cycle slips and code errors applied at same epochs

Considering the more common scenario where cycle slips occur on the phase observations of different satellites at different observation epochs, the performance of

Table 7.3.: Statistics for the MBAR positioning solutions in Figure 7.7, with simulated cycle slips within ±20cycles and code errors within ±20m applied at same epochs to the different satellites

Type	East (m)		North (m)		Up (m)		Simulated slips			Combined RMSE improvement of 'NEW'	
	RMSE	sigma	RMSE	sigma	RMSE	sigma	Not available			over RAW	Over HFT
RAW	1.97	1.43	1.87	1.27	5.09	2.58					
HFT	2.23	1.78	2.12	1.58	5.57	3.14				36%	42%
NEW	0.64	0.64	1.73	0.39	3.21	1.71	Total slips 1768	Detected 99.9%	Fixed 96.5%		

the new method under such a scenario was further investigated through simulation. Under this simulation, lower cycle slip values randomly generated from between -10 to 10cycles, and code error values randomly generated from within -10 to 10m, were applied respectively to the same epoch's phase and code observations of each satellite respectively, as described in 4.5. The simulation was done for all observed satellites, at different epochs for the different observed satellites, as specified by Equation (4.14), but at the same 20-epoch simulation interval. This test was also to enable examination of the efficiency of the proposed single-frequency CSDC algorithm in detecting and fixing smaller magnitude cycle slips on even phase observations, and to access the positioning improvement in the event of smaller code errors. The positioning solutions obtained with RAW, HFT and NEW methods under this simulated scenario are presented in Figure 7.8, while the corresponding positioning statistics are presented in Table 7.4.

In the case of lower cycle slip values from within -10 to 10cycles, we observe a lower percentage detection of 97.3% out of the total 1199 cycle slips, compared to the 99.9% out of the total 1768 cycle slips obtained in the previous simulation of comparatively larger cycle slip values from within -100 to 100cycles, above. The reduction in detection can be attributed to the possible increase in cycle slips with values 1 and 2 cycles, which have lower probability of detection with the CSDC algorithm because of the possible destructive combination of such cycle slips equivalent (in metres) with the differenced errors (see Equation (5.3) and Figure 5.2).

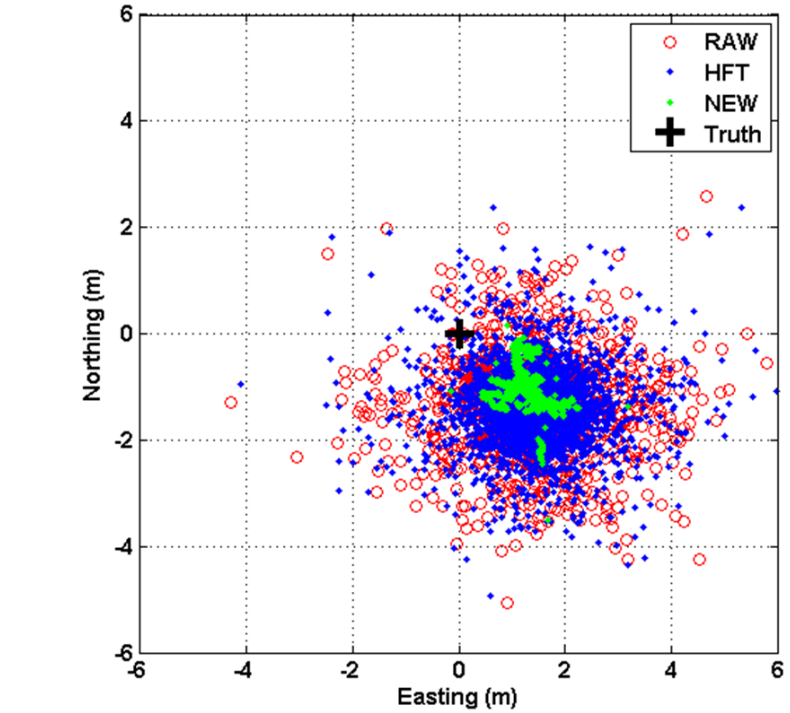

(a)

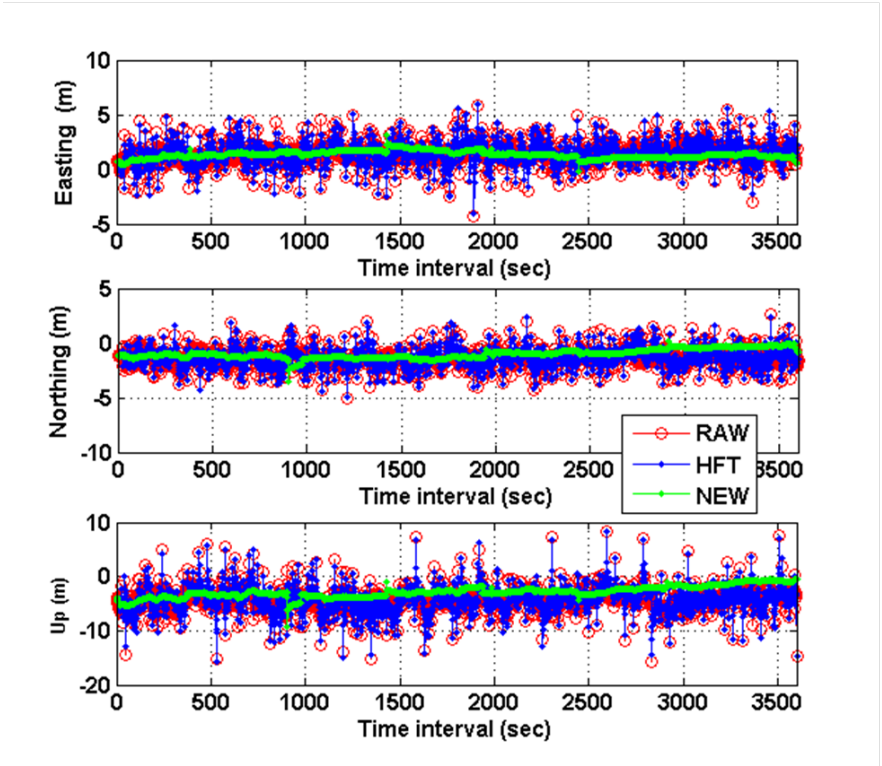

(b)

Figure 7.8.: MBAR positioning solutions, with simulated cycles slips from within ±10cycles and code errors from within ±10m, applied at different epochs to the different satellites: (a) 2D positioning and (b) 3D positioning

Table 7.4.: Statistics for the MBAR positioning solutions in Figure 7.8, with simulated cycle slips within ±10cycles and code errors within ±10m , applied at different epochs to the different satellites

Type	East (m)		North (m)		Up (m)		Simulated slips			Combined RMSE improvement of 'NEW'	
	RMSE	sigma	RMSE	sigma	RMSE	sigma	Not available			over RAW	Over HFT
RAW	1.54	0.72	1.50	0.60	4.63	1.71					
HFT	1.66	0.85	1.54	0.70	4.77	2.01				31%	34%
NEW	1.38	0.32	1.07	0.41	3.03	1.06	Total slips 1199	Detected 97.3%	Fixed 94.6%		

However, with the achieved 94.6% correct fix of the 1199 cycle slips from within -10 to 10cycles, the new method achieved 31% and 34% positioning accuracy improvements over the RAW and HFT positioning results respectively. The results again indicate the most improvement in the height components (Up) - more than 47% and 36% improvements over the HFT in height precision and accuracy respectively. The level of divergence in the positioning solution of NEW in Figure 7.8(b) can be traceable to the same reasons given in Section 7.4.1 for the divergence of the NEW solutions shown in Figure 7.4(b), while the offsets in Figure 7.8(a) can be attributed to the reasons initially given in Section 7.4.1 for the offsets in Figure 7.4(a).

7.4.2. Single-Frequency Kinematic Positioning Results

The performance of the new method (NEW) was further investigated for a kinematic receiver, SHIP. Firstly, using the true data, which is the observation data as recorded by the receiver on the moving SHIP without any alterations in form of cycle slips or code error simulations, and without any prior processing to correct for possible presence of cycle slips in the data; positioning solutions were obtained for the moving SHIP receiver using the RAW code observables, the HFT code observables with $M = 100$, and the NEW code observables, for an observation period of one hour.

The different positioning solutions are presented in Figure 7.9, and the corresponding positioning statistics given in Table 7.5. The HFT and NEW achieved 12% and 11% positioning accuracy improvement over the RAW, respectively. The 1% better performance indicated by the HFT over the NEW here, resulted from epoch 2888 where a clock jump of 1ms was detected to have been introduced to the receiver

clock, and the sensitivity of the CSDC algorithm, of course, identified it has cycle slips on all observed satellites at epoch 2888, which were not nulled, but were rather fixed to false integer values after 'eliminating' the estimated clock jump, mostly because of the inclusion of the two code observations in the estimation of the common receiver high-order variation and cycle slip float values.

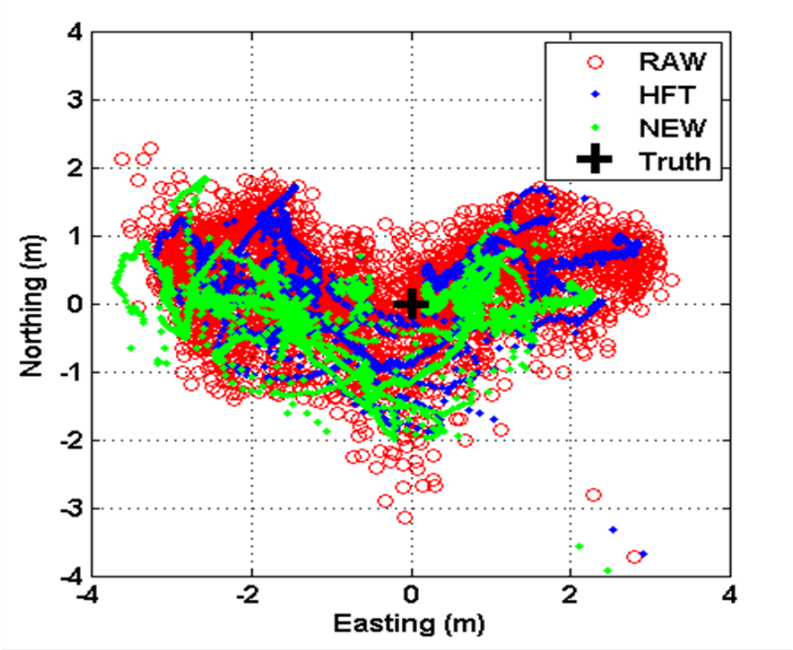

(a)

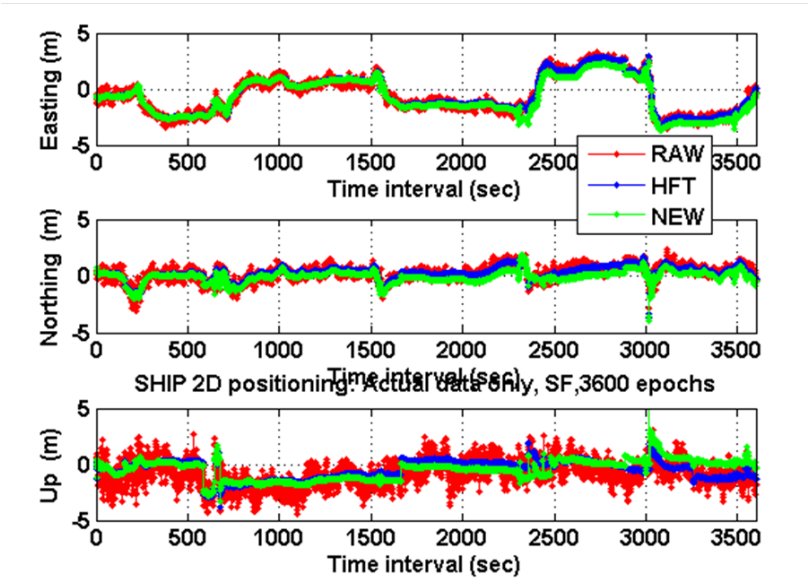

(b)

Figure 7.9.: SHIP positioning solutions with true data - without simulated cycle slips and code errors applied: (a) 2D positioning and (b) 3D positioning

The inclusion of two code observations in the CSDC algorithm when all satellites indicate cycle slips is a limiting factor for the new method, especially when the set criteria for nulling fixed cycle slips are not met (Section 5.2.3). Falsely fixed cycle slips were however observed to be within a few cycles (typically 1-3cycles) as observed from the test of the CSDC algorithm. Figure 7.10 shows the instantaneous (epoch by epoch) estimation of the common receiver clock high-order variation, ε_c, where a 1ms clock jump was detected at epoch 2888. The ε_c variations are estimated to be under half a meter with a standard deviation of $\sigma_\varepsilon = 3$cm and mean $\mu_\varepsilon = -0.36$mm, excluding the epoch of clock jump. As with the static MBAR, the adaptive-order of differencing, d, was also observed to vary between 2 to 4 for all satellites, in the 1 hour observation data of SHIP used but 3 was found to be the modal order.

Table 7.5.: Statistics for the SHIP positioning solutions in Figure 7.9

Type	East (m)		North (m)		Up (m)		Combined RMSE improvement over ' RAW'
	RMSE	sigma	RMSE	sigma	RMSE	sigma	
RAW	1.75	1.65	0.72	0.68	1.32	1.15	-
HFT	1.71	1.63	0.63	0.58	0.91	0.79	12%
NEW	1.78	1.60	0.50	0.52	0.90	0.88	11%

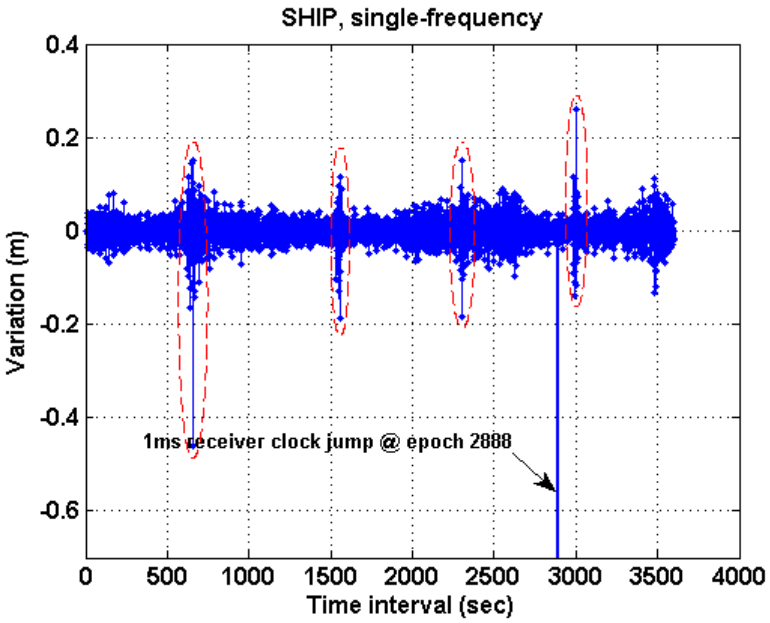

Figure 7.10.: Estimated common receiver clock high-order variation

7.4.2.1. Single-Frequency Kinematic Positioning in the Presence of Cycle Slips

The performance of the new method under the impact of frequent cycle slip was also examined with the kinematic SHIP receiver. Simulated cycle slip values randomly generated from within -10 to 10cycles and code error values randomly generated from within -10 to 10m, were applied respectively to the test epochs' phase and code observations from a given satellite. The simulation involving all observed satellites was done at 20-epoch test interval for each of the satellites, but at different test epochs for different satellites, following the procedure described in Section 4.5. Apart from investigating the kinematic mode performance of the new method, this simulation also enabled the investigation of the efficiency of the new method under small cycle slip values occurrences, with a kinematic receiver. The obtained positioning solutions from using the RAW, HFT and NEW code observables are given in Figure 7.11, whilst the corresponding positioning statistics are presented in Table 7.6. The results indicate that 98.0% of the total 920 simulated cycle slips were detected and 79.8% of the 920 cycle slips were correctly fixed, resulting in 25% improvement in positioning accuracy over the HFT with $M = 100$. The most improvement is observed in the height component (44%). The lower fixed rate of 79.8% (compared to the 94.6% achieved in the static mode) in this kinematic mode could be due to the dynamics of the receiver antenna, even though a different set of randomly generated cycle slips was used. This lower fixing of cycle slips could be due to possible phase wind-up effect, jerks in motion of SHIP, the effect of the common receiver clock high-order variations that may not always be accurately modelled due to the presence of the errors on the ADSs, and possible high antenna dynamics. Recalling that repeated turns, in the course of navigation and approaches, were made by the moving SHIP, the effect of antenna dynamics cannot be ruled out. The trajectory of the moving ship is shown in Figure 7.12. The trajectory is far from a regular pattern of motion even though the speed of the SHIP was under 4km/hr, and as such there should be likely presence of receiver antenna dynamics and phase wind-up effects that could be significant enough to impair the fixing of single-frequency cycle slip with the CSDC algorithm.

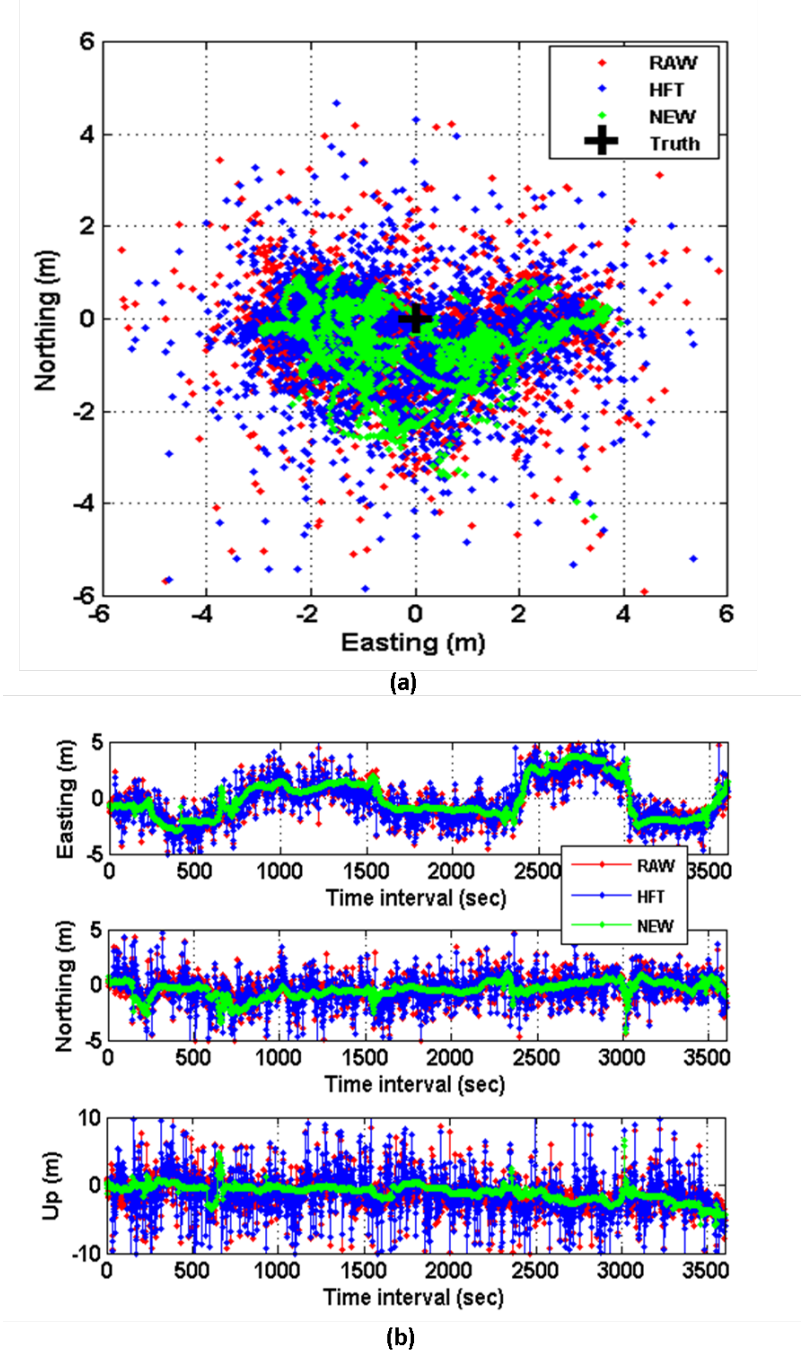

Figure 7.11.: SHIP 2D (top) and 3D (bottom) positioning solutions, with simulated cycle slips and code errors applied at different epochs for the different satellites

Further examination indicated that most of the wrongly fixed cycle slips were within the observation epochs highlighted with the red ellipsoids in Figure 7.10. Further investigation reveals that these are the epochs within and around which the SHIP made turns.

Table 7.6.: Statistics for the SHIP positioning solutions in Figure 7.11, with simulated cycle slips and code errors at different epochs for different satellites

Type	East (m)		North (m)		Up (m)		Simulated slips			Combined RMSE improvement of 'NEW'	
	RMSE	sigma	RMSE	sigma	RMSE	sigma	Not available			over RAW	Over HFT
RAW	1.80	1.78	1.04	0.97	2.61	2.20					
HFT	1.83	1.81	1.14	1.06	2.88	2.51				24%	25%
NEW	1.79	1.77	0.82	0.69	1.62	1.20	Total slips 920	Detected 98.0%	Fixed 79.8%		

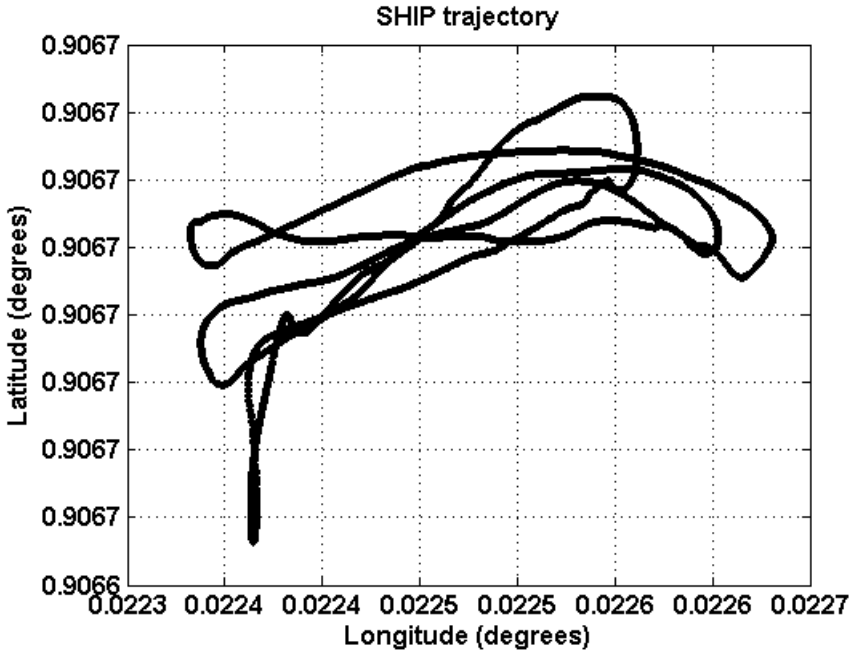

Figure 7.12.: SHIP trajectory

.

7.4.3. Improvement of the New Method

The proposed new method for code positioning, which involves single-frequency cycle slip detection and correction, improved ionospheric correction, and subsequent code-error mitigation, have been shown here to present improved single-frequency positioning results, especially under frequent cycle slip occurrence. As for the two receivers - MBAR operating in static mode and the SHIP operating in kinematic mode - the new method has shown better improvement in the positioning results

for the static MBAR receiver in the equatorial region compared to the moving SHIP, possibly because of the used improved single-frequency ionospheric correction model (IIC) rather than the broadcast Klobuchar model, and the absence of receiver antenna dynamics for the static station.

The obvious improved performance of the new method under cycle slip occurrence can be attributed largely to the non-initialisation of its code error mitigation procedure whenever a cycle slip occurs, unlike the HFT which does re-initialises. The short (300s) duration positioning solutions in the Northing direction for MBAR shown in Figure 7.13 clearly shows this difference between the HFT and NEW solutions. At every 20-epoch interval between test epochs, when simulated cycle slips

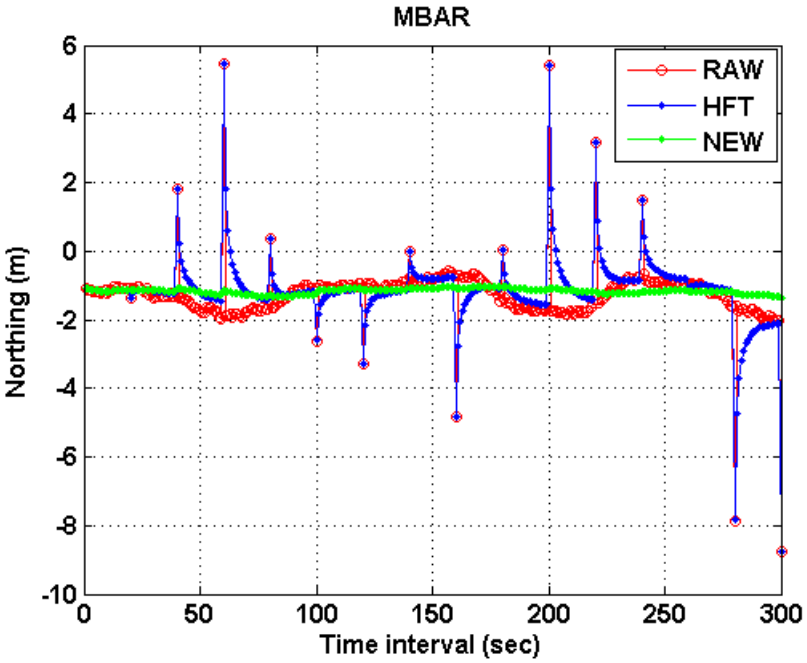

Figure 7.13.: Northing positioning solutions showing the re-initialisation of the HFT at test epochs of cycle slips. Positioning solutions are obtained for simulated cycle slips from within -100 to 100cycles and code error from within -10 to 10m applied at 20-epoch interval to all observed satellites but one at such test epochs.

and code errors are applied to all but one satellite, the HFT is seen to present positioning solutions with the same error level as the RAW since the HFT smoothed code is set (re-initialised) to the raw (unsmoothed) code observation at such epochs. The new method (NEW), on the other hand detects and corrects for such cycle slips and consequently, continuously mitigates the code errors on the raw code ob-

servations. The post-cycle-slip solution from the HFT may not achieve significant positioning accuracy prior to the occurrence of another cycle slip, thus indicating the poor performance of the HFT under frequent cycle slip conditions. The ability of the new method to establish continuous code error mitigation with or without cycle slip occurrence, is essentially the secret behind its better performance displayed in all the positioning results. On average, from all the results presented in this chapter, the NEW method has also shown better precision in the positioning results, as can be observed in the 1-sigma (standard deviation) values given in the tables of positioning statistics.

It is worth stating that if a conventional cycle slip fixing algorithm is used alongside the Hatch filter, it is envisaged that the presented HFT positioning results under the cycle slip tests, are bound to be improved upon, even though the level of further improvement has not been investigated and therefore cannot be currently ascertained. However, the simplicity and consequently, the computational speed of the proposed single-frequency cycle slip fixing algorithm, not to mention the achievable cycle slip detection and correction efficiencies, remains an attractive advantage for using the NEW method for single-frequency positioning operations.

7.5. Implementation and Related Issues

It can be observed that the proposed single-frequency, single-satellite, cycle slip detection algorithm that is based on the ATD technique is only implementable after a few continuous observation epochs have been recorded from an observed satellite. This number of epochs has been set to 10 epochs/seconds for the 1Hz data sets used throughout this research. For PPP, about 20-30 minutes of observation data could be required to achieve reliable ambiguity fixes (Carcanague *et al.*, 2011b). Hence, the required number of pre-detection observation epochs for the ATD process for cycle slip detection could be more, and can be required/used for resolving the initial integer ambiguity, N_1^s, for each observed satellite in view of a GNSS receiver, if required.

The proposed improved ionospheric correction (IIC) model and cycle slip detection

and correction (CSDC) algorithms can easily be implemented alongside the proposed cycle-slip-resilient code error mitigation algorithm, to improve single-frequency positioning performance in all environments. The computational load of the IIC algorithm is comparable to that of the Klobuchar or NeQuick model; the computational load of the cycle slip determination algorithm is quite low; and the computational load of the cycle-slip-resilient code error mitigation algorithm is as light as the conventional code-carrier smoothing (Hatch filter) technique. Hence, the integration and implementation of the proposed single-frequency algorithms are feasible for both real-time and post-processing GNSS single-frequency applications, and without any significant impact on a receiver's battery power.

This single-frequency CSDC and the code error mitigation algorithms can be implemented in a receiver operating in all environments. However, the errors in NLOS signals (Jiang & Groves, 2012), which are usually in the range of tens of metre, cannot be mitigated, even though prevalent cycle slips may be detected and corrected for.

7.6. Summary

The proposed algorithms for a single-frequency receiver unveiled in Chapter 5 have been tested, using single-frequency data obtained with receivers operating either in static or kinematic mode. The developed improved single-frequency ionospheric model showed improvement over the GPS broadcast Klobuchar ionospheric model, and proved significantly better to be used by a receiver in the equatorial region than by a receiver in the mid-latitude region. The single-frequency cycle slip detection, determination and correction algorithm has a high level of accuracy and it is also efficient. Under the simulated cycle slip scenarios, it achieved, for static and kinematic receivers, a minimum of 97.3% correct detection and a minimum of 79.8% correct fix. The point positioning results also showed the performance capability of the new (NEW) method that integrates the proposed simple cycle slip fixing and cycle-slip-resilient code error mitigation algorithms. The NEW method showed significant improvement over the conventional code-carrier smoothing (Hatch filter

technique (HFT) that does not include any cycle slip fixing algorithm. It achieved within 25-42% positioning accuracy improvement over the Hatch filtered code observable corrected for ionospheric delay with the broadcast Klobuchar ionospheric model. Without simulated cycle slips, the NEW and HFT positioning results presented comparable positioning results for a mid-latitude receiver. In positioning a receiver in the equatorial region, without simulated cycle slips, the NEW method outperformed the HFT by 21% in positioning accuracy, due to the improved ionospheric model used in NEW as against the broadcast Klobuchar model used with the HFT.

Chapter 8.

Dual-Frequency Tests, Results and Discussion

This chapter presents dual-frequency tests results, and the discussion of the results based on some performance metrics. The tests are performed with dual-frequency observations from GPS receivers operating in static or kinematic mode. The tests include investigation of the performance of the dual-frequency CSDC algorithm under simulated cycle slip conditions; and examining only code positioning performance of the new dual-frequency method presented in Chapter 6, with and without simulated cycle slips. The performance of the proposed gap-connect technique for mitigating positioning error and eliminating the usual convergence time, subsequent to an observation gap, is also examined via code positioning and with the Melbourne-Wubbena widelane observable that is widely used for ambiguity or cycle slip resolution. Except stated otherwise, the tests were done with the software developed in C++ and MATLAB environments, at University College London (UCL).

Under the cycle slips tests in this chapter, the comparison of the positioning results from the newly developed algorithms (NEW) and the conventional code-carrier smoothing (Hatch filter (HFT)) methods, is only aimed at revealing the possible improvements achievable by way of the integrated algorithms in the NEW method. The NEW method in dual-frequency operation, integrates the new simple dual-frequency cycle slip fixing and code error mitigation algorithms, unlike the conventional standalone code-carrier smoothing technique (HFT) without any included cycle slip fixing

algorithm. As such, the comparison results from the methods should be so interpreted. It is envisaged that if a conventional dual-frequency cycle slip fixing algorithm is used alongside the Hatch filter, the positioning results to be obtained from such an integration are bound to be more improved than the standalone HFT results presented in the cycle slip test sections of this chapter.

8.1. Dual-Frequency Test Data Sets

The static data sets used for the test presented in this chapter were downloaded from ftp://cddis.gsfc.nasa.gov, as provided by NASA/JPL, for station HRAO - an IGS station in South Africa. The 1Hz downloaded data was recorded by an Ashtech UZ-12 GPS receiver using the ASH701945C_M type antenna at HRAO on day 65 of 2008, starting from the 291600^{th} second of GPS week 1469. The downloaded dual-frequency code and phase observations were recorded for the L1 and L2 bands phase and code observations from GPS satellites. The HRAO station receiver clock runs on an active hydrogen maser (atomic clock standard). Also, dual-frequency data from the static MBAR receiver (described in Chapter 7) is used here to enable comparison of single- and dual-frequency results.

The kinematic data set is the dual-frequency data from SHIP receiver earlier introduced in Chapter 7, which recorded dual-frequency phase and code observations at 1Hz, collected on day 122 of 2008 starting from the 412328^{th} second of GPS week 1477.

For all days of observations, the corresponding GPS broadcast navigation files, obtainable from any of the IGS centre's website, were used as necessary.

8.2. Performance of the Dual-Frequency CSDC Algorithm

The performance of the CSDC algorithm for dual-frequency cycle slip detection, determination and correction, was tested on the dual-frequency phase observations observed by the static HRAO and the moving SHIP. The test involved the simulation

of cycle slips as already described in Section 4.5. Specifically for this test met to examine the performance of the dual-frequency CSDC algorithm, only a set from the special slip pairs having $\triangle N_1$ and $\triangle N_2$ cycle slip values selected from within ± 3 to ± 100cycles and with difference magnitude, $\lambda\triangle N = |\lambda_1\triangle N_1 - \lambda_2\triangle N_2| \leq 0.0285$m, were considered and tested for by this simulation. The subsequent cycle slip tests are performed with randomly generated cycle slip values which would include both special slip and non-special slip pairs.

The simulated special slip pairs were the special slip pairs defined by the sets of $\{\triangle N_1\}$ and $\{\triangle N_2\}$ below

$$\begin{aligned}\{\triangle N_1\} &= \Big\{4,-5,\ 9,-14,-18,-23,\ 27,-32,\ 36,-41,\ 45,-50,\ 54,\ 59,\ 63,-68,\ 72,-73,\ 77,\ 81,\ 82,-86,\ 91,-95,\ 100\Big\}\\ \{\triangle N_2\} &= \Big\{3,-4,\ 7,-11,-14,-18,\ 21,-25,\ 28,-32,\ 35,-39,\ 42,\ 46,\ 49,-53,\ 56,-57,\ 60,\ 63,\ 64,-67,\ 71,-74,\ 78\Big\}\end{aligned}$$

where any same-index values of $\{\triangle N_1\}$ and $\{\triangle N_2\}$ form a special slip pair. These pairs are chosen for this test because, as earlier explained in Chapter 6, they are often hardly detected by phase-only geometry-free observables. At a τ_{slip} =25-epoch interval, and at same test epochs, a total of 1440 (720 pairs of $\triangle N_1$ and $\triangle N_2$) cycle slips were simulated for five selected satellites from among all the satellites observed by HRAO. Also the same 1440 (720 pairs of $\triangle N_1$ and $\triangle N_2$) cycle slips were simulated for five selected satellites from among all the satellites observed by SHIP. Because there are 25 pairs in the sets defined by $\{\triangle N_1\}$ and $\{\triangle N_2\}$, each pair of the cycle slip pairs from same index of $\{\triangle N_1\}$ and $\{\triangle N_2\}$ repeats across the five selected satellites every 625epochs, over the 1 hour duration of 3600 epochs. This ensured that each cycle slip pair is tested up to 5 repeated times at different test epochs for each of the five selected satellites. For the static HRAO, the dual-frequency CSDC algorithm attained a 100% correct detection (detected all 720 simulated special slip pairs) and the 1440 (100%) cycle slips were correctly fixed to their integer values. The results for the special cycle slip pairs simulation for the moving SHIP indicated a 99.9% detection (could not detect 1 of the 720 special slip pairs) and 1424 (98.9%) of total simulated cycle slips pairs were correctly fixed to their integer values. For SHIP, it was observed that all of the 16 wrongly fixed cycle slips occurred at observation epochs (specifically, 75, 650, 1550, 1575, 2300, 2999,

3475) were the estimated receiver clock high-order variation, the ε_c values, were relatively high even though cycle slips were not detected for all observed satellites at those epochs.

Figure 8.1 shows the result from one of the selected cycle-slip-test satellites (PRN17), observed by SHIP, which had the most number of 6 wrongly fixed cycle slips that are indicated with arrows at epochs 1550, 1575 and 3475. Since a 99.9% correct

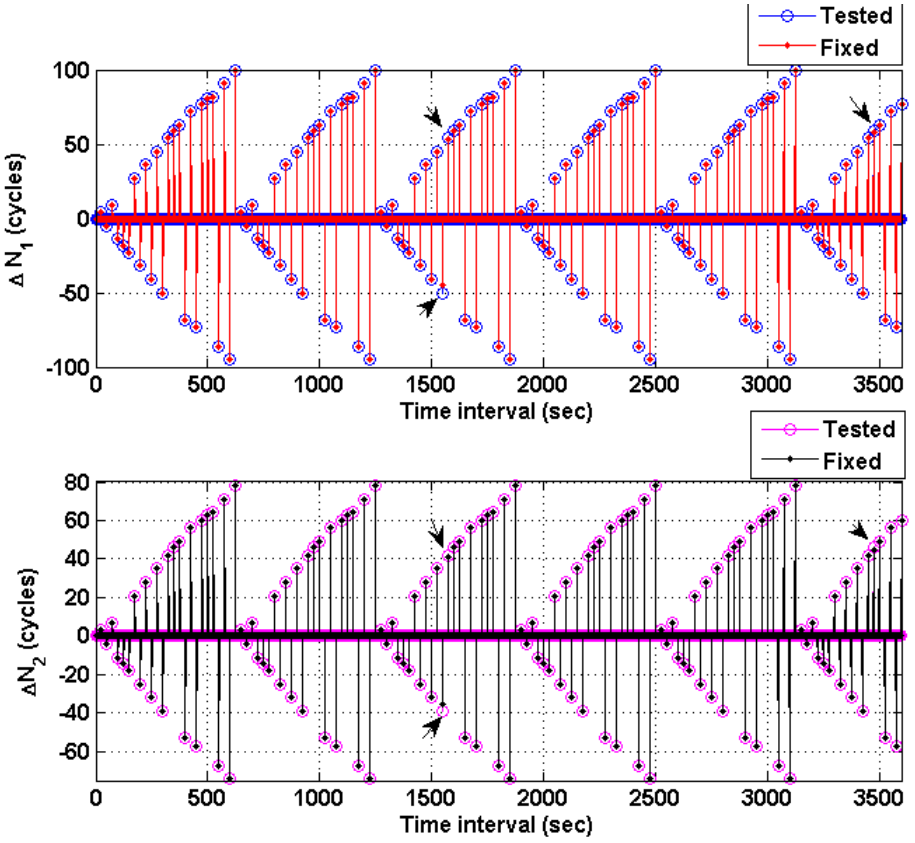

Figure 8.1.: Tested and fixed cycle slip pairs on PRN 17 observed by SHIP. All simulated pairs of $\triangle N_1$ and $\triangle N_2$ are special slip pairs that result in $|\lambda_1 \triangle N_1 - \lambda_2 \triangle N_2| \leq 0.285$m

detection was achieved, the resulting 98.9% and not 99.9% correctly fixed cycle slips for SHIP was judged to be due to the common SHIP receiver crystal oscillator clock drifts, which may have been poorly estimated at those epochs, and the SHIP's possible high antenna dynamics, which can result in poorly estimated ε_c values. The 100% correct fix achieved for HRAO may not be unconnected to the fact that the receiver of HRAO is driven by a more stable atomic clock, and its being static with

no antenna dynamics. In any case, the wrongly fixed cycle slips were off from the simulated cycle slip values by maximum of between 1 to 3 cycles.

It is important to mention that most of the other static stations tested for special cycle slip pairs through similar simulation, indicated 100% detection and 100% correct fix of cycle slips. Unfortunately, there was no other kinematic data set available other than SHIP's, with known truth trajectory for the period of this research, and as such one can only infer from the SHIP's results that the antenna dynamics may have contributed to impair the cycle slip detection and determination by the new dual-frequency CSDC algorithm.

8.3. Dual-Frequency Code Positioning Performance

The point positioning (using only code observables) performance of the proposed new dual-frequency method, which involves the new algorithm for dual-frequency CSDC and the subsequent code error mitigation algorithm presented in Chapter 6, was assessed using the dual-frequency observation data sets from the static HRAO and moving SHIP receivers. The point positioning with or without known (simulated) cycle slip occurrences, were examined. The new code error mitigation algorithm produces the error-mitigated dual-frequency code observables denoted as $\overline{P_1^s}$ and $\overline{P_2^s}$ for a continuously observed satellite s, or $\hat{P}_1^s$ and $\hat{P}_2^s$ for a gapped satellite s. Since the new dual-frequency code error mitigation algorithm is implemented in the range domain, the least squares (Cross, 1983) point positioning results are compared to the least squares based positioning results obtained with the commonly used range domain dual-frequency Hatch filtered code observables, so as to examine the comparative performance of the new dual-frequency method. Following from Section 5.2.2, it is assumed that the residual errors on the code observations/observables after filtering or smoothing the raw code observations/observables, are uncorrelated and homoscedastic. Hence in the used least squares positioning algorithm, a diagonal (unity) weight matrix is used. The use of the dual-frequency Hatch filtering technique (HFT) to smooth the dual-frequency code observations from satellite s is

simple and can be implemented as already given by Equation (3.9), for a non-fixed but varying filter length, M. M increases as the number of the continuously observed epochs from s increases, but re-initialises to $M = 1$ when a cycle slip is detected on any of the dual-frequency phase observations from s or whenever an observation gap occurs for s. To enable a measure of the level of improvement generally, the least squares based code positioning solutions obtained with the raw (unsmoothed) code observations are generated in addition.

The use of ionosphere-free code observables for a dual-frequency receiver positioning is very popular as an ionosphere-free code observable could be considered independent of the ionosphere. Hence, for a current epoch t corresponding to the L^s observation epoch of s, the ionosphere-free code observables, $P^{s,IF}_{NEW}$, obtained with the new dual-frequency error-mitigated code observables: $P^{s,IF}_{HFT}$ obtained with the dual-frequency HFT smoothed code observables; and $P^{s,IF}_{RAW}$ obtained with the raw code observable, are given as

$$P^{s,IF}_{NEW}(L^s) = \frac{f_1^2}{f_1^2 - f_2^2}\bar{P}^s_{1,}(L^s) - \frac{f_2^2}{f_1^2 - f_2^2}\bar{P}^s_2(L^s) \tag{8.1}$$

$$P^{s,IF}_{HFT}(L^s) = \frac{f_1^2}{f_1^2 - f_2^2}\bar{P}^s_{1,HFT}(L^s) - \frac{f_2^2}{f_1^2 - f_2^2}\bar{P}^s_{2,HFT}(L^s) \tag{8.2}$$

$$P^{s,IF}_{RAW}(L^s) = \frac{f_1^2}{f_1^2 - f_2^2}P^s_1(L^s) - \frac{f_2^2}{f_1^2 - f_2^2}P^s_2(L^s) \tag{8.3}$$

where f_1 and f_2 are the nominal dual-frequency transmit frequency of GPS L1 and L2 bands respectively. Though $\bar{P}^s_i$ $(i = 1, 2)$, are used in 8.1 for a continuously observed s, $\hat{P}^s_i$ are used if s becomes a gapped satellite. Whilst an ionosphere-free code observable is almost totally independent of ionospheric error, it is however an observable with an increased error level compared to the error level on a code observable from a given band. The positioning solutions obtained with $P^{s,IF}_{NEW}$, $P^{s,IF}_{HFT}$ and $P^{s,IF}_{RAW}$ are respectively denoted NEW, HFT and RAW in all positioning plots presented in this chapter.

The 'truth' position of the static HRAO receiver was obtained as the nominal position given in the header of its rinex file, while the 'truth' trajectory of SHIP was obtained as already described in Section 7.4.

8.3.1. Dual-Frequency Static Positioning Results

Firstly, the positioning solutions for the static HRAO receiver using the true data - the actual (downloaded) receiver recorded observations without any alterations by way of simulation of cycle slips or code error, and without any prior processing to correct for possible presence of cycle slips in the actual downloaded data. For an observation period of one hour, using the ionosphere-free code observables: $P^{s,IF}_{NEW}$, $P^{s,IF}_{HFT}$ and $P^{s,IF}_{RAW}$, the respective real-time code positioning results were obtained. The obtained 2D positioning solutions (the 3D is presented in Figure 8.16) and the table of the positioning statistics are shown in Figure 8.2 and Table 8.1 respectively. The positioning solutions obtained with $P^{s,IF}_{NEW}$, $P^{s,IF}_{HFT}$ and $P^{s,IF}_{RAW}$, are tagged as 'NEW', 'HFT' and 'RAW' respectively. Both the HFT and the NEW showed significant improvements over the RAW; indicating 47% and 51% positioning accuracy improvement over RAW respectively, as shown in Table 8.1. The relative offsets in

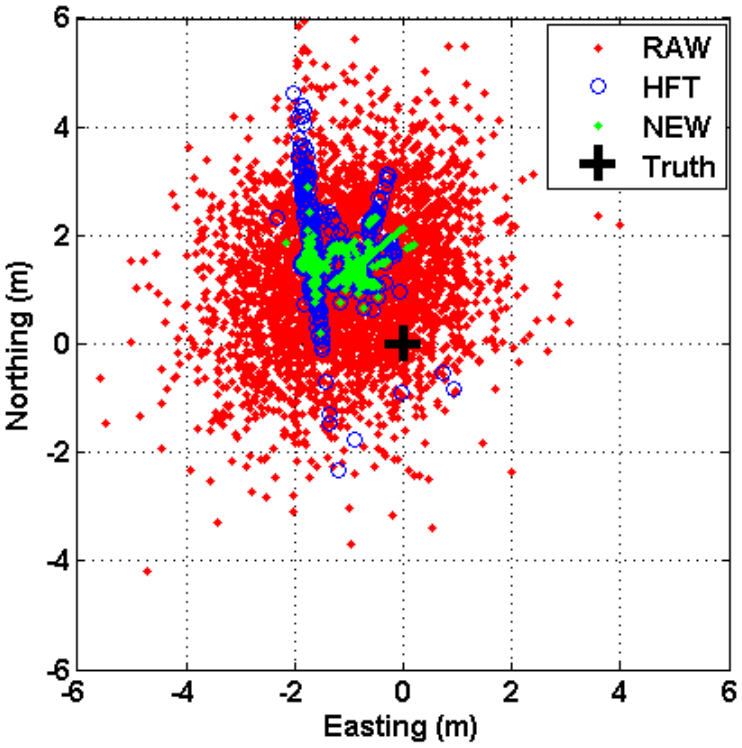

Figure 8.2.: HRAO 2D positioning solutions with true data - without simulated cycle slips and code errors

the positioning solutions, with respect to the 'truth' position, which can be observed

Table 8.1.: Statistics for the HRAO positioning solutions in Figure 8.2 and Figure 8.16(b)

Type	East (m)		North (m)		Up (m)		Combined RMSE improvement over 'RAW'
	RMSE	sigma	RMSE	sigma	RMSE	sigma	
RAW	1.61	1.22	1.82	1.35	3.05	3.03	-
HFT	1.15	0.42	1.34	0.38	1.05	0.97	47%
NEW	1.14	0.42	1.30	0.25	0.77	0.63	51%

in Figure 8.2, are believed to be as a result of the approximated truth position used for HRAO. It should be recalled that the 'truth' position was extracted from the header of the used rinex file of HRAO. The d adaptive-order of differencing was observed to vary between 2 to 4 for all satellites, within the 1hour HRAO observations used, even though 3 was again found to be the modal order of differencing in the 1Hz data set. The estimated HRAO common receiver clock high-order variation, ε, is shown in Figure 8.3. There was no clock jump epoch detected and there were no epochs where all satellites indicated cycle slips within the 1 hour observation data used for HRAO positioning. The estimated ε values are seen to be under ± 0.07cm with a 1-sigma (standard deviation) of $\sigma_\varepsilon = 1.08$cm and mean $\mu_\varepsilon = -0.016$mm, from the 3600 observation epochs. These lower range of ε_c values, compared to

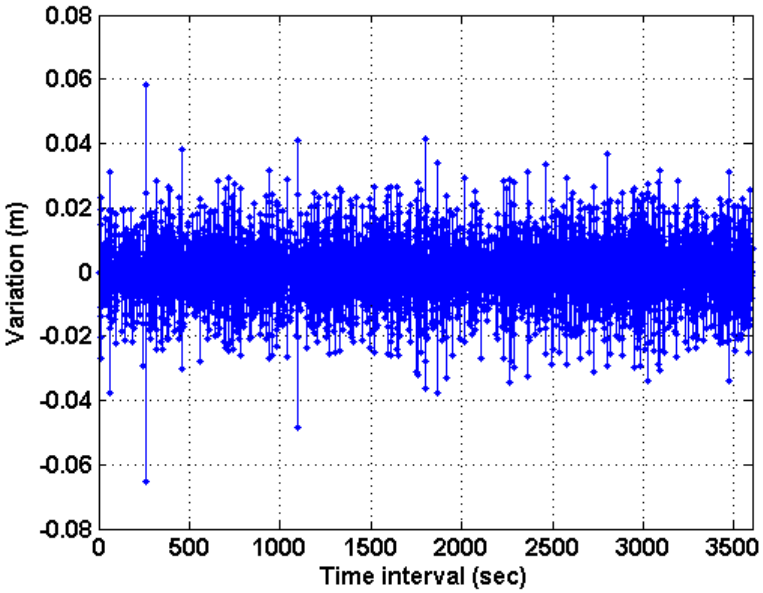

Figure 8.3.: Estimated common receiver clock high-order variation for HRAO

the ε_c values from MBAR and SHIP, are not surprising, recalling that the HRAO

receiver runs on an atomic clock, unlike the MBAR and SHIP receivers.

As a means to compare dual-frequency positioning solutions with single-frequency positioning solution of a receiver, the dual-frequency positioning of the MBAR receiver whose single-frequency positioning solutions are already shown in Figure 7.4, are generated. The obtained dual-frequency (DF) 2D positioning solutions (the 3D is presented in Figure 8.16) and the table of the positioning statistics, including the single-frequency (SF) for comparison, are shown in Figure 8.4 and Table 8.2 respectively. The first striking fact is that the positioning offsets indicated by all three solutions in the single-frequency positioning (see Figure 7.4) is eliminated in the dual-frequency positioning solutions, as the solutions are round about the true position in Figure 8.4 and not one-sided offsets as in Figure 7.4. This confirms the earlier inference that the initial ionospheric delay correction values for each s, $I_{Klob}^{s,0}$, used for s ionospheric corrections in the SF positioning solutions would have been highly inaccurate, recalling that the DF solutions are 'unaffected' by ionospheric delay (error) and as such, the single-frequency offsets (believed due to the residual ionospheric error) are eliminated in the DF solutions. Secondly, despite increased error levels on the ionosphere-free code observables due to the linear combination of the noisy code observables, the DF positioning solutions improved over the SF positioning solutions, which again is traceable to the ionospheric independence of the DF positioning solutions. For the DF solutions, the HFT and NEW attained different levels of improvement over the RAW, indicating 32% and 37% positioning accuracy improvements over the RAW respectively, as seen in Table 8.2. However, as earlier noticed from single-frequency positioning solutions in Chapter 7, the NEW method also outperformed the HFT mostly in the height component - by 7.5% and 17% improvement in positioning accuracy and precision respectively.

8.3.1.1. Dual-Frequency Static Positioning in the Presence of Cycle Slips

The performances of the dual-frequency CSDC algorithm under frequent cycle slip occurrence on the phase observations, and increased code error levels on the code observations, which are typical with positioning in a challenged environment were investigated. The performance tests were done by introducing, by way of simula-

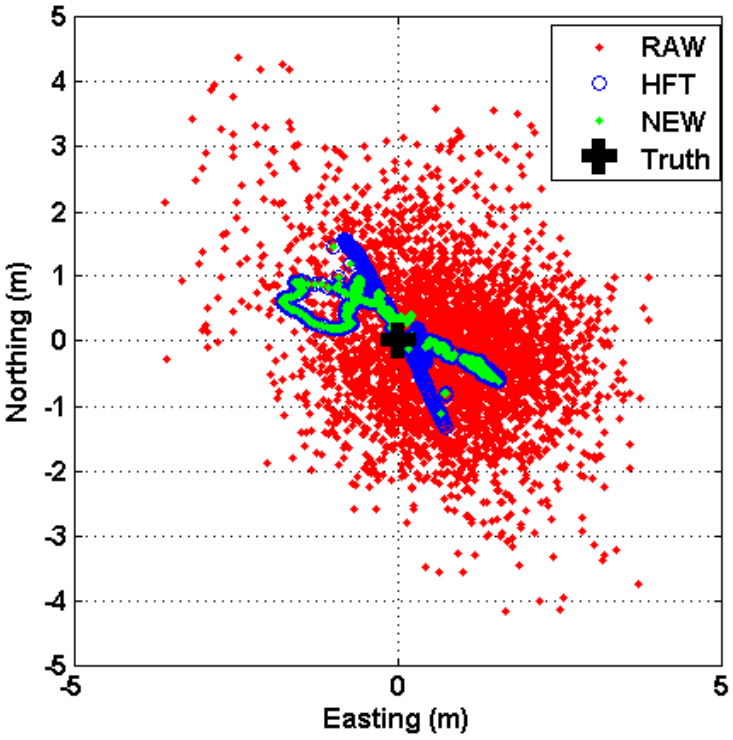

Figure 8.4.: MBAR 2D positioning solutions with true data - without simulated cycle slips and code errors

tion, known cycle slips and code error values respectively on the phase and code observations of different satellites, at known test epochs.

Under the cycle slip test scenarios in this chapter, the comparison of the positioning results with the conventional code-carrier smoothing technique, which is the Hatch filter, is only intended to reveal the level of performance improvement of the NEW method over the standalone Hatch filter that included no cycle slip fixing method. Unlike the standalone Hatch filter, the NEW method integrates the proposed code error mitigation algorithm and the simple dual-frequency cycle slip fixing algorithm.

Table 8.2.: Statistics for the MBAR positioning solutions in Figures 8.4, 7.4 and 8.16(a)

Type	East (m)		North (m)		Up (m)		Combined RMSE improvement over 'RAW'
	RMSE	sigma	RMSE	sigma	RMSE	sigma	
RAW (SF)	1.39	0.37	1.41	0.33	4.41	0.99	-
RAW (DF)	1.33	1.12	1.12	1.12	3.50	2.93	19% over SF
HFT (SF)	1.38	0.25	1.34	0.16	4.28	0.54	3% over SF
HFT (DF)	0.98	0.69	0.48	0.46	2.41	1.51	32% over DF
NEW (SF)	1.21	0.19	1.20	0.22	3.23	1.00	24% over SF
NEW (DF)	0.95	0.67	0.40	0.39	2.23	1.25	37% over DF

The cycle-slip-only test for the static HRAO receiver involved the use of known dual-frequency cycle slip values randomly generated from within -100 to 100cycles. The first cycle-slip-only test was performed to simulate the most critical scenario where all observed satellites experience cycle slips at the same observation epochs. This can happen, for instance when a moving vehicle with a GPS receiver passes through a tunnel and losses lock to all satellites, only to re-lock to the same satellites when the vehicle comes out of the tunnel. It can also be envisaged when a receiver clock reset or jump is done. The cycle slips were simulated at 25-epoch interval between successive test epochs for all observed satellites at given test epochs within the 1hour observation period of 3600 epochs. Figure 8.5 shows the 3D - Easting, Northing and Up positioning results; while the positioning statistics of the positioning solutions are presented in Table 8.3. The results show that, of the total 2556 simulated cycle slips, the dual-frequency CSDC algorithm correctly detected the 2556 (100%) cycle slips and fixed correctly 2460 (96.2%) of them thereby achieving 37% improvement over the HFT positioning solutions. It should be noted that the simulation indicates cycle slip flag to the HFT algorithm whenever a cycle slip is simulated at any test epoch, but the new dual-frequency CSDC algorithm detects and corrects for cycle slip on its own. The second cycle-slip-only test on the static HRAO was performed to simulate the more common practical scenario where different satellites experience cycle slips at different observation epochs, according to Equation (4.14). For this second cycle-slip-only simulation, simulated dual-frequency cycle slip values were randomly generated from within -100 to 100cycles, at 25-epoch interval between test epochs, for all the observed satellites. Figure 8.6 shows the 3D positioning results and the statistics of the positioning solutions are presented in Table 8.4. The

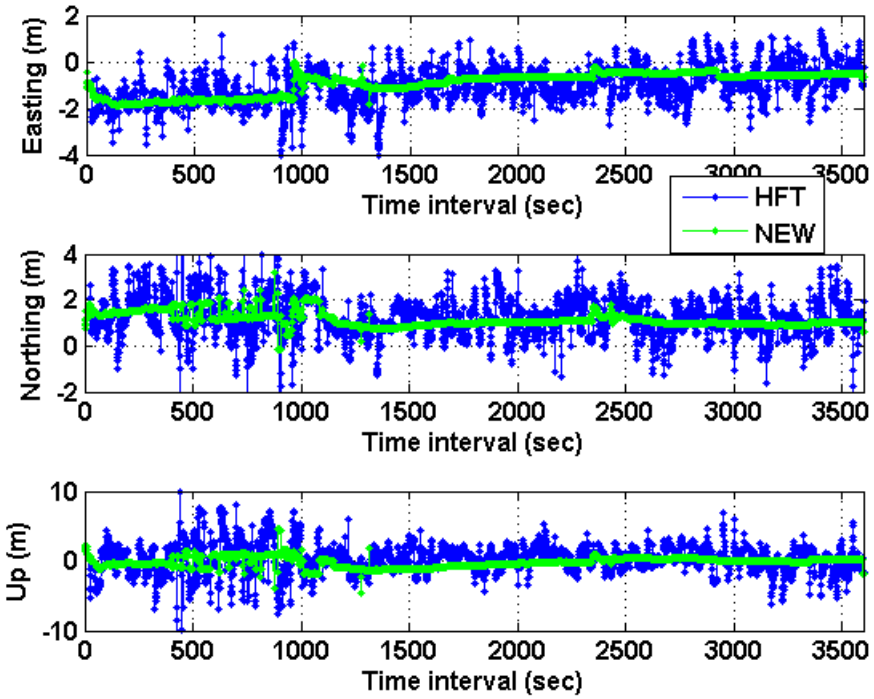

Figure 8.5.: HRAO 3D positioning solutions, with simulated cycle slips applied at same test epochs for all observed satellites

results show that, of the total 1556 simulated cycle slips, the new dual-frequency CSDC algorithm detected the 1556 (100%) cycle slips and fixed correctly the 1556 (100%) cycle slips to achieve 26% improvement over the HFT positioning solutions.

The last static test was to investigate the responsiveness of the new dual-frequency CSDC algorithm to small cycle slip values, and validate its 'independence' on code observations and the code errors. To this end, dual-frequency cycle slip values randomly generated from within -10 to 10cycles and dual-frequency code error values randomly generated from within -5 to 5m, were simulated at 25-epoch interval between successive test epochs, for different satellites at different epochs, in line with Equation (4.14), for all observed satellites. Figure 8.7 shows the obtained 3D positioning results while the statistics of the positioning solutions are presented in Table 8.5. The results show that, of the total 1556 simulated cycle slips, the dual-frequency CSDC algorithm correctly detected the 1556 (100%) cycle slips and correctly fixed

Table 8.3.: Statistics for the HRAO positioning solutions in Figure 8.5 with simulated cycle slips within ±100cycles for all satellites

Type	East (m)		North (m)		Up (m)		Simulated slips			Combined RMSE improvement of 'NEW' Over HFT
	RMSE	sigma	RMSE	sigma	RMSE	sigma	Not available			
HFT	1.29	0.73	1.49	0.82	1.98	1.96				37%
NEW	1.05	0.47	1.18	0.31	0.77	0.75	Total slips 2556	Detected 100%	Fixed 96.2%	

Table 8.4.: Statistics for the HRAO positioning solutions in Figure 8.6 with simulated cycle slips within ±100cycles for all satellites

Type	East (m)		North (m)		Up (m)		Simulated slips			Combined RMSE improvement of 'NEW' Over HFT
	RMSE	sigma	RMSE	sigma	RMSE	sigma	Not available			
HFT	1.25	0.68	1.40	0.72	1.76	1.72				26%
NEW	1.14	0.42	1.30	0.25	0.77	0.63	Total slips 1556	Detected 100%	Fixed 100%	

1552 (99.7%) of them to achieve 55% and 60% improvement over the HFT and the RAW positioning solutions respectively. Comparing the results in Table 8.4 and Table 8.5, and the plots in Figure 8.7, it can been seen that the additional code errors made no noticeable impact on the positioning solutions of NEW, and the NEW solutions still gave about the same CSDC performance, even though a different random pairs of cycle slips would have been generated. Moreover, the new CSDC shows its capability to detect and fix small cycle slip values.

Table 8.5.: Statistics for the HRAO positioning solutions in Figure 8.7 with simulated cycle slips within ±10cycles and code error within ±5m for all satellites

Type	East (m)		North (m)		Up (m)		Simulated slips			Combined RMSE improvement of 'NEW'	
	RMSE	sigma	RMSE	sigma	RMSE	sigma	Not available			over RAW	Over HFT
RAW	1.98	1.67	2.05	1.65	3.79	3.78					
HFT	1.93	1.57	1.81	1.37	3.21	3.21				60%	55%
NEW	1.14	0.44	1.26	0.26	0.75	0.63	Total slips 1556	Detected 100%	Fixed 99.7%		

In all these tests on the static HRAO involving dual-frequency cycle slip simulations, the proposed NEW method was shown to outperform the dual-frequency HFT method in both accuracy, measured by the root mean square error (RMSE) value, and precision measured by the 1-sigma values. The most improvement of

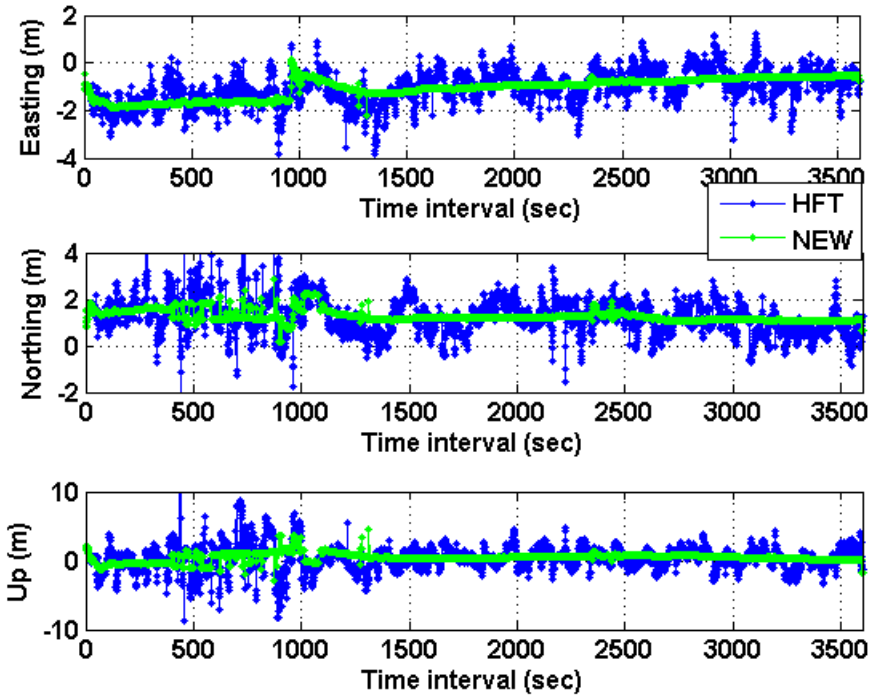

Figure 8.6.: HRAO 3D positioning solutions, with simulated cycle slips applied at different test epochs for different satellites

NEW over HFT can be observed in the height component, ranging between 27-77% in accuracy and between 35-80% in precision, in the presented results. The reason for the improvement of NEW over HFT, as earlier stated in Chapter 7, is mainly due to the non-reinitialisation in the new code error mitigation algorithm whenever cycle slips occur, but are rather detected and corrected for. It can be seen that the performances of the NEW and HFT are almost at the same level in the absence of simulated cycle slips.

8.3.2. Dual-Frequency Kinematic Positioning Results

The performance of NEW was further investigated for the kinematic receiver, SHIP. Firstly the true data set, which is the actual dual-frequency observation data recorded by the receiver on the moving SHIP, without any alterations in form of cycle slips or code error simulations and without any prior processing to correct for possible presence of cycle slips in the data, are used for positioning. Obtaining the different

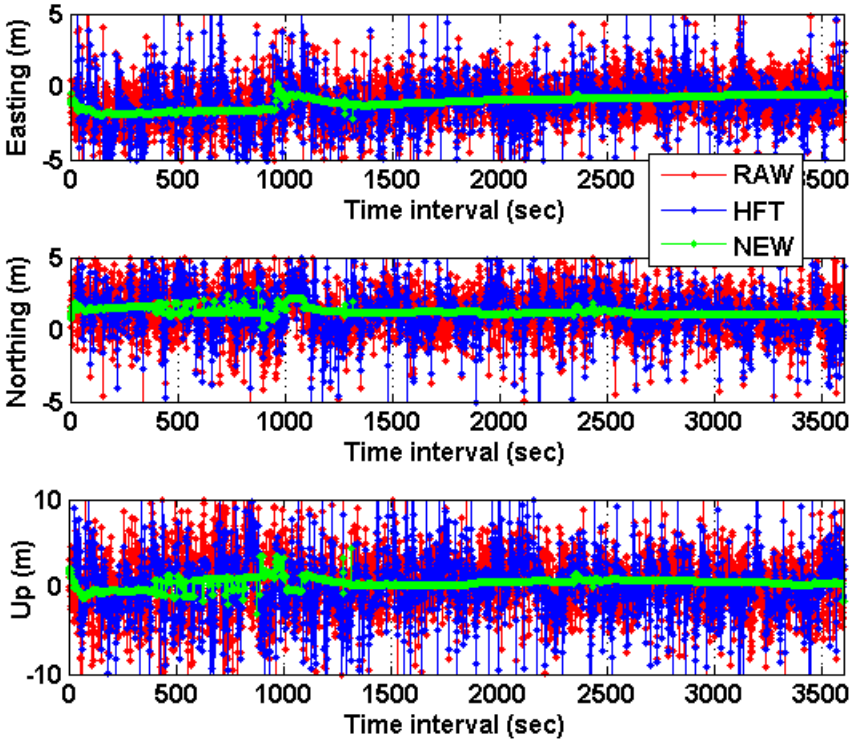

Figure 8.7.: HRAO 3D positioning solutions, with simulated cycle slips and code errors, at different epochs for different satellites

ionosphere-free code observables, $P^{s,IF}_{NEW}$, $P^{s,IF}_{HFT}$ and $P^{s,IF}_{RAW}$ as before, the corresponding NEW, HFT, and RAW real-time code positioning solutions were obtained, for an observation period of 1 hour of 3600 epochs. The obtained 2D positioning solutions (the 3D is presented in Figure 8.16) and the table of the positioning statistics are shown in Figure 8.8 and Table 8.6 respectively. As expected, both the HFT and the NEW showed significant improvements over the RAW; both indicating 29% improvement respectively, as shown in Table 8.6. The d adaptive-order of differencing

Table 8.6.: Statistics for the SHIP positioning solutions in Figure 8.8 and Figure 8.16(c)

Type	East (m)		North (m)		Up (m)		Combined RMSE improvement over 'RAW'
	RMSE	sigma	RMSE	sigma	RMSE	sigma	
RAW	1.85	1.83	1.31	1.27	3.07	2.71	-
HFT	1.70	1.69	0.79	0.66	1.95	1.05	29%
NEW	1.73	1.74	0.83	0.63	1.92	0.90	29%

was observed to also vary between 2 to 4 for all satellites observed by SHIP even

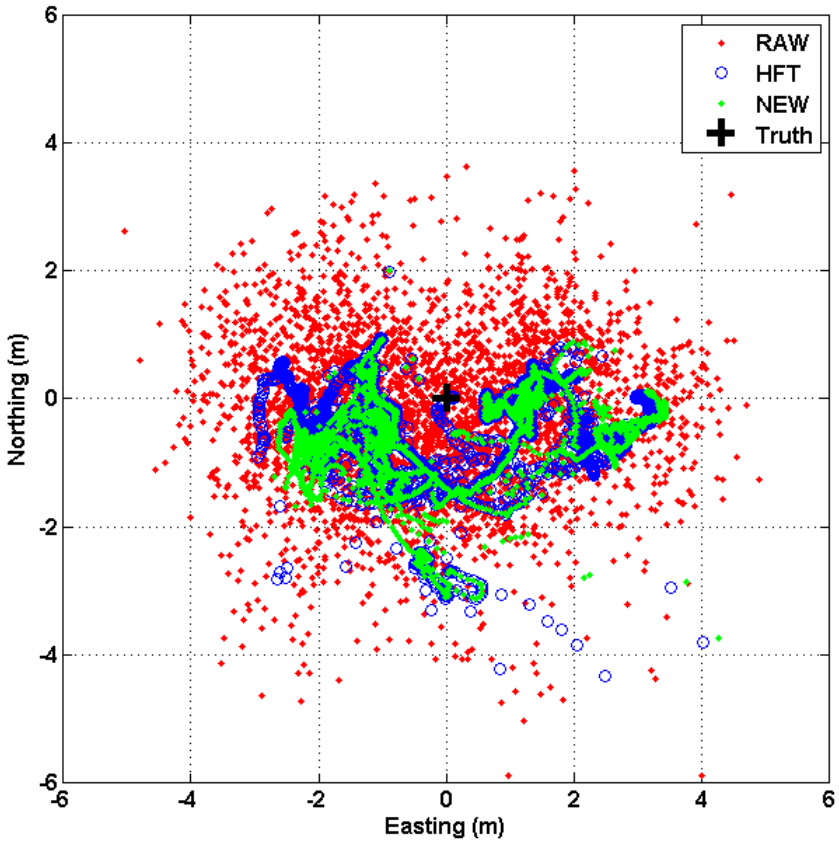

Figure 8.8.: SHIP dual-frequency 2D positioning solutions with true data - without simulated cycle slips and code errors

though 3 was still found to be the modal order of differencing. The dual-frequency estimated common SHIP receiver clock high-order variation, ε_c, shown in Figure 8.9 is not significantly different from the single-frequency estimated ε_c. There is the clock jump detected at epoch 2888 (as it was previously detected for single frequency data in Chapter 7). The estimated ε_c values are seen to be under $\pm$0.5m with a 1-sigma of $\sigma_\varepsilon = 3.83$cm and mean $\mu_\varepsilon = -0.23$mm, within the 3600 observation epochs excluding the clock jump epoch.

8.3.2.1. Dual-Frequency Kinematic Positioning in the Presence of Cycle Slips

The performance of the dual-frequency CSDC algorithm under frequent cycle slip occurrence on the phase observations and increased code error levels on the code observations, was also investigated for a receiver in kinematic mode using the same

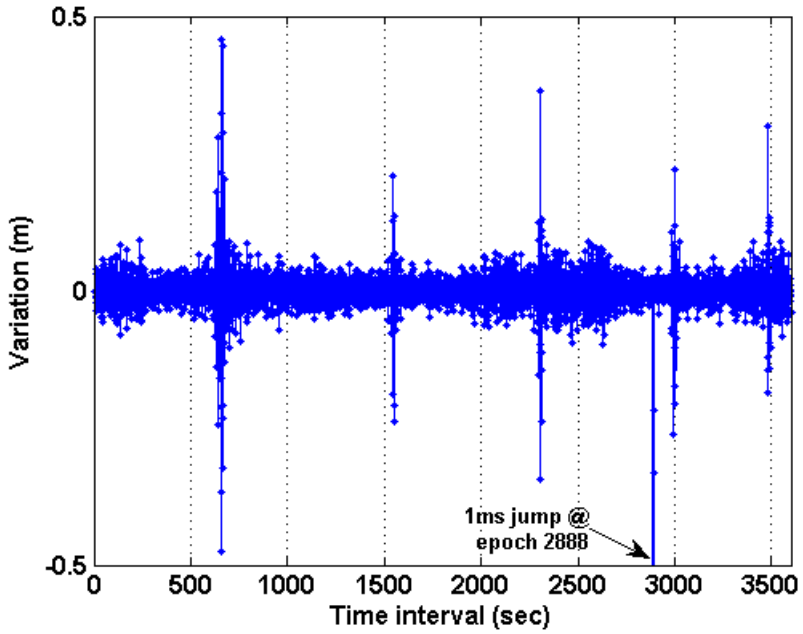

Figure 8.9.: Dual-frequency estimated common receiver clock high-order variation for SHIP

SHIP's dual-frequency data. The cycle-slip-only test for the SHIP involved the use of known dual-frequency cycle slip values randomly generated from within -100 to 100cycles, performed to simulate the most critical scenario where all observed satellites experience cycle slips at the same observation epochs. The cycle slips were simulated at 25-epoch interval between test epochs, for all observed satellites, within the 1 hour observation period of 3600 epochs. Figure 8.10 shows the 3D positioning results while the statistics of the positioning solutions are presented in Table 8.7. The results show that, of the total 2634 simulated cycle slips, the dual-frequency CSDC algorithm correctly detected the 2634 (100%) cycle slips and correctly fixed 2506 (95.1%) of them thereby achieving 18% improvement over the HFT positioning solutions. The results also reveal the most improvement of NEW over HFT in the height component, achieving improvement in positioning accuracy of 27% and 48% in precision over the HFT.

The responsiveness of the dual-frequency CSDC algorithm to small cycle slip values, and its 'independence' on code observations and code errors, were also investigated for the moving SHIP receiver. To this end, dual-frequency cycle slip values randomly generated from within -10 to 10cycles and dual-frequency code er-

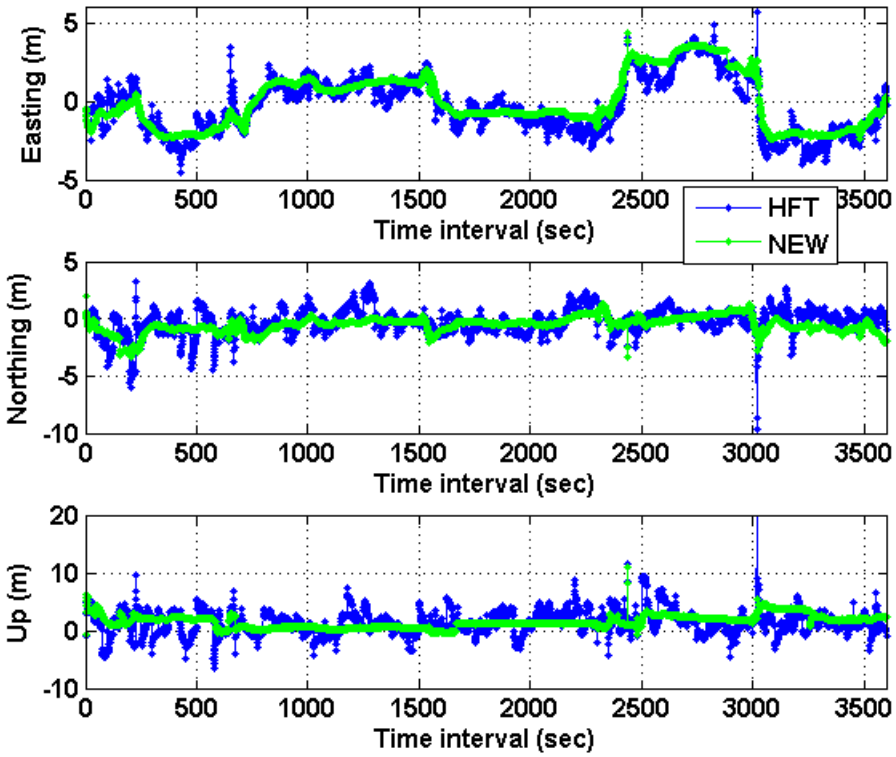

Figure 8.10.: SHIP 3D positioning solutions, with simulated cycle slips at same test epochs for all satellites

ror values randomly generated from within -5 to 5m, were simulated at 25-epoch interval between test epochs, applied at different epochs for different satellites in line with Equation (4.14), for all observed satellites. Figure 8.11 shows the obtained 3D positioning results and the statistics of the positioning solutions are presented in Table 8.8. The results show that, of the total 1602 simulated cycle slips, the dual-frequency CSDC algorithm correctly detected 1600 (99.9%) cycle slips and correctly fixed 1592 (99.4%) out of the 1602 cycle slips correctly to achieve 44% and 43% improvement over the HFT and the RAW positioning solutions respectively. Again, the NEW positioning results (Figure 8.11) reveals that the simulated code errors made no impact on the positioning solutions of NEW when cycle slip occurs, and the algorithm is also efficient in detecting small cycle slip values, even though only one pair could not be detected. Again, the most improvement of NEW over HFT was in the height component; achieving improvement of 55% in positioning accuracy and 75% in precision.

Table 8.7.: Statistics for the SHIP positioning solutions in Figure 8.10 with simulated cycle slips within ±100cycles for all satellites

Type	East (m)		North (m)		Up (m)		Simulated slips			Combined RMSE improvement of 'NEW' Over HFT
	RMSE	sigma	RMSE	sigma	RMSE	sigma	Not available			
HFT	1.77	1.76	1.08	1.05	2.55	2.07				18%
NEW	1.71	1.71	0.87	0.69	1.87	1.08	Total slips 2634	Detected 100%	Fixed 95.1%	

Table 8.8.: Statistics for the SHIP positioning solutions in Figure 8.11 with simulated cycle slips within ±10cycles and code error within ±5m for all satellites

Type	East (m)		North (m)		Up (m)		Simulated slips			Combined RMSE improvement of 'NEW'	
	RMSE	sigma	RMSE	sigma	RMSE	sigma	Not available			over RAW	Over HFT
RAW	2.00	1.98	1.60	1.56	4.03	3.78					
HFT	1.95	1.92	1.62	1.58	4.09	3.86				43%	44%
NEW	1.72	1.71	0.94	0.69	1.86	0.95	Total slips 1602	Detected 99.9%	Fixed 99.4%		

Mainly because of the non-reinitialisation in the new code error mitigation algorithm whenever cycle slips occurs, the NEW method also outperformed the HFT even for this SHIP receiver in kinematic mode. It can be seen from Table 8.6 that similar performance levels were achieved by the NEW and HFT methods in the absence of simulated cycle slips.

Again, it is worth stating that if a conventional cycle slip fixing algorithm is used alongside the Hatch filter, it is envisaged that the presented HFT positioning results under the cycle slip tests, are bound to be improved upon, even though the level of further improvement has not been investigated and therefore cannot be currently ascertained. However, the simplicity and consequently, the computational speed of the proposed dual-frequency cycle slip fixing algorithm, not to mention the achievable level of cycle slip detection and correction efficiencies, would make using the NEW method more attractive than a method that integrates, say, the LAMBDA method and the Hatch filter, for dual-frequency positioning operations.

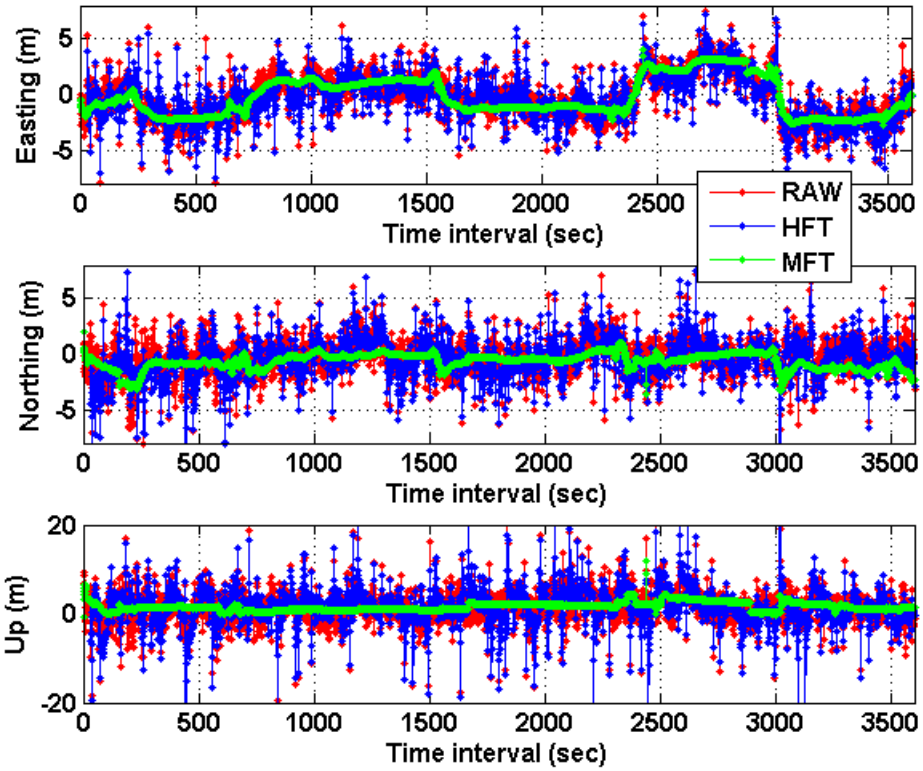

Figure 8.11.: SHIP 3D positioning solutions, with simulated cycle slips and code errors, applied at different test epochs for different satellites

8.4. Performance of the Gap-Connect Technique in Mitigating Impacts of Observation Gap

The possible decrease in positioning accuracy at a post-gap epoch and the usual convergence time required in resolving post-gap dual-frequency ambiguities and/or achieving significant code smoothing, can be identified as two negative impacts of an observation gap occurrence. Section 6.8 unveils the proposed gap-connect technique for mitigating these negative impacts, by predicting the relative ionospheric delay, determining the dual-frequency cycle slips, and subsequently mitigating the dual-frequency code errors; all at the first post-gap epoch after an observation gap occurrence for a satellite. The gap-connect technique, as earlier stated, does not only aim at mitigating the code errors at a post-gap epoch, but also, unlike with the conventional ambiguity and code smoothing techniques, it also aims at sustaining

the attained level of positioning accuracy prior to an observation gap occurrence, with a 'zero' convergence time. This section therefore investigates the capability of the gap-connect technique in realising this aims.

The performance of the gap-connect technique was examined by simulated observation gaps, and by examining the positioning results for different receivers at epochs where observation gaps actually occurred in the actual data sets. The accuracy of the predicted relative ionospheric delay and the corresponding time series Melbourne-Wubbena observable for a gapped satellite are subsequently examined to determine performance.

8.4.1. Examining the Predicted Relative Ionospheric Delay

The efficiency of the relative ionospheric prediction algorithm given by Equation (6.56) and the efficiency of the dual-frequency post-gap cycle slips determination algorithm presented in Section 6.8.2 are examined first by simulation, and secondly via results obtained from actual data sets. If an observation gap occurs for satellite s at the $(t_{gap}+1)^{th}$ receiver observation epoch and lasts for a gap duration of l^s_{gap} epochs before the receiver re-locks to s at a current post-gap epoch $t = t_{gap}+1+l^s_{gap}$ (t being the current receiver observation epoch), such a scenario was simulated by making all the code and phase observations from s within the l^s_{gap} gap interval equal to zero. Using the actual code and phase observations recorded at the post-gap t epoch, the gap-connect technique predicts the $I^{s,v}_1$ relative ionospheric delay from epoch $t_{gap}+1$ to t epoch, determines the $\triangle N^{s,gap}_1$ and $\triangle N^{s,gap}_2$ dual-frequency cycle slips between epochs t_{gap} (last epoch prior to the observation gap) and t (epoch after the observation gap), and obtains the post-gap error-mitigated$\hat{P}^s_1$ and $\hat{P}^s_2$ dual-frequency code observables, before finally generating the post-gap dual-frequency observables for use in the ATD process at subsequent epochs.

The Melbourne-Wubbena observable, WL_{MW} in cycles, is a dual-frequency wide-lane combination without a geometric range, satellite and receiver clock offsets, and ionospheric and tropospheric delays; it is the difference between the dual-frequency ambiguities, $N_{WL} = (N^s_1 + \triangle N_1) - (N^s_2 + \triangle N_2)$ corrupted by the sum of the inherent error levels of the combined phase and code observables and combined hard-

ware biases (see Equation (3.20)). The smoothed, filtered or averaged version of WL_{MW} is more appropriate for resolving N_{WL}, as done in (Blewitt, 1990; Liu, 2011). In the absence of hardware delays and observation errors, WL_{MW} would be a constant value as far as s remains lock to a receiver without cycle slips or observation gap/discontinuities, but would change to a new constant value when a cycle slip occurs or when the receiver re-locks to the gapped satellite with cycle slip(s) post-gap epoch. As such, a time series of WL_{MW} is found to be suitable for accessing the performance of the gap-connect technique by way of examining the smoothness and value of WL_{MW} post cycle-slip or at a post-gap epoch; and it also enables accessing post-gap convergence.

Seven observation gap occurrences lasting for 1, 5, 10, 15, 20, 40 and 60 epochs or seconds (for the 1Hz data sets) interval respectively, were simulated for selected satellites (gap-test satellites) observed by different receivers (MBAR, HRAO and SHIP) and the predicted relative ionospheric delay, and the time series WL_{MW} were examined. A 500-epoch interval was set between observation gap occurrences on a satellite while a maximum observation gap duration of $L_{gap} = 4$minutes interval was used. Figure 8.12 shows the time series WL_{MW} results for PRN1, one of the gap-test satellites, observed by HRAO. The time series of WL_{MW} tagged 'RAW' - obtained with the raw (unsmoothed) code and phase observations - are observed to vary between 1 and 2.5cycles in Figure 8.12; it is obviously undesirable for resolving N_{WL} as the error level and variation exceeds one widelane cycle, with or without observation gap occurrence and irrespective of the gap duration. The time series WL_{MW} tagged 'HFT' - obtained with the HFT smoothed code observables and the raw phase observations - shows a good smoothing improvement prior to the first gap at the 500^{th} epoch. Since the HFT re-initialises at every post-gap epoch, the performance deteriorated at post-gap epochs, and even after the 500seconds interval (analogous to a convergence time) after any observation gap, it does not really converge to produce smoothed and accurate WL_{MW} such as acquired prior to the first observation gap at the 500^{th} epoch. On the other hand, for the proposed gap-connect technique, the time series WL_{MW} tagged 'NEW' - obtained with the NEW smoothed code and cycle-slip-corrected phase observables - shows good smoothing

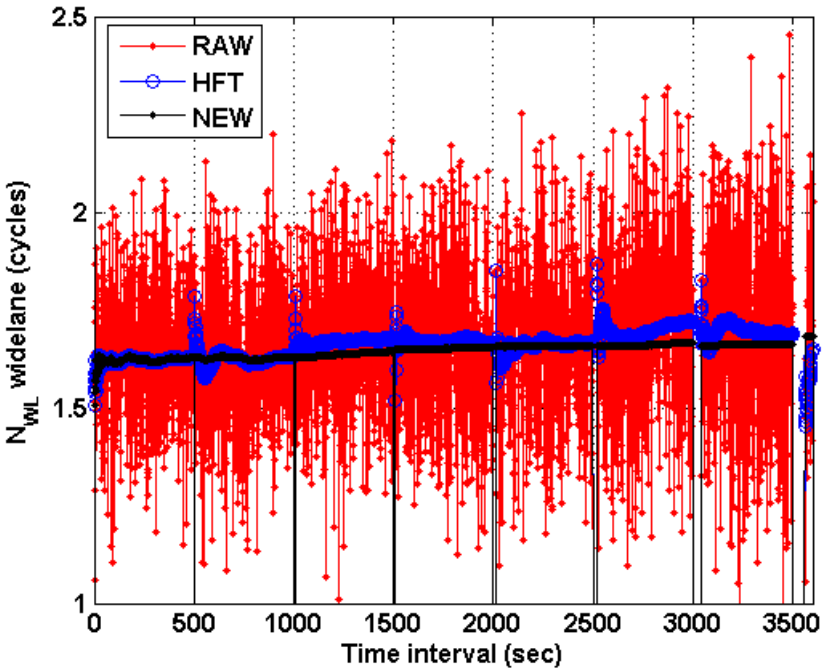

Figure 8.12.: Time series Melbourne-Wubbena observable. Simulated observation gaps of 1, 5, 10, 15, 20, 40 and 60sec duration on PRN 1 observed by HRAO

or error-mitigation improvement prior to the 500^{th} epoch, and fairly maintained that pre-gap accuracy and precision acquired prior to the first observation gap at the 500^{th} epoch with a zero convergence time, for all the different observation gap durations.

The efficiency of the ionospheric prediction was also investigated for the gap-test satellites simulated for observation gap occurrences. Figure 8.13 shows a zoom-in plot of the predicted relative ionospheric delay of PRN1 whose time series WL_{MW} results are already shown in Figure 8.12. The plots show the zoom into the epochs where a 40 and 60sec observation gap was simulated for the PRN 1. It can be observed from the plots that the predicted $I_1^{s,v}$ was accurate enough at the epochs of observation gaps; a maximum difference of 3.2mm error between the actual (Raw-truth) and the predicted (Pred) $I_1^{s,v}$ was obtained across the 7 observation gaps simulated for PRN1, within the 1 hour period of 3600 epochs. This error range (difference between 'Raw-truth' and 'Pred') is envisaged to increase as observation gap increases, recalling that the maximum allowable observation gap was set to $L_{gap} = 4$ minutes in the developed gap-connect technique. These shown comparison

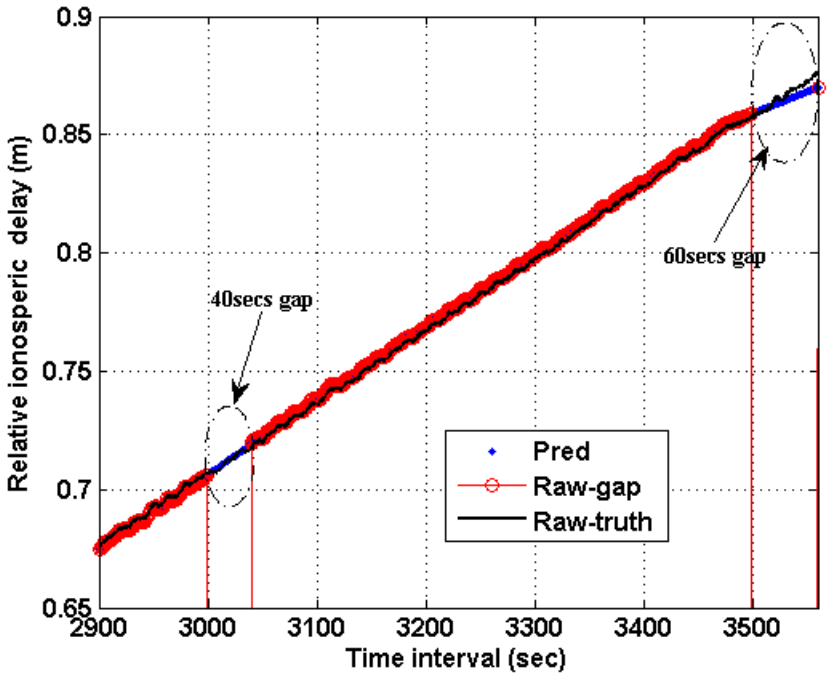

Figure 8.13.: Phase-only relative ionospheric delay on PRN 1 observed by HRAO, showing the actual relative ionospheric delay without simulated gaps (Raw-truth); the actual relative ionospheric delay but with simulated gaps (Raw-gap); and the predicted relative ionospheric delay with predicted relative ionospheric delay values at gap and post-gap epochs (Pred).

results for PRN 1 are similar to other simulated results obtained from other gap-test satellites observed by MBAR and SHIP that were tested for the same observation gaps lasting for 1, 5, 10, 15, 20, 40 and 60 epochs or seconds.

A few satellites with actual observation gap occurrences were noticed in the data sets from MBAR, HRAO and SHIP. For example, PRN 22, observed by HRAO, experienced the most observation gap occurrences, and quite frequently too. Figure 8.14 shows the actual phase-only $I_1^{s,v}$ obtained whilst the satellite was continuously observed (Raw); and the predicted (Pred) $I_1^{s,v}$, which is the predicted $I_1^{s,v}$ over the epochs when the satellite experienced the actual observation gap occurrences (including the post-gap epochs predicted $I_1^{s,v}$ values) whenever the HRAO receiver re-locked to the PRN 22. It can be seen that the predicted $I_1^{s,v}$ values seem to predict the varying $I_1^{s,v}$ with high accuracy. The zero-value relative ionospheric delay are associated with the different epochs between observation gaps and the epochs when the HRAO receiver re-locked to PRN 22.

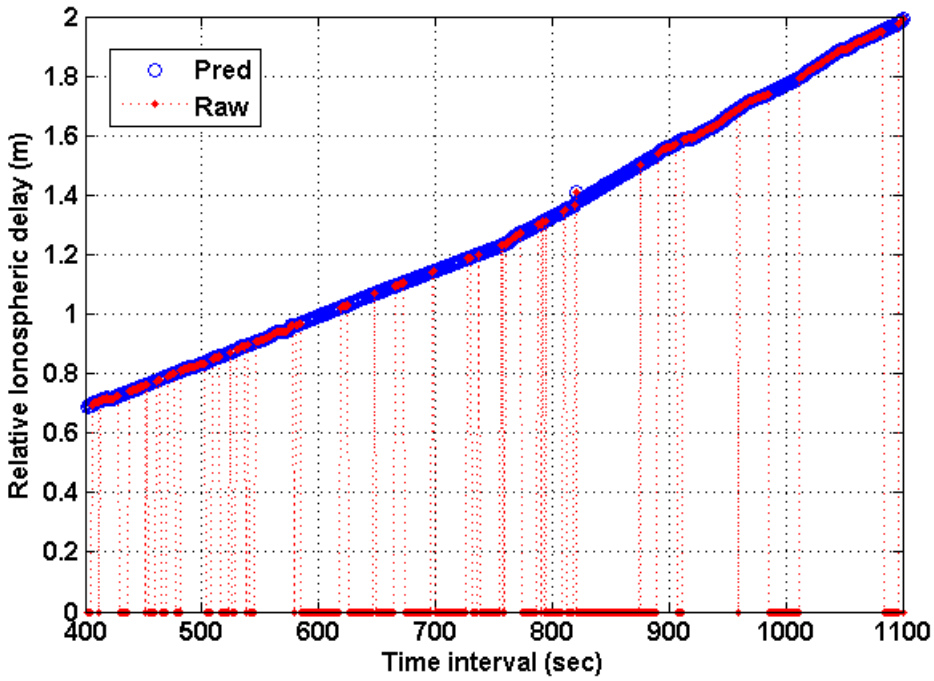

Figure 8.14.: Phase-only relative ionospheric delay, showing the actual and predicted ionospheric delay for gapped PRN 22, observed by HRAO

8.4.2. Eliminating Convergence Time and Improving Post-Gap Positioning

The time series of the WL_{MW} Melbourne-Wubbena observable can help access the level of code smoothness or error mitigation achieved by a smoothing/filtering technique, as well as give an insight to the period required for a post-gap convergence. The envisaged zero convergence time of the proposed gap-connect technique was further examined with the WL_{MW} observables obtained from a few satellites that experienced actual observation gaps. The impact on the positioning of the MBAR, HRAO and SHIP receivers was examined to access the improvement of the gap-connect technique at a post-gap epoch and few epochs after a post-gap epoch.

Three satellites, PRN 11, PRN 22 and PRN 28 were selected as representative satellites from amongst the satellites that experienced observation gap occurrences for MBAR, HRAO and SHIP respectively. The acquired time series plots of WL_{MW} in cycles, are presented in Figure 8.15.

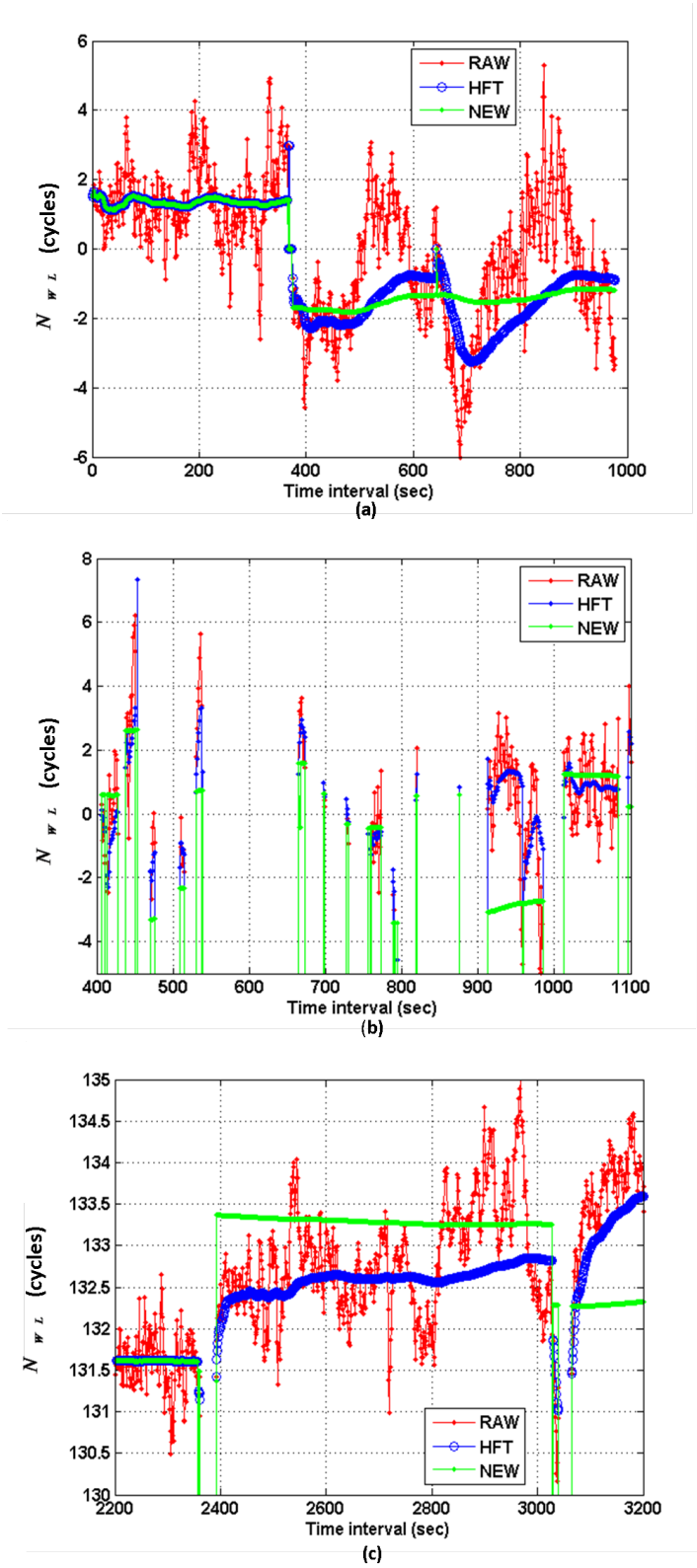

Figure 8.15.: Melbourne-Wubbena time series plots for different satellites with actual observation gap occurrences: (a) plots from PRN 11, observed by MBAR; (b) plots from PRN 22, observed by HRAO; and (c) plots from PRN 28, observed by SHIP

The WL_{MW} observables obtained with the dual-frequency raw code and phase observations are tagged 'RAW'; the WL_{MW} observables obtained with the HFT smoothed code observables and raw phase observations are tagged 'HFT'; and the WL_{MW} observables obtained with the NEW error mitigated code and cycle-slip-corrected phase observables are tagged 'NEW', respectively. For PRN 11 for instance, observation gaps occurred at the 366, 369 and 644^{th} observation epochs and the receiver re-locked to it at the 367, 374 and 645^{th} observation epochs respectively; and five different observation gaps occurred for PRN 28 observed by the SHIP receiver re-locking to PRN 28 at the 2358, 2392, 3029, 3064 and 3553^{th} observation epochs. As already revealed in the presented simulation results in Section 8.4.1, the results from the actual observation gap occurrences also show that the WL_{MW} observables obtained with RAW generate unacceptable range of values for N_{WL}, with high error levels exceeding one widelane cycle, within and outside the epoch regions of observation gaps. The HFT results shows that it re-initialises at every observation gap, thus producing the same WL_{MW} values as RAW at any post-gap epoch, and subsequently, converges slowly towards a new post-gap widelane ambiguity after an elapsed interval of time, as can be noticed on the three satellites plots. The new gap-connect technique showed its robustness to observation gap occurrence; indicating a swift convergence (a 'zero' convergence time) to a new post-gap widelane ambiguity value at any post-gap epoch, thereby outperforming the smoothness level achieved by the HFT.

The consequences of these observation gaps on code positioning accuracy was subsequently examined; specifically, monitoring the positioning solutions at the different post-gap epochs and at the epoch regions surrounding these observation gaps on these three satellites observed by three different receivers. Figure 8.16 shows the 3D positioning solutions using the actual data without any form of simulation, for MBAR, HRAO and SHIP, obtained with the corresponding $P^{s,IF}_{NEW}$, $P^{s,IF}_{HFT}$ and $P^{s,IF}_{RAW}$ as given by Equations (8.1) through (8.3). Dotted ellipses are used to show epoch regions surrounding observation gap occurrences on the three gapped satellites observed by the different receivers.

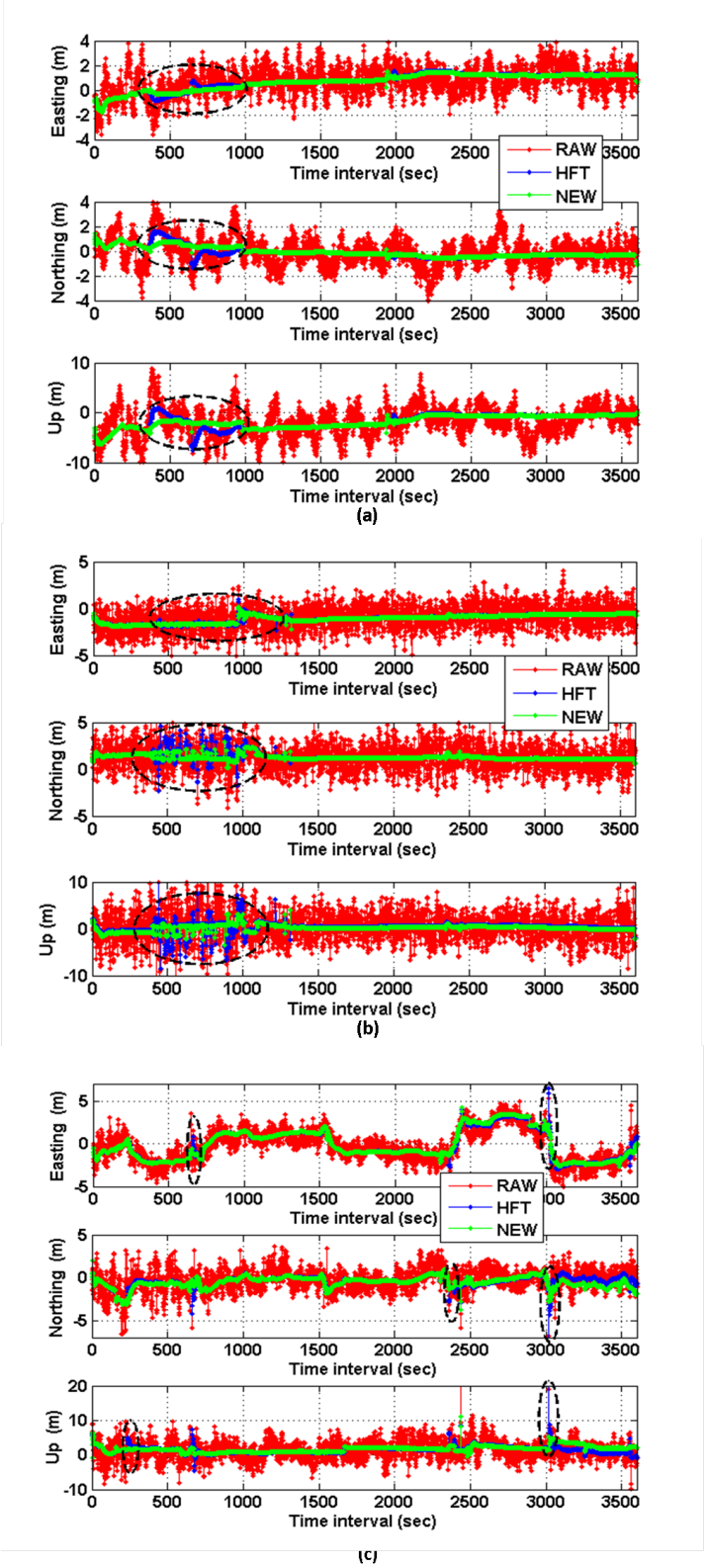

Figure 8.16.: 3D positioning solutions for different receivers, indicating impact of actual observation gap occurrences with dotted ellipses: (a) 3D positioning plots for MBAR; (b) 3D positioning plots for HRAO; and (c) 3D positioning plots for SHIP

To examine the specific impact from the three PRNs whose time series WL_{MW} are presented in Figure 8.15, the epoch regions of the observation gaps that occurred on the three gapped satellites are identified as indicated by the dotted ellipses. The observation gap occurrences on PRN 11 observed by MBAR are within the $366-645^{th}$ epochs; the observation gap occurrences on PRN 22 observed by HRAO are within the $400-1100^{th}$ epochs; and the observation gap occurrences on PRN 22 observed by HRAO are within the $2358-3553^{th}$ epochs. The improvement in the NEW positioning solutions for MBAR, HRAO and SHIP at these respective $366-645^{th}$, $400-1100^{th}$ and $2358-3553^{th}$ epochs regions is obvious in Figure 8.15, with the greatest improvement in the height component for all three receivers. The corresponding positioning statistics for the positioning solutions are already presented in Tables 8.2, 8.1 and 8.6 respectively. The NEW improved positioning accuracy at post-gap epochs, unlike the re-initialising HFT which presented non-improved positioning results at such epochs. The noticeable spikes still present in the NEW positioning solution within the $2358-3553^{th}$ epochs are due to the frequent change in DOP values as PRN 22 re-locks and gapped frequently.

Obviously, the gap-connect technique contributes to the high level of positioning performance of the new dual-frequency code positioning method and its ability to outperform the HFT with such large margins revealed in the tables of statistics obtained from the tests in this chapter.

8.5. Implementation and Related Issues

It can be observed that the proposed dual-frequency single-satellite cycle slip detection algorithm that is based on the ATD technique is only implementable after a few continuous observation epochs have been recorded from an observed satellite. This number of epochs has been set to 10 epochs/seconds for the 1Hz data sets used throughout this research. For PPP, about 20-30 minutes of observation data could be required to achieve reliable ambiguity fixes (Carcanague *et al.*, 2011b) for observed satellites. Hence, the required number of pre-detection observation epochs for the ATD process used for cycle slip detection could be more, and can be required

to resolve the initial integer ambiguity, N_i^s, for each observed satellite in view of a GNSS receiver, if required.

The search range for a detected cycle slip on a satellite, which is set to ± 5 cycles in the proposed dual-frequency cycle slip determination algorithm (Section 6.4.1), could be determined adaptively as the nearest integer value to the maximum of the two tripled standard errors (uncertainties) on the dual-frequency cycle slip float values estimated for each cycle-slipped satellite. When a few, and not all, observed satellites indicate cycle slip at the same epoch, the uncertainties on the phase-only estimated cycle slip float values are usually less than 0.5cycles (see Figure 6.3), which would often result in a search range of ± 2 cycles. Implementation of such an adaptive search range could further help increase the computational speed, especially when cycle slips, as often the case, are not detected on all observed satellites at a same epoch.

The proposed dual-frequency cycle slip detection and correction (CSDC) algorithm can easily be integrated with the proposed code error mitigation algorithm to improve positioning performance in all environments. The computational load of the cycle slip determination algorithm is much less than that of the widely used LAMBDA method; and the computational load of the cycle-slip resilient code error mitigation algorithm is as light as the conventional code-carrier smoothing (Hatch filter) technique. Hence, the integration and implementation of the proposed algorithms are feasible for both real-time and post-processing GNSS applications, time-critical applications, and without significant impact on a receiver's battery power.

The dual-frequency CSDC and the code error mitigation algorithms can be implemented in a receiver operating in all environments. However, the errors in NLOS signals (Jiang & Groves, 2012), which are usually in the range of tens of a metre, cannot be mitigated even though prevalent cycle slips may be detected and corrected in a difficult environment where cycle slips and short duration observation gaps may be rampant.

8.6. Summary

The proposed algorithms for a dual-frequency receiver, unveiled in Chapter 6, have been tested using dual-frequency data obtained with receivers operating either in static or kinematic mode. The developed gap-connect technique enables robustness to observation gap occurrences, as intended. The new dual-frequency cycle slip algorithm shows good efficiency in detecting all possible cycle slip pairs. The dual-frequency CSDC algorithm achieved, a minimum of 99.9% correct detection and a minimum of 95.1% correct fix of cycle slips simulated under different scenarios, and for different receivers in static and kinematic modes.

The point positioning results also showed the performance capability of the new (NEW) dual-frequency method that integrates the proposed simple cycle slip fixing and cycle-slip-resilient code error mitigation algorithms. Without simulated cycle slips, the NEW and HFT positioning results presented comparable positioning results for a mid-latitude moving receiver (SHIP). In positioning MBAR, a static receiver in the equatorial region, and HRAO, another static receiver in the southern hemisphere, under no simulated cycle slip condition, the NEW method outperformed the HFT by within 4-5% in positioning accuracy. Under the simulated cycle slip scenarios, for static and kinematic receivers, the NEW method showed significant improvement over the conventional code-carrier smoothing (Hatch filter technique (HFT) that does not include any cycle slip fixing algorithm; it achieved within 18-55% positioning accuracy improvement over the HFT. In almost all positioning results, the NEW method achieved the most positioning improvement in the height component. It is however envisaged that, if a conventional cycle slip fixing algorithm is used alongside the Hatch filter, the presented HFT positioning results under the simulated cycle slip test sections are bound to be improved upon, even though the level of further improvement has not been investigated and therefore cannot be currently ascertained.

Chapter 9.

Future and Modernised GNSSs: Effects on Proposed Algorithms

The evolvement of GNSSs due to modernisation of current GNSSs like GPS and GLONASS, and the addition of future GNSSs like Galileo and BeiDou (previously referred to as Compass), would ensure more signal availability to users in the different parts of the world. Notably, the signals to be transmitted by all GNSSs in the near future are at least different in terms of the used ranging code, applied modulation or transmit signal power, when compared to the representative GPS L1C/A and L2P signals that yield the data used in testing the proposed algorithms developed in this thesis. This chapter first presents a brief insight into the on-going modernisation of current GNSSs and the future GNSSs coded signals as well as the expected benefits to civilian users of GNSSs. Subsequently, the chapter discusses the effects of the new signal structure and the availability of triple civilian frequency on the performance of the proposed single-frequency improved ionospheric model, the cycle slip detection and determination algorithms as well as on the proposed cycle-slip-resilient code error mitigation algorithm.

9.1. Future GNSSs and Signals

The spectrum of the RNSS has become a scarce resource and there has been need to optimise the already saturated spectrum to accommodate the different GNSSs envi-

saged in the near future, which essentially include the American GPS, the Russian GLONASS, the European Galileo and the Chinese Compass. One means identified to address this need was by ensuring interoperability and compatibility of all GNSSs, thereby improving positioning accuracy and availability, to civil users of GNSSs worldwide.

To ensure interoperability and improved signal performance, the future GNSSs and modernisation of the current GNSSs would be CDMA signals with high chipping rate spreading codes, wider-band modulation and/or increased power of broadcast satellites' signals.

9.1.1. Modernisation, Spreading Codes and Modulations

The legacy CDMA GPS L1C/A - the first civilian GPS signal - employs a spreading code of 1.023Mcps chipping rate and binary phase shift keying - often referred to as BPSK(1) modulation. The future/modernised GNSS signals, which are based on CDMA, employ chipping rates and spreading modulations different from the fundamental 1.023Mcps and BPSK(1) respectively, for the purpose of presenting better performance for both military and civilian user.

The more than 30 GPS blocks IIA, IIR, IIR-M and IIF satellites currently in orbit broadcast the L1C/A, L1P(Y) and L2P signals, but the IIR-M and IIF satellites transmit the additional L1M, L2M and L2C code signals. The block IIF satellites transmit an additional L5 code signal, whilst the next generation block III satellites will transmit all current signals in addition to an L1C signal. The L1C signals would be received 25% higher power than the LIC/A signal, making it also more robust (Potukuchi *et al.*, 2010). The first IIR-M satellite that transmitted L2C signal was launched in 2005, and as of September 2010, there were seven GPS satellites transmitting the L2C; the first L5 signals were broadcast in 2009 from a modified IIR-M satellite, but the transmission resulted in faulty L1 and L2 signals, hence the satellite was never fully commissioned. However, as at December 2012 three operational satellites (PRN25, PRN1 and PRN24) transmit the L5 coded signals (NGIA, 2012), while we await the L1C signal envisaged from 2014.

The GPS L2C signal is the second civilian GPS signal, employing the same sprea-

ding code of 1.023Mcps chipping rate and binary phase shift keying BPSK(1) modulation as the L1C/A signal; thus should present the same level of performance obtainable with the L1C/A signal. The GPS L5 signal is the third GPS civilian signal. It employs a 10.23Mcps chipping rate and a binary phase shift keying denoted BPSK(10) modulation. The envisaged GPS block III satellites after 2014, will transmit the fourth civilian signal called L1C on the L1 band. The L1C was originally designed by the United States and Europe to enable interoperability between GPS and Galileo - to serve as a common civil signal - but other GNSS, such as Beidou, are adopting the L1C as a future standard for international interoperability. The joint United States and Europe recommended the multiplexed binary offset carrier (MBOC) spreading modulation for the L1C and the GALILEO L1 Open Service signals. The MBOC combines 90% of a higher-powered BOC(1,1) and 10% of a lower-powered BOC(6,1). A BOC(m,n) waveform is a Binary-Offset-Carrier (BOC) modulation where a square sub-carrier of frequency m-times the reference 1.023MHz frequency, multiplies a lower n-times 1.023Mcps chip rate signal. The BOC modulation reduces the interference with BPSK-modulated signals, enabling the spectrum of the modulated carrier signal to have low energy at the carrier/centre frequency and higher energy at some side-lobes away from the carrier frequency. This higher energy at higher frequency than at the centre frequency helps improve signal tracking performance at the expense of increased pre-correlation bandwidth. MBOC modulation could present multipath error envelop that diminishes at smaller multipath delay lengths relative to a direct signal from a satellite to the receiver, and that is better than that obtainable with the BOC- or BPSK-modulation (Hein *et al.*, 2006). Need to say, the GPS M-code on the L1 (L1M) and L2 (L2M) is a BOC code with a 10.23MHz sub-carrier frequency and 5.115MHz spreading code rate, called BOC(10,5) (Weill, 2003).

The Galileo E5a and E5b signals use the alternate-binary-offset-carrier (AltBOC) spreading modulation - a 15.345MHz sub-carrier frequency and 10.23Mcps spreading code rate - AltBOC(15,10). Galileo E5a and E5b signals are transmitted on the carrier frequencies of 1176.45MHz and 1207.14MHz respectively, and they carry different navigation messages. This AltBOC(15,10) modulation enables the peak-

power frequencies of E5a and E5b signals to be separated by 30.69MHz. The E5 AltBOC spread modulation enables the E5a and E5b signals to be tracked coherently at will as one signal centred at 1191.795MHz (Simsky *et al.*, 2006).

The current modernisation of GLONASS has led to the launch of the first of the GLONASS-K satellites to broadcast CDMA signals on the L3 band in 2011. The L3 signal uses 10.23Mcps spreading code and a BPSK(10) modulation to modulate the 1202.025MHz carrier. Future modernisation of GLONASS are planned to involve variants of the BOC-modulation in the L1, L2, L3 and L5 bands (RSS, 2012b)

The different spreading modulation, BPSK-, BOC-, and MBOC-modulation, provide different opportunities to trade between performance and receiver complexity. For example receivers with modest front-end bandwidths would not access the benefit of MBOC-modulation but would be less expensive and provide longer battery life if it only processes say the basic BPSK or BOC(1,1) modulated signal (Hein *et al.*, 2006). Expectedly, future single-frequency GNSS receivers to be produced for mass market or to be integrated in various mobile devices, used for non-precision GNSS applications, are expected to be modest in terms of their complexity and performance, unlike future multi-frequency receivers.

9.1.2. Future Availability of Civilian Triple-frequency Observations

The on-going GNSSs modernisation and the plan for future GNSSs herald the era of civilian triple-frequency signals from the L1, L2 and L5 bands. For instance, triple-frequency code and phase observations would be obtained with a GPS-only receiver receiving the L1C/A or L1C signal on the L1 band, the L2C signal on the L2 band, and the L5 signal on the L5 band; or with a receiver designed for Galileo Open Service receiving the signals on the E1/L1, E5a and E5b bands. Triple-frequency observations would also be obtainable from other GNSSs like GLONASS, and more complex receivers would be able to obtain and process observations from a combination of different observations from different GNSSs, taking advantage of their interoperability.

Based on the future and modernised code structures, triple-frequency receivers are

expected to be more complex in design, and probably more expensive than single- and dual-frequency receivers. As a result, it is perceived that both single- and dual-frequency receivers would still be available for handheld mobile users and even for other relatively precised applications, even in the presence of triple-frequency.

9.2. The Future GNSS Signals and the Proposed Algorithms

The proposed cycle slip detection and determination algorithms in this thesis have been designed and tested for both single- and dual-frequency operations, using only GPS L1C/A and L2P code and phase observations. While these new algorithms can easily be used for observations from other GNSSs, the new civilian signals are designed to present higher performance levels than the current civilian GPS L1C/A and that could also affect the level of performance of the proposed algorithms on future single- and multi-frequency GNSS observations. It is therefore necessary, based on theoretical results from published works, to discuss the possible effects and performance expected from the proposed algorithms on future and modernised signals of GNSSs.

9.2.1. Effect on the Cycle Slip Detection and Determination Algorithm

Some triple-frequency cycle slip detection and determination techniques have already been proposed as found in Dai *et al.* (2008, 2009); Xu & Kou (2011); de Lacey *et al.* (2011), but all these involve using the code observations in either or both detection and determination of cycle slips. Moreover, all of these references except the last, engage the computationally intensive LAMBDA method in fixing cycle slip integer values. The proposed single- and dual-frequency cycle slip detection and determination algorithms are phase-only-derived algorithms, involving a single satellite's search space.

The future GNSSs signals structure are not likely to affect phase observations

noticeably. The level of the phase noise would still be within a few millimetres as it is with the current GPS L1 and L2 phase observations, going by the phase noise results obtained by Simsky *et al.* (2006) in assessing the performance of Galileo signals and comparing same with GPS signals. However, the influence of thermal noise is proportional to a carrier wavelength, and the phase multipath error is known to be a function of the carrier wavelength (Avila-Rodriguez *et al.*, 2007). These multipath and noise effects would result in different phase error levels on different phase observations from different bands. This was considered in setting the error thresholds for the proposed dual-frequency CSDC algorithm. Theoretically, the phase observations from the L5, E5a and E5b signals would have maximum multipath errors of one-quarter of their corresponding wavelengths, which are respectively $\frac{c}{4f_5} \simeq 6.4$cm, $\frac{c}{4f_{5a}} \simeq 6.4$cm and $\frac{c}{4f_{5b}} \simeq 6.2$cm. It is usually sufficient to assume a 1-sigma noise level of 5mm for phase observations obtained from any band, as earlier done. In this way, the adaptive time differencing (ATD) process used for cycle slip detection by newly proposed CSDC algorithms, could result in the maximum differenced phase error levels on L5/E5a and E5b phase observations reaching twice the sum of multipath and 3-sigma noise level, i.e. $2(0.064 + 0.015) = 0.158$m (0.62cycles) and $2(0.062 + 0.015) = 0.154$m (0.62cycles) respectively for L5/E5a and E5b. As such, the absolute adaptively-differenced error values of $\triangle^{d_s} e^s_{\psi,5} = 0.158$m, $\triangle^{d_s} e^s_{\psi,5a} = 0.158$m and $\triangle^{d_s} e^s_{\psi,5b} = 0.154$m can be used when detecting or determining cycle slips on L5, E5a and E5b phase observations, which are larger in magnitude than $\triangle^{d_s} e^s_{\psi,1} = 0.126$m and $\triangle^{d_s} e^s_{\psi,2} = 0.152$m on L1 and L2 phase adaptively differenced values.

A single-frequency CSDC involving L1C/A, L2C, L5, E5a or E5b phase observation would follow the set-out procedure for single-frequency CSDC in Chapter 5, without any modifications. For a dual-frequency operation, e.g. involving L1C/A and L5, a widelane wavelength of $\lambda_{WL_{15}} \simeq 0.75$m as against $\lambda_{WL_{12}} \simeq 0.86$m for dual-frequency L1C/A and L2P operation, results. As in Equation (6.12), the maximum error level on an L1C/A and L5 phase-widelane ADS value is $\lambda_{WL_{15}} \Delta^{d_s} e_{\lambda_{WL_{15}}} < \lambda_{WL_{15}} \sqrt{\left(\frac{0.126}{\lambda_1}\right)^2 + \left(\frac{0.158}{\lambda_5}\right)^2} \simeq 0.68$m. This error value of 0.68m is smaller than the 0.78m value derived for the L1 and L2P dual-frequency combination in Section 6.3.2,

but the same expected maximum validation threshold $\Omega_{expt} = \frac{\lambda_{WL_{15}} \Delta^{d_s} e_{\lambda_{WL_{15}}}}{\lambda_{WL_{15}}} \simeq 0.90$ results, indicating that up to 0.9 widelane cycle slip error can be contributed to an estimated L1C/A and L5 phase widelane cycle slip float value, as earlier obtained for the L1C/A and L2P phase widelane cycle slip in Section 6.4.2. Also, a 0.68m error could cause up to four cycles of error on the L1 phase observation, and as such, a smaller or the same 100-value search space defined for the L1 and L2 dual-frequency observations, can also be used for L1C/A and L5. Putting these together suggests that similar dual-frequency CSDC performance would be likely obtained when the L5 band signal is used in dual-frequency operation with either of L1C/A or L1C. For the L2 and L5/E5a signals for dual-frequency operation, and following the same error estimation procedure, $\lambda_{WL_{25}} \simeq 5.86$m, $\lambda_{WL_{25}} \Delta^{d_s} e_{\lambda_{WL_{25}}} < 5.15$m and $\Omega_{expt_{25}} = \frac{5.15}{5.86} \simeq 0.88$, which indicates that the largest widelane wavelength is obtained by this combination, and it presents the least of the maximum widelane cycle slip error of 0.88 cycles on an estimated L2 and L5 widelane cycle slip float value. Consequently, it can be inferred that better dual-frequency CSDC performance could be obtained using the proposed CSDC algorithms on L1 and L5 dual-frequency signals when determining the widelane cycle slip; observing that the search space required for L2 and L5 simultaneous cycle slip values determination will be relatively large, observing that $\frac{5.15}{\lambda_5} \simeq 20$ cycles and $\frac{5.15}{\lambda_2} \simeq 21$cycles.

A significant performance improvement is envisaged under a triple-frequency operation with the modernised/future GNSSs. This is because, for every triple-frequency phase observations from a GNSS satellite, three phase-geometry-free ADS values and three phase-widelane ADS values, resulting to a total of six ADSs can be generated. A 2-degree of freedom thus exist for a single cycle-slipped satellite since only a maximum of four unknowns including three cycle slip values and a receiver higher-order variation value are to be estimated. It therefore means that, there will be no need to include the code observations in estimating cycle slip float values even if all observed satellites are detected to have cycle slips at a given epoch. Though subject to future investigation, the search space for determining the triple-frequency cycle slip can be made adaptive to the level of uncertainty in the estimated cycle slip float values, which was not the method used in fixing dual-frequency cycle slip in this work.

9.2.2. Effect on the Improved Ionospheric Model and Code Error Mitigation Algorithm

The new signals on future GNSS are designed to improve code tracking and multipath rejection, suggesting that the code error level on future code observations would be lower relative to code error level on an L1C/A code observations. Theoretical error bounds determined for some of the new coded signals have shown improved multipath rejection with code multipath error envelopes under a few metres (Weill, 2006). Performance comparison results presented by Simsky *et al.* (2006) showed multipath rejection improvement of the Galileo E5a, E5b and E5 AltBOC coded signal over the L1C/A coded signal; while Hein *et al.* (2006) through simulation, showed code multipath rejection improvement levels that could be reached with the L1C coded signal in the future.

Consequently, it would not be wrong to think that even without any form of code smoothing, code observations from future GNSS satellites will improve positioning accuracy compared to what is currently obtainable with the L1C/A code observation. It also follows that single-frequency receivers using the L1C or L5 signal, for instance, would be able to generate even more accurate receiver-generated Improved Ionospheric Correction (IIC) model as proposed in Chapter 5, compared to the IIC model generated with the L1C/A signal.

In the same vein, the application of a code smoothing or error-mitigation technique is therefore considered as a processes that will further mitigate error levels on the 'to-be-improved' code observation from modernised/future GNSSs signals - L1C, L5, E5b, etc, to further enhance position. The proposed cycle-slip-resilient code error mitigation algorithm is expected to further contribute to improving single and multi-frequency positioning, as it will further help mitigate code error without any foreseeable challenges. Considering that the ionospheric delay would be better estimated and eliminated with future signals, and that cycle slip determination and correction processes are likely to be improved, the proposed code error mitigation algorithm is only expected to give better performance under single- and multi-frequency operations.

Chapter 10.

Conclusions and Future Work

This last chapter presents as a summary, the findings, in line with the set-out objectives of this work, and the conclusions drawn from this research. The contributions and implications of this work are also highlighted. The future research work envisaged to proceed from this current stage of work are subsequently unveiled.

10.1. Summary and Conclusions

Various factors limiting accurate GNSS positioning with both a single- or dual-frequency receiver can be identified. Crucial among these factors are the inherent code error on the code observation and cycle slip occurrences on the phase observation from a satellite; the inadequate accuracy in the broadcast ionospheric model for single-frequency receivers; and the occurrence of observation gaps - a prevalent phenomenon in difficult environments. Continuous improvement in GNSS point positioning can only be achieved if adequate or robust processing techniques are developed to mitigate the impacts of these factors on a receiver positioning solution, as they cannot be completely avoided. This research was motivated by the need to proffer adequate solutions to improve point positioning in the presence of these limiting factors, as can be observed from the set-out objectives in Section 1.3 of this thesis.

The performance metrics: positioning and ionospheric modelling accuracies, precision, percentage of detected and rightly corrected cycle slips, and robustness to the

impact of observation gap occurrences, are been used to examine the performances of the newly developed algorithms in Chapters 5 and 6. The improved computational speed of the cycle slip fixing/determination (repair) algorithms, can be asserted, due to the lower computational load when compared to the widely used LAMBDA method for cycle slip determination. The suitability of the newly developed algorithms for real-time applications can also be asserted, as the used GPS data sets have been processed in real time mode, using data recorded by for different receivers driven by different clock.

In the sequel, and in line with the research objectives, the major findings and conclusions of this research are summarised as follows:

- *How would a real-time single-satellite phase-only-derived cycle slip detection and determination algorithm usable by a static or moving single-frequency GNSS receiver be developed? What percentage of correct detection and correct fix of cycle slips do we expect from such an algorithm?*

An algorithm, which uses ATD of a single-satellite time series phase-only-derived observable for cycle slip detection, and employs a cycle slip determination or fixing procedure based on only a single satellite's estimated cycle slip float value, as described in Section 5.2, has been developed and proposed. The algorithm which can be used by a static or moving single-frequency receiver, was also tested by way of simulated cycle slips. The tests results revealed that the single-frequency CSDC algorithm, on an average based on the different cycle slips tests performed under different scenarios, achieved more than 98% correct detection and 92% accurate determination (fix) of simulated cycle slips for different satellites observed by different receivers operating in both static and kinematic domains.

- *How would a single-satellite phase-only-derived cycle slip detection, fixing and validation algorithm, suitable for a dual-frequency receiver operating in either static or kinematic mode in real-time, be developed? What percentage of correct detection and correct fix of cycle slips do we expect from such an algorithm?*

Such a dual-frequency algorithm has been developed in this work. Each of the dual-frequency time series phase observables of a cycle-slipped satellite is adaptively

differenced to generate the corresponding dual-frequency phase ADSs used for dual-frequency cycle slips detection, as presented in Section 6.3. Subsequent to an all-satellite least squares based procedure for the estimation of cycle slips float values and common receiver high-order variations, the fixing and validation procedures are implemented as presented in Section 6.4, to fix dual-frequency cycle slips float values to integer values. The algorithm which can be used by a dual-frequency receiver operating in either static or kinematic mode, was tested by way of simulated cycle slips. From the different tests results, the algorithm achieved a minimum of 99.9% and a maximum of 100% correct detection of simulated cycle slips, while it achieved a minimum of 95.1% and a maximum of 100% correct fix of simulated cycle slips for different satellites observed by different receivers operating in both static and kinematic domains. Compared to the widely used LAMBDA method, this developed dual-frequency CSDC algorithm is simpler, engaging only a small search space of 100 values defined for individual cycle-slipped satellite. It is not computationally intensive and does not require determination of a decorrelating transformation matrix as it is with the LAMBDA method.

- *How can an improved broadcast ionospheric correction model be implemented on a single-frequency receiver in real-time, to enable better ionospheric delay corrections? From a case study, how accurate can such improved ionospheric model be for a single-frequency receiver in the mid-latitude region, and for a single-frequency receiver in the equatorial region?*

An algorithm for generating an improved broadcast ionospheric correction model, which is designed to be implemented within a single-frequency receiver, was derived in Section 5.3. The improved ionospheric model (IIC) is generated from the single-frequency code minus phase observable, and it is initialised by a broadcast ionospheric model. From a case study of two receivers: SHIP located in the mid-latitude region; and MBAR, located in the equatorial region; the generated single-frequency IIC, compared to the GPS broadcast Klobuchar model, achieved better ionospheric delay correction accuracy, for both receivers in the different regions. The ionospheric correction on two particular satellites observed by the SHIP and MBAR were examined to enable performance comparison. The IIC can outperformed the

broadcast Klobuchar model by more than 0.75m in the estimated ionospheric delay under 1 hour observation for the receiver in the equatorial region, and up to a few tens of centimetres for the receiver in the mid-latitude region, within the same interval of 1 hour. Subsequent to correcting for the ionospheric delay with the IIC, the positioning of the MBAR receiver in the equatorial region showed significant improvement. The positioning of the SHIP receiver in the mid-latitude region, subsequent to correcting for the ionospheric delay with the IIC, could not be seen to have resulted in any significant positioning improvement. This further suggests that the Klobuchar model may be accurate enough for a mid-latitude single-frequency user, and not likely to be accurate enough for a single-frequency receiver within the equatorial region.

- *How should dual-frequency receivers estimate phase-only-derived ionospheric delay in the presence or absence of cycle slips, and predict same in the event of an observation gap with acceptable level of accuracy and precision?*

The thesis proposed a procedure to estimate a phase-only-derived ionospheric delay in the presence or absence of cycle slips when a satellite is continuously observed without observation gap occurrences, in Section 6.5; and further unveiled a procedure for ionospheric delay prediction in the event of an observation gap, in Section 6.8.1. For a continuously observed satellite, the procedure models the ionospheric delay as a composition of a constant unknown initial component and a time-varying relative ionospheric delay component relative to the first observation epoch of a satellite. In the event of an observation gap, the relative ionospheric delay component is predicted as a linearly varying parameter within the observation gap intervals and up to a current post-gap epoch. The tests via simulation and actual data (with no form of simulation applied) performed to examine the accuracy and precision of the predicted ionospheric delay indicated accuracy under 4mm under short duration observation gaps. However, the longest duration of an observation gap experienced in the test data was 126seconds. It is envisaged that the prediction will become unreliable as the observation gap duration increases. Hence, it is suggested that the prediction algorithm be used for short duration observation gap of a few minutes - not more than 5minutes under relatively quiet ionospheric conditions, as the

ionospheric variation may vary widely within longer intervals.

- *Can an efficient code smoothing or error mitigation algorithm that has capability to mitigate the code observation error level(s) on the code observation(s) from a satellite, irrespective of cycle slip occurrences on the phase observation(s), be obtained? Can the algorithm be made robust to observation gap occurrence? Compared to the conventional code-carrier smoothing technique, what level of performance improvement in terms of positioning accuracy and precision would it offer?*

Unlike the currently existing code smoothing techniques, two efficient cycle-slip-resilient code error mitigation algorithms have been developed as part of this work, for a single-frequency receiver and a dual-frequency GNSS receiver operating in static or kinematic domain, as can been found in Sections 5.4 and 6.6. The dual-frequency code error mitigation algorithm is also made robust to observation gap occurrences. The efficiency of the code error mitigation algorithm is traceable to non-reinitialisation in the algorithm whenever a cycle slip occurs, as cycle slips are detected and resolved in real time, using the simple single- or dual-frequency CSDC algorithm proposed in this thesis. The robustness of the dual-frequency code error mitigation algorithm is anchored on the fact that, even at post-gap epochs, post-gap cycle slips are determined instead of re-initialisation to determine new ambiguity value as done by conventional technique. Compared to the conventional code-carrier smoothing technique, often called the Hatch filter, the achieved performance levels are fairly similar in the absence of cycle slips on phase observations.

However, in the presence of cycle slips or observation gap occurrences, the new algorithm outperforms a standalone Hatch filter technique (a technique that re-initialises when cycle slip occurs, since it does not integrate any cycle slip fixing algorithm) significantly. The tests under the simulated cycle slip scenarios reveal that the new method, which integrates the proposed cycle slip fixing algorithms, outperforms the standalone Hatch filter by 25-42% in positioning accuracy when using single-frequency data, and by 18-55% in positioning accuracy when using dual-frequency data. The most improvement of the new method over the Hatch filtered solutions was found in the height component, where height positioning accuracy and

precision that reached 77% and 80% respectively, were observed. The performance results of the new and the Hatch filter methods may be comparable under no-simulated cycle slips, and it is envisaged that if a conventional cycle slip fixing algorithm is used alongside the Hatch filter, the achieved Hatch filtered positioning results for the simulated cycle slip tests are bound to be improved upon, even though the level of this improvement has not been investigated and therefore cannot be currently ascertained.

- *How would a common receiver clock jump or reset value be reliably estimated in non-positioning domain in real-time, irrespective of the receiver oscillator type?*

In this work, the occurrence of clock jump was easily detected by two complimentary equations given by Equations (5.6) and (5.7). The estimation of the value of the clock jump or common receiver high-order variation that indicates the level of drift variation of the receiver clock oscillator, is done in the non-positioning domain; it involves the use of all satellites' phase ADSs, and only two code ADSs that may be included if necessary, in a combined least squares based estimation of the common receiver high-order variation and possible cycle slip float values. The determination of a common receiver clock jump or receiver common high-order variation is done irrespective of the receiver oscillator type. If a clock jump is detected for a given current epoch, the estimated value of the common receiver high-order variation then represents the value of the common clock jump. The clock jump is assumed common to all observations from all satellites at a given epoch, and its instantaneous estimation and elimination enables reliable cycle slip determination in real-time, and 'decorrelation' of all phase and code observations. However, tests results have shown as expected that quartz oscillator clocks presents higher common high-order variation or drift values than receivers running or connected to atomic clocks.

- *How can the algorithms to be developed be made robust to an observation gap occurrence, so as to improve positioning accuracy and precision even in difficult environments such as urban canyons? Can the post-gap convergence time usually associated with ambiguity fixes on phase observations and the usual*

many-post-gap-epoch observation required for achieving significant code error mitigation be reduced or eliminated at a post-gap epoch?

The algorithms developed for a dual-frequency operation are robust to observation gaps of short duration (less than four minutes). This is made possible through the prediction of the relative ionospheric delay for gapped and post-gap epochs, the estimation of the cycle slip values between a pre-gap epoch's and a post-gap epoch's dual-frequency phase observations, and the subsequent generation of the error-mitigated dual-frequency code observables at a post-gap epoch for a gapped satellite. The technique incorporating these three processes has been dubbed 'gap-connect' technique, and has been developed for use on dual-frequency data as presented in Section 6.8. This robust capability does not exist for the single-frequency algorithms developed in this work. The gap-connect technique, unlike conventional ambiguity and code smoothing techniques, avoids the usual re-initialisation associated with such existing techniques whenever an observation gap occurs. As such, rather than use unsmoothed code observables resulting from a re-initialising technique, the gap-connect technique continues the error mitigation or smoothing process to generate error-mitigated code observables that result in improving positioning rather than degrading positioning as could be done by a re-initilised (conventional) technique. Because the gap-connect technique does not re-initialise when an observation gap occurs, it also eliminates the long convergence time associated with conventional ambiguity resolution or code smoothing techniques after an observation gap occurrence. The obtained code-based positioning results indicate significant improvement of the gap-connect technique over a re-initialising technique (Hatch Filter), at all post-gap epochs and up to tens of epochs subsequent to a post-gap epoch. The tens of epochs subsequent to a post-gap epoch is a measure of the convergence time taken to re-achieve significant level of smoothing in the re-initialising Hatch filter technique.

- *Identify the possible limitations, if any, in the developed algorithms or techniques and give appropriate measures or recommendations for use and implementation, accordingly.*

Though achieve very high level of performance efficiency, the developed algorithms are not perfect as they are established under certain assumptions and boundary conditions that cannot always be guaranteed to be true. The CSDC algorithms for single and dual-frequency receivers are limited by the magnitude of the adaptively-differenced errors. The ATD process for cycle slips detection is quite sensitive to receiver clock drift variations, and also to receiver antenna dynamics for the case of a moving receiver. The possible inclusion of code ADSs when all satellites indicate cycle slip, is another drawback - because of the associated code error levels. As a result, the CSDC process could indicate a false cycle slip when actually there is none, or generate cycle slip float values that could be subsequently fixed to 'false' integer values. There is also the implication of no-detection for a truly occurring cycle slip if the magnitude of the adaptively-differenced error or high-order receiver clock variation combines destructively with the value of a cycle slip, or a if cycle slip pair, in the case of dual-frequency, becomes too small a value to reach the set threshold(s) for a cycle slip detection. As measures, the algorithms attempt to limit these occurrences by setting threshold values for different scenarios, and implementing a process called Nulling of Fixed Cycle Slips (NFCS), as presented in Section 5.2.3 and Section 6.4.3, to eliminate already fixed cycle slip(s) considered as 'false' cycle slip(s). However, the tests results showed that the magnitude of the cycle slip error is usually within 1 to 3 cycles when an incorrect fix of a truly occurring cycle slip happens, and a falsely detected and fixed cycle slip value by the CSDC algorithms is usually under 5 cycles. It is perceived that a further scrutiny of the CSDC algorithms with different data sets would enable its further improvement.

10.2. Contributions of this Research

In the course of this research work, significant contributions to knowledge have been made. The main contributions are highlighted as follows

- The research introduces a new single-satellite phase-only-derived cycle slip detection algorithms independent of code observations, for single-frequency and dual-frequency GNSS receivers operating in static or kinematic mode.

- The research contributes a new single-satellite cycle slip determination process, which is much less computationally intensive than currently used cycle slip determination algorithms such as the LAMBDA method.

- It proposes a new algorithm for mitigating code errors in GNSS code observations even in the presence of cycle slips on phase observations, which is not possible with existing code smoothing techniques such as the Hatch filter or its derivatives.

- The research presents a new algorithm for improving the broadcast ionospheric correction model, which is implemented within a single-frequency receiver, and virtually requires no mapping function.

- The research introduced a gap-connect technique suitable for avoiding the usual re-initialisation of conventional ambiguity resolution or code smoothing techniques, to achieve robustness to observation gap occurrences, and improve positioning in all environments.

- The research introduced a novel procedure for determining a common receiver clock jump value and of a receiver common high-order drift variation from a non-positioning domain, irrespective of the receiver clock oscillator type.

10.3. Implications of this Research

The implications of this research, by way of the contributions listed above, can also be identified as follows:

- The implementation of these newly developed CSDC algorithms would enable efficient and faster cycle slip determination in real-time, since they are phase-only-derived algorithms employing relatively small search spaces and reduced computational load.

- The use of the cycle-slip-resilient and error-mitigated code observables will improved point positioning significantly, especially in difficult environments where cycle slip occurrence is prevalent.

- The robustness to observation gap occurrence provided by the gap-connect technique would help improve both point and precise point positioning in all environments, as cycle slips can be determined and continuous code smoothing achievable at post-gap epochs. This provides huge benefit to a receiver used in a difficult environment where observation gaps and cycle slips are frequent.

- The introduced ATD process to generate ADSs and the non-position domain estimation of the common receiver high-order variation, present means to 'de-correlate' satellites' code and phase observables, and obtain their appropriate covariances for adaptive generation of the required weight matrix for weighted least squares or Kalman filter based positioning algorithms.

10.4. Future Work

Considering the current state and results of this research, some future work can be identified. Firstly, it will be gainful to use actual single-frequency data collected by single-frequency receivers in open sky and difficult environments and different regions of the world, with known truth positions or trajectories, to further investigate the actual performance of the proposed single-frequency algorithms with actual single-frequency data sets. In addition, the efficiency of the single-frequency CSDC, and a critical performance analysis of the cycle-slip-resilient code error mitigation algorithm would be further performed with collected static and kinematic single-frequency data, so as to be able to build more confidence in the proposed techniques developed in this thesis.

Secondly, there is need to further investigate the proposed dual-frequency CSDC performance, in terms of achievable success rate in fixing cycle slips, and the comparative performance analysis of the cycle slip fixing efficiency and computational speed relative to the LAMBDA method, using both static and kinematic data. Since true values of cycle slips are only known if simulated, cycle slip simulation plays a critical role in taking forward this research, particularly cycle slip simulation under different receiver antenna dynamics and different code observation error scenarios. These would enable further sensitivity analysis of the proposed CSDC and code er-

ror mitigation algorithms. The single-frequency and dual-frequency performances of the new code error-mitigation and CSDC algorithms in precise point positioning, under different environments. These will also enable performance comparison of the proposed algorithms with different precise point positioning solutions obtained by least squares and Kalman filter based algorithms.

Thirdly, it will be interesting to investigate and see the performance of these algorithms or their modified versions in an ambiguity resolution process, and the impact on convergence time. The performance of this integrated algorithms in resolving initial ambiguity values, and subsequent determination and correction of cycle slip values in precise point positioning, under frequent observation gap occurrences in dense urban canyon, needs to be further investigated.

Fourthly, with the determination of the common receiver clock high-order variation, the ability to model receiver clocks irrespective of the receiver oscillator type, would be investigated. A successful receiver model realisation would enable use of only three satellites for receiver positioning especially when enough satellites are unavailable, and also the decorrelation of positioning solutions from receiver clock offset estimation in the positioning domain.

There is also the need to examine the impact of active ionosphere on the proposed dual-frequency CSDC algorithm, using data obtained on known days of ionospheric disturbances. This investigation would be coupled with modification of the newly developed CSDC algorithms for triple-frequency operations. This would be investigated for both single- and dual-frequency receivers.

Lastly, the efficiency in using adaptively determined epoch by epoch covariance matrix obtainable from the phase and code ADSs of observed satellites, as the measurement covariance matrix required for a Kalman filter or least squares based positioning algorithm, would also be investigated. This successful, it would stand as a better alternative to conjectured covariance matrices often used in many weighted least squares and Kalman filter positioning algorithms.

Bibliography

Alnaqbi, A. (2010). Precise GPS positioning with low-cost single-frequency system in multipath enviroment. *The Journal of Navigation*, **63**, 301–312.

Ambardar, A. (1999). *Analog and digital signal processing*. Brooks/Cole Publishing Company.

Amin, M.G. & Sun, W. (2005). A novel interference suppression scheme for global navigation satellite systems using antenna array. *IEEE Journal on Selected Areas in Communications*, **23**, 999–1012.

Andrei, C.O., Chen, R., Kuusniemi, H., Hernandez-Pajares, M., Juan, J.M. & Salazar, D. (2009). Ionosphere effect mitigation for single-frequency precise point positioning. In *22nd ITM of Satellite Division of ION Savannah, GA, September 2009*.

Angrisano, A., Gaglione, S., Gioia, C., Massaro, M., Robustelli, U. & Santamaria, R. (2011). Ionospheric models comparison for single-frequency gnss positioning. In *European Navigation Conference, 2011*.

Aragon-Angel, A., Orus, R., Amarillo, F., Hernandez-Pajares, M., Juan, J.M. & Sanz, J. (2005). Preliminary NeQuick assessment for future single frequency users of GALILEO. In *6th Geomatic Week, Barcelona, February 2005*.

Avila-Rodriguez, J.A., Wallner, S., Hein, G.W., Eissfeller, B., Irsigler, M. & Issler, J.L. (2007). A vision on new frequencies, signals and concepts for future GNSS systems. In *ITM of ION, forth Worth, TX, September 2007*.

Banville, S. & Langley, R.B. (2009). Improving real-time kinematic PPP with instantaneous cycle -slip correction. In *22nd ITM of the Satellite Division of ION, Savannah, GA, September 2009*.

Baroni, L., Kuga, H.K. & O'Keefe, K. (2009). Analysis of three ambiguity resolution methods for real time static and kinematic positioning of a GPS receiver. In *22nd International Meeting of th Satellite Division of The ION, Savannah, GA, Septemeber 2009*.

Beidou (2012). http://www.beidou.gov.cn, accessed 14 november, 2012.

Bensky, A. (2008). *Wireless positioning technologies and applications*. Artech House.

Beran, T., Kim, D. & Langley, R.B. (2003). High-precision single-frequency GPS point positioning. In *ION GPS 2003, September 2003, Portland Oregon*.

Beran, T., Langley, R.B., Bisnath, S.B. & Serrano, L. (2005). High-accuracy point positioning with low-cost GPS receivers: how good can it get? In *ION 2005, Long Beach, CA, 2005*.

Bhuyan, P.K. & Borah, R.R. (2007). TEC derived from GPS network in India and comparison with the IRI. *Advances in Space Research*, **39**, 830–840.

Bisnath, S.B. (2000). Efficient, automated cycle-slip correction of dual-frequency kinematic GPS data. In *Proceedings of ION GPS 2000, Salt Lake, Utah, September 2000*.

Bisnath, S.B. & Langley, R.B. (2001a). High-precision platform positioning with a single GPS receiver. In *ION GPS 2001, September 2001, Salt Lake, Utah*.

Bisnath, S.B. & Langley, R.B. (2001b). Pseudorange multipath mitigation by means of multipath monitoring and de-weighting. In *Proceedings of the International Symposium on Kinematic Systems in Geodesy, Geomatics and Navigation, 2001, Alberta, Canada, June 2001*.

Bisnath, S.B., Collins, J.P. & Langley, R.B. (1997). GPS multipath assessment of the Hibernia oil platform. Tech. rep., Cougar Helicopters Ltd.

Blewitt, G. (1990). An automatic editing algorithm for GPS data. *Geophysical Research Letters*, **17**, 199–202.

Braasch, M. & van Dierendonck, A.J. (1999). GPS receiver architectures and measurements. *Proceedings of the IEEE*, **87**, 48–64.

Braasch, M.S. (2001). Performance comparison of multipath mitigating receiver architectures. In *Proceedings of the IEEE Aerospace Conference, Big Sky, Mont, USA, March 2001*.

Bromiley, P.A. (2008). Tutorial: Least-squares fitting. Tech. rep., Internal Memo No. 2008-005, Imaging Science and Biomedical Engineering Division, Medical School, University of Manchester (www.tina-vision.net/docs/memos/2008-005.pdf).

Brown, R.G. & Hwang, P.Y. (2012). *Introduction to random signals and applied Kalman filtering with MATLAB exercises, fourth edition*. John Wiley and Sons Ltd.

Bykhanov, E. (1999). Timing and positioning with GLONASS and GPS. *GPS Solutions*, **3 (1)**, 26–31.

Carcanague, S., Julien, O., Vigneau, W. & Macabiau, C. (2011a). A new algorithm for GNSS precise positioning in constrained area. In *International Technical Meeting of The Institute of Navigation, San Diego, CA, January 2011, 24-26,*.

Carcanague, S., Julien, O., Vigneau, W. & Macabiau, C. (2011b). Undifferenced Ambiguity Resolution Applied to RTK. In *ITM of ION, Portland, OR, 2011*.

Chang, C.L. & Juang, J.C. (2008). An adaptive multipath mitigation filter for GNSS applications. *EURASIP Journal on Advances in Signal Processing*, **vol.2008, Article ID 214815**, 10 pages.

Chang, X.W., Yang, X. & Zhou, T. (2005). MLAMBDA: a modified LAMBDA method for integer least-squares estimation. *Journal of Geodesy*, **79**, 552–565.

Chen, K. & Gao, Y. (2005). Real-time precise point positioning using single frequency data. In *ION GNSS 2004, September 2005, Long Beach, CA*.

Choy, S. (2011). High accuracy precise point positioning using a single frequency GPS receiver. *Journal of Applied Geodesy, DOI 10.1515/JAG.2011.008*, **5**, 59–69.

Choy, S., Zhang, K. & Silcock, D. (2008). An evaluation of various ionospheric error mitigation methods used in single frequency PPP. *Journal of Global Positioning Systems*, **7**, 62–71.

Collins, J.P. (1999). An overview of GPS inter-frequency carrier phase combinations (available on-line: http://gauss.gge.unb.ca/papers.pdf/l1l2combinations.collins.pdf (accessed 16 may 2012)).

Colombo, O.L. (2008). Real-time, wide-area, precise point positioning using data from internet NTRIP streams. In *Proceedings of the ION GNSS 2008, Network RTK Session, Savannah, Georgia, September 2008*.

Cross, P.A. (1983). Advance least squares applied to position-fixing. In *Working paper No.6*, Department of Land Surveying, North East London Polytechnic, ISSN 0260-9142.

D. S. Coco, C.D.C., Dahlke, S.R. & Clynch, J.R. (1991). Variability of GPS satellite differential group delay biases. *IEEE Transactions on Aerospace Electron. Syst.*, **27**, 931–938.

Dai, Z., Knedlik, S. & Loffeld, O. (2008). Cycle-slip detection, determination, and validation for triple-frequency GPS. In *Proceedings of Position, Location and Navigation Symposium, 2008 IEEE/ION*.

Dai, Z., Knedlik, S. & Loffeld, O. (2009). Instantaneous triple-frequency GPS cycle-slip detection and repair. *International Journal of Navigation and Observation*, **doi: 10.1155/2009/407231**.

Dammalage, T.L., Satirapod, C., Kibe, S. & Ogaja, C. (2010). C/A code multipath mititgation at GPS base stations for improved DGPS corrections using wavelets. *Survey Review*, **42**, 240–255.

Datta-Barua, S., Doherty, P., Delay, S., Dehel, T. & Klobuchar, J. (2003). Ionospheric scintillation effects on single and dual frequency GPS positioning. In *Proceedings of ION GPS/GNSS 2003, September 2003, Portland OR.*

de Lacey, M.C., Reguzzoni, M. & Sanso, F. (2011). Real-time cycle slip detection in triple frequency GNSS. *GPS Sol*, **doi 10.1007/s10291-011-0237-5**.

de Lacy, M.C., Reguzzoni, M., Sanso, F. & Venuti, G. (2008). The Bayesian detection of discontinuities in a polynomial regression and its application to the cycle-slip problem. *Journal of Geodesy*, **82**, 527–542.

de Oliveria Carmago, P., Monico, J.F.G. & Ferreira, L.D.D. (2000). Application of ionspheric corrections in the equatorial region for L1 GPS user. *Earth Planets Space*, **52**, 1083–1089.

Devi, M., Barbara, A.K., Depueva, A. & Depuev, V. (2008). Preliminary results of TEC measurements in Guwahati, India. *Advances in Space Research*, **42**, 753–756.

Doherty, P.H., Delay, S.H., Valladares, C.E. & Klobuchar, J.A. (2000). Ionospheric scintillation effects in the equatorial and auroral regions. In *ION GPS 2000, September 2000, Salt Lake City, UT.*.

Euler, H.J. & Goad, C.C. (1991). On optimal filtering of GPS dual frequency observations without using orbit information. *Journal of*, **65**, 130–143.

Farah, A., Moore, T. & Hill, C.J. (2005). High spatial variation tropospheric model for GPS-data simulation. *Journal of Navigation*, **58**, 459–470.

Fath-Allah, T.F. (2010). A new approach for cycle slips repairing using GPS single frequency data. *World Applied Sciences Journal*, **8**, 315–325.

Feess, W.A. & Stephens, S.G. (1987). Evaluation of GPS ionospheric time-delay model. *IEEE Transactions on Aerospace and Electronic Systems*, **23**, 332–338.

Ferreira, T.G. & Dunes, F.D. (2007). Advanced multipath mitigation techniques for GNSS receivers. In *Ist Seminar - Portuguese Committee of URSI - "Radiocommunications - New paradigms and health impact", Lisbon, December 2007*.

GALILEOICD (2008). Galileo Open Service - Signal In Space Interface Control Document OS SIS ICD, draft 1, February. Tech. rep., European Space Agency/ European GNSS Supervisory Authority.

Gao, Y. & Liu, Z.Z. (2002). Precise ionospheric modelling using regional GPS network data. *Journal of Global Positioning Systems*, **1**, 18–24.

Gao, Y. & Wojciechowski, A. (2004). High precision kinematic positioning using single dual-frequncy GPS receiver. In *proceedings of the XXth ISPRS Congress, Istanbul, Turkey, July 2004*.

Garcia-Fernandez, M., Markgraf, M. & Montenbruck, O. (2008). Spin rate estimation of sounding rockets using GPS wind-up. *GPS Solutions*, **12**, 155–161.

Ge, L., Han, S. & Rizos, C. (2000). Multipath mitigation of continous GPS measurments using an adaptive filter. *GPS Solutions*, **4**, 19–30.

Gleason, S. & Gebre-Egziabher, D. (2009). *GNSS applications and methods*, chap. 1, 1–21. Artech House.

GPS-800A (2010). GPS Interface Specification IS-GPS-800. Tech. rep.

GPSICD (1997). Navstar GPS Interface Control Document. Tech. rep.

Groves, P.D. (2008). *Principles of GNSS, Inertial, and Multisensor Integrated Naigation Systems,*. Artech House.

Groves, P.D. (2013). *Principles of GNSS, Inertial, and Multisensor Integrated Naigation Systems, 2nd Edition (Submitted for publication in 2013)*. Artech House.

GUNTHER, C. & HENKEL, P. (2010). Reduced-noise ionosphere-free carrier smoothed code. *IEEE Transactions on Aerospace and Electronic Systems*, **46**, 323–334.

HAMMING, R. (1973). *Numerical Methods for Scientists and Engineers, 2nd Edition*. Dover Publications Inc., New York.

HARRIS, R.B. & LIGHTSEY, E.G. (2009). The effect of M-code multipath on ephemeris generation. In *22nd Int. Meeting of the Satelite Division of ION, Savannah, GA, September 2009*.

HATCH, R.R. (1982). The synergism of GPS code and carrier measurements. In *Proceedings of the 3rd International Geodetic Symposium on Satellite Doppler Positioning, New Mexico*.

HEGARTY, C.J. (2006). *Understanding GPS Principles and Applications*, chap. Appendix A, 663–664. Artech House.

HEIN, G.W., AVILA-RODRIGUEZ, J.A., WALLNER, S., PRATT, A.R., OWEN, J., ISSLER, J.L., BETZ, J.W., HEGARTY, C.J., LENAHAN, L.S., RUSHANAN, J.J., KRAAY, A.L. & STANSELL, T.A. (2006). MBOC: the new optimized spreading modulation recommended for Galileo L1 OS and GPS L1C. In *Proceeding of IEEE/ION PLANS, San Diego, CA, April 2006*.

HOFMANN-WELLENHOF, B., LICHTENEGGER, H. & WASLE, E. (2008). *GNSS Global Navigation Satellite Systems GPS, GLONASS, Galileo and more*. Springer-Wien New York.

HOQUE, M.M. & JAKOWSKI, N. (2007). Higher order ionospheric effects in precise GNSS positioning. *Journal of Geodesy*, **81**, 259–268.

HOREMUZ, M. & SJOBERG, L.E. (2002). Rapid GPS ambiguity resolution for short and long baselines. *Journal of Geodesy*, **76**, 381–391.

HUANG, Z. & YUAN, H. (2007). Improving the ionospheric delay correction of satellite-based augmentation systems in equatorial regions. *Advances in Space Research*, **39**, 1552–1558.

Hwang, P.Y., McGraw, G.A. & Bader, J.R. (1999). Enhanced differential GPS carrier-smoothed code processing using dual-frequency measurements. *Navigation*, **46(2),**, 127–137.

IGS (2012). International GNSS Service. *http://igscb.jpl.nasa.gov/components/prods.html*, accessed 4 March 2012.

Janssen, V. (2009). Understanding coordinate reference systems, datums and transformation. *International Journal of Geoinformatics*, **5**, 41–53.

Jentzsch, G., Knudsen, P. & Ramatschi, M. (2000). Ocean tidal loading affecting precise geodetic observations on Greenland: error account of surface deformations by tidal gravity measurements. *Phys. Chem. Earth (A)*, **25**, 401–407.

Jia, P. & Wu, L. (2001). An algorithm for detecting and estimating cycle slips in single-frequency GPS. *Chinese Astronomy and Astrophysics*, **25**, 515–521.

Jiang, Z. & Groves, P. (2012). GNSS NLOS and multipath error mitigation using advanced multi-constellation consistency checking with height aiding. In *ION GNSS, Nashville, Tennesse.*.

Joosten, P. & Tiberius, C. (2002). LAMBDA: FAQs. *GPS Solutions*, **6**, 109–114.

Kalyanaraman, S.K., Braasch, M.S. & Kelly, J.M. (2006). Code tracking architecture influence on GPS carrier multipath. *IEEE Transactions on Aerospace and Electronic Systems*, **42**, 548–561.

Kamimura, M., Tomita, R., Nagano, T., Chabata, A., Kubo, Y. & Sugimo, S. (2011). Detection of cycle slips and multipath in GNSS RTK precise point positioning. In *ITM of ION, Portland, OR, 2011*.

Kim, B.C. & Tinin, M. (2007a). Contributions of ionospheric irregularities to the error of dual-frequcency GNSS positioning. *Journal of Geodesy*, **81**, 189–199.

Kim, B.C. & Tinin, M.V. (2007b). Effect of ionospheric irregularities on accuracy of dual-frequency GPS systems. *Geomagnetism and Aeronomy*, **47**, 238–243.

Kim, D. & Langley, R.B. (2000). The multipath divergence problem in GPS carrier-smoothed code pseudorange. In *Proceedings of the 47th Annual Conference of the Canadian Aeronautics and Space Institute, Ottawa, May 2000*.

Kim, D. & Langley, R.B. (2001). Instantaneous real-time cycle-slip correction of dual-frequency GPS data. In *Proceedings of the International Symposium on Kinematic Systems in Geodesy, Geomatics and Navigation, Banff, Alberta, Canada, June 2001*.

Kim, D., Serrano, L. & Langley, R. (2006). Phase wind-up analysis: assessing real-time kinematic performance. *GPS World*, **17**, 58–64.

Kim, E., Walter, T. & Powell, J.D. (2007). Adaptive carrier smoothing using code and carrier divergence. In *ION NTM 2007, January 2007, San Diego, CA*.

Kleusberg, A., Georgiadou, Y., van dan Heuvel, F. & Heroux, P. (1993). Gps data preprocessing with dipop 3.0. Tech. rep., internal memorandum, Department of Surveying Engineering (now Department of Geodesy and Geomatics Engineering), University of New Brunswick.

Klobuchar, J.A. (1987). Ionospheric time-delay algorithm for single-frequency GPS users. *IEEE Transactions on Aerospace and Electronic Systems*, **23**, 325–331.

Klobuchar, J.A. & Kunches, J.M. (2003). Comparative range delay and variability of the earth's troposphere and the ionosphere. *GPS Solutions*, **7**, 55–58.

Konno, H. (2007). Dual-frequency smoothing for CAT III LAAS: performance assessment considering ionosphere anomalies. In *Proceedings of ION GNSS 2007, Fort Worth, TX, Septemeber 2007.*.

Konno, H., sam Pullen, Rife, J. & Enge, P. (2006). Evaluation of two types of dual-freqency differential GPS techniques under anomalous ionosphere conditions. In *Proceedings of ION National Technical Meeting, Monterey, CA, January 2006*.

Langley, R.B. (1998). GPS receivers and the observables. In *GPS for Geodesy*, Springer.

Lau, L. & Cross, P. (2006). A new Signal-to-Noise-Ratio based stochastic model for GNSS high precision carrier phase data processing algorithms in the presence of multipath errors. In *Proceedings of the ION ITM of the Satellite Division, Fort Worth, September 2006*.

Lau, L. & Cross, P. (2007). Investigations into phase multipath mitigation techniques for high precision positioning in difficult environments. *The Journal of Navigation*, **60**, 457–482.

Le, A.Q. & Teunissen, P. (2006). Recursive least-squares filtering of peseudorange measurements. In *European Navigation Conference, May 2006, Manchester, UK*.

Le, A.Q. & Tiberius, C. (2007). Single-frequency precise point positioning with optimal filtering. *GPS Solutions*, **11**, 61–69.

Lee, H.K. & Rizos, C. (2008). Position-domain Hatch filter for kinematic differential GPS/GNSS. *IEEE Transactions on Aerospace and Electronic Systems*, **44**, 30–39.

Lee, H.K., Rizos, C. & Jee, G.I. (2004). Design of kinematic DGPS filters with consistent error covariance information. *IEE Proc. - Radar, Sonar and Navigation*, **151**, 382–388.

Lee, H.K., Rizos, C. & Jee, G.I. (2005). Position domain filtering and range domain filtering for carrier-smoothed-code DGNSS: an anlytical Comparison. *IEE Proc. - Radar, Sonar and Navigation*, **154**, 271–276.

Lee, J., Pullen, S., Datta-Burua, S. & Enge, P. (2006). Assessment of nominal ionosphere spatial decorrelation for LAAS. In *Proceedings of IEEE/ION PLANS 2006, Coronado, CA, 2006*.

Leick, A. (2004). *GPS satellite surveying, 3rd edition*. John Wiley and Sons, Inc., New Jersey.

Liu, Z. (2011). A new automated cycle slip detection and repair method for a single dual-frequency GPS receiver. *Journal of Geodesy*, **doi 10.1007/s00190-010-0426-y**.

Lyons, R.G. (2011). *Understanding Digital Signal Processing, Third Edition*. Prentice Hall.

Ma, G. & Maruyama, T. (2003). Derivation of TEC and estimation of instrumental biases from GEONET in japan. *Annales Geophysicae*, **21**, 2083–2093.

Mallat, S. (2009). *A wavelet tour of signal processing*. AP Elsevier.

Manning, D.M. (2005). NGA GPS Monitor station high-performance Cesium frequency standard stability: from NGA Kalman filter clock estimates. In *Proceedings of the 37th Annual Precise Time and Time Interval (PTTI) Systems and Applications Meeting, August 2005, Vancouver, Canada*.

McDonald, K.D. (2002). The modernization of GPS: plans, new capabilites and the future relationship to GALILEO. *Journal of Global Positioning Systems*, **1**, 1–17.

McGraw, G.A. & Young, R.S.Y. (2005). Dual frequency smoothing DGPS performance evaluation studies. In *Proceedings of the ION NTM 2005, San Diego, CA*.

McGraw, G.A., Murphy, T., Brenner, M., Pullen, S. & Dierendonck, A.J.V. (2000). Development of the LAAS accuracy models. In *Proceedings of the ION GPS 2000, Salt Lake, UT, September*.

Misra, P. & Enge, P. (2006). *Global Positioning System signals, measurements, and performance, 2nd edition*. Ganja-Jamuma Press, Massachusetts.

Misra, P. & Enge, P. (2011). *Global Positionig System Signals, Measurements, and Performance*. Ganja-Jamuma Press, Massachusetts.

Mitra, S.K. (2006). *Digital signal processing a computer-base approach, 3rd edition*. McGraw-Hill Int.

Momoh, J.A. (2012). Time differencing and filtering technique for mitigating errors in GPS carrier phase and pseudorange observations. In *ION GNSS, September 2012, Nashville, TN*.

Morujao, D. & Mendes, V. (2008). Investigation of instantaneous carrier phase ambiguity resolution with GPS/GALILEO combination using the general ambiguity search criterion. *Journal of Global Positioning Systems*, **7**, 35–45.

NGIA (2012). http://earth-info.nga.mil/gandg/sathtml/satinfo.html, accessed 10 december, 2012.

Oaks, J., Senior, K., Largay, M., Beard, R. & Buisson, J. (2005). NRL analysis of GPS on-orbit clocks. In *Proceeding of the 2005 Joint IEEE International Frequency Control Symposium and Precise Time and Time Interval (PTTI) Systems and Applications Meeting, August 2005*.

Oaks, J., Buisson, J.A. & Largay, M.M. (2007). A summary of the GPS constellation clock performance. In *Proceedings of the 39th Annual Precise Time and Time Interval (PTTI) Meeting*.

Ogaja, C. & Satirapod, C. (2007). Analysis of high frequency multipath in 1-Hz GPS kinematic solutions. *GPS Solutions*, **11**, 269–280.

Opperman, B.D., Cilliers, P.J., McKinell, L.A. & Haggard, R. (2007). Developmnet of a regional GPS-based ionospheric TEC model for South Africa. *Advances in Space Research*, **39**, 808–815.

Ouzeau, C., Macabiau, C., Escher, A.C. & Roturier, B. (2007). Compliance of single frequency ionospheric delay estimation and cycle slip detection with civil aviation requirements. In *ION NTM 2007, San Diego, CA*.

Ovstedal, O. (2002). Absolute positioning with single-frequency GPS receivers. *GPS Solutions*, **5**, 33–44.

Paielli, R. & ARC (1987). Range filtering for sequential GPS receivers with external sensor augmentation [microform]. *Russell Pailli National Aeronautics and*

Space Administration, Ames Research Cente; National Technical Information Service, distibutor, Moffett Field, California..

Pany, T., Irsigler, M. & Eissfeller, B. (2005). S-curve shaping: a new method for optimum discriminator based code multipath mitigation. In *Proceedings of the ION International Technical Meeting (ION-GPS/GNSS'05), Long Beach, California, September 2005*.

Park, B. & Kee, C. (2005). Optimal Hatch filter with a flexible smoothing window width. In *ION GNSS 18th ITM of the Satellite Division, Long Beach, CA, September*.

Park, B., Sohn, K. & Kee, C. (2008). Optimal Hatch filter with an adaptive smoothing window width. *The Journal of Navigation*, **61**, 435–454.

Parkins, A.J. (2009). *Performance of precise marine positioning using future modernised global satellite positioning systems and a novel partial ambiguity resolution technique*. Ph.D. thesis, University College London.

Piriz, R., marta Cueto, Fernandez, V., Tavella, P., Sesia, I., Cerretto, G. & Hahn, J. (2006). GPS/GALILEO interoperability: GGTO, timing biases, and GIOVE-A experience. In *Proceedings of the 38th Annual Precise Time and Time Interval (PTTI) Meeting*.

Potukuchi, J., Bauer, P. & Rios, J. (2010). Global Navigation Sateliite System of systems implications for civil users. In *ITM of ION, Portland, OR, September*.

Proakis, J.G. & Manolakis, D.G. (1996). *Digital Signal Processing - Principles, Algorithm, and Applications*. Prentice Hall.

Radicella, S.M. (2009). The NeQuick model genesis, uses and evolution. *Annales Geophysics*, **52**, 417–422.

Ren, Z., Li, L., Zhong, J., Zhao, M. & Shen, Y. (2011). A real-time cycle-slip detection and repair method for single frequency GPS receiver. In *2nd International Conference on Networking and Information Technology IPCSIT 2011*.

Revnivykh, S. (2011). GLONASS status and modernization. In *6th International Committee on GNSS, September 2011*.

Rho, H. & Langley, R.B. (2005). Dual-frequency GPS precise point positioning with WADGPS corrections. In *Proceedings of ION GNSS 2005, 18th International Technical Meeting of the Institute of Navigation, Long Beach, CA, September 2005*.

Roberts, G.W., Meng, X. & Dodson, A.H. (2002a). Using adaptive filtering to detect multipath and cycle slips in GPS / accelorometer bridge deflection monitoring data. In *FIG XXII International Congress, TS6.2 Engineering Surveys for Construction Works and Structural Engineering, Washington DC, April 2002*.

Roberts, G.W., Meng, X., Dodson, A.H. & Cosser, E. (2002b). Multipath mitigation for bridge deformation monitoring. *Journal of Global Positioning Systems*, **1**, 25–33.

Rost, C. & Wanninger, L. (2009). Carrier phase multipath mitigation based on GNSS signal quality measurements. *Journal of Applied Geodesy*, **3**, 81–87.

RSA (2012). http://www.glonass-ianc.rsa.ru/en/glonass/, accessed 14 november, 2012.

RSS (2012a). http://spacecorp.ru/en/press/publications/item2738.php, accessed 10 december, 2012.

RSS (2012b). http://spacecorp.ru/en/press/publications/item2738.php, accessed 14 march, 2012.

RTCA (2004). Minimum Aviation System Performance Standards for Local Area Augmentation (LAAS). Tech. rep., RTCA SC-159, WG-4A, DO-245A.

Sardon, E. & Zarraoa, N. (1997). Estimation of total electron content using GPS data: How stable are the differential satellite and receiver instrumental biases? *Radio Science*, **32**, 1899–1910.

Satirapod, C., Khoonphool, R. & Rizos, C. (2003). Multipath mitigation of permanent GPS stations using wavelet. In *International Symposium on GPS/GNSS, Tokyo, 2003*.

Schaer, S., Gurtner, W. & Feltens, J. (1998). IONEX: The IONosphere map EXchange format Version 1 . In *Proceedings of the IGS AC Workshop, Darmstadt, Germany, February 1998*.

Sen, S. & Rife, J. (2008). Reduction of ionosphere divergence error in GPS code measurement smoothing by use of a non-linear process. In *Proceedings of Position, Location and Navigation Symposium, 2008*.

Shi, C., Gu, S., Lou, Y. & Ge, M. (2012). An improved approach to model ionospheric delays for single-frequency precise point positioning. *Advances in Space Research, doi:10.1016/j.asr.2012.03.016*.

Shin, K. & Hammond, J.K. (2008). *Fundamentals of signal processing for sound and vibration engineers*. John Wiley and Sons Ltd.

Simsky, A., Sleewaegen, J.M. & Hollreiser, M. (2006). Performance assessment of Galileo ranging signals transmitted by GSTB-V2. In *ITM of ION, Forth Worth, TX, September 2006*.

Smith, J.O. (2007). *Introduction to Digutal filters with Audio Applications*. BookSurge Publishing.

Somieski, A., Burgi, C. & Favey, E. (2007). Evaluation and comparison of different methods of ionospheric delay mitigation for future Galileo mass market receivers. In *ION GNSS 20th International Technical Meeting of the Satellite Division, Fort Worth, TX, September 2007*.

Souza, E.M. & Monico, J.F.G. (2004). Wavelet shrinkage: high frequency multipath reduction from GPS relative positioning. *GPS*, **8**, 152–159.

SpaceComm (2012). http://www.space.commerce.gov/gps/modernization.shtm, accessed 14 march, 2012.

Stein, J.Y. (2000). *Digital Signal Processing - a Computer Science Perspective*. Wiley & Sons.

Tapley, B.D., Schutz, B.E. & Born, G.H. (2004). *Statistical orbit determination*. Elsevier Academic Press.

Teunissen, P.J.G. (1995). The least-squares ambiguity decorrelation adjustment: a method for fast GPS integer ambiguity estimation. *Journal of Geodesy*, **70**, 65–82.

Ueno, M., Hoshinoo, K., Matsunaga, K., Kawai, M., Nakao, H., Langley, R.B. & Bisnath, S.B. (2001). Assessment of atmospheric delay correction models for the Japanese MSAS. In *Proceedings of the ION GPS, Salt Lake City, UT, September 2001*.

Vallado, D.A. (2007). *Fundamentals of Astrodynamics and Applications, Third Edition*. Microcosm Press, and Springer.

van Leeuwen, S.S., van der Marel, H., Tossaint, M. & Martelluci, A. (2004). Validation of SBAS MOPS troposphere model over the EGNOS service area. Tech. rep., National Aerospace Laboratory NLR.

Waller, P., Gonzalez, F., Hahn, J., Binda, S., Piriz, R., Hidalgo, I., Tobias, G., Sesia, I., Tavella, P. & Cerretto, G. (2008). In-orbit performance assessment of GIOVE clocks. In *40th Annual Precise Time and Time Interval PTTI Meeting, Virginia, December 2008*.

Walter, T., Datta-Burua, S., Blanch, J. & Enge, P. (2004). The effects of large ionospheric gradients on single frequency airborne smoothing filters for WAAS and LAAS. In *Proceedings of ION National Technical Meeting, San Diego, CA., January 2004*.

Wang, J., Stewart, M. & M.Tsakiri (2000). A comparative study of the integer ambiguity validation procedures. *Earth Planest Space*, **52**, 813–817.

Wang, J., Satirapod, C. & Rizos, C. (2002). Stochastic assessmnet of GPS carrier phase measurements for precise static relative positioning. *Journal of Geodesy*, **76**, 95–104.

Wang, J., wang, J. & Roberts, C. (2009). Reducing GPS carrier phase errors with EMD wavelet for precise static positioning. *Survey Review*, **41**, 152–161.

Wang, Z., Wu, Y., Zhang, K. & Meng, Y. (2005). Triple-frequency method for high-order ionospheric refractive error modelling in GPS modernization. *Journal of Global Positioning Systems*, **4**, 291–295.

Warren, D.L.M. & Raquet, J.F. (2003). Broadcast vs. precise GPS ephemerides: a historical perspective. *GPS Solutions*, **7**, 151–156.

Weill, L.R. (2003). Multipath mitigation: how good can it get with new signals? *GPS World,*, 106–113.

Weill, L.R. (2006). Achieving theoretical bounds for receiver-based multipath using Galileo OS signals. In *ITM of ION, Forth Worth, TX, September 2006*.

Weinbach, U. & Schon, S. (2009). Evaluation of the clock stability of geodetic GPS receivers connected to an external oscillator. In *22nd International Meeting of the Satellite Division of ION, Savannah, GA*.

Weinbach, U. & Schon, S. (2011). GNSS receiver clock modeling when using high-precision oscillators and its impact on PPP. *Advances in Space Research*, **47**, 229–238.

Xiaohong, Z. & Xingxing, L. (2011). Instantaneous re-initialization in real-time kinematic PPP with cycle slip fixing. *GPS Solutions*, **doi 10.1007/s10291-011-0233-9**.

Xu, D. & Kou, Y. (2011). Instantaneous cycle slip detection and repair for a standalone triple-frequency GPS receiver. In *ITM of ION, Portland, OR, 2011*.

Xu, G. (2003). *GPS theory, algorithms and applications*. Springer-Verlag Berlin Heidelberg New York.

Ya'acob, N., mardina Abdullah & Ismail, M. (2009). Multipath mitigation from GPS carrier phase observations using wavelet technique. *MASAUM Journal of Basic and Applied Sciences*, **1**, 426–430.

Yang, Y., Hatch, R.R. & Sharpe, R.T. (2004). GPS multipath mitigation in measurement domain and its applications for high accuracy navigation. In *ION GNSS 17th ITM of th Satellite Division, 21-24 September 2004, Long Beach, CA*.

Zhang, Y., Lee, S. & Chen, C. (2009). Achieving sub 20cm autonomous positioning accuracy using Nexteq PAD dual-frequency receivers. In *22nd International Meeting of the Satellite Division of The Institute of Navigation, Savannah, GA, Septemeber, 2009*.

Zhao, L., Li, L. & Zhao, X. (2009). An adaptive Hatch filter to minimize the effects of ionosphere and multipath for GPS single point positioning. In *Proceedings of the 2009 IEEE International Conference on Mechatronics and Automation, August 2009, Changchun, China*.

Zhenggang, H., Zhigang, H. & Yanbo, Z. (2008). A new Hatch filter to minimize the effects of ionosphere gradients for GBAS. *Chinese Journal of Aeronautics*, **21**, 526–532.

Zhong, P., Ding, X., Zheng, D. & Chen, W. (2008). Adaptive wavelet transform based on cross-validation method and its application to GPS multipath mitigation. *GPS Solutions*, **12**, 109–117.

Ziebart, M. & Dare, P. (2001). Analytical solar radiation pressure modelling for GLONASS using a pixel array. *Journal of Geodesy*, **75**, 587–599.

Ziebart, M., Adhya, S., Sibthorpe, A., Edwards, S. & Cross, P. (2005). Combined radiation pressure and thermal modelling of complex satellites: Algorithms and on-orbit tests. *Advances in Space Research*, **36**, 424–430.

Appendix A.

A.1. Updating the Mean of Code Error

Following from Equation (5.42), when there is no cycle slip in a current epoch's phase observation from satellite s, then

$$MP^s(L^s) = 2I^{s,0} - \lambda_1 N_1^s + D_1^s + e_{p_1}^s \tag{A.1}$$

as earlier stated. The mean of the past $L^s - 1$ values of the MP^s observable is simply computed as

$$\langle MP^s(1 : L^s - 1)\rangle = \frac{\sum_{k=1}^{L^s-1} MP^s(k)}{L^s - 1} \tag{A.2}$$

Thus,

$$(L^s - 1)\,\langle MP^s(1 : L^s - 1)\rangle = \sum_{k=1}^{L^s-1} MP^s(k) \tag{A.3}$$

When cycle slip occurs on a current epoch's phase observation of s, then Equation (A.1) modifies as follows

$$MP^s(L^s) = P_{IF}^s(L^s) - \psi_{IF}^s(L^s) = 2I^{s,0} - \lambda_1 N_1^s - \lambda_1 \triangle N_1^s + D_1^s + e_{p_1}^s \tag{A.4}$$

The difference between Equations (A.4) and (A.1) is the $-\lambda_1 \triangle N_1^s$ term in (A.4). To level the past epochs' MP^s values with the current epoch's MP^s value, this $-\lambda_1 \triangle N_1^s$ is added to all past epochs' values of MP^s. We can thus compute the

updated mean at the current epoch as

$$\begin{aligned}\langle MP^s(1:L^s-1)\rangle &= \frac{\left[\sum_{k=1}^{L^s-1}\{MP^s(k)-\lambda_1\triangle N_1^s\}\right]+MP^s(L^s)}{L^s-1}\\ &= \tfrac{1}{L^s}\quad [(L^s-1)\langle MP^s(1:L^s-1)\rangle + MP^s(L^s)] \end{aligned} \tag{A.5}$$

Equation (A.5) is given by Equation (5.43) in Section 5.4 as

$$\langle MP^s(1:L^s-1)\rangle = \frac{1}{L^s}\left[(L^s-1)\langle MP^s(1:L^s-1)\rangle + MP^s(L^s)\right]$$

A.2. Least Squares

Consider a functional model

$$f(y_l, x) = z_l - e_l \tag{A.6}$$

which relates the true observation, y_l, with the true parameters $n \times 1$ vector $x = [x_1, x_2, ...x_n]^T$ containing the true values of the n parameters in x, where the observed value of y_l is recorded as the observation, z_l, as it is corrupted by the error level, e_l. If $f(y_l, x)$ is a linear model comprised of the linear combination of the n parameters/variables, the aim of the LS algorithm is to estimate the unknown vector x. With q different linear observations available, and made $q \geq n$, then the vector of observations, $z = [z_1, z_2, ...z_q]^T$, and the vector of the true residual, r, are sets of linear equations represented in a matrix form as

$$Ax = z + r \tag{A.7}$$

As such, A is an $q \times n$ coefficient matrix called the design matrix, z is an $q \times 1$ vector and r is an $q \times 1$ vector. The LS algorithm vector estimate, $\bar{x}$, of x at a single observation epoch and the resulting estimation residual vector, $\bar{r} = [\bar{r}_1, \bar{r}_2, ...\bar{r}_q]^T$, are given as

$$\bar{x} = [A^T W A]^{-1} A^T W z \tag{A.8}$$

$$\bar{r} = A\bar{x} - z \tag{A.9}$$

where $W = C^{-1}$ is the weight matrix defined as the inverse of the covariance matrix of the observations in z while A has elements $A_{l,j} = \frac{\partial f(y_l,x)}{\partial x_j}$ for $j = 1, 2, ...n$ and $l = 1, 2, ...q$. By definition, the least squares estimate is that optimum set of the unknown variables/parameters that minimises the sum of the squares of the estimation residuals, i.e, the estimate that results in the minimum $(r^T W r)$ (see proof in Cross (1983)).

When $f(y_l, x)$ is non-linear in the unknown parameters of x, it is first linearised and the estimation process then involves iteration. At each iteration within a given observation epoch, the model is linearised as an approximation to a first-order Taylor series expansion about $\bar{x}^k$, where $\bar{x}^k$ is a vector of the provisional (assumed) values of the unknown variables x_j of x. Thus, denoting k as an iteration step count, and at every iteration, the first-order Taylor series expansion yields

$$f(y_l, x) \simeq f(y_l, x^k) + \sum_j^n \frac{\partial f(y_l, x^k)}{\partial x_j}(x_j - x_j^k) \simeq f(y_l, x^k) + \sum_j^n A_{l,j} \triangle x_j \tag{A.10}$$

$$b_l - e_l = f(y_l, x) - f(y_l, x^k) \simeq \sum_j^n A_{l,j} \triangle x_j \tag{A.11}$$

with

$$\triangle x_j = x_j - x_j^k \tag{A.12}$$

In Equation (A.11), $f(y_l, x) = z_l - e_l$ is an observation/observable value and $f(y_l, x^k)$ is the corresponding computed value with the x^k at the k^{th} iteration step ($k = [1, 2....]$). Hence $f(y_l, x) - f(y_l, x^k)$ is commonly referred to as the "observed-minus-computed" observable, and in terms of the residual r_l, Equation (A.11) can be rewritten as

$$b_l + r_l = \sum_j^n A_{l,j} \triangle x_j \tag{A.13}$$

The "observed-minus-computed" vector $b = [b_1, b_2, ...b_q]^T$ associated with q such non-linear observations that have been linearised, results in a set of linear equations

that can be represented in matrix form as

$$A\triangle x = b + r \tag{A.14}$$

that leads to the LS algorithm estimate, $\triangle\bar{x}$, as

$$\triangle\bar{x} = [A^T W A]^{-1} A^T W b \tag{A.15}$$

and The estimated $\triangle\bar{x}$ is the small increment (or correction) that is needed to 'adjust' the provisional $\bar{x}^k$ assumed and used in the current k^{th} iteration step. For the next iteration step, k increases to $k+1$, and the needed $\bar{x}^{k+1}$ is generated as

$$\bar{x}^{k+1} = \bar{x}^k + \triangle\bar{x} \tag{A.16}$$

This $(k+1)^{th}$ iteration step begins with $\bar{x}^{k+1}$ as the new provisional vector of the unknown variables used in the $(k+1)^{th}$ step linearisation as in Equation (A.10). Finally, within a few iteration steps when the solution converges or when a convergence criterion is satisfied, the iterative process is terminated and the $\bar{x}^{k+1}$ from the last $(k+1)^{th}$ iteration result from Equation (A.16) is accepted as the current epoch LS estimate of x. The estimation residual, as in the linear LS algorithm, thus becomes

$$\bar{r} = A\bar{x} - z \tag{A.17}$$

The iteration step count k is reset to 1 for any new set of observation/observables such as obtained from a new observation epoch. It should be noted in Equation (A.14) that the matrix A is a Jacobian matrix, which is a function of constants and the parameters; and the LS algorithm for a linear model does not require any initial assumed values of the unknown parameters, only the linearised LS does. Equation (A.15) results in the weighted LS estimate of x if C and consequently W are not identity matrices.

Weighted least squares are commonly used. Having equal weights or no weights on all code and phase observations/observables used in a LS algorithm, for instance, would be illogical. The weighting helps in placing reliabilities in the ob-

servations/observables; more reliable observations/observables usually with smaller variances, are weighted more than observations/observables with larger variances. This is because, the variance, being the inverse of the square of a weighting value, is a measure of the estimated uncertainty in an observation/observable.

A.3. Kalman Filtering

In simple terms, a Kalman filter (KF) could be described as a recursive observation processing algorithm that utilizes all available information, including the observations and a prori knowledge of the system, to estimate the unknown parameters or variables called the state, in such a manner that error is statistically minimized. It operates recursively on noisy or error contaminated observation/observable to produce a statistically optimal estimate of the underlying system state. Following from Brown & Hwang (2012), the Kalman filter considered optimal for linear system can be modelled by the dynamic model in the form

$$x(t) = \Phi(t, t-1)x(t-1) + w(t) \tag{A.18}$$

and the observation model in the form

$$z(t) = H(t)x(t) + v(t) \tag{A.19}$$

where $x(t)$ denotes the $n \times 1$ state vector that comprises all n unknown parameters to be estimated at current discrete epoch t; $\Phi(t, t-1)$ is the $n \times n$ state transition matrix for a discrete time step, relating $x(t-1)$ to $x(t)$; $w(t)$ is the $n \times 1$ process noise vector assumed with known covariance structure, and being the input noise contribution to the state vector from previous epoch $t-1$ to the current epoch t; $z(t)$ is the $q \times 1$ observation vector, where q is the number of observations or observables used at epoch t; H is the $q \times n$ design matrix giving the linear connection between the observation/observable and the state vector at epoch t; and $v(t)$ is the $q \times 1$ observation/observable error vector, assumed to be a sequence with known covariance structure and having zero crosscorrelation with $w(t)$. The covariance

matrices of $w(t)$ and $v(t)$ are denoted as $Q(t)$, the system noise covariance matrix, and $R(t)$, the measurement noise covariance matrix, respectively.

The KF algorithm, based on the estimated state variables and covariance matrix derived from the immediate past epoch, predicts the current-epoch state variables and their uncertainties (covariance matrix); and with the current epoch's observation that is essentially contaminated with some level of error, the KF produces the final estimate of the current epoch state variables through an update process that involves weighting the filter predicted values of the current state and the state values derived from the current observations/observables. This weighting is implied by the Kalman gain, which is a function of $H(t)$, $\Phi(t, t-1)$, $R(t)$ and $Q(t)$, and can be "tuned" to achieve particular performance. Further details can be obtained from Groves (2008); Brown & Hwang (2012). The sequential least squares method is actually a special case of the Kalman filter; it is a Kalman filter applied to parameters assumed not to change with time Cross (1983). Compared to the LS algorithm, the KF algorithm could be described as more complicated and with a higher processor load, even though it may be more efficient at dealing with measurements from multiple epochs. Unlike in the KF algorithm, the typical least squares estimation does not employ a dynamic model. However, the KF through its dynamic model, presents a means to effect the 'known' state dynamics that could help improve the estimation of the state variables.

The Bayes filter is often described as a form of Kalman filter, being a recursive algorithm that allows continuous update of state variables, based on the most recently acquired observation.